Models for IVIVE Risk Assessment of Airway Chronic Inflammation Targeting Cigarette Smoking
(喫煙を対象とした慢性炎症性呼吸器疾患の IVIVE 毒性評価モデル)

Akina Mori

Contents

Abbreviations

AhR	Aryl hydrocarbon receptor
AO	Adverse outcome
AOP	Adverse outcome pathway
ASL	Apical surface liquid
BM	Biomarker
BN	Bayesian network
BoC	Bronchus-on-a-Chip
COPD	Chronic obstructive pulmonary disease
CSE	Cigarette smoke extract
DAG	Directed acyclic graph
DBN	Dynamic Bayesian network
EGF	Epidermal growth factor
GBN	Gaussian Bayesian network
GCH	Goblet cell hyperplasia
IL	Interleukin
IVIVE	*In vitro* to *in vivo* extrapolation
KE	Key event
LOOCV	Leave-one-out cross validation
MIE	Molecular initiating event

MPPD	Multiple-Path Particle Dosimetry
NAMs	New approach/alternative methodologies
NHBE	Normal human bronchial epithelial cell
OoC	Organ-on-a-Chip
qAOP	Quantitative adverse outcome pathway
VUS	Volume under surface

Notes

List of publications related to the dissertation

The contents of *Chapter 1* are based on the article: Ito, S., Mukherjee, S., Erami, K., Muratani, S., Mori, A., Ichikawa, S., White, W., Yoshino, K., & Fallacara, D. (2024). Proof of concept for quantitative adverse outcome pathway modeling of chronic toxicity in repeated exposure. *Scientific reports*, 14(1), 4741.

The contents of *Chapter 2* are based on the article: Mori, A., Matsumoto, R., Ichikawa, S., Ishimori, K., & Ito, S. Enhancement of cigarette smoke extract-induced goblet cell hyperplasia exerted through IL-13 receptor α1 expression. *Toxicology letters*, under review.

The contents of *Chapter 3* are based on the article: Mori, A., Vermeer, M., van den Broek, L. J., Heijmans, J., Nicolas, A., Bouwhuis, J., Burton, T., Matsumura, K., Ohashi, K., Ito, S., & Kramer, B. (2024). High-throughput Bronchus-on-a-Chip system for modeling the human bronchus. *Scientific reports*, 14(1), 26248.

The contents of *Chapter 4* are based on the article: Mori, A., Ito, S., & Sekine, T. (2024). A revision of the multiple-path particle dosimetry model focusing on tobacco product aerosol dynamics. *International journal for numerical methods in biomedical engineering*, 40(3), e3796.

Preface

This thesis is the culmination of my research on airway chronic inflammation associated with cigarette smoking. My work aims to develop risk assessment methods utilizing *in vitro* to *in vivo* extrapolation (IVIVE) approaches, instead of relying on animal testing.

Chapter 1 presents a proof of concept for quantitative risk assessment using the quantitative adverse outcome pathway (qAOP) based on Bayesian network modeling. ***Chapter 2*** explores the mechanism of cigarette smoke-induced goblet cell hyperplasia (GCH), focusing on interleukin (IL)-13 receptor sensitivity *in vitro*. This approach helps mimic the presence of immune cells without co-culture. ***Chapter 3*** describes the development of an Organ-on-a-Chip with tubular-structured airway epithelial cells, called Bronchus-on-a-Chip (BoC), to reproduce stenosis *in vitro*. The BoC maintained high throughput, which is critical for toxicological risk assessment. ***Chapter 4*** introduces a revised Multiple-Path Particle Dosimetry (MPPD) model. The dosimetry of tobacco aerosol in the airway was estimated after a sensitivity analysis.

Every model introduced in this thesis contributes to the IVIVE risk assessment by enhancing the understanding of each mechanism in airway chronic inflammatory diseases. Furthermore, I believe that integrating these models will lead to an accurate qAOP model for airway chronic inflammatory disease associated with cigarette smoking without the need for animal testing.

General Introduction

1. Airway chronic inflammation

Airway diseases are a significant global health issue. Chronic obstructive pulmonary disease (COPD) was the fourth leading cause of death in 2021 (World Health Organization, 2024b), and asthma affected an estimated 262 million people in 2019 (World Health Organization, 2024a). A characteristic of airway diseases is their negative impact on breathing, which not only reduces quality of life but can also be fatal. These severe diseases, COPD and asthma, are caused by airway chronic inflammation. In these diseases, inflammation occurs in multiple areas of the airway, leading to various symptoms (Aghasafari *et al.*, 2019; Raby *et al.*, 2023; Sutherland & Martin, 2003; Welte & Groneberg, 2006). The human airway is composed of two parts: the upper respiratory tract, including the nose, pharynx, and larynx, and the lower respiratory tract, including the trachea, bronchi, bronchioles, alveolar ducts, and alveoli (Mete & Akbudak, 2018; Patwa & Shah, 2015). A representative symptom of airway chronic inflammation is airway stenosis, which is particularly evident in the bronchi (Esterly & Heard, 1965; Jeffery, 2004).

The airways, including the bronchi, are constantly exposed to the external environment through breathing. Lung epithelial cells serve as the first line of defense against atmospheric components, such as air pollutants and pathogens. A typical defense mechanism is mucociliary clearance, which extends from the trachea to just before the alveoli. The epithelia in this region include ciliated cells and mucus-producing cells (Chakraborty *et al.*, 2022). Goblet cells, a type of mucus-producing cell, produce fluids containing gel-forming mucins, MUC5AC and MUC5B, that capture airborne materials. Ciliated cells, which have cilia on the apical side of the epithelium, elevate airborne materials out of the body (Curran & Cohn, 2010; Davis & Wypych, 2021). An inflammatory response, such as the interleukin (IL)-4/13 axis, can perturb the mucociliary clearance. Irritated epithelial cells release cytokines that stimulate immune cells. Activated immune cells release IL-13 to promote mucin production, thereby protecting the airway surface from irritants (Gabryelska *et al.*, 2019; Gour & Wills-Karp, 2015; Hong *et al.*, 2020). However, when inflammation becomes chronic, this response becomes excessive, compromising normal organ function. In the bronchi, continuous

cytokine stimulation alters the epithelial cell population, leading to goblet cell hyperplasia (GCH). This results in mucus hyperproduction and thickening of the bronchial epithelial cell layer. Consequently, the airway tube becomes mucus-plugged and narrows, obstructing airflow and making breathing difficult (Angelis *et al.*, 2014; Raby et al., 2023; Saetta *et al.*, 2000).

2. Characteristics of cigarette smoke

Airborne materials such as cigarette smoke, air pollutants, allergens, and pesticides can irritate the airways (Hamid & Tulic, 2009; Li *et al.*, 2018; Mokarizadeh *et al.*, 2015). Previous epidemiological studies have shown that cigarettes are one of the risk factors for COPD, which disturbs airflow in the bronchi (Castaldi *et al.*, 2014; Kim *et al.*, 1998; Soriano & Rodríguez-Roisin, 2011; Yoshida & Tuder, 2007). With this background, regulators around the world, including the U.S. Food and Drug Administration and the European Commission, control the tobacco products in the market (U.S. Food and Drug Administration, 2024; European Commission, 2024). Although many studies have been conducted, there is still a need for research into the risks of tobacco products due to their complex characteristics. Cigarette smoke is composed of various constituents with different chemical properties, which induce different biological responses (Jaccard *et al.*, 2019; Takahashi *et al.*, 2018). Additionally, cigarettes are consumed daily by typical smokers. Chronic exposure to aerosol induces various responses over time. There are risk assessment methods for fundamental cell responses, such as cytotoxicity, mutagenicity, and genotoxicity (Gunduz *et al.*, 2025; Hashizume *et al.*, 2023; Takahashi et al., 2018). However, a comprehensive risk assessment method for chronic diseases, for which cigarette smoking is a risk factor, has not yet been established.

3. IVIVE for chronic disease

Inhalation animal testing has traditionally been used for modeling airway diseases and evaluating the effects of tobacco products, chemicals, pesticides, and pharmaceuticals (Pauluhn & Mohr, 2000; Sécher *et al.*, 2020; Wright *et al.*, 2008). However, extrapolating these results to human chronic inflammation is challenging. In the respiratory system, in addition to the species differences that are present in other organs, there are unique

species-specific differences, such as variations in breathing patterns and anatomical structures (Harkema *et al.*, 2006; Wu *et al.*, 2024; Zwicker *et al.*, 2018). Furthermore, the growing emphasis on animal welfare has driven the development of new approach methodologies (NAMs) (Krewski *et al.*, 2010).

In vitro to *in vivo* extrapolation (IVIVE) is an approach that integrates *in vitro* data to estimate *in vivo* responses (Bell *et al.*, 2018). This process measures cell-level or tissue-specific responses to a chemical *in vitro*. *In vivo* responses, such as disease development, cannot be estimated solely based on a single type of *in vitro* response. To estimate *in vivo* responses, IVIVE integrates various *in vitro* data using computational models.

Recently, the toxicological community, including regulators, has acknowledged the effectiveness of the adverse outcome pathway (AOP), which is a simplified pathway from a molecular initiating event (MIE) to adverse outcomes (AO) (Ankley *et al.*, 2009; Tollefsen *et al.*, 2014). AOP allows for focusing on major pathways that significantly contribute to the progression of adverse outcomes or diseases. While AOP can help in decision-making, such as the selection of assays that are fit-for-purpose, there was a need for a tool specifically designed for the quantitative risk assessment of chemicals and products. In response to this need, quantitative AOPs (qAOPs) have been developed (Paini *et al.*, 2022). However, the chronic inflammation associated with cigarette smoking is still more complex than what existing qAOP models can directly account for. This complexity arises because a single puff of cigarette smoke hardly becomes toxic immediately. Similar to the toxicity of chemicals such as heavy metals and pesticides (Mwilola *et al.*, 2020; Thompson *et al.*, 2017), their risk assessments must consider the accumulation of exposure. Therefore, especially for cigarette smoking, a qAOP model for airway inflammatory disease needs to include cumulative biological responses to repeated exposure as well as rapid biological responses.

4. *In vitro* models for airway chronic disease

Advanced *in vitro* models of the airway are employed for data collection instead of animal testing. A recent advancement in airway *in vitro* models is the three-dimensional (3D) culture model for the airway epithelium. In the 3D culture, airway epithelial cells are grown in an insert that maintains an air-liquid interface (Fig. 3.1a). When airway epithelial basal cells are cultured using this method, they differentiate into a

pseudostratified structure composed of basal, epithelial, and goblet cells, which resembles the structure of the bronchial epithelium (Hiemstra *et al.*, 2018; Prytherch *et al.*, 2011). Additionally, 3D-cultured airway epithelial cells are suitable for long-term culture, which can reproduce chronic conditions (Casalino-Matsuda *et al.*, 2006; Kistemaker *et al.*, 2015). These characteristics, human similarity and long-life, are advantageous for assessing airway chronic inflammation *in vitro*.

To further advance, Huh *et al.* (2010) reported the first Organ-on-a-Chip (OoC), which mimics lung surface stretching on a small chip. As demonstrated in this example, OoC reproduces the organ tissue environment by combining biological cell culture methods with chip engineering. One controversial point of OoC for the airway is its throughput capacity. While specialized devices allow for high organ similarity, most OoCs do not meet the requirements for high-throughput data collection (Gao *et al.*, 2024; Lagowala *et al.*, 2021; Park & Young, 2021). Toxicological assessments require high-throughput OoCs because these analyses are often conducted based on dose-response relationships.

Although there has been a notable advance in *in vitro* testing methods, not all phenomena in airway chronic inflammation are fully reproduced. Airway inflammation involves various types of cells. As stated in *Section 1*, not only airway tissue cells but also immune cells contribute to the pathogenesis. Therefore, co-culture with the specific immune cells responsible for the targeted disease is an essential factor to accurately reproduce the complex disease mechanisms. However, co-culture of different types of cells still requires significant effort for optimization. *In vitro* cultures require different nutrients and durations for response depending on the cell types. For example, the culture medium for specific cell types may result in unexpected phenotypic alterations in the co-cultured cells (Arigony *et al.*, 2013; Kimura *et al.*, 2023; Ochiai *et al.*, 2018). To utilize advanced *in vitro* culture systems, such as OoC, for IVIVE risk assessments, efforts to optimize culture methods should be further intensified.

5. Aerosol dynamics model in the human airway

For IVIVE, the chemical dose at the target tissue must be known to estimate the *in vivo* response. Besides the fact that the airway directly contacts aerosol without passing through other organs, the dynamics of aerosol inside the airway itself are complex because the aerosol travels from the mouth to the deep lungs through airway tubules branched at

different angles. There is a publicly available aerosol simulator called the Multiple-Path Particle Dosimetry (MPPD) model to estimate the deposition amount of single solid particles in the human airway (Anjilvel & Asgharian, 1995; Asgharian *et al.*, 2001). However, tobacco product aerosol contains multiple constituents, including solid particles, volatile gases, and semi-volatile droplets. Thus, the original MPPD model falls short in predicting tobacco product aerosol dosimetry. Furthermore, aerosol deposition is influenced by smoking behavior because dilution and mixing of aerosol with inhaled and residual air in the airway alter the dynamics of aerosol. To estimate the dynamics of tobacco product aerosol, a specific simulator that considers its complexity is required.

6. The purpose of this thesis

Airway chronic inflammation is linked to severe diseases; however, its risk assessment method is not fully established. Especially for the risk assessment of cigarette smoking, more effort is needed due to its complex mechanism. To advance in this area without animal testing, by adapting the IVIVE approach to disease risk, the following *in vitro* and *in silico* subjects are set:

1. Demonstration of the qAOP model of chronic disease using Bayesian network modeling with a hypothetical dataset.
2. Elucidating the relationship between cigarette smoke exposure and the sensitivity of airway epithelial cells to IL-13, aiming to include the inflammatory aspect in an *in vitro* model without co-culture.
3. Development of a high-throughput OoC for the bronchus, termed Bronchus-on-a-Chip (BoC), to mimic stenosis as a disease state response.
4. Revising the MPPD model by including formulae for detailed geometry, air mixing in the oral and deep lung, and transportation on the lung surface to optimize the aerosol dynamics of cigarette smoke.

7. The goal of this thesis and expected outcome

The goal of this thesis is to propose IVIVE methods for the toxicological risk assessments of airway chronic inflammatory diseases targeting cigarette smoking.

First, I evaluated a framework of qAOP for a quantitative risk assessment of chronic disease, considering dose-response and response-response relationships in repeated exposures. Bayesian network modeling was used to estimate the possibilities of each node based on a hypothetical dataset, which includes acute-phase and chronic-phase responses.

In the later stage of chronic inflammation, airway stenosis contributes to adverse outcomes as it can directly disturb breathing. There were two issues to overcome for the development of the stenosis model. One is the difficulty of co-culturing bronchial epithelial cells and immune cells. GCH results from the interaction between immune cells and epithelial cells. To model the effects of immune cells *in vitro*, interaction between epithelial cells and immune cells was researched in the context of GCH. The second issue is that a horizontal plane 3D airway model cannot reproduce airway stenosis. In this study, OoC is employed to mimic the microenvironment of the bronchus. Although existing airway OoCs are not optimized as high-throughput models, toxicological assessments require large sample sizes. I aimed to develop BoC, which has a tubular structure enabling the reproduction of airway stenosis while maintaining high-throughput.

For the estimation of risk *in vivo*, the exposure level should be known. However, no method can measure cigarette smoke dosimetry at the bronchi. An aerosol simulator in the human airway, the MPPD model, addresses this point. The MPPD model was originally developed for the simulation of solid particles' dynamics but can be modified to adapt to the dynamics of cigarette smoke. In this thesis, dosimetry of cigarette smoke is estimated using the revised MPPD model.

Models for airway chronic disease introduced in this thesis will provide data to help understand the risk of cigarette smoking-associated airway chronic inflammation from an IVIVE perspective. Furthermore, there is a possibility that qAOP will integrate data derived from an *in vitro* model considering the immune cell response, high-throughput BoC, and the simulator of dosimetry (Graphical Abstract). Based on this effort, this qAOP should become a powerful tool to assess the toxicological risk of airway chronic inflammatory disease from regulatory and other perspectives.

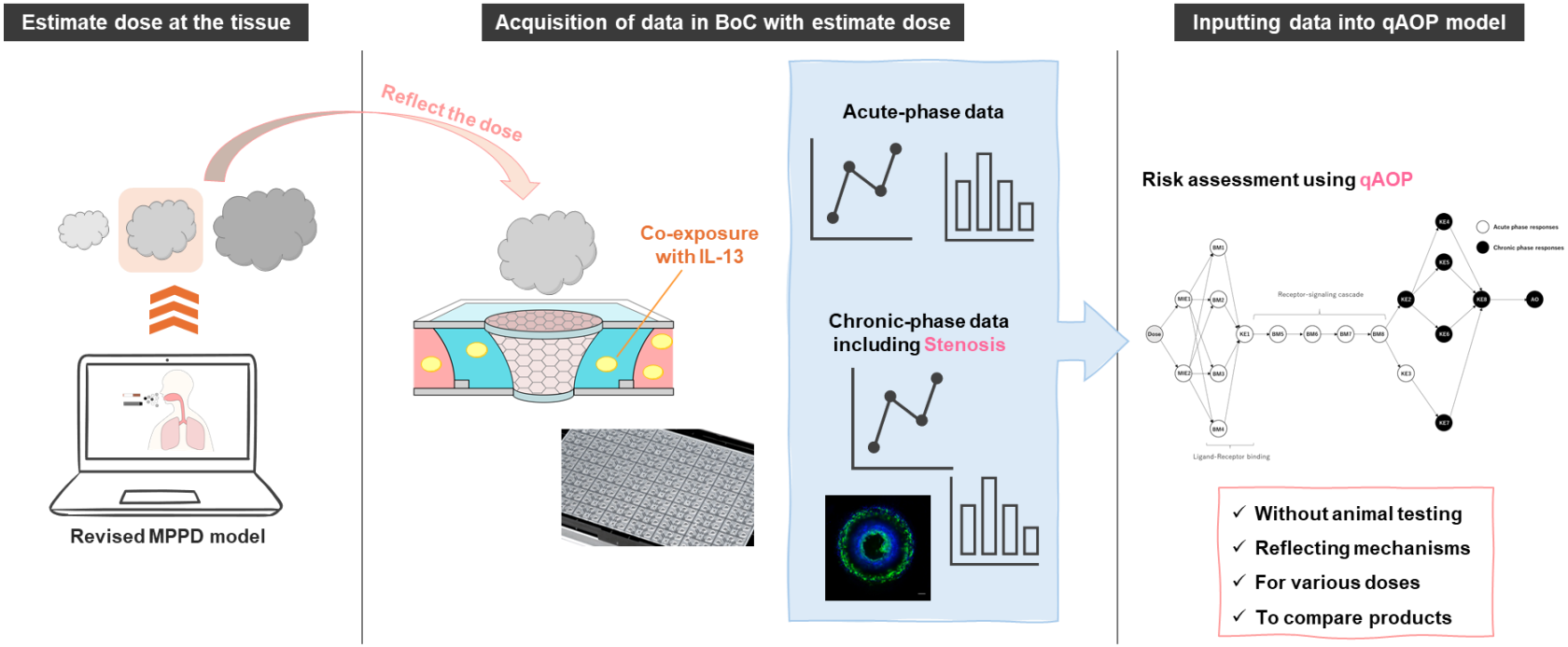

Graphical Abstract. Integration of IVIVE approach for risk assessment of cigarette smoking.

The deposition of cigarette smoke could be simulated using the revised Multiple-Path Particle Dosimetry (MPPD) model. Data reflecting the calculated concentration of cigarette smoke will be acquired in the Bronchus-on-a-Chip (BoC). The levels of goblet cell hyperplasia and stenosis in the BoC will be measured with the addition of interleukin (IL)-13 to mimic the presence of immune cells. Finally, the risk of adverse outcomes (AOs) could be estimated using the quantitative Adverse Outcome Pathway (qAOP) model by inputting the acquired data.

Chapter 1

Proof of concept for quantitative adverse outcome pathway modeling of chronic toxicity in repeated exposure

Abstract

The adverse outcome pathway (AOP) is a useful tool to understand the mode of action of a chemical. However, in order to use it for the purpose of risk assessment, an AOP needs to be quantified using *in vitro* or *in vivo* data. The majority of quantitative AOPs (qAOPs) developed so far have been for single exposures to progressively higher doses. Limited attempts have been made to include time in the modeling. Here, as a proof-of-concept, a hypothetical AOP was developed and quantified using a virtual dataset for six repeated exposures within a Bayesian Network (BN) analysis framework. The virtual data were generated using realistic assumptions. The effects of each exposure were analyzed separately using a static BN model and in combination using a dynamic BN (DBN) model. This work shows that the DBN model can be used to calculate the probability of adverse outcomes when other upstream key events (KEs) were observed earlier. These probabilities can help in the identification of early indicators of AO. In addition, a data-driven AOP pruning technique was developed using a lasso-based subset selection, and it showed that the structure of AOP is itself dynamic and changes over time. This proof-of-concept study revealed the possibility of expanding the applicability of the AOP framework to incorporate biological dynamism in toxicity appearance due to repeated insult.

1. Introduction

Regulatory agencies such as the U.S. Environmental Protection Agency (EPA), the U.S. Food and Drug Administration (FDA), the European Chemical Agency (ECHA), and others are adopting the use of new approach methodologies (NAMs) to reduce animal use as part of their 3Rs (refinement, reduction, and replacement) agenda (van der Zalm *et al.*, 2022). Fit-for-purpose *in vitro* NAMs are now used to interrogate a "system" at different layers of biological organization, from molecular to phenotypical. Integrating all this information together into a cohesive predictive model of an adverse outcome, however, is not so easy.

One solution to this problem is the adverse outcome pathway (AOP) framework (Ankley et al., 2009; Vinken, 2013). The AOP framework proposes a simplification of holistic and systemic approaches where an apical adverse outcome (AO) is causally linked to an early molecular initiating event (MIE), such as receptor binding or production of reactive oxygen species, by subsuming hundreds and thousands of intermediate biological processes, from molecular, cellular, to organism level, into a handful of causally linked intermediate key events (KEs).

Although the AOP framework is expected to be a crucial tool for regulatory decision-making, the qualitative nature of AOPs makes direct application in quantitative risk assessment challenging. This limitation highlights the need for quantitative AOPs (qAOPs) to bridge the gap between qualitative AOPs and the quantitative requirements of risk assessment. To circumvent this difficulty, several mathematical approaches were proposed and reviewed to render AOPs quantitative (qAOPs), starting from simple dose-response modeling to more complicated Bayesian network modeling and differential equation-based Systems Biology approaches (Alepee *et al.*, 2014; Perkins *et al.*, 2019; Spinu *et al.*, 2020). Bayesian network (BN) formalism gained popularity as it can harmonize different types of data, provide a robust paradigm for causal modeling, and can be used prospectively for exploring multiple hypotheses. BNs have been used in studies spanning reproductive toxicity, developmental neural toxicity, cardiotoxicity, kidney injury, etc. (Blanchette *et al.*, 2020; De Blasi *et al.*, 2021; Jeong *et al.*, 2018; Kirsten *et al.*, 2017; Moe *et al.*, 2021; Perkins et al., 2019; Spinu et al., 2020; Spinu *et al.*, 2022) (others can be found in Spinu's article in 2020). In particular, Elias *et al.* (2019) reported several options for qAOP modeling approaches for chronic toxicity, in which they applied the Dynamic Bayesian Network (DBN) approach for chronic kidney disease by adapting

time-series *in vitro* data into the qAOP model. However, the appearance of chronic toxicity/disease is often more complex, especially those associated with phenotypical changes in tissue or at the organ level from chronic exposure to low doses of chemicals. For example, very low-level exposure to cadmium is not a serious concern as cadmium is contained in food to some extent. However, repeated (chronic) exposure to even low doses of cadmium can cause severe health impacts (Qu *et al.*, 2012). Cigarette smoking is a known risk factor for chronic diseases, but a single puff is hardly a health risk. As such, while adverse outcomes typically arise following the rapid biological responses triggered by certain reactive chemicals, there are others that require cumulative biological reactions elicited by repeated and chronic exposure.

With the advancement of *in vitro* NAMs, it is now feasible to perform experiments that can probe chronic toxic endpoints from repeated exposures (Haswell *et al.*, 2021; Jennings *et al.*, 2004; Koppelstaetter *et al.*, 2004; Qu et al., 2012; Samardzija Nenadov *et al.*, 2022; Tratnjek *et al.*, 2021). Such technological innovations make it possible to expand the scope of the AOP framework: AOPs which consist of acute-phase responses and chronic-phase responses could be now realistic applications for risk assessment strategy if appropriate risk quantification methods are adopted.

Here, as a proof of concept, I developed a "hypothetical" AOP that has two distinct but interconnected modules, one for acute-phase KEs and the other for chronic-phase KEs (Fig. 1.1). It was assumed that the chronic-phase KEs can be elicited only after repeated/chronic exposures to an agent. Furthermore, in the context of repeated exposures, there is individual variation in the timing of manifestation of chronic toxicity, much like *in vivo*, where the onset of chronic toxicity may vary among donors of primary cells even under the same repeated exposure. To reflect this, in this proof-of-concept study, the timing of chronic toxicity appearance is varied for each donor. I used virtual data – generated using realistic assumptions – for this proof-of-concept study and quantified the AOP using a combination of static and dynamic Bayesian network formalisms (BN and DBN, respectively). The probabilities of adverse outcomes were suggested to be estimated based on the activation of upstream KEs earlier. I also used a data-driven AOP pruning approach to quantify the dynamic nature of causal links in an AOP, as well as how these links evolve as a function of repeated insults.

2. Methods

2.1. Notation convention

Exposure repetition is indexed by $e = 1,2,\ldots,E$. Donors are denoted by $n = 1,2,\ldots,N$. The dose (i.e., exposure concentration) is denoted by $d \in D$, where D is the set of all doses including non-treatment control. MIEs, KEs, BMs, and AO are collectively referred to as nodes and denoted by $v \in V$, where V is the set of all nodes. The total number of elements in a set is denoted by $|..|$; $|V|$ for example, stands for total number of nodes. Replicates for each donor will be denoted by $r = 1,2,\ldots,\mathcal{R}$. Matrices are written in double struck upper case letters: $\mathbb{X}_{M\times|V|}$ is a matrix with M rows and $|V|$ columns. Furthermore, a symbol such as $\mathbb{X}^{(e)}$ means a matrix $\mathbb{X}$ for a specific exposure repetition e. Similarly, $\mathbb{X}^{(e,n)}$ is understood as a matrix for a specific exposure repetition e and a donor n. Elements of a matrix and scalars in general are written in lower-case fonts. A vector is always a column vector and denoted in bold: $\boldsymbol{\beta} \in R^P$ is a vector with P components. A one vector, $\mathbb{1}_{P\times 1} \in R^P$, is a column vector of P ones. The transpose of a matrix or a vector is denoted by the capital letter T in the superscript. A node v is assumed to take continuous values and in Bayesian formalism, the probability that it takes a value x depends only on the values of its parents, i.e., $P\left(x^{(v)} \mid \boldsymbol{x} \in R^V\right) = P\left(x^{(v)} \mid \boldsymbol{x}^{(\Pi_v)} \in R^{|\Pi_v|}\right)$, where Π_v denotes the set of parents of node v.

2.2. Software and algorithms

Microsoft Excel was used for the generation of the primary dataset. All other analyses and visualizations were performed using R statistics software version 4.0.4. The algorithms and R packages used are summarized in Supplementary material 1.1.

2.3. Structure of hypothetical AOP

The network structure is shown in Fig. 1.1. To model chronic toxicity, I constructed a hypothetical AOP with two MIEs, two acute-phase KEs, eight acute-phase biomarkers (BMs), six chronic-phase KEs, and an AO. Activation of some biomarkers, such as ligands for receptor-ligand binding, and activation of downstream signaling molecules for signal

transduction are crucial for the elicitation of AO. They were included in the AOP and denoted as BMs. While BMs are usually not included in AOPs, they were included in this proof-of-concept study to highlight that additional assays capturing relevant endpoints upstream of or related to a specific KE are usually obtained in a lab. For example, one may collect activation of biomarkers in the MAP kinase pathway upstream of any apoptotic KE. Moreover, from a modeling point of view, any number of BMs can be included in the modeling if their wiring does not violate the fundamental assumption of Bayesian Network analysis, namely the generation of feedback loops and cycles. To keep the discussion as general as possible, biomarkers that lead to KEs are also included in the model. Specifically, BM1 through BM4 mimic ligands for KE1 (e.g., receptor activation), and BM5 through BM8 represent the downstream signal transduction cascade. KE2 and KE3 represent the products of signal transduction, but KE2 only appears in the chronic phase, while KE3 appears upon every exposure. Once a chronic-phase response appears, a series of chronic-phase responses simultaneously appear as a chain reaction. They have been collectively referred to as nodes (19 nodes in total). In this AOP, it was assumed that twelve biological events, including MIEs, acute-phase KEs, and biomarkers were elicited in a dose-dependent manner for every exposure repetition. Chronic-phase KEs were also elicited in a dose-dependent manner but only after being subjected to a given number of exposure repetitions. The specific timing of a chronic-phase KE varied across donors (Table 1.1).

2.4. Primary virtual date generation

For this proof-of-concept study, a fully virtual dataset was used rather than actual data because there are hardly any available data appropriate for chronic toxicity-related repeated exposure-based qAOP modeling.

The assumptions and parameters used for the primary virtual dataset are:

i. Four doses including non-treated control ($|D| = 4$), total number of donors $N = 8$, and the number of exposures $E = 6$

ii. Acute-phase biological responses (i.e., MIEs, KE1, KE3, and BM1 through BM8) show robust dose dependence for all exposures.

iii. The timing of appearance of chronic-phase responses (i.e., KE2 and KE4 through KE8, and AO) is donor-dependent (Table 1.1).

iv. Once elicited, chronic-phase responses also increase in a dose-dependent manner. They also exhibit a robust exposure-repetition dependence upon elicitation.

v. Denoting the replicate average and standard deviation of fold change at a dose d by $\bar{\boldsymbol{f}}^{(d)}$ and $\boldsymbol{s}^{(d)}$, $\boldsymbol{s}^{(d+1)}$ was assumed to be affected by the difference in $\bar{\boldsymbol{f}}^{(d)}$ and $\bar{\boldsymbol{f}}^{(d+1)}$: the larger the difference, the larger is $\boldsymbol{s}^{(d+1)}$.

vi. The fold changes follow a log-normal distribution.

First, the mean fold changes for all nodes for $d = 0$ (air control) were set to 1, i.e., $\bar{f}^{(v,d=0,n)} = 1\ \forall v, n$. Mean fold changes for subsequent doses and exposures for all acute-phase nodes (MIE, KE1, KE3, and all BMs) were then generated using the formulae $\bar{f}^{(d+1,v,n,e)} = \bar{f}^{(d,v,n,e)} + \zeta_d$ and $\bar{f}^{(e+1,v,n,d)} = \bar{f}^{(e,v,n,d)} + \zeta_e$ respectively, where $\bar{f}^{(d,e,n,v)}$ stands for mean fold change of node v of donor n at dose d, exposure e, and $\zeta_d \in U(0,1)$ and $\zeta_e \in U(0,0.2)$ are uniform random numbers. Denoting the onset time of a chronic response for a donor n by e_{ch}^n (Table 1.1), mean fold change for chronic-phase KEs were generated using the formulae above for exposure repetitions $e > e_{ch}^n$. For $e < e_{ch}^n$, the mean fold changes for the chronic-phase KEs were randomly populated using the formula $0.8 + 0.4\zeta \in U(0,1)$, thereby ensuring that they were not elicited. Similarly, standard deviation of acute-phase biomarkers for all exposures and chronic-phase biomarkers for $e > e_{ch}^n$ were generated using the formula $s^{(d+1,v,n,e)} = \left(\bar{f}^{(d,v,n,e)} + \zeta \times \left(\bar{f}^{(d+1,v,n,e)} - \bar{f}^{(d,v,n,e)}\right)\right)/(4 + 6\zeta)$, where $s^{(d+1)}$ is the standard deviation of fold change for that dose.

The mean fold changes of each node as functions of dose and exposure repetition for all $N = 8$ donors are summarized in Supplementary material 1.2.

2.5. Consideration of correlation co-efficient for resampling the primary dataset

For each donor, dose, and exposure repetition, the mean fold changes were log-transformed. I constructed the *mean log-fold change* vector $\boldsymbol{\mu}^{(n,e,d)} \in R^{|V|}$ such that its

components $\mu^{(n,e,d,v)}, v = 1,2,.,|V|$, were given by the formula

$$\mu^{(n,e,d,v)} = ln\left(\frac{\left(\bar{f}^{(n,e,d,v)}\right)^2}{\sqrt{\left(\bar{f}^{(n,e,d,v)}\right)^2+\left(s^{(n,e,d,v)}\right)^2}}\right) \qquad (1)$$

Biological responses elicited by a common stimulus are usually correlated with each other, especially when they show clear dose responses. Therefore, I accounted for response-response correlation at the donor level for each exposure repetition. Correlations were calculated from the primary dataset. The elements of response-response covariance matrix $\mathbb{O}_{|V|\times|V|}^{(n,e,d)}$, were given by

$$o_{vv'}^{(n,e,d)} = \left(\sigma^{(n,e,d,v)}\right)^2 = ln\left(1+\frac{\left(s^{(n,e,d,v)}\right)^2}{\left(\bar{f}^{(n,e,d,v)}\right)^2}\right) for\ v = v'$$
$$o_{vv'}^{(n,e,d)} = \rho_{vv'}^{(e)}\sqrt{o_{vv}^{(n,e,d)} * o_{v'v'}^{(n,e,d)}}\ for\ v \neq v' \qquad (2)$$

, where the correlation co-efficient $\rho_{vv'}^{(e)} = \sigma_{vv'}^{(e)}/\sqrt{\sigma_{vv}^{(e)} \times \sigma_{v'v'}^{(e)}}$.

Using Eq. (1) and Eq. (2), samples were drawn from a multivariate normal distribution $\mathcal{MN}\left(\boldsymbol{\mu}^{(n,e,d)}, \mathbb{O}_{|V|\times|V|}^{(n,e,d)}\right)$ for each donor, exposure repetition, and dose.

2.6. Bayesian updating approach for resampling the primary dataset

In addition, I considered the possibility that the data from a previous exposure repetition could be informative for the next exposure repetition. To account for that, causation between each node with a Gaussian Bayesian network (GBN) update scheme was explicitly introduced.

Commonly, parameter learning of a GBNs entails maximizing a Gaussian likelihood of the form $\mathcal{MN}\left(\boldsymbol{x}^{(v)}|\mathbb{X}_{M\times|\Pi_v|}\boldsymbol{\beta}+\beta_0,\sigma^2\mathbb{I}\right)$, where Π_v is the parent set of a node v, M is the number of samples, σ^2 is the residual, and $(\boldsymbol{\beta},\beta_0)$ are the parameters to be estimated. Maximum Likelihood Estimate (MLE) for a Gaussian likelihood is simply $\widehat{\boldsymbol{\beta}}_{\boldsymbol{OLS}}=\left({\mathbb{X}_{M\times\Pi_v}}^T\mathbb{X}_{M\times\Pi_v}\right)^{-\mathbf{1}}{\mathbb{X}_{M\times\Pi_v}}^T\boldsymbol{x}^{(v)}$ (ordinary linear regression estimates). Alternatively, $\boldsymbol{\beta}$ can be estimated by using a Gaussian prior of the form $\mathcal{MN}\left(\boldsymbol{\beta}|\boldsymbol{\beta}_{\boldsymbol{pr}},\mathbb{V}_{pr}\right)$. When σ^2 is known, the posterior of $\boldsymbol{\beta}$ is a multivariate Gaussian $\mathcal{MN}\left(\boldsymbol{\beta}|\widehat{\boldsymbol{\beta}}_{pos},\mathbb{V}_{pos}\right)$, where

$$\begin{aligned}\widehat{\boldsymbol{\beta}}_{pos}&=\mathbb{V}_{pos}\left({\mathbb{V}_{pr}}^{-1}\boldsymbol{\beta}_{\boldsymbol{pr}}+\frac{\mathbf{1}}{\sigma^2}{\mathbb{X}_{M\times\Pi_v}}^T\boldsymbol{x}_v\right)\\ \mathbb{V}_{pos}^{-1}&={\mathbb{V}_{pr}}^{-1}+\frac{1}{\sigma^2}{\mathbb{X}_{M\times\Pi_v}}^T\mathbb{X}_{M\times\Pi_v}\end{aligned}\qquad(3)$$

First, for each exposure e, dose d and donor n, I drew κ samples $\mathbb{X}_{\kappa\times|V|}^{(n,e,d)}\sim\mathcal{MN}\left(\boldsymbol{\mu}^{(n,e,d)},\mathbb{O}_{|V|\times|V|}^{(n,e,d)}\right)$. Then, I learned the parameters ${\widehat{\boldsymbol{\beta}}^{(n,e,d)}}_{pos}$ and ${\mathbb{V}^{(n,e,d)}}_{pos}$ iteratively using $\mathbb{X}_{\kappa\times\Pi_v}$ (relevant sub-matrix of $\mathbb{X}_{\kappa\times|V|}^{(n,e,d)}$) and Eq. (3) by replacing $\boldsymbol{\beta}_{\boldsymbol{pr}}$ and $\mathbb{V}_{pr}$ in Eq. (3) with ${\widehat{\boldsymbol{\beta}}^{(n,e-1,d)}}_{pos}$ and ${\mathbb{V}^{(n,e-1,d)}}_{pos}$ respectively. For the e=0, OLS estimate for $\boldsymbol{\beta}$ was used. Usually, σ^2 is unknown. Prior over σ^2 (Inverse Wishart distribution) can be used and standard results can be applied. Instead, it was pretended to know σ^2 by setting it to the ordinary least square estimate

$$\left(\hat{\sigma}^{(n,e,d)}\right)^2=\frac{{\boldsymbol{x}^{(v)}}^T\left(\boldsymbol{x}^{(v)}-\mathbb{X}_{\kappa\times|\Pi_v|}^{(n,e,d)}\widehat{\boldsymbol{\beta}}^{(e)}{}_{\boldsymbol{OLS}}\right)}{\kappa-|\Pi_v|}\qquad(4)$$

Please note that the causal structure of the AOP (Fig. 1.1) was explicitly used for estimating these parameters.

Subsequently, a virtual dataset $\mathbb{X}_{\mathcal{R}\times|V|}^{(n,e,d)}$ was constructed by resampling from this trained network using the standard formula $P\left(\boldsymbol{x}^{(v)}{}_{pred}|\mathbb{X}^{(test)},\sigma^2\mathbb{I}\right)=\mathcal{MN}\left(\boldsymbol{x}^{(v)}{}_{pred}|\mathbb{X}^{(test)}\widehat{\boldsymbol{\beta}}_{pos},\sigma^2\mathbb{I}+\mathbb{X}^{(test)}\mathbb{V}_{pos}\left(\mathbb{X}^{(test)}\right)^T\right)$. Replicate averaged virtual data $\boldsymbol{x}^{(n,e,d)}=\left(\left(X_{\mathcal{R}\times|V|}^{(n,e,d)}\right)^T\mathbb{1}\right)/\mathcal{R}\in R^V$ was used for all downstream analysis.

2.7. Dose-response and response-response analysis

Dose-response analysis was performed using a linear mixed model (LMM) with a donor-specific random effect of the form

$$\boldsymbol{x}^{(v,n,e)} = \beta_0 \mathbb{1}_{|D|\times 1} + \beta_1 \boldsymbol{d}_{|D|\times 1} + \gamma^{(n)} \mathbb{1}_{|D|\times 1} + \varepsilon \qquad (5)$$

, where $\gamma^{(n)} \sim \mathcal{N}(0, \sigma_n^2)$ is the random effect on the intercept. $\boldsymbol{d}$ is the vector of doses, and $\boldsymbol{x}^{(v,n,e)}$ is a replicate averaged fold-change vector for a given node v, donor n, and exposure repetition e.

For response-response relationships, two models were used, a) an LMM model with donor-specific random effect on the intercept, and b) a cubic polynomial model of the forms

$$\left.\begin{aligned} \boldsymbol{x}^{(v,n)} &= \left(\beta_0 + \gamma^{(n)}\right)\mathbb{1}_{|D|*E\times 1} + \beta_1 \boldsymbol{x}^{(v',n)} + \varepsilon \\ \boldsymbol{x}^{(v)} &= \beta_0 \mathbb{1}_{|D|*E*N\times 1} + \beta_1 \boldsymbol{x}^{(v')} + \beta_2 \left[\boldsymbol{x}^{(v')}\right]^2 + \beta_2 \left[\boldsymbol{x}^{(v')}\right]^3 + \varepsilon \end{aligned}\right\} \qquad (6)$$

, where $\left[\boldsymbol{x}^{(v')}\right]^2$, $\left[\boldsymbol{x}^{(v')}\right]^3$ imply element wise exponentiation. Owing to large number of possible pairs (v, v'), the data were not analyzed separately for each exposure repetition; instead, the combined dataset for all exposure repetition was analyzed.

2.8. Bayesian modeling and probability calculation of AO

Here, I looked at each exposure repetition separately. The underlying assumption here is that the time gap between successive exposures is much longer compared to the time scale associated with the emergence of the AO. Clearly, for chronic conditions, this assumption is not true. Yet, this hypothetical scenario was modeled as a proof-of-concept for acute conditions where such an assumption may find more merit. A GBN was used— a directed acyclic graph (DAG) $\mathcal{G} = (V, E)$, where V is the set of nodes and $\mathcal{E}$ is the set of edges between nodes in V. A DAG can be topologically ordered such that

the edges point from topological ancestors to their successors. In Bayesian formalism, the joint probability of a realization $\boldsymbol{x} \in R^{|V|}$ can be factorized as follows

$$P(\boldsymbol{x}) = \prod_{v=1}^{|V|} P\left(x^{(v)} \mid \boldsymbol{x}^{(\Pi_v)}\right) \qquad (7)$$

, where Π_v is the set of parents of node v, and $\boldsymbol{x}^{(\Pi_v)}$ is the value that they take. The likelihood $P\left(x^{(v)} \mid \boldsymbol{x}^{(\Pi_v)}\right)$ is given by $P\left(x^{(v)} \mid \boldsymbol{x}^{(\Pi_v)}\right) = \mathcal{N}\left(x^{(v)} | \boldsymbol{x}^{(\Pi_v)^T}\boldsymbol{\beta}, \sigma^2\right)$ where unknown parameter $\boldsymbol{\beta}$ is learned by fitting a linear regression model (Koller & Friedman, 2009; Scutari & Denis, 2014).

The DAG of the hypothetical AOP is shown in Fig. 1.2. Dose was included as a root node without parent nodes. Dose was assumed to be a continuous variable. The parameters of the model were learned by fitting the AOP to $\mathbb{X}^{(e)}$ (data for each exposure repetition) using a function from the bnlearn package called bn.fit (Scutari, 2010). The fitted parameter values are summarized in Supplementary table 1.1. The trained GBNs were resampled to estimate the probability of activation of KEs ($P(KE > \Delta | d \in [d \pm \varepsilon])$) for each exposure repetition using logic sampling. A typical $\Delta = log_{10} 2$ was chosen. I also varied Δ and the dose d to investigate how this probability changed as a function of d and Δ. The volume under the probability surface (VUS) was also calculated using the standard trapezoid rule.

2.9. Dynamic Bayesian modeling and probability of adverse outcome conditioned on activation of upstream chronic events at earlier exposure repetitions.

A dynamic Bayesian model (DBN) was developed to estimate transition probabilities of AO by conditioning it on the upstream events at a previous exposure repetition ($e - \tau$) using a multivariate Markov process of the form (Nagarajan *et al.*).

$$\boldsymbol{x}^{(e,v)} = \mathbb{X}^{(e-1,\Pi_v)}\boldsymbol{\beta}^{(e,v)} + \boldsymbol{\varepsilon}^{(e,v)} \sim \mathcal{N}(0, \sigma^2 \mathbb{I}) \qquad (8)$$

Diagrammatic representations of the logic and structure of DBNs are shown in Fig. 1.2. In brief, it was assumed that events at a previous exposure influenced events at the current exposure. For example, the amplitude of KE6 at $e = 4$ was influenced by its parent node, i.e., amplitude of KE2 at $e = 3$, which was in turn influenced by its parent node, BM8, at $e = 2$, so and so forth. It was further assumed that no causal links exist among nodes for the same exposure repetition. Formally, nodes at a given exposure e were conditionally independent of each other when their values at the previous exposure were known. Furthermore, it was assumed that values at present were only conditionally determined by values in the immediate past, i.e., $\boldsymbol{x}^{(e)} \leftarrow \boldsymbol{x}^{(e-1)}$ (Markov process), but not by remote pasts $e-2, e-3$, etc. The last two assumptions were not essential, but they were necessary to avoid the number of parameters from exploding and thereby rendering parameter learning unfeasible. In addition, dose was not included as a root node in this framework. I assumed that dose-MIE interaction, which for a vast majority of AOPs are ligand-receptor types of interaction, occurs at a timescale much faster compared to the time gap between successive exposures. As a result, the dose was treated as a discrete variable, and subsequently, all the doses were either pooled together or each of the three doses was examined separately.

Although time-series analysis typically assumes that the process is weakly stationary, weak stationarity criteria were relaxed as evidenced by the fact that $\boldsymbol{\beta}$ explicitly depended on the exposure repetition index e (see Eq. 8) and needed to be learned for each pair of exposure slices (for example, $\boldsymbol{\beta}^{(e=3)} \neq \boldsymbol{\beta}^{(e=5)}$: $\boldsymbol{\beta}^{(e=3)}$ was estimated using data from exposure slice $(e = 2, e = 3)$, whereas $\boldsymbol{\beta}^{(e=5)}$ was estimated using data from exposure slice $(e = 4, e = 5)$). Moreover, I also observed very strong correlations between chronic-phase responses (see Results section), which made straightforward interpretation of ordinary multivariate linear regression difficult. As subset selection algorithms would prune the causal links between nodes of AOP, they were not used here. Instead, ridge regularization was used (Hastie *et al.*, 2009). The parameters were learned using the glmnet package (Zou & Hastie, 2005) and the appropriate penalty λ^* was selected using leave-one-out-cross-validation (LOOCV). For this exercise, I used an activation cut-off $\Delta = log_{10} 2$. Combining data for all dose and donors, I numerically calculated **a)** $P\left(AO^{(e)} > \Delta \mid KE8^{(e-1)} > \Delta\right)$ for $e = 3,.,6$ (4 probabilities in total), **b)** $P\left(AO^{(e)} > \Delta \mid KE6^{(e-2)} > \Delta\right)$, $P\left(AO^{(e)} > \Delta \mid KE5^{(e-2)} > \Delta\right)$, $P\left(AO^{(e)} > \Delta \mid KE4^{(e-2)} > \Delta\right)$, $P\left(AO^{(e)} > \Delta \mid KE7^{(e-2)} > \Delta\right)$ for $e = 4,5,6$ (3 probabilities in total for each KEs), &

finally **c)** $P\left(AO^{(e)} > \Delta \mid KE2^{(e-3)} > \Delta\right)$, $P\left(AO^{(e)} > \Delta \mid KE3^{(e-3)} > \Delta\right)$ for $e = 5, 6$ (2 probabilities in total for each KEs) by resampling data from DBNs and using likelihood weighing. Probabilities of AO for specific dose was also calculated, $P\left(AO^{(e,d)} > \Delta \mid KE^{(e-\tau,d)} > \Delta\right)$, where the interaction strengths $\boldsymbol{\beta}$s were not only learned between successive exposure repetition slices but also for specific doses as shown below

$$\boldsymbol{x}^{(e,v,d)} = \mathbb{X}^{(e-1,\Pi_v,d)}\boldsymbol{\beta}^{(e,v,d)} + \boldsymbol{\varepsilon}^{(e,v,d)} \sim \mathcal{N}(0, \sigma^2\mathbb{I}) \qquad (9)$$

2.10. Data driven pruning of AOP

As an additional analysis, a data-driven approach was further implemented to restructure the AOP, where AOP in Fig. 1.1 was pruned using a subset selection strategy: for nodes regulated by more than one predictor node, I implemented a LOOCV-based lasso regularization that shrinks coefficients for uninformative or irrelevant predictors towards zero; for nodes that were regulated by a single predictor, I only included it if the p value of the slope parameter was < 0.05. The customized BN was further scrutinized to only include those nodes for which at least one path existed to AO (for example, if the path from KE6 ⟶ KE8 had a non-zero coefficient but KE8 ⟶ AO was zero, and since AO could not be reached from KE6 without visiting KE8, KE6 was pruned as well).

3. Results

3.1. Virtual data generation

The primary dataset was generated using a random number generation function to suit the assumptions described earlier (see Methods section 2.3). Because there are only a few real-life datasets for qAOP modeling of chronic toxicity, the primary dataset was considered as the ground truth. The generated primary dataset is summarized in Supplementary material 1.2. For a large number of replicates $r = 1,2,\ldots,\mathcal{R}$, the mean and the standard deviation of fold change, $\sum_r f^{(n,e,d,v,r)}/\mathcal{R}$, $\sum_r\left(f^{(n,e,d,v,r)} - \bar{f}^{(n,e,d,v)}\right)^2/\mathcal{R}$, would approach the mean fold change ($\bar{f}^{(n,e,d,v)}$) and standard deviation ($s^{(n,e,d,v)}$) in the primary dataset. However, for a small number of replicates (typically ~ 3), the small sample size effect can be significant. One way to account for small sample size is by using confidence intervals. Alternatively, one can re-sample a small number of samples $R \ll \mathcal{R}$ as discussed in the Methods section, and then take the replicate average of fold change $f^{(n,e,d,v,r)}$. In this study, the primary dataset was resampled using a Bayesian updating approach as described in the Methods section 2.5-2.6. As expected, the virtually generated dataset showed that the chronic-phase biomarkers were not readily activated, but after three successive exposure repetitions, moderate to high expression of chronic-phase responses was observed (Supplementary Fig. 1.1).

3.2. Dose-response and response-response relationship

Fig 1.3 shows the conditional R^2 values for dose-response and response-response modeling when LMM was used, and the standard training R^2 value for the polynomial regression model. As expected, the acute-phase nodes generally showed strong dose-response for all exposure repetitions, whereas the chronic-phase nodes started to show dose-response only for $e \geq 3$. Response-response analysis was performed on the combined dataset for all exposures using an LMM and a polynomial regression model. It was found that LMM outperformed the polynomial regression model overall (Fig 1.3), except for chronic-phase nodes, where they were comparable. Using analysis from LMM, it was observed that all acute-phase nodes were highly correlated with each other. Similarly, all chronic-phase nodes were also correlated with each other; however, there was a low correlation between acute-phase nodes and chronic-phase nodes (Fig. 1.3c).

3.3. Probability analysis with Bayesian modeling approach

GBNs were fitted to the data for each exposure repetition separately. Fig. 1.4 shows the R^2 values of those fits. Except for KE2 and KE7, R^2 values of other chronic KEs were consistently > 0.6 for exposure repetition $e = 3$ onwards. The fits for KE7 and KE2 did not perform well for any exposure repetition because they were both regulated by upstream acute-phase nodes KE3 and BM8 with which they were very poorly correlated (Fig. 1.4). R^2 values for other acute-phase KEs were also > 0.6 by and large.

GBNs were resampled, and the probabilities of KEs at a given dose, $P(v > \Delta | d \in [d \pm \varepsilon])$, were estimated using logic sampling. Fig. 1.5 shows these probabilities when the activation threshold was set to $\Delta = log_{10}2$. $P(KE1 > \Delta | d \in [d \pm \varepsilon])$ increased monotonically with d and showed a strong dose dependence for all exposure repetitions. Similarly, $P(KE3 > \Delta | d \in [d \pm \varepsilon])$ also increased but the dose dependence was not as strong as for KE1. As expected, probabilities $P(v > \Delta | d \in [d \pm \varepsilon])$ for the chronic-phase nodes, on the other hand, were practically zero for $e = 1, 2$, demonstrating that chronic-phase nodes were activated only after a certain exposure repetition. From $e = 3$ onwards, $P(v > \Delta | d \in [d \pm \varepsilon])$ for all chronic-phase nodes increased consistently with successive exposures ($P_{e=5}(v > \Delta | d \in [d \pm \varepsilon]) > P_{e=4}(v > \Delta | d \in [d \pm \varepsilon])$, and so forth), but did not show a strong dose dependence. Additionally, these probabilities were consistently higher than 30% only from e = 5 onwards. The choice of $\Delta = log_{10}2$ was ad hoc and applied uniformly across all KEs. I also varied Δ and estimated how probabilities $P(v > \Delta | d \in [d \pm \varepsilon])$ varied as a function of both the activation threshold and dose. The plots are shown in Supplementary Fig. 1.2. A more succinct way of visualizing these surfaces was by calculating the volume under the surface (VUS), $\int P(v > \Delta | d \in [d \pm \varepsilon])$. The VUS plot (Fig. 1.6) showed clearly that the VUSs for two acute-phase key events, KE1 and KE3, were comparable across exposure repetitions, highlighting that their activations were exposure repetition independent, but VUSs for chronic-phase KEs progressively grew with exposure repetitions post $e = 3$, showing once again that chronic-phase responses required repeated exposures for their activation (Fig. 1.6).

While this work was done using virtual data, it showed the kind of information researchers can extract from this type of modeling once *in vitro* data become available. This work also demonstrates that the qAOP formalism is highly flexible and can be used as a tool for prospective studies.

3.4. DBN modeling for AO probability calculation

3.4.1. general trend of pooled dose

I explored how the earlier activation of an upstream KE influenced AO subsequently. Formally, the transition probability $P(AO^{(e)} > \Delta \mid KE^{(e-\tau)} > \Delta)$ was estimated by first fitting the DBN (Eq. (8), and Fig. 1.2) to the data, resampling from the fitted DBNs, and finally estimating the probability using likelihood weighting. For the first part of this work, all doses were pooled together. As shown in Fig. 1.2, the arrows connect nodes between two successive exposure repetitions. It is worth repeating that unlike time-invariant time-series analysis, the strengths of interactions (the thickness of arrows) between two nodes were not constant, but changed dynamically with e. For example, the strength of interaction $KE8^{(e-1)} \longrightarrow AO^{(e)}$ was not the same for $e = 3$ and $e = 4$: the interaction strength was weak for $e = 3$, but strong for $e = 4$ and onwards (Fig. 1.7). It was observed that $P(AO^{(e)} > \Delta \mid KE8^{(e-\tau)} > \Delta)$ (denoted as $KE8^{(e-\tau)} \longrightarrow AO^{(e)}$ in Fig. 1.7), increased monotonically as $e \to E = 6$ for all $\tau = 1, 2,$ & 3. In addition, the activation of KE8 at or after e = 4 was highly predictive of an adverse outcome (~0.96). For KEs that were separated by $\tau = 2$, namely KE4, KE5, KE6, & KE7, a similar increasing trend was found: the probability of AO reached values close to 0.8 for $e - \tau$ =4. For $e - \tau$ =3, the probability of AO was approximately 0.6. KE3 is an acute-phase response in the model, and although it regulated KE7, they were poorly correlated (Fig. 1.4). Consequently, the probabilities $P(AO^{(e)} > \Delta \mid KE3^{(e-3)} > \Delta), e = 5,6$ were not expected to depend on the specific exposure repetition e. The analysis confirmed that indeed $P(AO^{(e=5)} > \Delta \mid KE3^{(e-3=2)} > \Delta) \cong (AO^{(e=6)} > \Delta \mid KE3^{(e-3=3)} > \Delta)$ (Fig. 1.7). $P(AO^{(E)} > \Delta \mid KE2^{(e=3)} > \Delta)$, oddly, was very close to 1. The reason remains unclear, but it may be because the outgoing degree (number of outgoing edges) for KE2 is the highest among all the chronic KEs.

3.4.2. Dose-specific trends

The general trends for dose-specific transition probabilities, $P(AO^{(e,d)} > \Delta \mid KE^{(e-\tau,d)} > \Delta)$, by and large met expectations: probabilities increased as $e \to E = 6$ for all $\tau = 1, 2, 3,$ and as the dose $d \uparrow$. Notable exceptions were-$P(AO^{(e=4,d=200)} > \Delta \mid KE6^{(e-2=2,d=200)} >$

$\Delta)$, and $P(AO^{(e=5,d=200)} > \Delta \mid KE2^{(e-3=2,d=200)} > \Delta)$ (Fig. 1.8a). One plausible explanation is that the DBNs were fitted with only eight donor-level data points for each dose, rendering them error-prone. A deep dive was taken to visualize log-fold changes of $AO^{(e=3,d)}$ vs $KE8^{(e-1=2,d)}$ for all three doses (Fig. 1.8b). For such an early exposure ($e = 3, e-1 = 2$), chronic responses were not elicited, and no correlation between the two chronic events was expected. Yet, a positive correlation was found for low doses but a negative correlation at mid and high doses between AO and KE8. These inconsistent correlations were considered purely coincidental and artifacts of the small sample size.

3.5. Data-driven AOP restructuring

I also developed a data-driven AOP restructuring method based on lasso regression: an interaction was considered important if pruning that interaction resulted in a significant decline in the quality of the fit. To accomplish the task of pruning, the GBNs were parameterized using Lasso regression (Methods section 2.10). For nodes with only one parent regulator, the interaction was preserved if the p value of the slope parameter was < 0.05.

In the repeated dosing study, it could be expected that the strength of causal links would vary based on exposure repetitions. In addition, changes in the causal relationships could result in some of the predictors becoming uninformative. The data-driven pruning of DBNs is shown in Fig. 1.9a. The uninformative predictors and their links are shown in gray. It was found that KE8 at $e = 2$ did not exert any influence on AO at $e = 3$: the probability of AO at $e = 3$ was conditionally independent of KE8, i.e., $P(AO^{(e=3)} > \Delta | KE8^{(e=2)} > \Delta) = P(AO^{(e=3)} > \Delta)$. For all subsequent exposure slices, KE8 exerted influence on AO outcomes. Similarly, it was found that KE4, KE5, KE6, and KE7 at $e = 2$ had no bearing on AO at $e = 4$; KE4 and KE5 at $e = 3$ conditionally influenced AO at $e = 5$. All these KEs were conditional determinants of AO only for $e = 6$. KE3 was never a conditional determinant, and KE2 at $e = 3$ influenced AO at $e = 6$ but not for any earlier time slices. This data-driven remodeling enabled the reevaluation of transition probabilities and the extraction of only the relevant conditional probabilities ($P(AO^{(e)} > \Delta | KE^{(e-\tau)} > \Delta) \neq P(AO^{(e=3)} > \Delta)$), as shown in Fig. 1.9b. It was suggested that while the numerical values of transition probabilities were slightly different from the DBN with the whole AOP structure, their qualitative characteristics were still the same:

$P\left(AO^{(e)} > \Delta | KE8^{(e-1)} > \Delta\right)$ was very high for $e \geq 4$; $P\left(AO^{(e)} > \Delta | KE5^{(e-2)} > \Delta\right)$ was $\gtrsim$ 0.8 for $e = 5$ but went down to ~ 0.7 for $e = 6$; $P\left(AO^{(e)} > \Delta | KE4^{(e-2)} > \Delta\right)$ increased from 0.5 for $e = 5$ to ~ 0.8 for $e = 6$; $P\left(AO^{(e)} > \Delta | KE6^{(e-2)} > \Delta\right)$ was ~ 0.8 for $e = 6$ and it was the only instance when AO was conditionally dependent on KE6; $P\left(AO^{(e)} > \Delta | KE7^{(e-2)} > \Delta\right)$ was ~ 0.6 for $e = 6$; $P\left(AO^{(e)} > \Delta | KE2^{(e-3)} > \Delta\right)$ ~ 1 for $e = 6$. A possible explanation for this high value was discussed in the previous section.

4. Discussion

The goal of the AOP framework is to provide a principled approach to better understand the pathway to adverse outcomes by synergistically integrating information from different layers of biological organization and advancing a more informed testing strategy (Ankley et al., 2009). Owing to its flexibility and its ability to ingest information, not just from *in vivo* animal models but also from *in vitro* new approach methodologies, the AOP framework has emerged as a powerful tool for chemical testing and risk assessment. Cost-effective *in vitro* methods enable toxicologists to collect information from different layers of biological organizations that can then be integrated into a cohesive AOP framework and used as a roadmap for adverse outcomes. Over the years, the number of expert-derived AOP submissions has grown (https://aopwiki.org/). There are several AOPs that deal with chronic toxicity as the AO, however, AOPs that deal with repeated exposure and donor-dependent onset of chronic events are still sparse. One reason for this humble showing could be the difficulty in AOP representing the dynamism of biological pathway perturbation during repeated exposure to stimuli. Regardless, the dearth of repeated exposure-related AOPs that deal with acute-phase and chronic-phase KEs differently and account for donor-dependent onset of chronic events, needs to be addressed.

Additionally, the generation of data alone is not sufficient. Data arising from molecular to phenotypic levels need to be integrated and interpreted unambiguously to truly render an AOP useful. Moreover, the associations between different layers of biological organization need to be quantified and made clear. How these associations evolve over different exposure repetitions needs to be quantified. Only a principled quantitative approach can achieve this.

To demonstrate the utility of a chronic qAOP framework by taking repeated exposure into consideration, a hypothetical AOP with acute-phase responses (KEs and BMs), chronic-phase KEs, and AO was used. As mentioned, BMs are involved in this hypothetical AOP because some secondary measures outside the AOP could be also obtained in real experimental situations, and they could be informative of AOP perturbation. Separation of acute-phase KEs and chronic-phase KEs/AO enabled the consideration of the dynamism of biological perturbation. A virtual dataset was generated to quantify this AOP. In generating this dataset, it was assumed that the chronic KEs were initiated only after repeated insults, whereas the acute KEs were readily activated. In this study, a six-time repeated exposure study was assumed as a proof of concept, although

user-defined study designs are acceptable for the model. The acute KEs showed a strong dose-response, while the chronic KEs showed a dose-response and exposure repetition-response only after they were activated. It was further assumed that the onset of chronic KEs varied from donor to donor, as *in vitro* models with which the researcher can perform repeated exposure studies are often composed of primary cells. Primary cells generally possess their original characteristics and could thus show donor-dependent variation in response to the same stimuli (Bovard *et al.*, 2020; Jetten *et al.*, 2016; Mori *et al.*, 2022).

Using a GBN, several pertinent questions regarding the probability of an adverse event can be answered quantitatively, and the qAOP model can be used prospectively in risk assessment. Specifically, the GBN model calculated probabilities of KEs and AO to be activated above a certain threshold Δ given a dose d and an exposure repetition e. Various Δ, and d were set, and the probability of KEs change was investigated. While what constitutes a threshold is debatable and subjective, one quick way to estimate Δ can be from the dose-response curve. The point here is that even when Δ is unknown, the BN framework gives the flexibility to prospectively study the effect of varying Δ on probabilities of KEs and AOs. Therefore, the function was implemented to depict the changes in probability as a three-dimensional plot. The volume under the cumulative distribution (i.e., volume under the probability surface, VUS) can then be calculated as an index of AOP perturbation with varied Δ (Fig. 1.6). The result of the VUS calculation demonstrates that acute KEs and chronic KEs behave very differently: the VUS of acute KEs does not change significantly with exposure repetitions, whereas VUS for chronic KEs show strong exposure repetition dependence. The point to note is that this proof-of-concept study utilizes virtually generated data; real biological samples may not be as conclusive. The most important point here is that the approach enables the formulation of different types of analysis, as the model demonstrates what was intuitively clear: the probability of chronic-phase outcomes increases with repeated exposure.

The DBN and the repeated exposure data were used to estimate the probability of AO being activated when a certain KE was activated earlier (transition probability). The earlier activation of chronic KEs can be used as a reliable proxy for later AO activation. Not surprisingly, the closer the proximity of the KE to the AO node, the better predictor it was of AO activation. It was also demonstrated what can happen when acute-phase events are poorly correlated with chronic events. Such an information bottleneck, when present, can seriously limit the ability to infer the likelihood of AO based on early evidence of acute-phase responses. As is clear from Fig. 1.7 and Fig. 1.8a (P(AO> cut off | KE2>

cut off), inference of AO can be compromised when based solely on upstream events that are information bottlenecks. These transition probabilities also showed a clear dose dependence. Furthermore, the data-driven restructuring of AOP showed the possibility to eliminate uninformative KEs from the probability calculations. This approach would help in reducing the calculation cost and complexity of the AOP in repeated-exposure-oriented chronic toxicity. Using lasso-based pruning, it was demonstrated that the wiring in an AOP is itself dynamic, changing over time (Fig. 1.9). Such flexibility is well known in biology and must be taken into account when drawing inferences on AO. Here, the DBN method can be used in the detection of early events that are strong proxies for AO. The DBN formalism is extremely flexible and very pertinent for biology in general because it can model feedback loops that are ubiquitous in any biological process. While I fully acknowledge that all the potential confounders of a real dataset were not incorporated, I believe that the *in silico* approach can serve as a proof of concept and highlight that several specific questions regarding an adverse event, including dose- and early response-dependent probabilities of adverse outcomes, can be answered quantitatively.

The current study utilizes a hypothetical AOP with two MIEs. Typically, AOPs do not have multiple MIEs. The reasons for having two MIEs are really two folds. First, multiple assays can be used to measure an MIE. While it is entirely feasible to combine all these endpoints, nothing in principle prevents them from being treated separately for modeling. Second, having multiple MIEs in the framework enables this method to be seamlessly translated to an AOP-network scenario, where multiple MIEs can influence a downstream KE (Burgoon *et al.*, 2020).

In addition, using high-throughput screening assays and high-content imaging, molecular and phenotypic endpoints can be captured more intensively than ever. AI and machine learning (ML) approaches with these data streams could be highly compatible with the AOP framework. So far, inference of outcomes by stimulation is largely dependent on molecular-level information, thus limited to early and apical outcomes. However, AOPs provide a natural framework for the integration of molecular, phenotypic, and organ-level information. qAOPs – quantified using HTS, HC imaging, and other NAM data – can be used for the estimation of AO conditioned on early evidence. Here, two such scenarios are shown in Fig. 1.5 and Supplementary Fig. 1.2. In principle, evidence of arbitrary complexity can be modeled. For prospective studies, qAOP can be used to simulate perturbations and test alternate hypotheses. qAOP wirings can be altered *in silico*, and

various scenarios that can potentially decrease the likelihood of AO can be explored. Furthermore, and most importantly, qAOPs can be used for data-poor chemicals as a read-across by considering qAOPs of structural analogs.

For the practical implementation of NAMs, including qAOP models, within the regulatory framework, several key points need to be addressed. It is crucial to promote the evolution of science through knowledge sharing by reusing both input and output data across different studies. Therefore, the use of a common reporting template is essential (Carnesecchi *et al.*, 2023). Additionally, the modeling approach should always be evaluated in terms of its domains of applicability, potential bias, and level of certainty or uncertainty (Brozek *et al.*, 2021). When focusing on qAOP modeling, transparency in the modeling approach, dataset, and their quality and reliability is of utmost importance for decision-making (Paini et al., 2022). To this end, guidelines and workflows have already been proposed, and researchers are encouraged to follow them when using qAOP models, including the models developed in this study. By adhering to these practices, greater consistency and reliability can be ensured in the application of qAOP models in regulatory decision-making processes.

5. Short summary

Although several reports have attempted to model chronic toxicity (Conolly *et al.*, 2017; Elias et al., 2019), they mostly rely on a simple sequence from MIE through AO, in which cumulative effects are not modeled. Here, I demonstrated that BN and DBN formalisms could enable the incorporation of cumulative effects as well as repeated perturbations of biological pathways. This means that the AOP structure itself could become dynamic, as KEs can be annotated as acute or chronic phases. I believe the proof-of-concept study was able to explore the possibility that the AOP framework could be expanded for more flexible toxicity considerations. However, it should be acknowledged that this model was developed with a virtual setup (i.e., a hypothetical AOP with a virtual dataset). To develop a practical qAOP, inputting actual data is essential. The concept of the AOP framework could be a future application for the risk assessment of chronic diseases if relevant *in vitro* NAMs and AOPs are available.

Figures and tables

Table 1.1. Assumption of donor dependent appearance of chronic toxicity.

Donor	Appearance of chronic toxicity	Severity
1	Exposure rep 4	Severe
2	Exposure rep 3	Severe
3	Exposure rep 4	Moderate
4	Exposure rep 3	Moderate
5	Exposure rep 4	Weak
6	Exposure rep 3	Weak
7	No	No
8	No	No

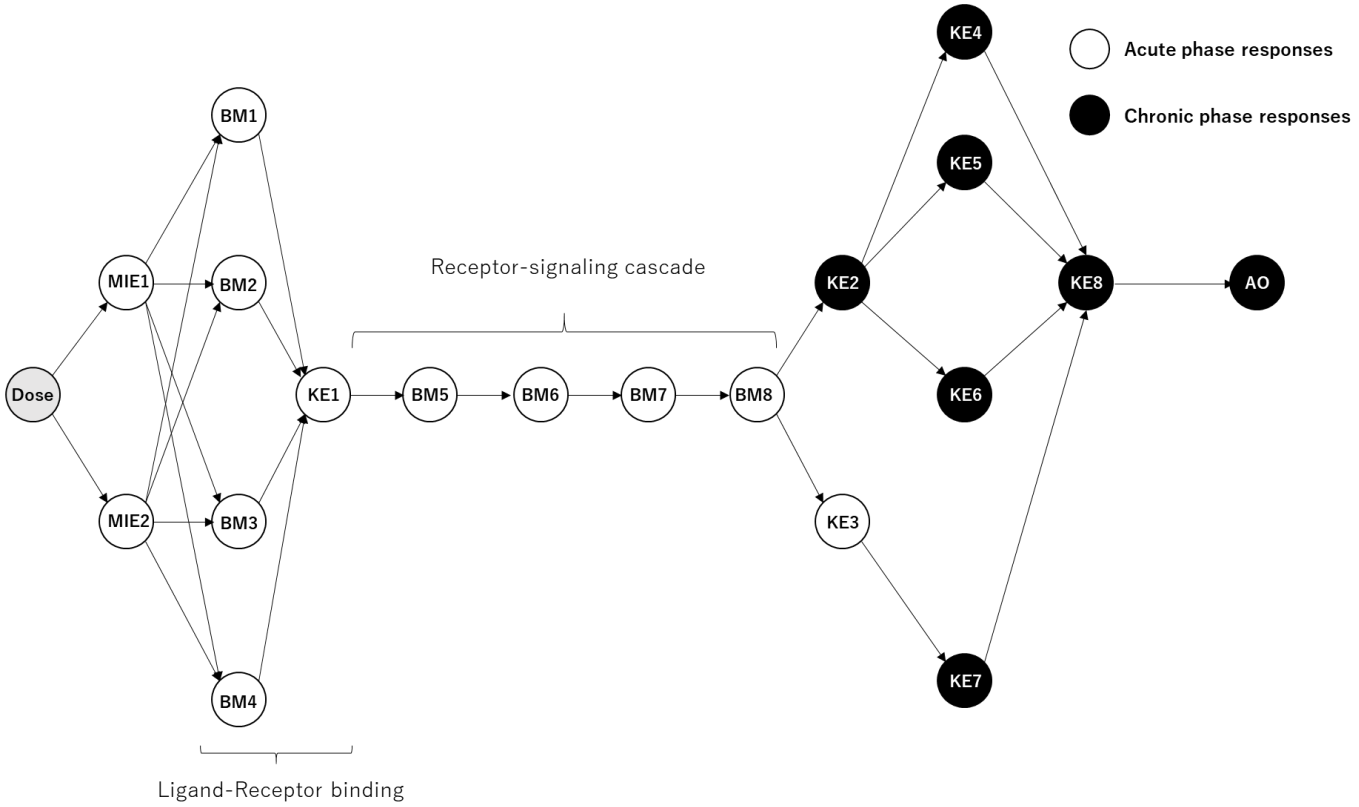

Fig. 1.1. A directed acyclic graph of hypothetical AOP.

Directed acyclic graph was used for Bayesian statistics-based approaches. BM1 through BM4 are ligands of the receptor (KE1). KE1 induces receptor signaling cascades of BM5 through BM8, which results in the downstream responses including chronic-phase KEs. MIEs, acute-phase KEs, and acute-phase BMs are represented in white. Chronic-phase KEs and AO are shown in solid black circles. MIE: Molecular Initiating Event, KE: Key Event, BM: Biomarker, AO: Adverse Outcome.

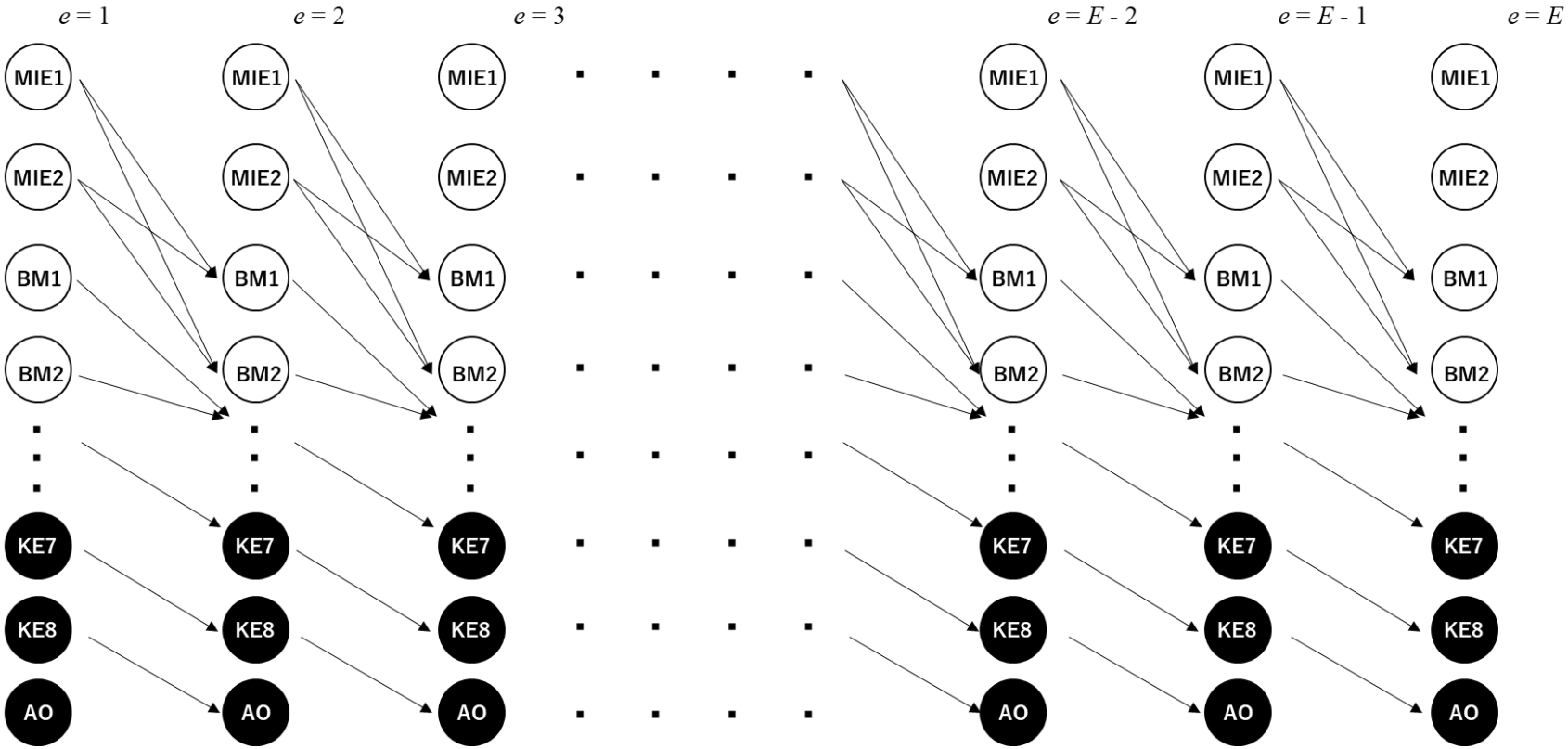

Fig. 1.2. Diagrammatic representation of the Dynamic Bayesian Network of the AOP.

The nodes are connected across exposure repetitions, where a parent node at a previous exposure can influence a child node at a later exposure. Any causal links between nodes at a given exposure were not included. It was assumed that a first-order Markov process $\boldsymbol{x}^{(e)} \leftarrow \boldsymbol{x}^{(e-1)}$, and stationarity was not assumed.

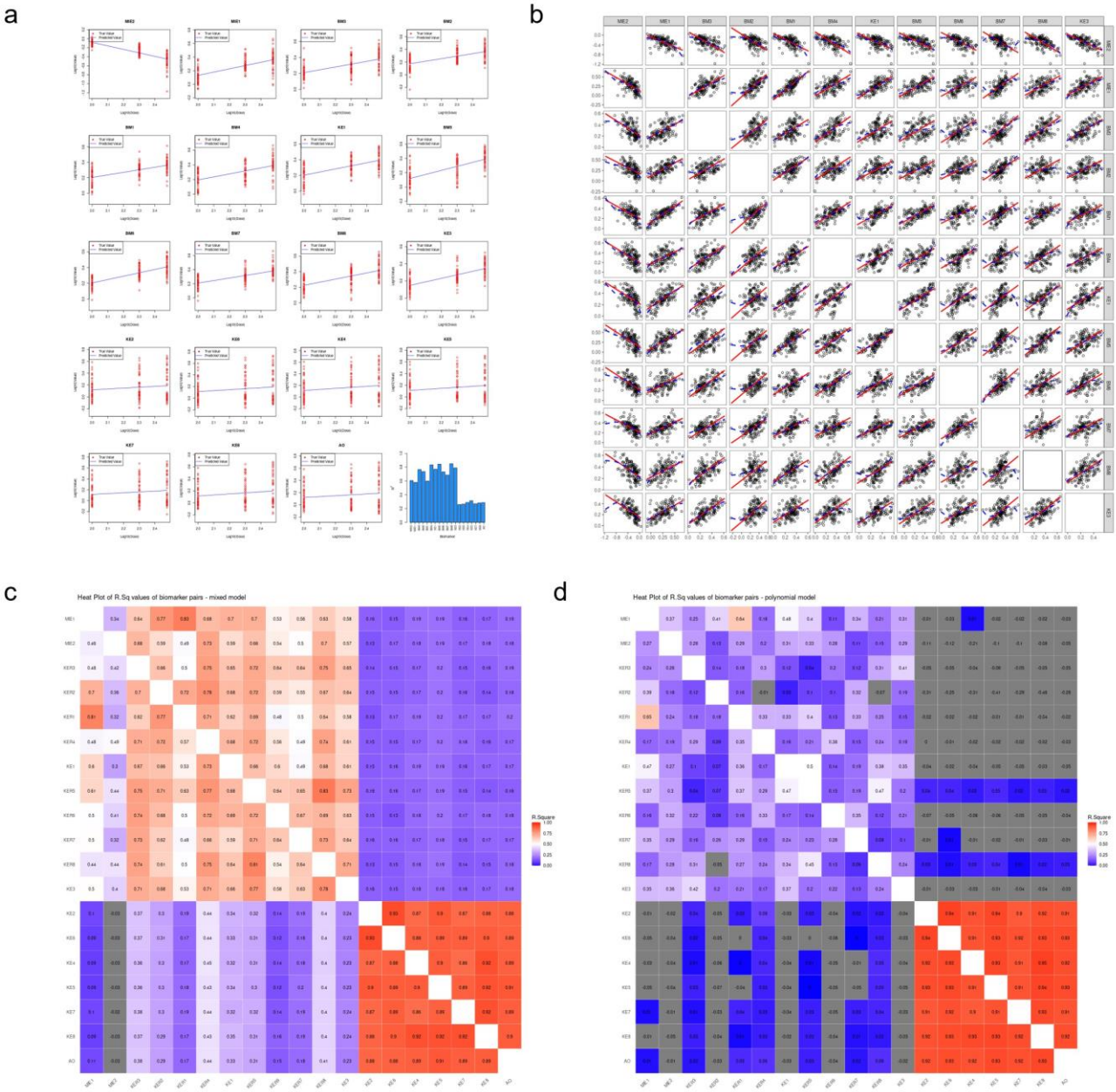

Fig. 1.3. R^2 values for dose-response and response-response models.

A Linear mixed model (LMM) was used for both dose-response (Eq. (5)) and response-response modeling (Eq. (6a)). The conditional R^2 values (Shinichi & Holger, 2013) were reported for both dose-response (a) and response-response modeling (b). For dose-response, each exposure repetition was analyzed separately. For response-response modeling, all exposure repetitions were pooled together. (c) Heatmap of R^2 values of biomarker pairs. (d) Same as (b) and (c), except polynomial regression (Eq. (6b)) was used and R^2 coefficient was calculated using the standard formula. These analyses and visualizations were performed using R statistical software version 4.0.4.

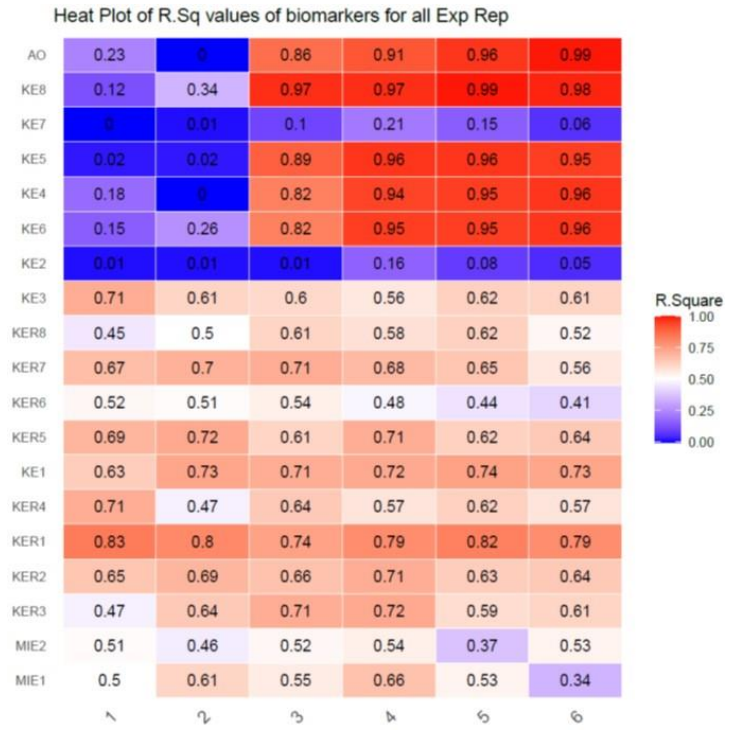

Fig. 1.4. R^2 of biomarkers for all exposure repetitions.

R^2 for each node was calculated using bnlearn that implements standard linear regression model. The predictors for each node were their parent set Π_v. The analysis and visualization were performed using R statistical software version 4.0.4.

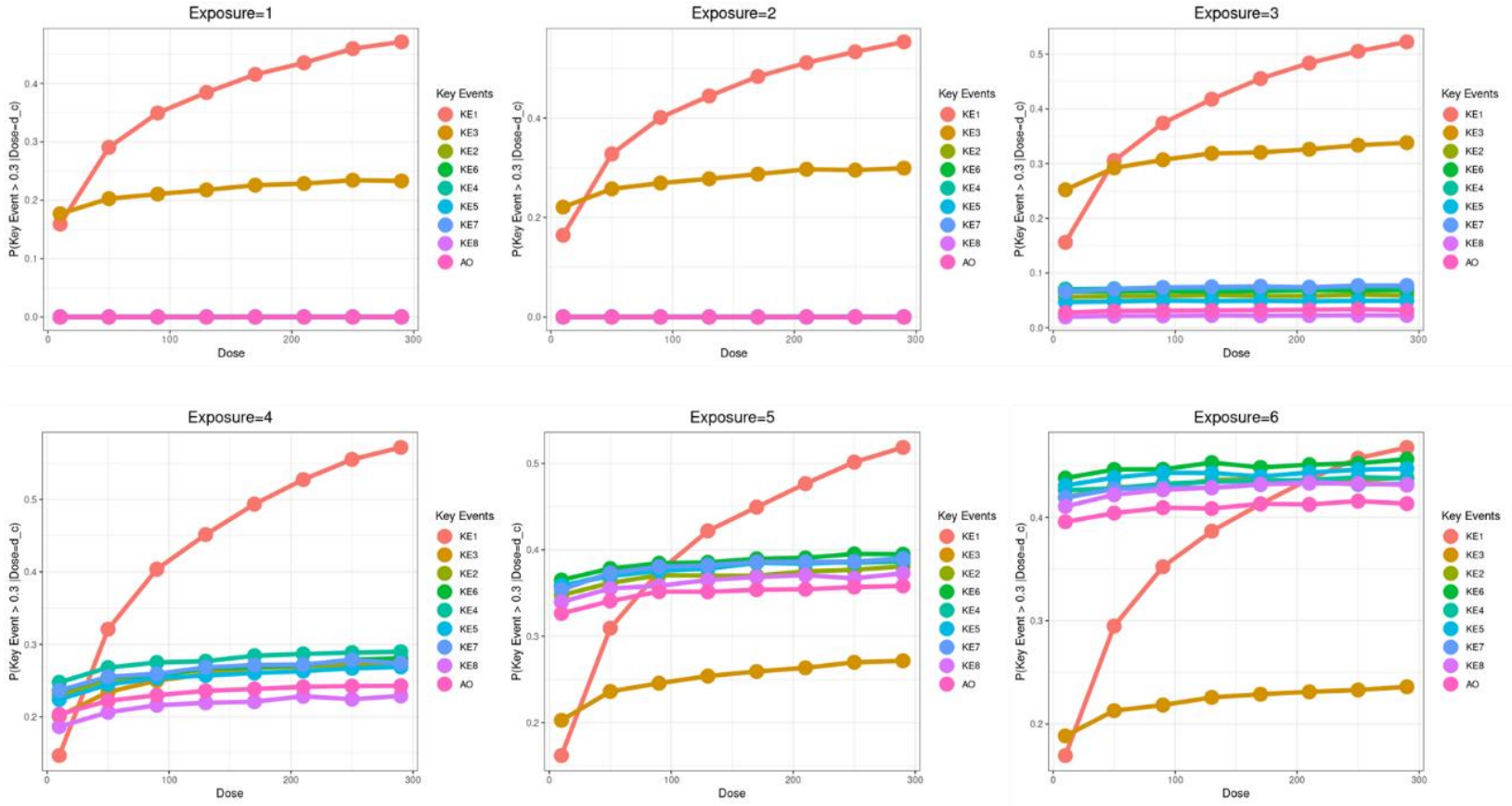

Fig. 1.5. Dose-probability curves of Bayesian Network analysis.

The probabilities were calculated by fitting the GBN to the virtual data, followed by logic sampling. The threshold of activation Δ was set to $log_{10} 2$. The analysis and visualization were performed using R statistical software version 4.0.4. The lines corresponding to KE2, 4, 5, 6, 7, and 8 at the exposure 1 and 2 are hidden by the line of AO.

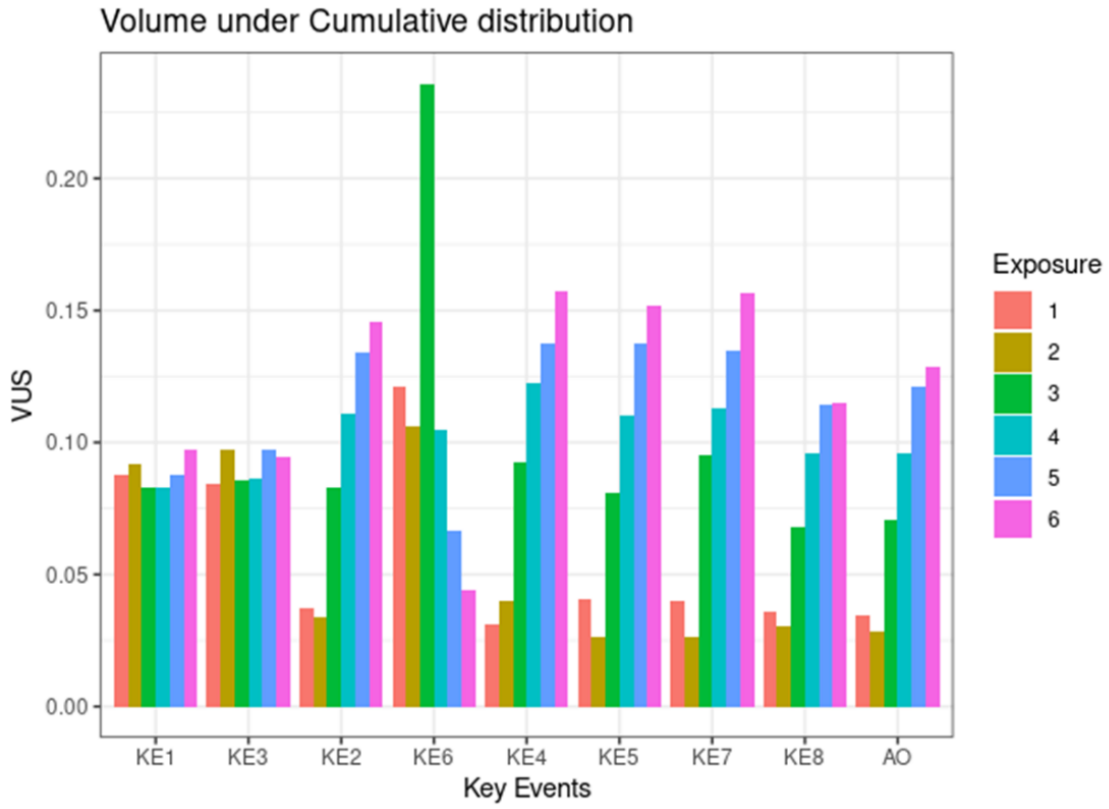

Fig. 1.6. Volume under surfaces of KEs at each exposure repetition.

Probability surfaces were calculated by varying the activation threshold Δ and the dose d. The volume under the surface (VUS) of those variables was calculated using the trapezoid rule. The analysis and visualization were performed using R statistical software version 4.0.4.

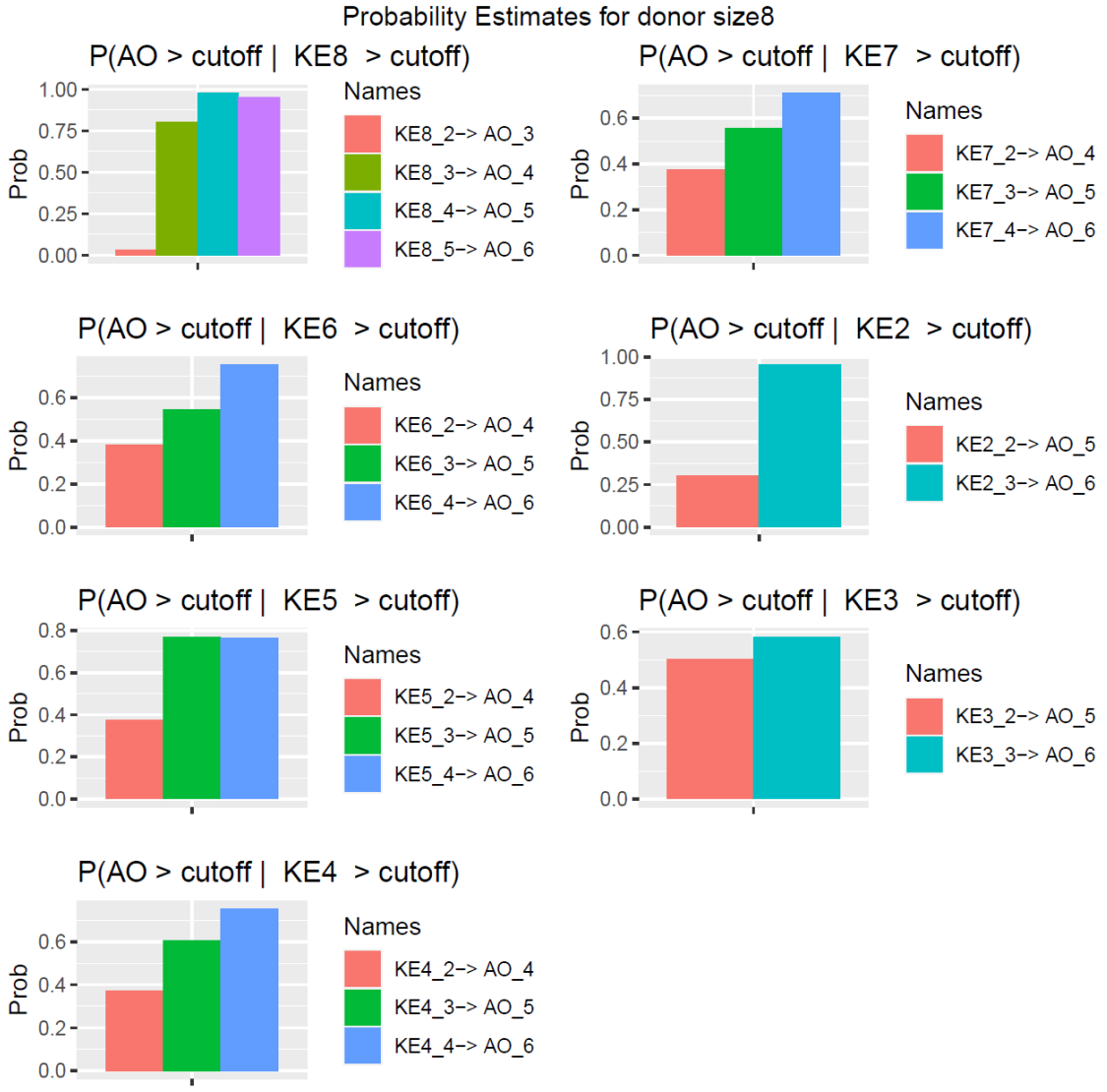

Fig. 1.7. Transition probabilities with all dose groups combined.

The transition probabilities were calculated using likelihood weighting after the dynamic Bayesian Network (DBN) was trained with data from successive exposures. The notation $KEv\_i \longrightarrow AO\_j$ was used to denote $P(AO^{e=j} > \Delta | KEv^{e-\tau=i} > \Delta)$. The probabilities were calculated when all dose groups were combined. The analysis and visualization were performed using R statistical software version 4.0.4.

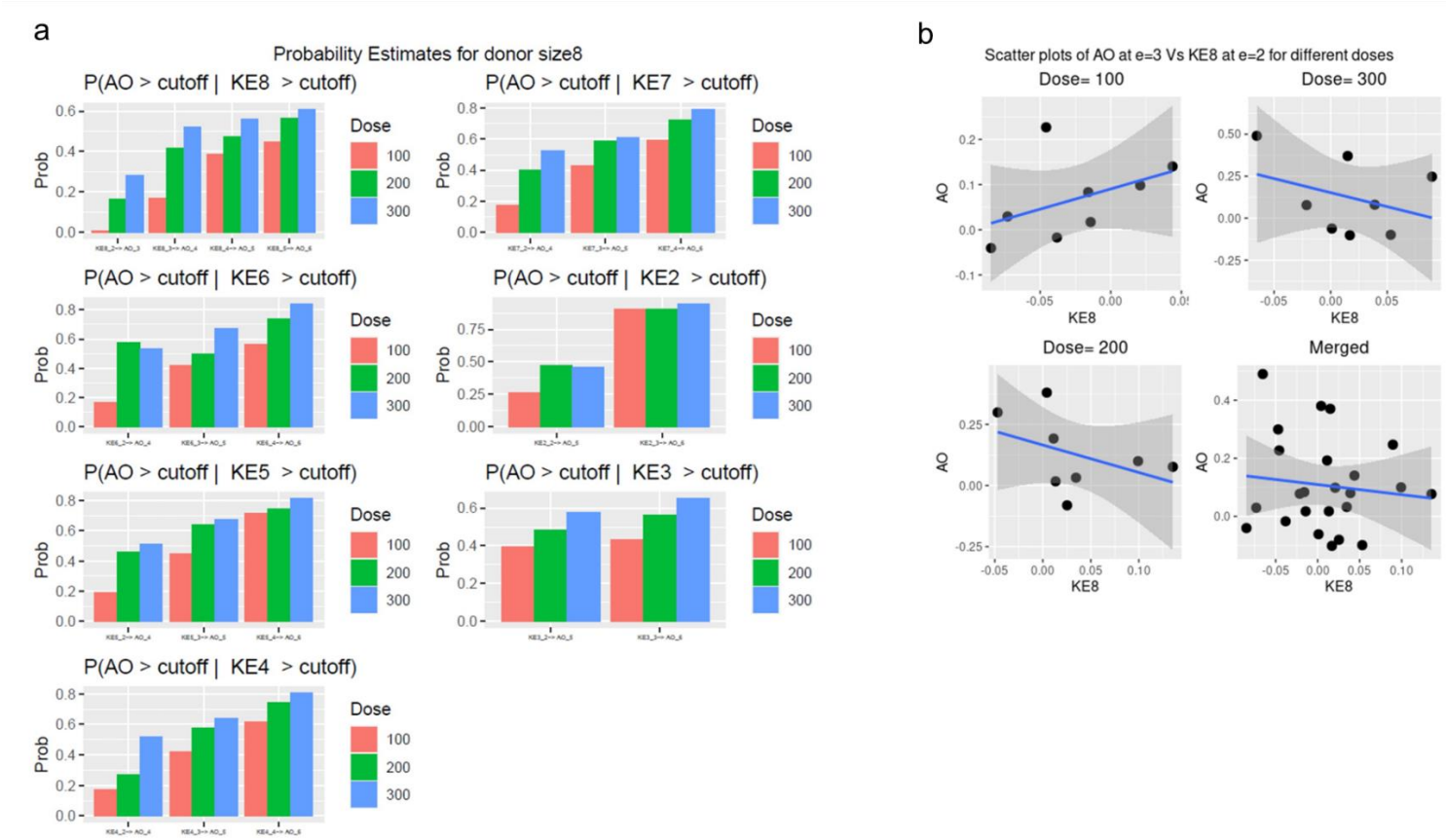

Fig. 1.8. Transition probabilities for each dose separately.

(a) The transition probabilities were calculated for each dose separately. The dose groups are color-coded and as before, $KEv\_i \longrightarrow AO\_j$ stood for $P(AO^{e=j,d} > \Delta | KEv^{e-\tau=i,d} > \Delta)$ (b) Scatter plots of AO at e=3 and KE8 at e=2 for each separate dose and pooled dose. These analyses and visualizations were performed using R statistical software version 4.0.4.

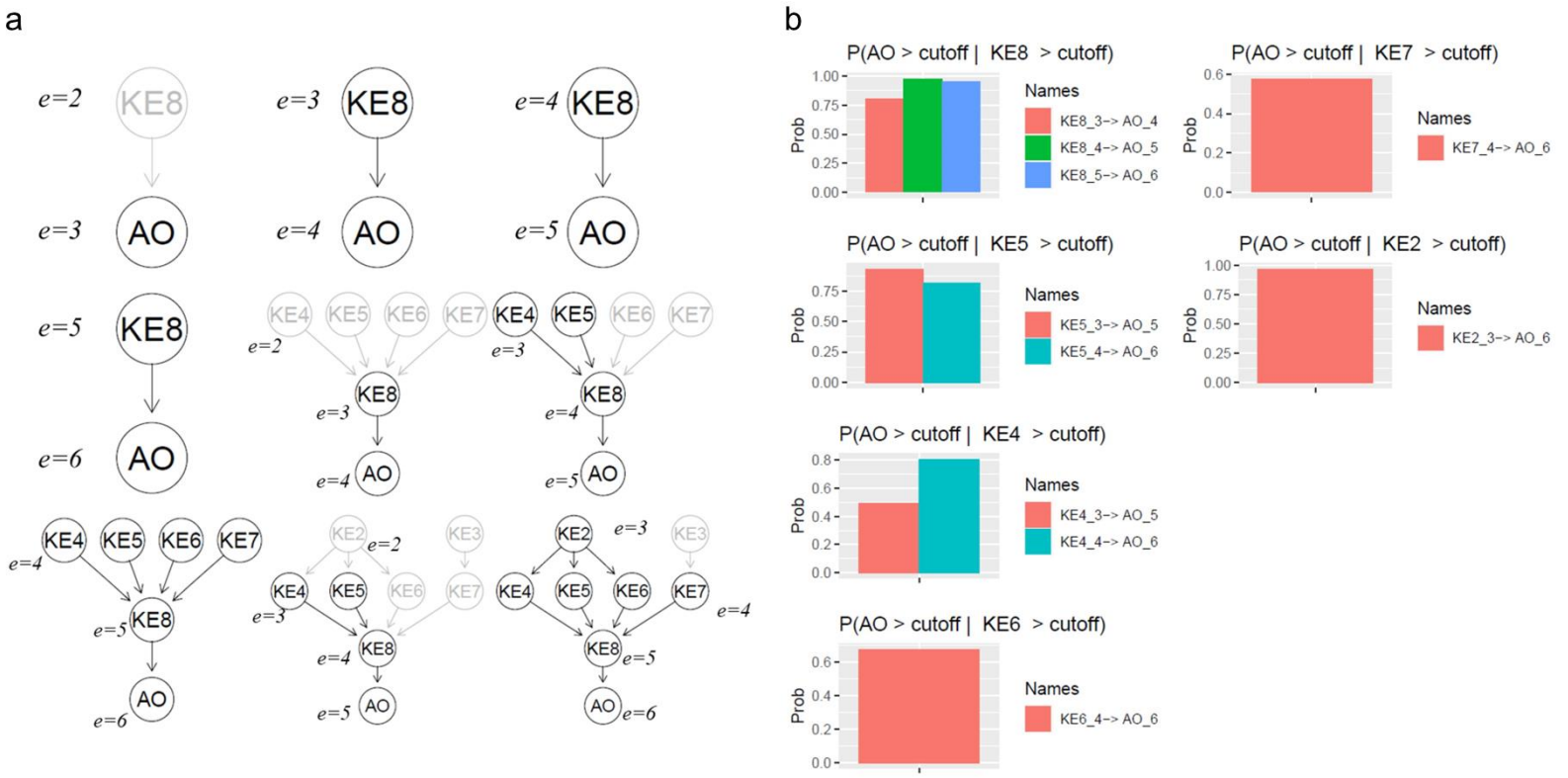

Fig. 1.9. Data-driven AOP restructuring and recalculation of transition probabilities.

(a) The DBN was trained using lasso regression. The causal links deemed insignificant were shown in gray. (b) Probabilities were calculated using likelihood weighting, and only those transition probabilities where $P(AO^{(e)} > \Delta | KE^{(e-\tau)} > \Delta) \neq P(AO^{(e=3)} > \Delta)$, were shown. As before, $KEv\_i \longrightarrow AO\_j$ was used to denote $P(AO^{e=j} > \Delta | KEv^{e-\tau=i} > \Delta)$. These analyses and visualizations were performed using R statistical software version 4.0.4.

Chapter 2

Enhancement of cigarette smoke extract-induced goblet cell hyperplasia exerted through IL-13 receptor α1 expression

Abstract

Chronic inflammation and goblet cell hyperplasia (GCH) in the airways are induced through a complex mechanism involving various factors, including immune cells. Previous studies reported direct effects of cigarette smoke on epithelial cells. Replicating the physiological condition of immune cells, I assessed the interaction between cigarette smoke extract (CSE) and interleukin (IL)-13, a GCH inducer, on air-liquid interface-cultured normal human bronchial epithelial cells (NHBEs). While single exposure to IL-13 or CSE induced mucus production, as previously reported, co-exposure to IL-13 and CSE synergistically enhanced this effect. I also investigated IL-13 receptor expression, which revealed that CSE exposure significantly induced the expression of the functional IL-13 receptor subunit, IL-13Rα1. To analyze the signaling pathway involved, NHBE cultures were exposed to benzo(a)pyrene, an aryl hydrocarbon receptor (AhR) ligand and constituent of CSE, which increased IL-13Rα1 expression in a concentration-dependent manner. Furthermore, treatment with the AhR inhibitor resveratrol erased the effects of CSE on mucus production and IL-13Rα1 expression. Here, I present a novel pathway to GCH by which cigarette smoke extract induces IL-13Rα1 expression through AhR stimulation, making epithelial cells sensitive to IL-13. This discovery not only contributes to the understanding of airway chronic inflammation but also supports the use of *in vitro* models to reproduce chronic inflammation without the co-culture of epithelial cells and immune cells.

1. Introduction

Chronic inflammation usually alters the cell population of affected organs, disturbing normal functioning and inducing adverse effects on the human body (Galkina & Ley, 2009; Koyama & Brenner, 2017; Rock *et al.*, 2010). In the bronchial epithelium, chronic inflammation induces goblet cell hyperplasia (GCH), which results in airway stenosis caused by epithelium thickening and mucus hypersecretion. Innate barrier-mediated protection of airway tissue from infection and irritants is essential for homeostasis because of the tissue's exposure to the outside via respiration. The airways are not only protected by mucus, which traps pathogens and irritants, they are also lined with cilia, which sweep irritant-laden mucus toward the throat (Knowles & Boucher, 2002; Linden *et al.*, 2008). However, when the balance between production and clearance of mucus is lost following GCH, thickened cells and an overabundance of mucus can disturb the airflow. Such airway remodeling leads to the characteristic symptom of limited airflow in patients with chronic obstructive pulmonary disease (COPD) (Fahy & Dickey, 2010; Jeffery, 2001).

The pathology of COPD includes cigarette smoke-related GCH and metaplasia (Hill *et al.*, 2022; Nikula & Green, 2000; Rose & Voynow, 2006; Yoshida & Tuder, 2007). The mechanism of GCH induction is complicated by the various chemical constituents of cigarette smoke, which have different modes of action (Hashizume et al., 2023; Sakai *et al.*, 2020; Takahashi et al., 2018). Furthermore, in addition to airway epithelial cells, immune cells take part in the pathological condition (Calderon *et al.*, 2023). A well-known signaling pathway involving immune cells is the interleukin (IL)-13 axis. Epithelial cells irritated by infection or chemicals, including those in cigarette smoke, release cytokines, including IL-33 and thymic stromal lymphopoietin. These cytokines activate various types of immune cells, such as type 2-innate lymphoid cells and T-helper (Th)2 cells, which release IL-13 to promote mucin production (Gabryelska et al., 2019; Gour & Wills-Karp, 2015; Hong et al., 2020).

Because of the complexity of this phenomenon, *in vivo* inhalation testing in animals has been used to model chronic inflammation induced by cigarettes, pesticides, pharmaceuticals, and other chemicals (Pauluhn & Mohr, 2000; Sécher et al., 2020; Wright et al., 2008). *In vivo* tests targeting GCH have also been conducted with animals (Kato *et al.*, 2020; Komori *et al.*, 2001). Alternative *in vitro* methods are needed, not only to respond to the growing calls to reduce animal testing, but also to address potential

miscalculation of risks owing to differences between species (Krewski et al., 2010). As an *in vitro* testing method that mimics chronic inflammatory diseases, three-dimensional (3D) normal human bronchial epithelial (NHBE) culture has been widely employed because of its similarity to tissue (i.e., cell population and thickness) and long lifespan (Hiemstra et al., 2018; Prytherch et al., 2011; Rayner *et al.*, 2019). IL-13 exposure successfully mimics GCH in 3D NHBE culture-derived tissues (Kistemaker et al., 2015; Marescotti *et al.*, 2020). In addition, recent efforts have enabled co-culture of 3D NHBE cells and immune cells. Co-culture of 3D NHBE cells with immune cells is considered the optimal *in vitro* method to reproduce the complexity of chronic inflammation. However, the many factors involved in cigarette smoke-associated airway remodeling have made it difficult to elucidate the underlying pathology.

IL-13 binds to two types of receptors: heterodimers of IL-13Rα1 and IL-4Rα, known as type II IL-4R, and IL-13Rα2 (Zurawski *et al.*, 1995). When type II IL-4R activation conveys the downstream signaling cascade, it increases mucus production by enhancing the production of epithelial cells and their alteration into mucus-producing cells. In contrast, IL-13Rα2 acts as a decoy receptor, attenuating the overproduction of mucus (Gour & Wills-Karp, 2015; Tanabe *et al.*, 2008).

In previous reports, cigarette smoke-related GCH was reproduced *in vitro* by exposing airway epithelial cells to cigarette smoke alone (Bodas *et al.*, 2020; Cao *et al.*, 2017; Cao *et al.*, 2018; Haswell et al., 2021; Shao *et al.*, 2004). However, *in vivo*, epithelial cells are exposed to not only cigarette smoke, but also to the cytokines produced in the chronic inflammatory state. Therefore, I simultaneously exposed 3D NHBE cells to both cigarette smoke and IL-13, and examined their effects on GCH. The findings propose the relationship between cigarette smoke and IL-13 receptor expression as a new aspect to explain the effects of cigarette smoke.

2. Materials and Methods

2.1. Cigarette smoke extract (CSE) preparation

Reference cigarettes (1R6F) were purchased from the University of Kentucky Center of Tobacco Reference Products and were conditioned for more than 48 h at 22 ± 2°C and 60 ± 5% relative humidity prior to use, in accordance with International Organization for Standardization (ISO) 3402 (*Tobacco and tobacco products − Atmosphere for conditioning and testing*, 1999). The 1R6F smoke was generated by a Borgwaldt RM20H smoking machine (Borgwaldt KC) under ISO 20778: 55 mL puff volume, 30-second puff interval, 2-second puff duration, bell-shaped puff profile, and 100% blocked ventilation holes (*Cigarettes -Routine Analytical Cigarette Smoking Machine - Definitions and Standard Conditions with an Intense Smoking Regime*, 2018). Total particulate matter was collected with a 44-mm Cambridge filter pad. The pad contents were extracted using dimethyl sulfoxide (DMSO) purchased from FUJIFILM Wako Pure Chemical Corporation (049-07213) to prepare a 40 mg/mL CSE solution (accumulated from 10 sticks). The CSE was aliquoted for single use and stored at −80°C until testing.

2.2. 3D NHBE cell culture

Primary NHBE cells derived from a healthy 63-year-old female African American nonsmoker were purchased from Lonza (CC-2540) and cultured in PneumaCult™-Ex Plus culture medium (STEMCELL Technologies, ST-05040) supplemented with hydrocortisone (StemCell Technologies, 07925) at 37°C and 5% CO_2. When NHBE cells reached 70%–80% confluence, they were dissociated and seeded on 6.5-mm Transwell inserts (Corning, CLS3458) coated with 50 μg/mL collagen type IV (Sigma-Aldrich, C5533) 1 day prior to seeding. NHBE cells were expanded in PneumaCult™-Ex Plus culture medium for 5 days. For air-liquid interface (ALI) culture, the apical medium was removed and changed to PneumaCult-ALI Medium (STEMCELL Technologies, ST-05001) containing 1% penicillin/streptomycin, supplemented with heparin solution (StemCell Technologies, 07980) and hydrocortisone to support differentiation. Cells were fully differentiated within 4–5 weeks of culture, with medium change every 2–3 days. Prior to exposure, apical mucus was removed by washing with 37°C Dulbecco's phosphate-buffered saline (DPBS) (Thermo Fisher Scientific, 14040133).

2.3. Test sample exposure

Test samples of 3D NHBE cells were exposed to recombinant IL-13 (Pepro Tech, 200-13), CSE, benzo(a)pyrene (BaP) (FUJIFILM Wako Pure Chemical Corporation, 026-16751), and resveratrol (FUJIFILM Wako Pure Chemical Corporation, 185-01721) dissolved in basolateral medium and replaced fresh with every medium change for 14 days to observe differentiation from epithelial cells to goblet cells while cytotoxicity by CSE-accumulative effect is not expected (Ito *et al.*, 2020). BaP and resveratrol were dissolved in DMSO and subsequently diluted in the medium. The DMSO concentration in medium was set at 1% for every condition, including negative control medium.

2.4. Functional analyses of airway epithelial cells

At exposure day 14, ciliary function was assessed as a measure of the cilia beating frequency (CBF) using a high-speed digital camera with Sisson-Ammons Video Analysis software (Ammons Engineering), as previously described (Mori *et al.*, 2022). A Primovert inverted microscope (Carl Zeiss) captured images at a sampling rate of 120 frames per second with an objective strength of 4× magnification. For measurements, the slides were placed on a ThermoPlate (Tokai Hit) to maintain a tissue temperature of 37°C. Gaussian whole field analysis was used for the CBF measurement, after which the surface of each culture insert was washed twice with 200 µL DPBS. Data on trans-epithelial electric resistance (TEER) were collected as a parameter of the barrier function of epithelial cells. TEER was measured using a resistance meter (World Precision Instruments) after adding 37°C PBS to the apical surface.

2.5. Cytotoxicity measurement

Following 14 days of CSE exposure, the medium from each 3D NHBE tissue culture was collected for cytotoxicity analysis. The enzymatic activity of adenylate kinase (AK) released from damaged cells was measured using ToxiLight (Lonza, LT17-217), in accordance with the manufacturer's instructions. Briefly, the culture medium and AK detection reagent were mixed in 96-well plates at room temperature. A BioTek Cytation

5 system (Agilent) was then used to measure the relative luminescence unit value.

2.6. ELISA of mucin-5AC (MUC5AC)

At the end of CSE exposure, apical surface liquid (ASL) was collected by washing the surface of each culture insert twice with 200 µL DPBS as stated 2.4. and stored at −20°C until testing. MUC5AC in ASL was measured by ELISA as follows. A high-protein-binding 96-well plate (Thermo Fisher Scientific, 467466) was coated with 10 µg/mL mouse anti-MUC5AC monoclonal antibody (Bio-Rad Laboratories, OBT1746) overnight. All wells were washed four times with wash buffer (0.05% polyoxyethylene sorbitan monolaurate in PBS) and then blocked with 2% bovine serum albumin in PBS for 2 hours at 37°C. ASL samples were diluted 100× with DPBS and reacted with coated antibody on the plate for 1 hour at 37°C. Following four washes with wash buffer, captured MUC5AC was detected using biotin-conjugated mouse anti-MUC5AC monoclonal antibody (Thermo Fisher Scientific, MS-145-B) prepared at 0.2 µg/mL in sample diluent (1% bovine serum albumin and 0.05% polyoxyethylene sorbitan monolaurate in PBS). Horseradish peroxide-conjugated streptavidin (Proteintech, SA00001-0) was diluted 4000× with sample diluent and added to each well following four washes. Chromogenic substrate TMB (Thermo Fisher Scientific, 34018) was added to all wells and reacted for 10 minutes. Color reactions were stopped by adding 2N H_2SO_4. The optical density (OD) was detected using a BioTek Cytation 5 (Agilent). The relative MUC5AC content was determined by comparison with the ODs of negative control samples.

2.7. Histological assay

3D NHBE tissues were fixed in 4% paraformaldehyde, embedded in paraffin, and sliced into 4-µm thick sections for periodic acid-Schiff/Alcian blue (PAS/AB) staining. Digital images of histological samples were generated by a NanoZoomer 2.0-HT digital slide scanner (Hamamatsu Photonics). PAS/AB-positive area and tissue slice length were measured using ImageJ software (version 1.53k). The mucus area for each tissue was calculated by dividing the PAS/AB positive area by the tissue length.

2.8. Western blotting

After mucus collection at exposure day 14, cell lysates were obtained by lysing cells with RIPA buffer (Nacalai Tesque, 16488-34) and protease inhibitor (Merck, 11836170001). The lysates were centrifuged for 15 min at 15000 rpm at 4 °C and the supernatant was collected. Proteins were separated by 4-20% Mini-PROTEAN TGX™ Precast Gels (Bio-Rad Laboratories, 4561095 and 4561096) and transferred to nitrocellulose membrane (Bio-Rad Laboratories, 1620097). I employed rabbit anti-IL-13Rα1 monoclonal antibody (500× dilution, Bioss Antibodies, bsm-54211R), rabbit anti-IL-4Rα polyclonal antibody (5000×, Proteintech, 28331-1-AP), and goat anti-IL-13Rα2 polyclonal antibody (500×, R&D Systems, AF146) as the primary antibodies for IL-13Rα1, IL-4R, and IL-13Rα2, respectively. These antibodies were detected using two horseradish peroxidase-conjugated antibodies: donkey anti-rabbit IgG (5000×, Global Life Sciences Technologies Japan, NA934) and rabbit anti-goat IgG (5000×, R&D Systems, HAF017). The band densities of each receptor were normalized against that of β-actin, which was detected using a horseradish peroxidase-conjugated sheep antibody to mouse IgG (5000×, Global Life Sciences Technologies Japan, NA9310) following incubation with a mouse anti-β-actin monoclonal antibody (5000×, Abcam, ab6276). The protein bands were visualized with ImageQuant 800 (Cytiva). ImageJ software was used to measure the intensity of the protein bands. The protein levels were normalized using the intensity of the β-actin bands. Quantification of IL-4R and IL-13Rα2 was performed using the protein bands corresponding to their relevant molecular weights, despite the presence of non-specific protein bands in the western blot images. (Supplementary Fig. 2.1–3)

2.9. Transcriptomic Studies of IL-13 receptors

Public transcriptomic data was analyzed to investigate the difference in IL-13 receptors between the airway epithelium of current smokers and never smokers. The gene set experiments (GSE)994 (Spira *et al.*, 2004), GSE3320 (Harvey *et al.*, 2005), GSE4498 (Heguy *et al.*, 2006), GSE4635 (Steiling *et al.*, 2009), GSE5057 (Carolan *et al.*, 2006b), GSE5058 (Carolan *et al.*, 2006c), GSE5059 (Carolan *et al.*, 2006a), GSE7895 (Beane & Spira, 2007), GSE8545 (Ammous *et al.*, 2008), GSE10006 (Carolan *et al.*, 2008), GSE10135 (Vanni *et al.*, 2009), GSE11952 (Hübner *et al.*, 2009), GSE13931 (Carolan *et al.*, 2011), GSE13933 (Turetz *et al.*, 2009) were selected from the National Center for

Biotechnology Information (NCBI) Gene Expression Omnibus (GEO), based on a previously reported summary (Gower *et al.*, 2011). These GSEs were individually analyzed using the GEO2R tool available in the GEO database. I defined the groups as "Current Smoker" or "Never Smoker" according to the smoking status information found in each GSE. After analyzing each GSE using GEO2R, the full gene lists with the log fold change (LogFC) and statistical analysis results were downloaded. I then extracted the LogFC of genes of interest, IL-13Rα1, IL-13Rα2, and IL-4R, where these genes are denoted as IL13RA1, IL13RA2, and IL4R, respectively. For IL13RA1, multiple probes were employed in the studies. IL13RA1 expression was analyzed by averaging data from probes 201887_at, 201888_s_at, and 211612_s_at, which target the whole IL13RA1 gene (USCS Genome Browser). Of note, I did not set any criteria for the analysis, such as cut-off values of LogFC and adjusted *p* value, because I intended to capture the overall trend of these genes between current smokers and never smokers across the experiments.

2.10. Statistical analysis

Student's *t*-test and Dunnett's test were employed to examine statistically significant differences between two and three samples, respectively, for each condition. The results presented represent three different 3D NHBE samples for each condition. A *p* value less than 0.05 was considered to indicate statistical significance.

3. Results

3.1. CSE-induced GCH

To reproduce the airway epithelial environment under smoking-related chronic inflammation, in which IL-13 plays a key role, 3D NHBE cells was exposed to CSE and IL-13 simultaneously for 14 days. Referring to previous studies of non-cytotoxic concentrations of CSE (Ito et al., 2020), it confirmed that exposure to CSE ≤ 25 μg/mL did not induce cytotoxicity (Fig. 2.1a). Although it did not reach statistical significance, CBF showed a marked decrease with IL-13 exposure (p=0.06), while no substantial difference was observed with CSE exposure (Fig. 2.1b). Under the same IL-13 concentration, TEER decreased with CSE exposure at 12.5 and 25 μg/mL (Fig. 2.1c). ELISA measurements of MUC5AC were used as an indicator of the amount of mucus released from NHBE cells. Although there was a trend of increased MUC5AC level with exposure to 0.5 ng/mL IL-13, no statistical significance was detected. Under exposure to 12.5 or 25 μg/mL CSE, MUC5AC levels were significantly increased by 2.0- to 2.4-fold compared to the negative control. In the setting of CSE exposure, additional exposure to 0.5 ng/mL IL-13, MUC5AC levels showed a significant 2.7- to 3.1-fold increase over those without IL-13 (Fig. 2.1d). Histological analysis was used to evaluate intracellular stores of MUC5AC. Dissimilar to the measurements of released mucus, intracellular MUC5AC production was significantly increased by exposure to IL-13. An increase in MUC5AC was also detected within NHBE cells exposed to 12.5 or 25 μg/mL CSE compared to MUC5AC in negative control cells, with and without IL-13 exposure (Fig. 2.1e and f).

3.2. CSE-induced IL-13 receptor expression

Next, I examined the possible mechanism of synergistic effect of CSE and IL-13 on mucus production. Hypothesizing that IL-13 receptor expression is controlled by CSE, thereby altering the sensitivity of epithelial cells to IL-13, I measured the protein levels of IL-13Rα1, IL-4Rα, and IL-13Rα2 using western blotting of day 14 cell lysates. The expression of an IL-13 receptor subunit, IL-13Rα1, was significantly increased upon exposure to 12.5 or 25 μg/mL CSE compared to the control group with no CSE and without IL-13. Similar to without IL-13, in the presence of 0.5 ng/mL IL-13, a significant

increase in IL-13Rα1 expression was induced by 12.5 μg/mL CSE, and its expression tended to rise with 25 μg/mL CSE, although this increase was not statistically significant. Specifically, the protein level of IL-13Rα1 was 2.4- to 3.0-fold higher in CSE-exposed cultures than in non-CSE-exposed controls (Fig. 2.2b and c). By contrast, the protein level of the IL-4Rαsubunit, which heterodimerizes with IL-13Rα1, was significantly decreased under 12.5 μg/mL CSE exposure. CSE exposure at 25 μg/mL significantly decreased the IL-4Rα expression with 0.5 ng/mL IL-13 exposure (Fig. 2.2d and e). Although the difference was not statistically significant, the IL-13 decoy receptor, IL-13Rα2, also showed a decreasing trend under CSE (Fig. 2.2f and g).

Using public data, gene expressions of IL13RA1, IL13RA2, and IL4R in the human airway epithelium were analyzed. In the small airways, 6 out of 8 studies (75%) showed that gene expression levels of IL13RA1 are higher in cigarette smokers than in non-smokers. In contrast, in the large airways, 4 out of 9 studies (44%) showed higher gene expression levels of IL13RA1 in cigarette smokers than in non-smokers. Additionally, studies showing high Log FC tend to be conducted in the small airways. This tendency is not observed in gene expressions of IL13RA2 and IL4R (Supplementary Fig. 2.4–6).

3.3. Aryl hydrocarbon receptor (AhR) ligand-mediated induction of IL-13 receptor expression

To elucidate the signaling pathways affecting expression of IL-13Rα1, 3D NHBEs were exposed to two chemicals found in cigarette smoke: BaP and H_2O_2. BaP stimulates the AhR pathway, while H_2O_2 stimulates the oxidative stress pathway. Expression levels of IL-13Rα1 and IL-4Rα were measured in western blots of 3D NHBE cell lysates at exposure day 14. Exposure of the cultures to BaP at ≤ 50 μM and to H_2O_2 at ≤ 10 μM for 14 days did not cause cytotoxicity (Fig. 2.3a and b). However, after 14 days of exposure, 50 μM BaP significantly enhanced IL-13Rα1 expression. Exposure to BaP at 5 and 10 μM also showed an increasing trend of IL-13Rα1 expression after 14 days, but did not reach statistical significance. No significant changes in IL-4Rα expression were detected with any exposure to BaP, in contrast to that with CSE (Fig. 2.3d and e). Similarly, no concentration of H_2O_2 (0, 1, 5, and 10 μM) led to a significant change in the expression levels of IL-13Rα1 or IL-4Rα (Fig. 2.3f and g).

3.4. AhR inhibitor-mediated attenuation of CSE-induced mucus production

Since the AhR signaling pathway has been suggested to play a key role in CSE-induced mucus production, I attempted to inhibit this signal transduction using resveratrol, a known AhR inhibitor (Beedanagari *et al.*, 2009). In contrast to the results shown in Fig. 2.1d–f, exposure to 25 μg/mL CSE under conditions of 1–100 μM resveratrol did not promote the release or storage of mucus in NHBE cells (Fig. 2.4a and b). Additionally, exposure to CSE under 1 μM resveratrol did not elevate the expression of IL-13Rα1 or IL-4R while cells did not show any cytotoxicity (Fig. 2.4c–f). Furthermore, the highest concentration of resveratrol, 100 μM, suppressed mucus production to a greater degree than lower concentrations (1 and 10 μM). This suppressive effect was observed regardless of the exposure to CSE (Fig. 2.4a and b). Additionally, exposure to 100 μM resveratrol suppressed mucus production compared to no CSE and no resveratrol exposure (Fig. 2.1d and e).

4. Discussion

Inflammation that becomes chronic can alter cell populations and organ function. In the human bronchi, chronic inflammation induces GCH, causing hyperproduction of mucus that results in breathing difficulties in patients with conditions such as COPD. Cigarette smoking is one risk factor of chronic inflammation in the respiratory tract (Qiu *et al.*, 2016). While Th1 cytokines contribute to exacerbation of inflammation in GCH, the Th2 cytokine IL-13 is an essential factor for the development of GCH (Strzelak *et al.*, 2018). To elucidate the interaction between the inflammatory airway environment and epithelial cells *in vitro*, 3D NHBE cultures was exposed to CSE and IL-13 simultaneously.

In this study, both released MUC5AC and intracellular mucus levels following the exposure were measured. I observed a tendency for differences between released and stored mucus. With 0.5 ng/mL IL-13 exposure, mucus was significantly increased only within cells. Conversely, upon exposure to CSE in the presence of 0.5 ng/mL IL-13, released MUC5AC was significantly increased. Mucus is stored in cells prior to release (Davis & Dickey, 2008). Since the concentration of 0.5 ng/ml IL-13 used in this study was lower than concentrations used in previous studies (Kimura et al., 2023; Zhen *et al.*, 2007), the stimulation level of IL-13 did not reach a threshold sufficient to induce mucus release. Exposure to CSE with IL-13 induced mucus production in 3D NHBE cells. This result is consistent with previous reports suggesting two CSE-induced pathways to GCH: the Notch signaling and epidermal growth factor receptor pathways (Bodas et al., 2020; Cao et al., 2017; Cao et al., 2018; Haswell et al., 2021; Shao et al., 2004). Because barrier function becomes weakened by the transition from ciliated cells to goblet cells, a decrease in the TEER value indicates a change in the cell population (Thavagnanam *et al.*, 2011). Interestingly, the CSE-induced increase in MUC5AC production in this study was higher under IL-13 exposure than without it. The decrease in TEER values also suggested that epithelial cells in the culture differentiated into goblet cells in response to the presence of IL-13. Exposure of NHBE cultures to CSE also led to a non-significant tendency for cells to store increased levels of mucus and a significant increase in the amount of released mucus. These findings suggested that CSE enhances the acute release of mucus from goblet cells.

IL-13 binds to IL-13Rα1 and IL-13Rα2. IL-13Rα1 forms heterodimers with IL-4Rα to generate functional receptors known as type II IL-4R. Binding of IL-13 to type II IL-4R on epithelial cells activates the JAK2–STAT6 signaling pathway (Murata *et al.*, 1998;

Palmer-Crocker *et al.*, 1996). Activation of this pathway induces differentiation of epithelial cells into goblet cells, which produce mucus (Curran & Cohn, 2010; Marone *et al.*, 2019). In the 3D NHBE culture system, CSE exposure increased production of the functional IL-13Rα1 subunit of type II IL-4R, regardless of the presence of IL-13. Interestingly, expression of the other type II IL-4R subunit, IL-4R, was significantly reduced under CSE exposure. The simultaneously increased expression of IL-13α1 and decreased expression of IL-4Rα is somewhat inconsistent from the viewpoint of sensitivity to IL-13. However, Liang *et al.* (2022) previously reported that IL-13 first binds to IL-13Rα1, forming an IL-13/IL-13 Rα1 complex that binds to IL-4Rα with an E13 moiety to generate a functional type II IL-4R. Therefore, the increased expression of IL-13Rα1 may contribute to the effective capture of IL-13, thus enhancing the formation of functional IL-13 receptors (i.e., type II IL-4R). IL-4 also binds to type II IL-4R and induces GCMH (Dabbagh *et al.*, 1999; Munitz *et al.*, 2008). IL-4 is expected to induce similar response to IL-13. Some of previous transcriptomic studies have shown that IL-13R α 1 expression is higher in cigarette smokers than in non-smokers. This suggests that the increase in IL-13R α 1 expression observed in 3D NHBE represents a group of smokers. Additionally, the results are more pronounced in the small airways compared to the large airways. If it is hypothesize that increase in IL-13R α 1 expression is more significant in the deep airways, the NHBE cells used in this study may possess the characteristics of deeper airway. Shaykhiev and Crystal (2014) reported that the earliest changes relevant to COPD pathogenesis are observed in the small airways. These changes include tissue remodeling and mucus exudates (Hogg *et al.*, 2004), those which are well reproduced in the current study. The mechanism of increased sensitivity to IL-13 may be part of these earliest changes.

I found that CSE exposure tended to reduce production of another IL-13 receptor, IL-13Rα2. Although the function of IL-13α2 remains debated, reports suggest that IL-13Rα2 has high affinity for IL-13 but lacks the signaling function, thus modulating mucus overproduction as a decoy receptor (Gour & Wills-Karp, 2015; Tanabe et al., 2008). Meanwhile, a recent study suggested that binding of IL-13 to IL-13Rα2 induces a fibrotic reaction via the transforming growth factor-αaxis in mice (Fichtner-Feigl *et al.*, 2006). This implies that marked downregulation of IL-13Rα2 contributes to the enhanced binding of IL-13 to IL-13Rα1, or directs epithelial cells to form goblet cells, rather than inducing a fibrotic phenotype change. Furthermore, the results showed that mucus production rose with the increase in IL-13Rα1 expression, without a concomitant increase

in IL-4R expression. This finding is consistent with the study by Mattes *et al.* (2001), which reported that IL-13 increases mucus-producing cells independently of the IL-4Rα chain in the allergic airway *in vivo*. Therefore, IL-13Rα2 may contribute to homeostasis by acting as a decoy receptor of IL-13, thereby preventing intense reactions via IL-13Rα1. While IL-13Rα1 showed enhanced expression under CSE exposure, IL-13Rα2 expression showed only a non-significant tendency of decrease. Therefore, IL-13Rα2 suppression may be a mechanism of CSE-induced GCH.

To further investigated the specific constituents of CSE involved in hyperexpression of IL-13Rα1, I focused on two known inducers of adverse effects: BaP and the reactive oxygen species (ROS) H_2O_2. BaP is a ligand of AhR. Following binding, the AhR-BaP complex is translocated into the nucleus, where it acts as a transcription factor of multiple proteins related to inflammation (Fu *et al.*, 2022). It was found that exposure of 3D NHBE cultures to BaP induced IL-13Rα1 expression. This result suggested that AhR complex or a downstream protein enhances IL13RA1 transcription. By contrast, exposure of 3D NHBE cultures to H_2O_2 did not affect expression of IL-13Rα1. Although ROS have been related to GCH, they are not a direct factor in GCH-mediated stimulation of IL-13 Rα1 expression (Bukowska & Duchnowicz, 2022; Rogers, 2007; Sun *et al.*, 2021).

Resveratrol, a widely known polyphenol with anti-oxidative stress properties (de la Lastra & Villegas, 2007; Truong *et al.*, 2018), has also been reported to inhibit transfer of the AhR complex to nuclei and production of ROS in mitochondria (Beedanagari et al., 2009). To confirm that the AhR ligand was related to IL-13Rα1 expression, 3D NHBE cultures were exposed to resveratrol together with CSE and IL-13. Resveratrol successfully diminished the CSE-mediated upregulation of IL-13Rα1 expression, suggesting a pathway whereby CSE enhances IL-13Rα1 expression through BaP-activated AhR. Notably, the highest concentration of resveratrol led to low production of mucus, regardless of CSE exposure. Additionally, the suppression was even observed compared to no CSE and no resveratrol exposure. Reductions in AhR ligands, such as BaP, and oxidative stress may contribute to efforts to control GCH in chronic inflammatory situations as well as in normal situations.

Here, I focused on the interaction between epithelial cells and a cytokine to discover a new pathway of CSE-induced GCH that can be utilized to simplify *in vitro* co-culture modeling. Indeed, co-culture systems are useful to recreate complex interactions between different cell types; however, they can be challenging in terms of cost, labor, and time

(Blom *et al.*, 2016; Ronaghan *et al.*, 2022). IL-13 is stable and can be used to refresh culture medium more easily than immune cells. Co-exposure of 3D NHBE cells to IL-13 and a test sample could be a useful first step of testing and screening for airway chronic inflammation. Co-exposure of a test sample and IL-13 not only expands the dynamic range of mucus production, but also mimics the interaction of epithelial cells and immune cells in airway chronic inflammation.

5. Short summary

Overall, the results suggest that the AhR signaling pathway plays a critical role in regulating mucus production as well as GCH. The AhR gene is highly polymorphic and is known to be associated with cancer risk (Chen *et al.*, 2009; Gu *et al.*, 2012; Vázquez-Gómez *et al.*, 2018). Therefore, testing with multiple donors of 3D NHBE cells to investigate the relationship between the AhR polymorphism and GCH would provide deeper mechanistic insights. Previous studies of cigarette smoke-associated airway inflammation and GCH focused on the direct effects of cigarette smoke and elevations in inflammatory cytokines. In contrast, I sought to elucidate the importance of sensitivity of epithelial cells to IL-13. CSE-induced GCH was promoted by the presence of IL-13. Furthermore, I demonstrated that CSE makes epithelial cells sensitive to IL-13, possibly through a mechanism that alters IL-13Rα1 expression through AhR stimulation. Considering that treatment with resveratrol diminished the effect of CSE on GCH, even in the presence of IL-13, I propose that inhibition of the AhR axis may weaken the development of GCH. Polyaromatic hydrocarbons including BaP, which are found not only in cigarette smoke but also as known air pollutants, are the dominant ligands for AhR. This suggests that reduced exposure to polyaromatic hydrocarbons overall could be beneficial for slowing the progression of GCH. In addition, I anticipate that the application of this novel *in vitro* modeling system comprising added IL-13 with testing sample will be useful to mimic inflammatory situations, leading to effective alternatives to animal testing.

Figures

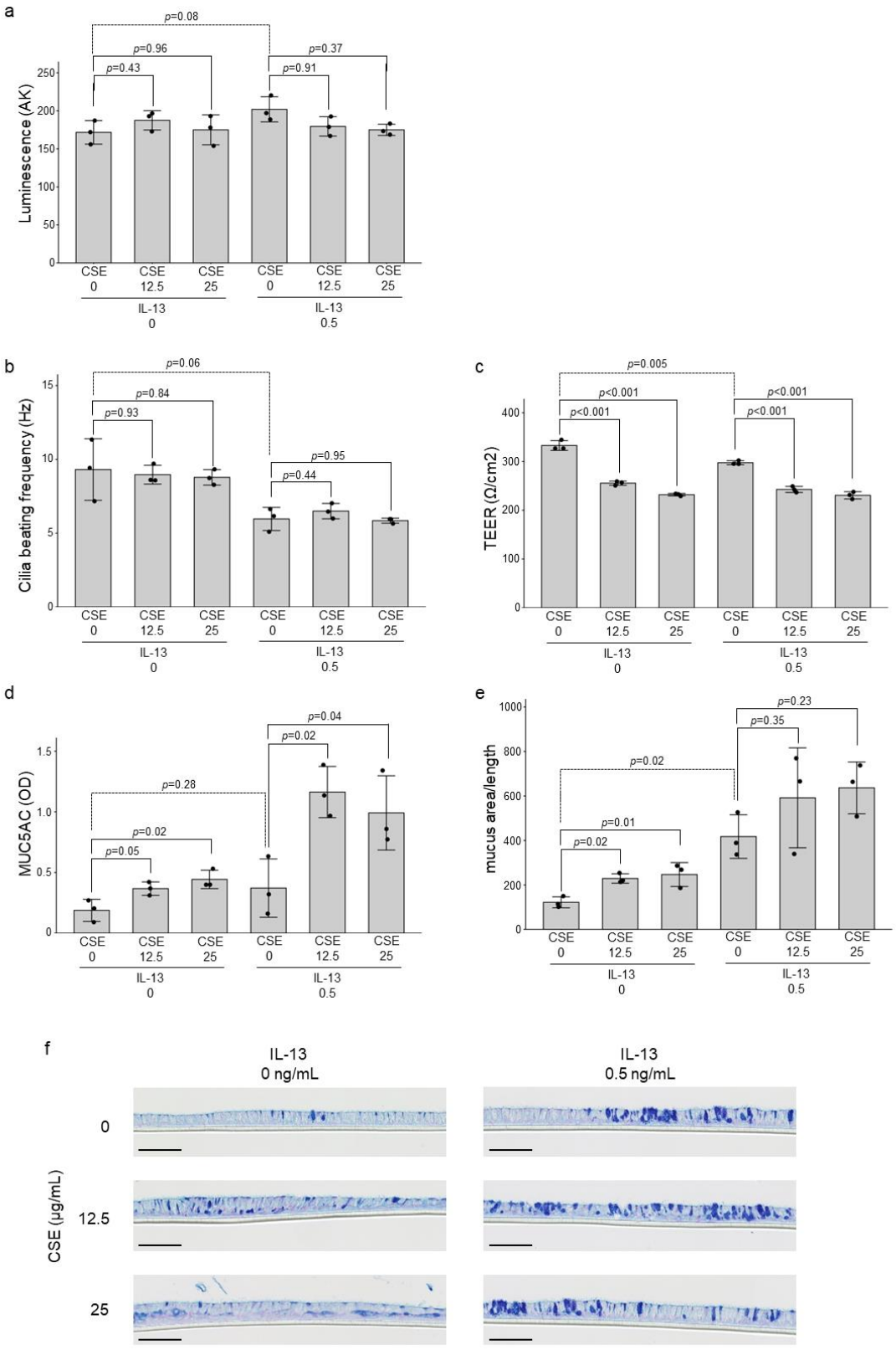
a
Luminescence (AK)
p=0.08
p=0.96
p=0.37
p=0.43
p=0.91
b
Cilia beating frequency (Hz)
p=0.06
p=0.84
p=0.93
p=0.95
p=0.44
c
TEER (Ω/cm2)
p=0.005
p<0.001
p<0.001
p<0.001
p<0.001
d
MUC5AC (OD)
p=0.04
p=0.02
p=0.28
p=0.02
p=0.05
e
mucus area/length
p=0.23
p=0.35
p=0.02
p=0.01
p=0.02
CSE 0
CSE 12.5
CSE 25
IL-13 0
IL-13 0.5
f
IL-13 0 ng/mL
IL-13 0.5 ng/mL
CSE (µg/mL)
0
12.5
25

Fig. 2.1. Three-dimensionally cultured human bronchial epithelial cells (n=3) were exposed to cigarette smoke extract (CSE) and interleukin (IL)-13 for 14 days. (a): adenylate kinase (AK) in the medium was detected by luminescence as an indicator of cytotoxicity. (b) and (c): cilia beating frequency and trans-epithelial electric resistance (TEER) were measured by using a high-speed digital camera and a resistance meter respectively. (d): At the end of exposure, apical surface liquid was collected. MUC5AC in the apical surface liquid was detected by ELISA. The amount of MUC5AC was relatively evaluated by optical density (OD) compared to OD of negative control samples. E and F: fixed tissues were sliced for periodic acid-Schiff /Alcian Blue (PAS/AB) staining. PAS/AB positive areas were normalized to tissue length (e). Representative images of tissues are shown (f).

Results are presented as the mean ± SD (n = 3 per group). For samples of three conditions, p value was derived by Dunnett's test comparing to the control sample (solid line). For samples of two conditions, p value was derived by Student's t-test (dashed line). Scale bar: 100 μm.

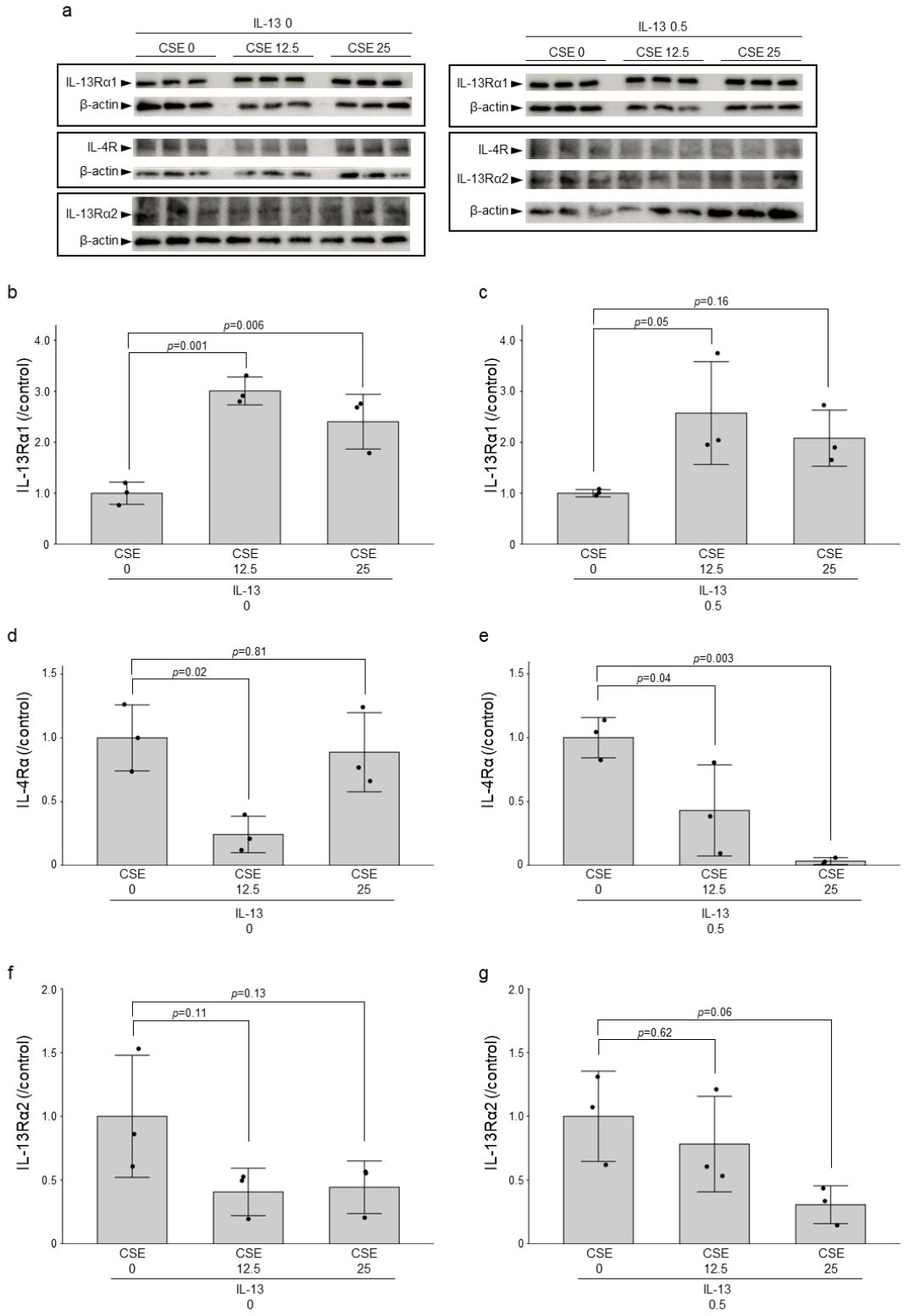
a
IL-13 0
CSE 0
CSE 12.5
CSE 25
IL-13Rα1
β-actin
IL-4R
IL-13Rα2
IL-13 0.5
b
c
d
e
f
g
IL-13Rα1 (/control)
IL-4Rα (/control)
IL-13Rα2 (/control)
p=0.006
p=0.001
p=0.16
p=0.05
p=0.81
p=0.02
p=0.003
p=0.04
p=0.13
p=0.11
p=0.06
p=0.62
IL-13
0
0.5

Fig. 2.2. Interleukin (IL)-13 receptor expression in bronchial epithelial cells was measured by western blotting on day 14 post exposure of cigarette smoke extract (CSE) and IL-13. Images of bands are shown in (a). Bands of IL-13 receptor (R) α1 (b and c), IL-4Rα (d and e), and IL-13α2 (f and g) were quantified by normalization to β-actin. Results are presented as the mean ± SD (n = 3 per group). P values: Dunnett's test comparing to the control sample.

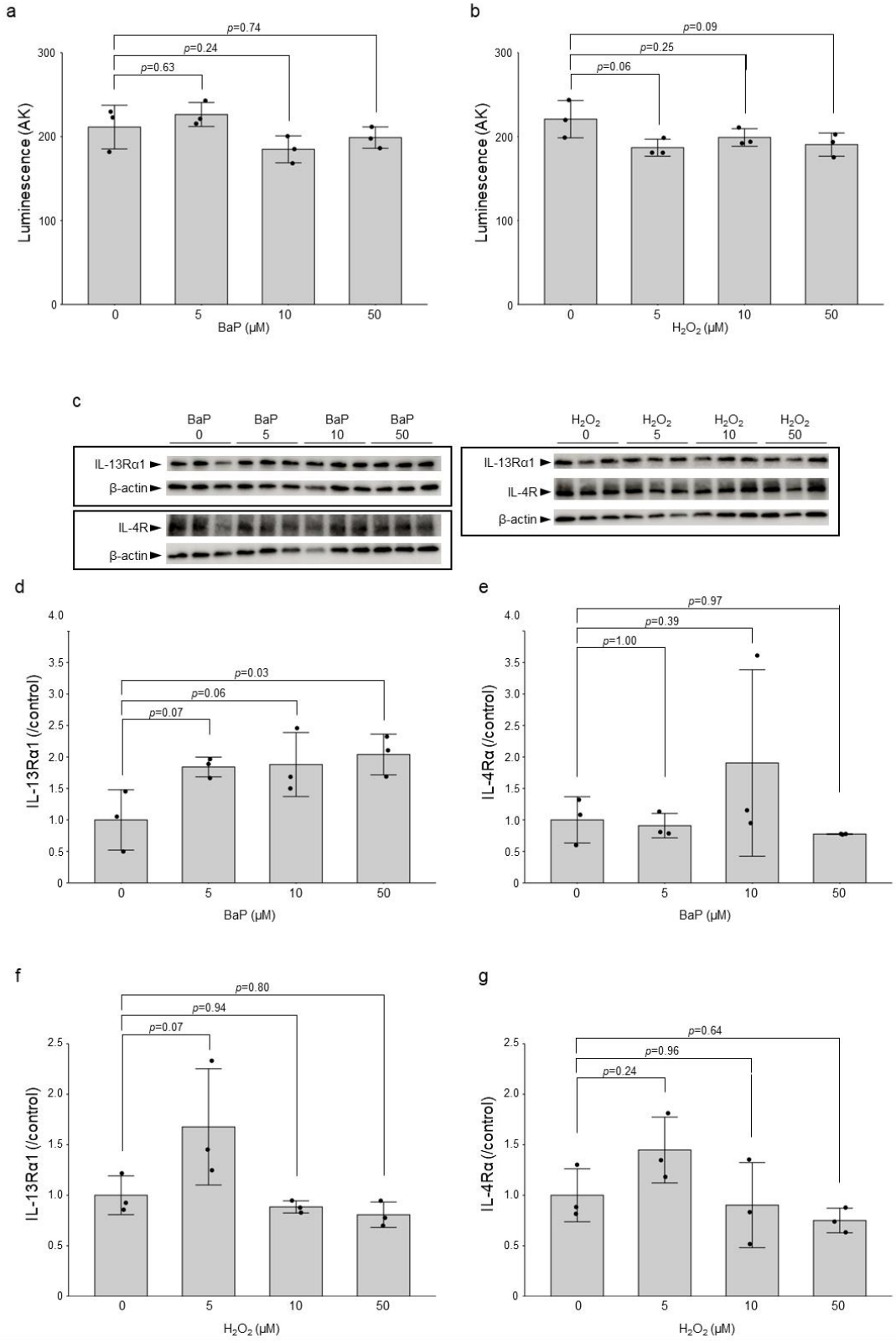
a
p=0.74
p=0.24
p=0.63
Luminescence (AK)
BaP (μM)
b
p=0.09
p=0.25
p=0.06
Luminescence (AK)
H2O2 (μM)
c
BaP 0
BaP 5
BaP 10
BaP 50
IL-13Rα1
β-actin
IL-4R
β-actin
H2O2 0
H2O2 5
H2O2 10
H2O2 50
IL-13Rα1
IL-4R
β-actin
d
p=0.03
p=0.06
p=0.07
IL-13Rα1 (/control)
BaP (μM)
e
p=0.97
p=0.39
p=1.00
IL-4Rα (/control)
BaP (μM)
f
p=0.80
p=0.94
p=0.07
IL-13Rα1 (/control)
H2O2 (μM)
g
p=0.64
p=0.96
p=0.24
IL-4Rα (/control)
H2O2 (μM)

Fig. 2.3. Three-dimensionally cultured human bronchial epithelial cells (n=3) were exposed to benzo(a)pyrene (BaP) (a, d, and e) and H2O2 (b, f, and g) for 14 days. (a) and (b): adenylate kinase (AK) in the medium was detected by luminescence as an indicator of cytotoxicity. (c) – (g): Interleukin (IL)-13 receptor expression in cells was measured by western blotting. Images of bands are shown in (c). Bands of IL-13 receptor (R) α1 (d and f) and IL-4Rα (e and g) were quantified by normalization to β-actin. Results are presented as the mean ± SD (n = 3 per group). P values: Dunnett's test comparing to the control sample.

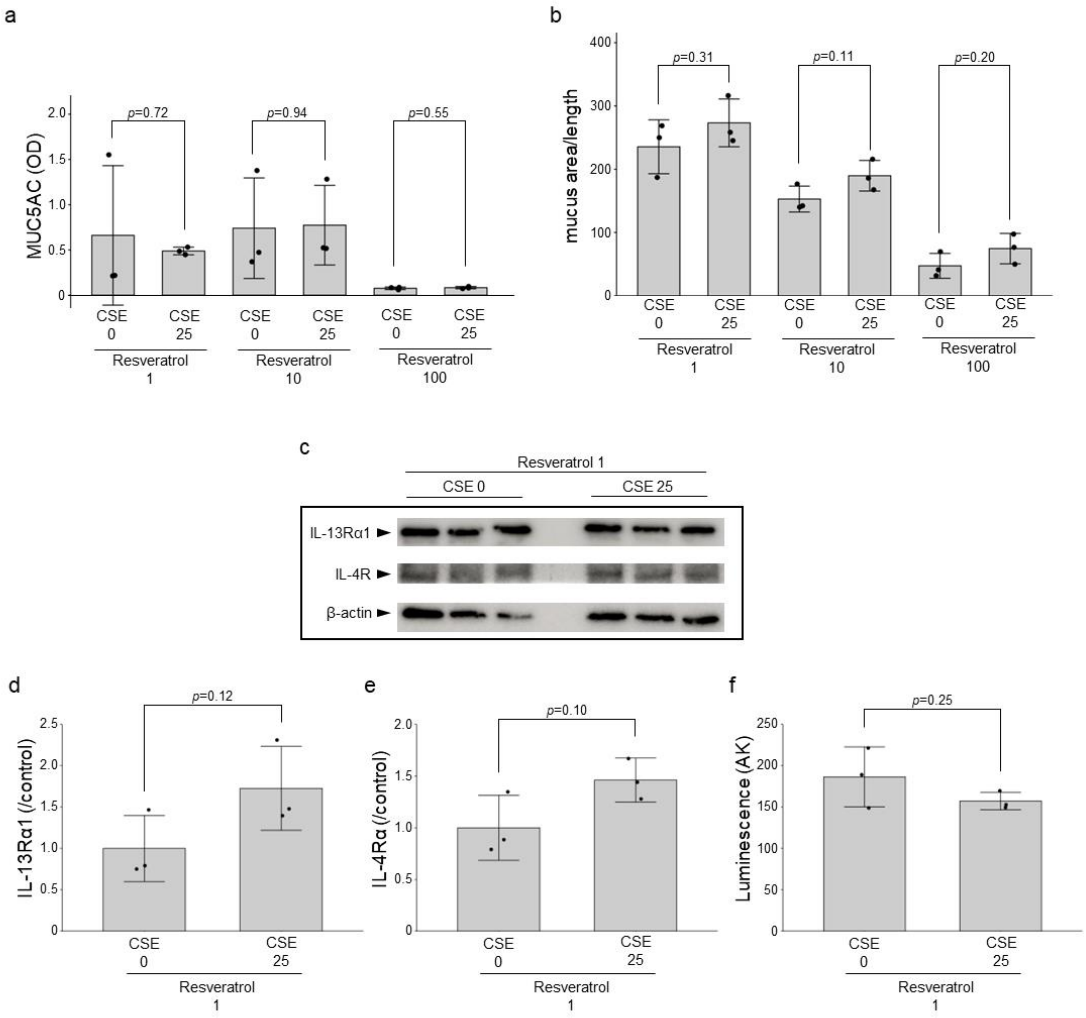

Fig. 2.4. Resveratrol and cigarette smoke extract (CSE) were added to the medium of three-dimensionally cultured human bronchial epithelial cells (n=3) with Interleukin (IL)-13 for 14 days. (a): At the end of exposure, apical surface liquid was collected. MUC5AC in apical surface liquid were detected by ELISA. MUC5AC amount was relatively evaluated by optical density (OD) compared to the OD of negative control samples. (b): fixed tissues were sliced for periodic acid-Schiff /Alcian Blue (PAS/AB) staining. PAS/AB positive areas were compensated by tissue length. (c): Images of western blotting bands. (d) and (e): Interleukin (IL)-13 receptor (R) expression in cells was measured by western blotting. Bands of IL-13 Rα1 (d) and IL-4Rα (e) were quantified by normalization to β-actin. (f): adenylate kinase (AK) in the medium was detected by luminescence as an indicator of cytotoxicity. Results are presented as the mean ± SD (n = 3 per group). P values: Student's t-test comparing to the control sample.

Chapter 3
High-throughput Bronchus-on-a-Chip system for modeling the human bronchus

Abstract

Chronic bronchitis induces goblet cell hyperplasia and metaplasia, obstructing airflow. Traditional animal testing is often replaced by *in vitro* three-dimensional cultures of human epithelial cells to assess chronic cell responses. However, these cells are cultured horizontally, differing from the tubular structure of the human airway and failing to accurately reproduce airway stenosis. To address this, I developed the Bronchus-on-a-Chip (BoC) system. The BoC uses a novel microfluidic design in a standard laboratory plate, embedding 62 chips in one plate. Human bronchial epithelial cells were cultured against a collagen extracellular matrix for up to 35 days. Characterization included barrier integrity assays, microscopy, and histological examination. Cells were successfully cultured in a tubular structure, with the apical side air-lifted. Epithelial cells differentiated into basal, ciliated, and secretory cells, mimicking human bronchial epithelium. Upon exposure to inducers of goblet cell hyperplasia and metaplasia, the BoC system showed mucus hyperproduction, replicating chronic epithelial responses. This BoC system enhances *in vitro* testing for bronchial inflammation, providing a more human-relevant and high-throughput method.

1. Introduction

A critical defense mechanism to airborne materials is the barrier function, which is achieved by tight and gap junctions in the epithelium, physically preventing airborne materials from invading the subepithelial compartment. In addition, the tracheal and bronchial epithelia play crucial roles in mucociliary clearance. The tracheobronchial epithelium comprised of basal, ciliated, and secretory cells. Ciliated cells express hair-like structures (cilia) on their surface, and secretory cells (including goblet and club cells) secrete mucus. Mucus captures inhaled airborne materials, which are cleared out of the respiratory tract by the beating cilia of ciliated cells (Crystal *et al.*, 2008). However, once these defense mechanisms are impaired, inhaled materials can reach cellular compartments and trigger various cellular responses, including inflammation.

Airway inflammation is a protective response of the body to airborne materials, such as toxins, pollutants, irritants, and allergens, and is normally a temporal biological event. However, when inflammation becomes severe and chronic, it can disrupt normal organ function, leading to conditions such as chronic obstructive pulmonary disease and asthma (Aghasafari et al., 2019; Larsen & Holt, 2000).

The mechanisms underlying airway chronic inflammation are complex, and its symptoms often manifest at multiple sites within the airway (Bousquet *et al.*, 2000; Holz *et al.*, 2000). In the bronchial region, chronic inflammation in the airways often leads to bronchitis, during which bronchial tissues exhibit abnormal cell populations and impaired mucociliary clearance function. These results are due to inflammation-induced hyperplasia and metaplasia of goblet cells, leading to hyperproduction of mucus and thickening of epithelial cell layers. As a result, patients with chronic bronchitis often experience difficulty breathing due to airflow obstruction caused by mucus hyperproduction and airway remodeling (Fahy & Dickey, 2010; Jeffery, 2001; Rogers, 2002).

Two culture methods are commonly used for *in vitro* toxicological assessment and analysis of disease mechanisms in the human bronchi. The first is the two-dimensional culture system, which is a simple and low-cost culture method, in which airway epithelial cells are cultured in flasks or plates as monolayers. This system is mainly used for acute cell response analyses, such as cytotoxicity and cytokine production, and is useful for screening purposes in toxicological and pharmacological evaluations. However, this can

lead to misinterpretation because the cells lack polarization and functionality, and thus do not effectively represent airway cells *in vivo*.

Conversely, a three-dimensional (3D) culture system is a more sophisticated approach that mimics the tracheobronchial epithelium more accurately (Fig. 3.1a). Such 3D cultures contain functional epithelium with pseudostratified columnar and multitype cells, including basal cells at the bottom of the layer, ciliated cells, and goblet cells containing mucus(Hiemstra et al., 2018; Prytherch et al., 2011). In addition, 3D-cultured airway epithelial cells are suitable for long-term culture, which enables the induction of chronic states. For example, increased epidermal growth factor (EGF) levels and continuous treatment with interleukin (IL)-13 can lead to goblet cell hyperplasia and metaplasia in 3D human bronchial epithelial cells (HBECs) (Casalino-Matsuda et al., 2006; Kistemaker et al., 2015). The result of 3D HBECs show promise for mimicking chronic bronchial responses. However, considering the actual human bronchial structure, such cultures have room for improvement.

Most of the current structure of 3D HBECs is a horizontal plane, which differs from the physiological tubular structure of human bronchi. Considering the effect of surrounding cell populations on cell growth, the tubular structure of HBEC cultures would be more representative of the human bronchial system. In addition, considering airborne material exposure through human inhalation, modeling a tubular structure would be more biologically relevant because inhaled substances are normally exposed to airway epithelial cells in the tubular lumen. Furthermore, stenosis and airflow obstruction of chronic bronchitis are not reproduced in a planar culturing method but can be reproduced in a tubular structure. Development of a culture method that mimics such a physiological environment could be beneficial for developing more predictive test methods.

Recently, physiologically relevant *in vitro* culture methods have been progressively developed, and they are anticipated to serve as an alternative for animal testing. Organ-on-a-Chip (OoC) technology has emerged and mimics the physiological environment in thumb-size, or smaller, microfluidic chips(Kimura *et al.*, 2018; Wu *et al.*, 2020). They can be broadly classified into high-throughput and high-function models. High-throughput OoCs typically use systems that are compatible with standard labware, such as multi-channel pipettes and robotics. They allow for conducting experiments with many replicates and conditions(Azizgolshani *et al.*, 2021). However, to achieve high-throughput capability, these chips may sacrifice some functionality, such as organ

structure and dynamics. Conversely, high-function OoCs are designed to mimic organ-specific structure or dynamics by recreating the spatial environment of cells and by incorporating special devices that realize *in vivo* conditions, e.g., organ substructure, motion, and blood flow, at the cost of throughput. In high-function OoCs, the dynamics of the cells and material being tested are well reproduced (Huh et al., 2010; Jang & Suh, 2010).

The development of Airway-on-a-Chip technology has mainly focused on alveolar models (Sengupta *et al.*, 2023), resulting in a limited number of reported tracheal and bronchial models. Benam *et al.* (2016) reported a 'small airway-on-a-chip', which incorporates functional airway epithelium and is capable of mimicking breathing motion, air, and blood flow. This model demonstrated potential for studying airway inflammation. Similar models have also been reported, as summarized by Lagowala et al. (2021). Moreover, Park and Young (2021) reported "E-FLOAT" which enables on-chip as well as off-chip analyses under physiological airflow, and Gao et al. (2024) recently reported that tubular airway-on-chip model which enables to investigate ventilation dynamics. Thus, advancements in Airway-on-a-Chip technology offer opportunities for selecting an appropriate *in vitro* model based on research objectives. Nevertheless, the throughput of these models is generally low, and improving throughput while maintaining high physiological relevance remains a challenging issue.

In this study, I developed Bronchus-on-a-Chip (BoC) with both tubular structured functional epithelial cells and high-throughput capabilities on a specialized plate, the OrganoPlate Air. This tubular structured culture system represents a human-relevant environment for aerosol exposure inside a tube, mimicking the actual route of exposure. I believe that this hybrid approach, combining high functionality and high-throughput performance in the BoC, will be valuable for studying airway inflammation and chronic-phase biological responses that reflect the complexity of *in vivo* situations in humans. Additionally, the model offers expanded options for the fit-for-purpose use of airway-on-a-chip models.

2. Materials and Methods

2.1. Cell culture

HBECs (Lonza, CC-2540, lot 623950) were expanded in T75 culture flasks (ThermoFisher, 156499) with PneumaCult ExPlus medium (StemCell Technologies, 05040) containing 1% penicillin/streptomycin (Sigma, P4333). Medium aliquots were supplemented with hydrocortisone (StemCell Technologies, 07925) according to the manufacturer's instruction. Cells were detached with trypsin/ethylenediaminetetraacetic acid (Lonza, CC-5012) for 5 min and neutralized with Trypsin Neutralization Solution (Lonza, CC-5002). Cells were frozen in passage 2 in ExPlus medium with 40% fetal bovine serum (Gibco, 16140-071) and 10% dimethyl sulfoxide (Sigma, D8418) and stored at −150 °C. To initiate an experiment, HBECs were thawed in ExPlus medium and directly seeded into OrganoPlate Air (see next section). After the cells formed a confluent layer, the medium was switched to PneumaCult ALI medium (differentiation medium, StemCell Technologies, 05001) containing 1% penicillin/streptomycin. Medium aliquots were supplemented with heparin solution (StemCell Technologies, 07980) and hydrocortisone according to the manufacturer's instructions and were used within 2 weeks. Immediately prior to medium change with differentiation medium, 250 nM matrix metalloproteinases-inhibitor GM6001 (Abcam, ab120845) was added to avoid degradation of the collagen scaffold.

2.2. OrganoPlate Air

HBEC cultures were established in a newly developed plate, the OrganoPlate Air (Mimetas BV), which consists of 62 microfluidic chips patterned underneath a 384-well titer plate (Fig. 3.1b). Each chip connects six wells that contain two perfusion channels and a gel channel leading towards a central chamber (Fig. 3.1c; well B2). The design of the novel OrganoPlate Air is adapted from the OrganoPlate Graft (Mimetas BV) (Bonanini *et al.*, 2022), with an opening at both the top and bottom glass layer of the central chamber. To maintain sterility, a bottom cover was placed underneath the plate. The PhaseGuides present on either side of the central chamber prevent the liquid extracellular matrix (ECM) from overflowing into the adjacent channels before it solidifies (Vulto *et al.*, 2011), omitting the need for artificial membranes. In this manner,

the adjacent perfusion channels can be used for perfusion and diffusion of nutrients through the ECM in the central chamber. In a similar manner, the surface tension of the openings in the glass at the top and bottom of the central chamber also prevent the liquid ECM from overflowing into the opening itself, leaving a tapered tubular cavity from top to bottom within the ECM filled central chamber after it solidifies. In this cavity, cells can be cultured in a tubular fashion, leaving full access to the apical surface.

Bovine collagen (5 mg/mL; PureCol EZ, Advanced BioMatrix, 5074) was used as an ECM inside the central chamber. PureCol EZ (3 µL) was loaded to the gel inlet (Fig. 3.1c; well A2) to fill the chamber. After ECM loading, the plate was placed at 37 °C for 40 min, and then 50 µL of phosphate-buffered saline (PBS) (Gibco, 70013065) was added to the gel inlet to keep the ECM hydrated. After 1 day at 37 °C, 1 µL of PBS was added to all perfusion channel inlets (Fig. 3.1c; wells A1 and A3), and the plates were incubated at 37 °C for at least 6 days. Then the chip is ready for cell seeding within the open cylinder structure in the ECM (Fig. 3.1d).

Immediately prior to cell seeding, ExPlus medium was added to the perfusion channels (50 µL into each perfusion inlet and outlet; Fig. 3.1c; wells A1, A3, B1, and B3). Cells were seeded inside the cavity in the central chamber by pipetting 0.25 µL of a 20000 cells/µL cell suspension, resulting in 5000 cells/chip. The surface tension at the bottom of the cavity facilitated cells or medium from remaining within the cavity. The plate was incubated at 37 °C for 4 h on one of the long sides of the plate and then switched to the opposite long side of the plate overnight to allow the cells to settle all around the gel (Fig. 3.1e). After cell attachment, 50 µL of ExPlus medium was carefully added to the central chamber (Fig. 3.1c; well B2), and the plate was placed on a rocking platform (OrganoFlow, Mimetas BV) set at a 14° inclination with an 8-min interval to initiate submerged cell culture with bidirectional flow through the perfusion channels (Fig. 3.1f). After 3 days of culture, a confluent cell layer of epithelium was formed growing within the cavity against the ECM; the medium in the perfusion channels was changed to differentiation medium, and the medium in the central chamber was replaced with Hanks' Balanced Salt Solution (HBSS, Sigma, H6648).

On day 10 after cell seeding, air-liquid interface culture was initiated and maintained until the end. Culture medium is supplied through the perfusion channels throughout the experiment. To achieve this air-liquid interface culture, the liquid in the central chamber and perfusion channels was removed, and then the bottom cover was removed. The plate

was then inverted and left to air dry for approximately 3 min. Next, the bottom cover was placed back on the plate, medium was added to the perfusion channel inlets and outlets as described before, and culture was continued with an air-liquid interface present (Fig. 3.1g).

2.3. Cilia assessment

From day 14 onwards, the presence of cilia was assessed. To increase the visibility of the air-liquid interface cultures, 50 µL of HBSS was added to the central chamber. The number of beating cilia per chip was observed with an optical microscope and categorized from 0 to 3: 0 indicates absence of cilia, 1 indicates small patches of cilia, 2 indicates larger patches of cilia, and 3 indicates large areas of cilia. After the assessment, the air-liquid interface was re-initiated as previously stated. Statistics were performed with the 'one-way ANOVA' function in GraphPad Prism version 10.

2.4. Immunohistochemistry

HBEC cultures were fixed with 3.7% formaldehyde (Sigma, 252549) in HBSS for 10 min, washed once with PBS for 5 min, and stored with 50 µL of PBS per well at 4 °C until immunofluorescent staining.

Fixed HBEC cultures were simultaneously permeabilized and blocked for 45 min with 2% fetal calf serum (FCS, Gibco, A13450), 2% bovine serum albumin (Sigma, A2153), and 0.3% Triton X-100 (Sigma, T8787) in PBS. Afterwards, the cultures were incubated overnight with primary antibodies in antibody solution containing 2% FCS + 2% bovine serum albumin + 0.1% Triton X-100 in PBS, adding 20 µL to all wells except gel inlet After a 5 min wash with 4% FCS in PBS, the cultures were incubated for 1–2 h with secondary antibodies in antibody solution, including Sytoxgreen (1:5000; ThermoFisher, S7020) as a nuclear stain. After the incubation, the cultures were washed once with PBS, and then 30 µL CUBIC-R+ (TCI, T3741) was added to all wells, except the gel inlet, at least 4 h prior to imaging. All the steps were performed at room temperature. The following primary antibodies were used: rabbit anti-human cytokeratin 5 (1:100; Abcam, ab52635), mouse anti-human βIV tubulin (1:100; Sigma, T7941), mouse anti-human

mucin (MUC) 5AC (1:100; ThermoFisher, MA512178), and rabbit anti-human ZO-1 (1:100; ThermoFisher, 61-7300). The following secondary antibodies were used: donkey anti-mouse AF555 (ThermoFisher, A31570), goat anti-mouse AF555 (ThermoFisher, A21422), goat anti-rabbit AF488 (ThermoFisher, A11008), and donkey anti-rabbit AF647 (Sigma, SAB4600177), all at a dilution of 1:250. Immunofluorescent images were captured with an ImageXPress XLS-C HCI system (Molecular Devices) at 10× magnification, acquiring z-stacks with a distance of 5 µm. The maximum projection images were used for visual representation. The sum projection images were analyzed and quantified in FIJI, the 'measure integrated density' function was used for quantification of the marker expression of the area captured during imaging. The 'analyze particles' function was used for quantification of the number of nuclei. Statistics were performed with the 'unpaired one-way ANOVA' function in GraphPad Prism version 10. The color coding of the nuclear z-location was done as post-image analysis by applying a color gradient to the z-location of the nucleus signal using FIJI through "Temporal-color code" function.

2.5. Barrier integrity assay

As shown in *Chapter 2* Fig. 2.1c, 3D HBECs has barrier function. The barrier integrity of HBECs cultured on the OrganoPlate Air was also assessed. For this, 0.5 mg/mL FITC-Dextran (150 kDa; Sigma, 46946) in PBS was added to the apical side of the cell layer, and its diffusion to the basal side of the cell layer was measured. HBSS was aspirated from the central chamber if present, and 50 µL of FITC-Dextran was added to the central chamber and incubated for 15 min at 37 °C after which it was aspirated. The central chamber was washed once with PBS and aspirated prior to acquiring images with an ImageXPress XLS Micro HCI System (Molecular Devices) at 4× magnification. The fluorescence intensity of the ECM in the central chamber was quantified in FIJI, excluding the area of the center hole (Fig. 3.4a). Statistics were performed with the 'unpaired two-tailed *t*-test' function in GraphPad Prism version 10.

2.6. Exposure

On day 21 of culture, differentiated HBEC cultures were exposed to EGF (PeproTech,

AF-100-15) for 7 days by adding 1 or 5 ng/mL EGF to the differentiation medium in the perfusion channels. EGF was re-added with every medium change. On day 28, the cultures were exposed to 0.5, 1, or 5 ng/mL IL-13 (PeproTech, 200-013) for 7 days in a similar manner (Fig. 3.5a). Both exposures were performed during air-liquid interface culture, and no medium or HBSS was present in the central chamber.

3. Results

3.1. The OrganoPlate Air enables tubular cell cultures

The OrganoPlate Air is a novel microfluidic device consisting of 62 chips patterned underneath a standard 384-well titer plate, enabling perfusion and nutrient diffusion through a central chamber filled with an ECM (Fig. 3.1b and c). It enables both submerged and air-liquid interface cell cultures with access to the culture medium or air on the apical surface, respectively. In this study, the OrganoPlate Air was used to culture HBECs in a tubular fashion against a collagen ECM.

After cell seeding, the cells formed a confluent monolayer within the cavity against the ECM by day 3 (Fig. 3.2a and b). The cell layer remained confluent throughout the culture period (magnified images in Fig. 3.2b). On day 10, the culture was transitioned to an air-liquid interface setup, allowing direct exposure of the cells to air for the remaining duration of the culture. This resulted in a shadow being cast on the area against the ECM, thereby limiting visibility visual inspection and imaging (Fig. 3.2b, day 12). To mitigate this issue, HBSS was added to the central chamber immediately prior to observation to improve visibility. HBSS was subsequently removed to re-establish the air-liquid interface, and culturing was continued with cells directly exposed to air. To assess the confluency and tubular structure of the HBEC culture, Sytoxgreen nuclear fluorescent stain was used for visualization. Processing of the acquired images with a color-coding gradient for the z-location within the chip, confluency across the entire area against the ECM could be qualified (Fig. 3.2c). The complete area against the ECM was covered with cells, creating a confluent and stable tubular structure of bronchial epithelium. The bottom and top of the tubular structure remain open, allowing for unobstructed airflow through the chip.

3.2. Bronchial epithelium cultured in the OrganoPlate Air differentiates and forms a polarized tubular structure

For the differentiation of HBECs into a polarized and ciliated epithelium, the medium was switched from expansion medium to differentiation medium, which was applied to the basal side of cells. Subsequently, the apical side was cultured in an air-liquid interface environment. On days 14, 22, and 36 of culture, cilia were visually categorized as follows: no cilia (0), small patches (1), large patches (2), or large areas (3) (Fig. 3.3a). An evident

increase in the abundance of cilia was observed: the average score was 0.2 on day 14 and 2.7 on day 21, which remained almost consistent up to day 35.

In addition to the visual assessment of cilia, cultures were fixed on day 35 and stained for cytokeratin 5 (basal cells) and βIV-tubulin (cilia) to confirm HBEC differentiation. Maximum projection images showed consistent cytokeratin 5 expression in the BoC. The presence of cilia was also revealed by βIV-tubulin staining, which was observed in cultures in either large areas or small patches (Fig. 3.3b). To enhance visualization of the tubular structure of the cultures, a 3D reconstruction was generated from the immunofluorescent staining of nuclei, cytokeratin 5, and βIV-tubulin. This demonstrated the confluency around the area against the ECM (Fig. 3.3c). Furthermore, it illustrated that the basal cells were located at the basal side against the ECM, whereas cilia were present at the apical side facing the lumen. This morphology was further confirmed in a cross-section (Fig. 3.3c) with the basal cells and cilia present at the basal side and inside of the tubular structure, respectively.

3.3. Cells in the BoC display barrier formation

To evaluate the barrier formation and function of cells in the BoC, a barrier integrity assay was performed on day 21 of culture. When cells have leak-tight barrier function, they inhibit dextran diffusion from center hole (Fig. 3.4a). In wells without cells and barrier function as a control, the diffusion of a fluorescently labeled dextran molecule was detected in the ECM. Conversely, a functional cell barrier was observed as a lack of fluorescent signal in the ECM area of the central chamber on day 21 (Fig. 3.4b).

Quantification of the fluorescent signal in the ECM of the central chamber revealed a 35% higher fluorescence intensity in cell-free chips compared to BoCs (Fig. 3.4c). Presence of tight junctions at the cell borders was confirmed by ZO-1 staining (Fig. 3.4d), further indicating barrier function of the BoC.

3.4. Compound exposure on BoCs leads to increased mucus production

To assess the chronic response of BoC cells to compound exposure, cultures were exposed to EGF and IL-13, which are involved in airway inflammation and remodeling pathways.

On day 21 (11 days after initiation of the air-liquid interface), cultures were exposed to EGF for 7 days, and then to IL-13 for 7 days, adding up to a culture time of 35 days (Fig. 3.5a). The air-liquid interface was maintained throughout the entire exposure period. The consecutive exposure to EGF and IL-13 led to an increase in mucus production as characterized by an increased signal for MUC5AC (Fig. 3.5b). This increased mucus production did not depend on IL-13 concentration, which was confirmed with MUC5AC signal quantification. A 2.5–3.5-fold increase in signal intensity was detected after EGF and IL-13 exposures compared to the control condition (Fig. 3.5c). Conversely, the presence of basal cells displayed a 0.5–0.8-fold decrease after exposure to EGF and IL-13, as revealed by cytokeratin 5 signal quantification (Fig. 3.5d).

Another characteristic of airway inflammation and remodeling is thickening of the cell layer, which can be triggered through an inflammatory pathway(Booth *et al.*, 2001). Although methods for visualizing cross-sectioned BoC and quantifying the cell population require further improvement, I nevertheless observed that 2-week exposure to EGF and IL-13 resulted in an increase in the number of nuclei from cross-sectioned images (Fig. 3.5e). Despite no statistical difference, a trend of increasing numbers of nuclei with increasing IL-13 concentrations can be observed in the quantification of nuclei in the cross-sections (Fig. 3.5f).

4. Discussion

The BoC was developed by combining a 384-well titer plate with a novel microfluidic system. The design enables the use of standard labware equipment and achieves high-throughput with 62 chips/plate. This chip system belongs to the category of OoC systems with the highest throughput, which enables flexible study designs.

The characteristic structure of the OrganoPlate Air facilitates a tubular structural cell culture similar to that of bronchi, which is suitable for air exposures. To achieve this, I intentionally designed the opening (top side) hole to be larger than the end (bottom side) hole in the OrganoPlate Air, resulting in a gentle slope of the bronchial tubule. This slope enhances the visibility of the culture under microscopic examination during submerged culture. Upon initiating the air-liquid interface, the cells become invisible due to light refraction and scattering, indicating a successful air-liquid interface.

The bronchial tubule-on-a-chip possesses a leak-tight cell layer shown by confluency in magnified images and barrier integrity assay. It also demonstrated an appropriate cell population, resembling the characteristics of traditional 3D HBECs and *in vivo* bronchi (Gohy *et al.*, 2019; Rayner et al., 2019; Schamberger *et al.*, 2015). In addition, similarly to human airway and 3D HBECs culture, the ciliated cells with beating cilia were located in the apical layer, whereas basal cells resided in the basolateral layer. Mucus-producing cells (*i.e.*, MUC5AC-positive cells) were rarely observed. To reproduce a disease-state, the cell population and its functionality should be similar to those of *in vivo* tissues because airway disorders are often associated with abnormal and dysfunctional tissue structures caused by aberrant cell differentiation (Celly *et al.*, 2006; Varricchi *et al.*, 2022). In such disease-state airway tissues, impairment of both barrier and ciliary functions is generally observed (Ancel *et al.*, 2021; Heijink *et al.*, 2020). The BoC enabled the assessment of ciliary function and cell population alterations; therefore, I believe that it is useful for assessing disease risk. In addition, the BoC could be maintained for up to at least 35 days, which could be long enough to induce chronic effects of stimuli.

To demonstrate the effect of prolonged cytokine exposure in the BoC, a proof-of-concept study was performed involving prolonged exposure to EGF and IL-13. The regulation of the EGF receptor (EGFR) signaling pathway is pivotal for the maintaining differentiation and proliferation of airway epithelial cells (O'Boyle *et al.*, 2018; Shaykhiev *et al.*, 2013). However, aberrant EGFR activation causes anti-apoptotic effects and thus leads to

abnormal basal cell proliferation (Curran & Cohn, 2010). Activation of the EGFR signaling pathway is also related to mucus production in airway epithelial cells via the specificity protein-1 (Sp1) axis (Perrais *et al.*, 2002). In addition, IL-13 is a well-known inducer of goblet cell metaplasia and hyperplasia both *in vitro* and *in vivo* (Atherton *et al.*, 2003; Eenjes *et al.*, 2018; Wills-Karp *et al.*, 1998). As a result of 2-week exposure to EGF and IL-13, I observed an expected increase in MUC5AC-positive cell numbers and a decrease in basal cell numbers. This suggests that basal cells turned into mucus-producing cells, resulting in increased mucus production. These results demonstrate the utility of BoC in chronic exposure studies and for inducing disease states.

Traditionally, 3D HBECs are used for exposure studies of airborne materials, and thus various exposure apparatuses are available for these culture methods (Chandrala *et al.*, 2019; Ding *et al.*, 2020; Thorne & Adamson, 2013). However, most of them expose aerosols from top to bottom in a vertical manner. Consequently, the dynamics of aerosols cannot be fully reproduced with horizontally cultured cells. This approach can result in uneven aerosol deposition within a single sample (Oldham *et al.*, 2020). In the human bronchi, aerosols travel from the mouth or nose to deep lungs through airway tubules. Previous studies showed shear stress alters cell characteristics such as protein expression, barrier function, and nano particle delivery (Gupta *et al.*, 2021; Sidhaye *et al.*, 2008). Here, I achieved airway epithelial cell cultures with a tubular structure that closely mimics human airways. This opens up the possibility of reproducing exposure scenarios that are more relevant to humans. The air flow could provide shear stress to the HBECs in BoC, expecting manifestation of air-flow-associated functional characteristics such as coordinated cilia movement (Sone *et al.*, 2021). For this purpose, I am developing an aerosol exposure apparatus for horizontal 3D HBECs which is capable of reproducing human-relevant airflow and exposure scenario. For instance, aerosol exposure apparatus for horizontal 3D HBECs can adopt to BoC when I develop an attachment for BoC which allows to flow air and aerosol inside the BoC tubule, from the top to bottom.

I recognize that the BoC still has room for improvement. Handling BoCs can be technically challenging, and I sometimes experienced that the ECM sporadically failed to construct a robust culture interface. This could be due to secreted MMPs from HBECs (Ito *et al.*, 2018), therefore, MMP inhibitor (GM6001) was used to prevent biological degradation of ECM. However, MMPs play a critical role in inflammation and the pathogenesis of lung diseases (Atkinson & Senior, 2003; Houghton, 2015). ECM stability should be therefore improved without MMP inhibitors. In addition, one donor of HBEC

was tested for this proof-of-concept study. As reported previously, response to stimuli could vary depending on the donor characteristics (Mori et al., 2022; Muratani *et al.*, 2023). Therefore, using multiple donors for toxicological and pharmacological testing with this BoC is warranted. Visualization of the BoC is also challenging issue because unlike 3D planer HBEC, cells in the BoC is aligned almost vertically. Laser-scanning confocal microscopy could be one of the options to capture the fluorescent images of the BoC, because of its high spatial resolution which enables depth-wise imaging. Assessment of the cilia function is also a challenging issue, because the visibility of beating cilia is very limited. Although the difficulty for time-course experiment due to such a limited visibility should be overcome, fluorescence imaging could be rather easier, therefore assessment method of ciliary function should be replaced with fluorescent beads-based method (Khelloufi *et al.*, 2018). In addition, assessing ciliary function with high-speed camera and a specific software (e.g., SAVA system (Sisson *et al.*, 2003)) could be an alternative way, would thus be further investigated. In addition, an appropriate exposure apparatus compatible with the microfluidic device should be developed for controlled airway exposure inside the BoC.

5. Short summary

The novel microfluidic system BoC enabled a high-throughput OoC with an air-lifted tubular cell layer. The BoC contained three types of differentiated cells (basal, ciliated, and secretory cells), and thus has similar cell properties as human bronchi. In addition, EGF and IL-13, which are known inducers of airway epithelial remodeling *in vitro* and *in vivo*, induced a chronic response of mucus hypersecretion. These results show that this model can reproduce disease-state tissue characteristics through chronic exposure to known inducers and can be used as a high-function and high-throughput OoC assessment platform. As a next step, other toxicological (acute) assessments will be conducted with the BoC via medium exposure. Furthermore, because aerosols can pass through the BoC tube, a direct aerosol exposure assessment will be conducted with the development of an exposure device.

Figures

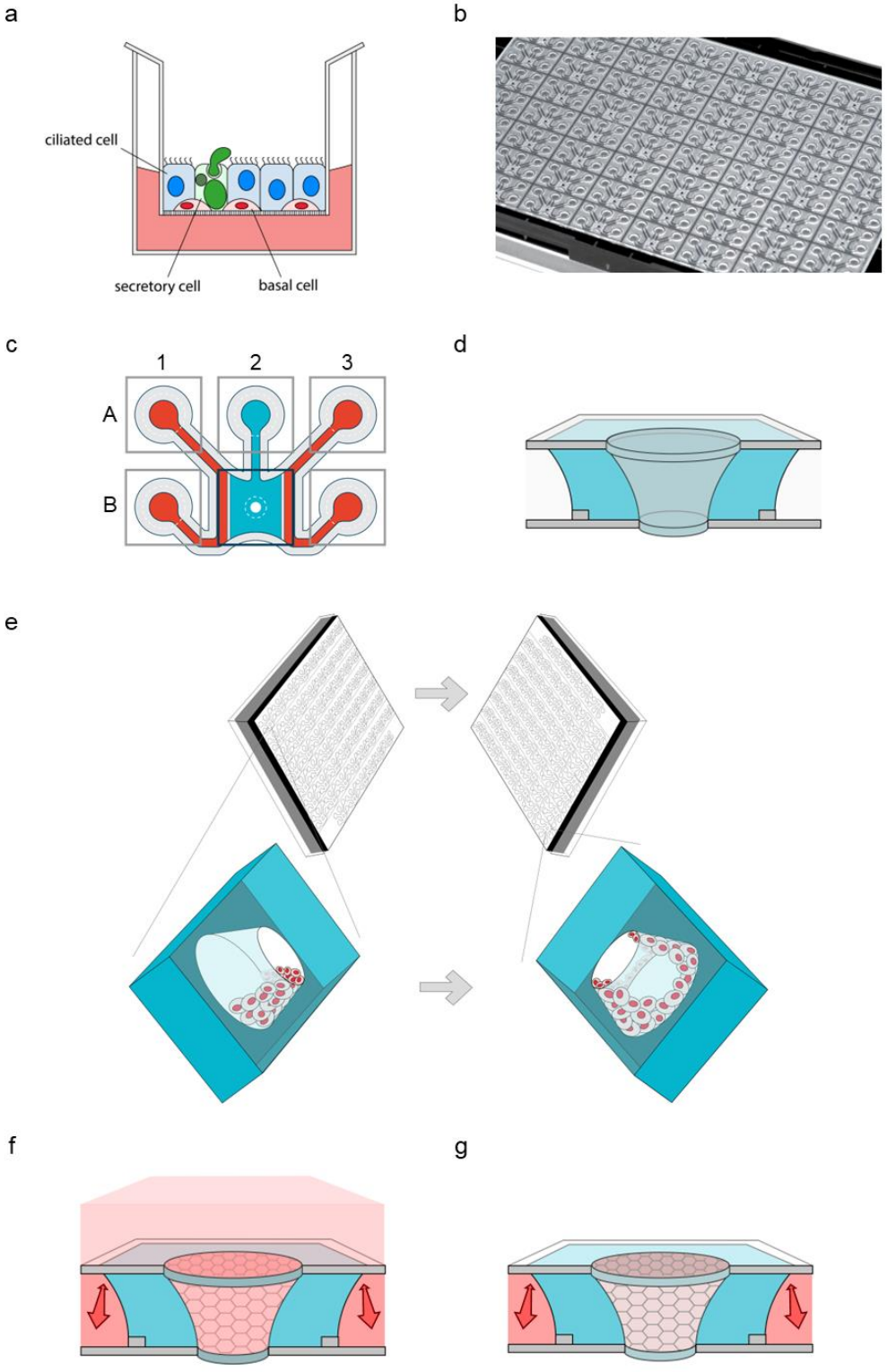
a
ciliated cell
secretory cell
basal cell
b
c
1
2
3
A
B
d
e
f
g

Fig. 3.1. The microfluidic air exposure system OrganoPlate Air.

(a) A schematic image of a three-dimensional culture system. The cell layers consist of basal, ciliated, and goblet cells on the membrane in the insert. The apical side is exposed to air. (b) A photograph of the bottom of the OrganoPlate Air, showing microfluidic chips based on a standard 384-well titer plate format. (c) A schematic overview of the chip layout in the OrganoPlate Air, comprising six wells connected by microfluidic channels. Perfusion channel inlets are in A1 and A3, perfusion channel outlets are in B1 and B3, the Gel Inlet is in A2, and the central chamber is in B2. Extracellular matrix (ECM; blue) is loaded into the chip through the gel inlet, and the surface tension of the loaded ECM at the edges prevents flowing of the ECM into the center hole, leaving the central cylinder in the central chamber empty. The cells can be seeded in this cylindrical lumen, forming a tubular structure. During culture, medium (red) can be added to the perfusion channels and to the central chamber for submerged culture (pink). The air-liquid interface can be initiated by removing medium from the central chamber. The perfusion channels supply the culture with medium, via nutrient diffusion through the ECM in the central chamber.

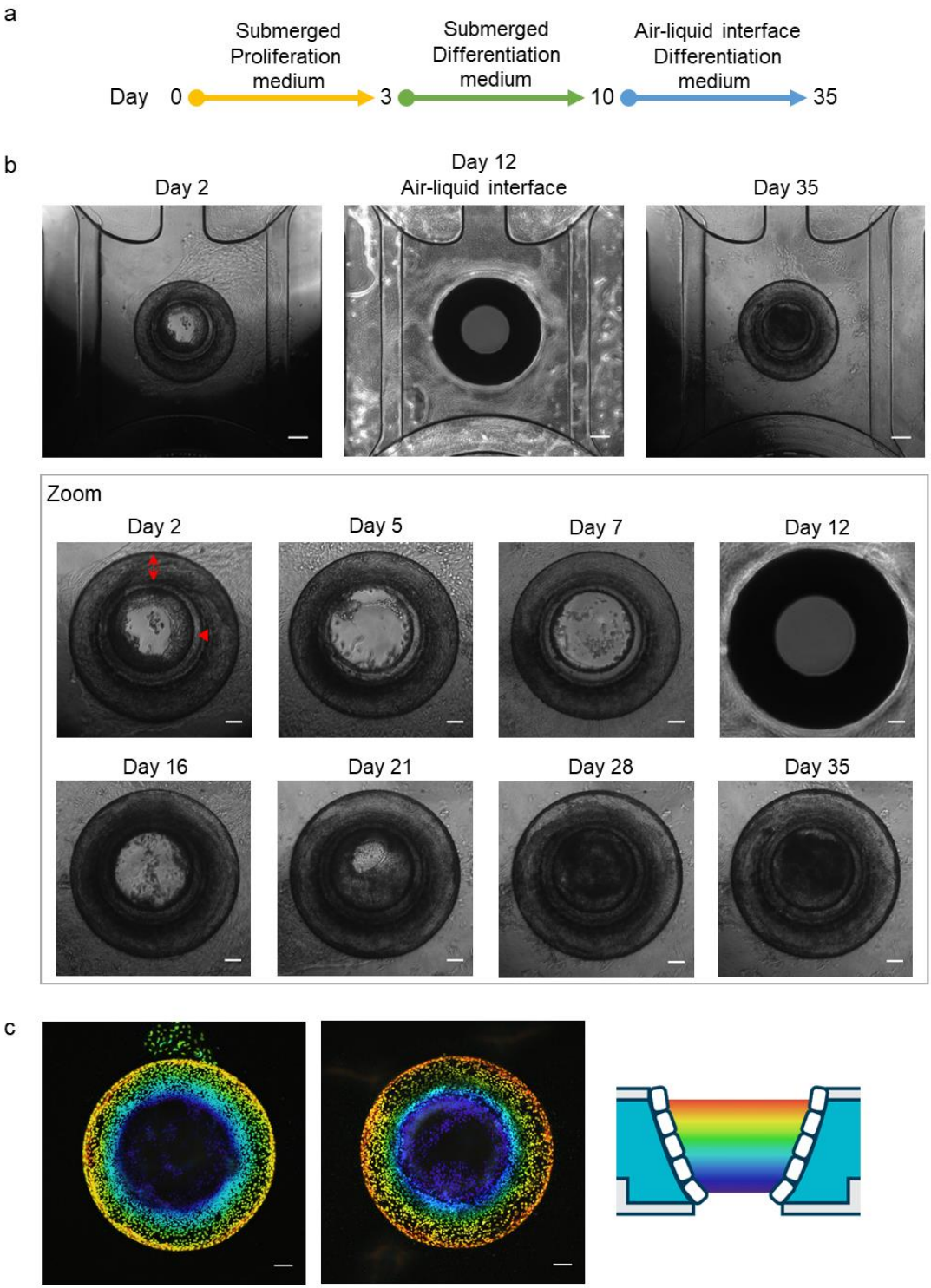
a
Submerged
Proliferation
medium
Submerged
Differentiation
medium
Air-liquid interface
Differentiation
medium
Day 0
3
10
35
b
Day 2
Day 12
Air-liquid interface
Day 35
Zoom
Day 2
Day 5
Day 7
Day 12
Day 16
Day 21
Day 28
Day 35
c

Fig. 3.2. Bronchus-on-a-Chip culture in the OrganoPlate Air.

(a) The experimental timeline of bronchial epithelial cell cultures in the OrganoPlate Air. Cells are seeded in the OrganoPlate Air on day 0, switched to differentiation medium on day 3, and air-liquid interface culture is initiated on day 10. Cultures are maintained up to day 35. (b) Phase-contrast images of cultures over time. For regular imaging, Hanks' Balanced Salt Solution (HBSS) was added to the central chamber prior to imaging to improve visibility of the culture. Double arrow and arrow head show gel surface and bottom glass respectively. The image on day 12 was taken without HBSS in the central chamber. Scalebars = 200 μm and 100 μm for magnified images. (c) Nuclear staining after fixation on day 35 with color coding for the z location within the chip, as indicated by the schematic. Scalebar = 100 μm

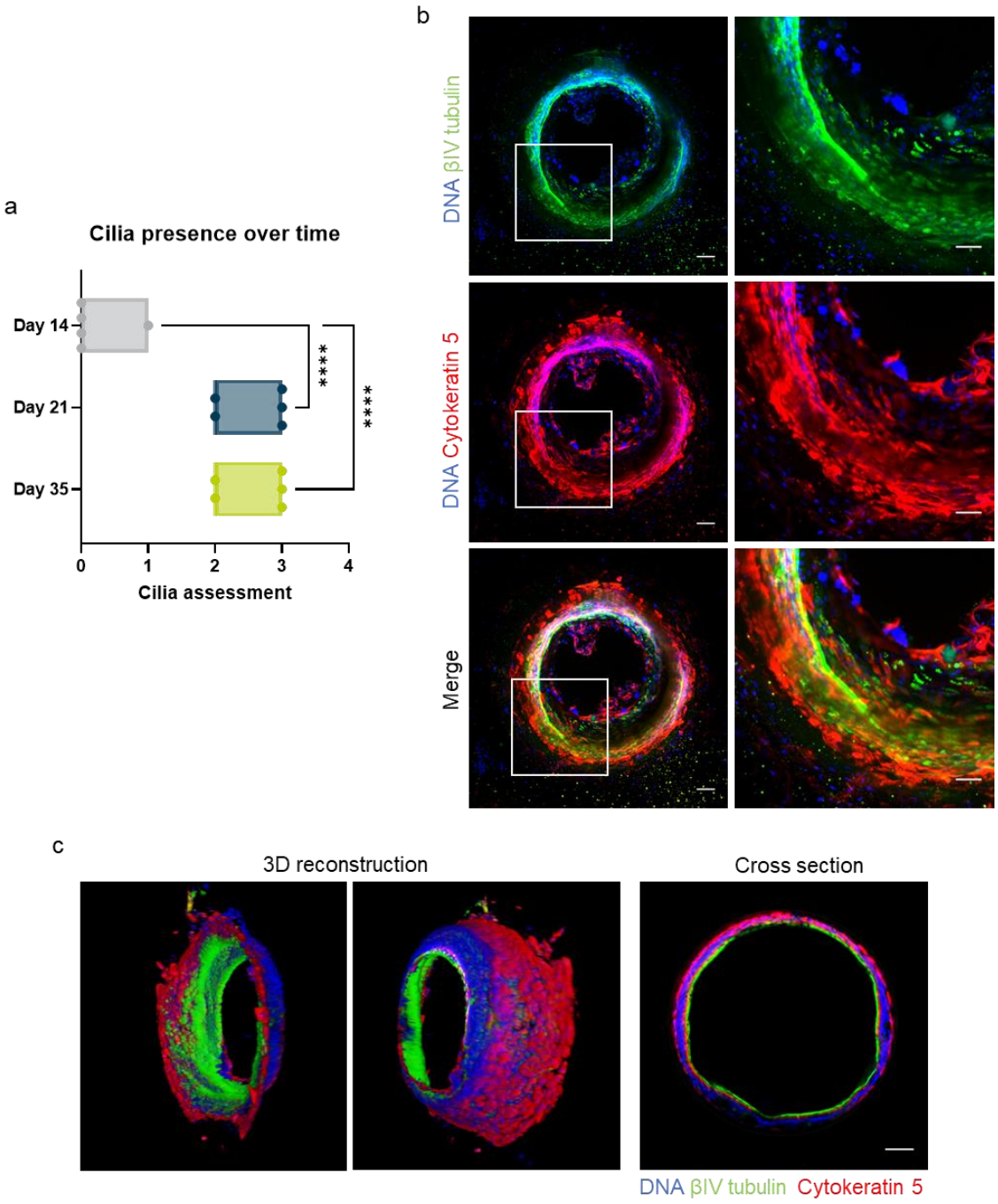
a
Cilia presence over time
Day 14
Day 21
Day 35
****
****
0
1
2
3
4
Cilia assessment
b
DNA βIV tubulin
DNA Cytokeratin 5
Merge
c
3D reconstruction
Cross section
DNA βIV tubulin Cytokeratin 5

Fig. 3.3. Differentiated and polarized tubular structure of Bronchus-on-a-Chip.

(a) Visual cilia assessment on days 14, 21, and 35 of culture: 0 (no cilia), 1 (small patches), 2 (large patches), and 3 (large areas) categorized by microscopic observation; five replicates for all days. Mean with error bars ± SD, statistical test – ordinary one-way ANOVA (**** $p < 0.0001$). (b) Immunofluorescence images of cells in Bronchus-on-a-Chip on day 35 of culture: 10× maximum projection images of βIV tubulin (green), cytokeratin 5 (red), and DNA (blue) in the left images and a magnification of the framed area in the right images. Scalebars = 100 µm (left images) and 50 µm (right images). (c) Three-dimensional reconstruction images and a cross-section of Bronchus-on-a-Chip showing a polarized tubular structure: βIV tubulin (green), cytokeratin 5 (red), and DNA (blue). Scalebar = 100 µm.

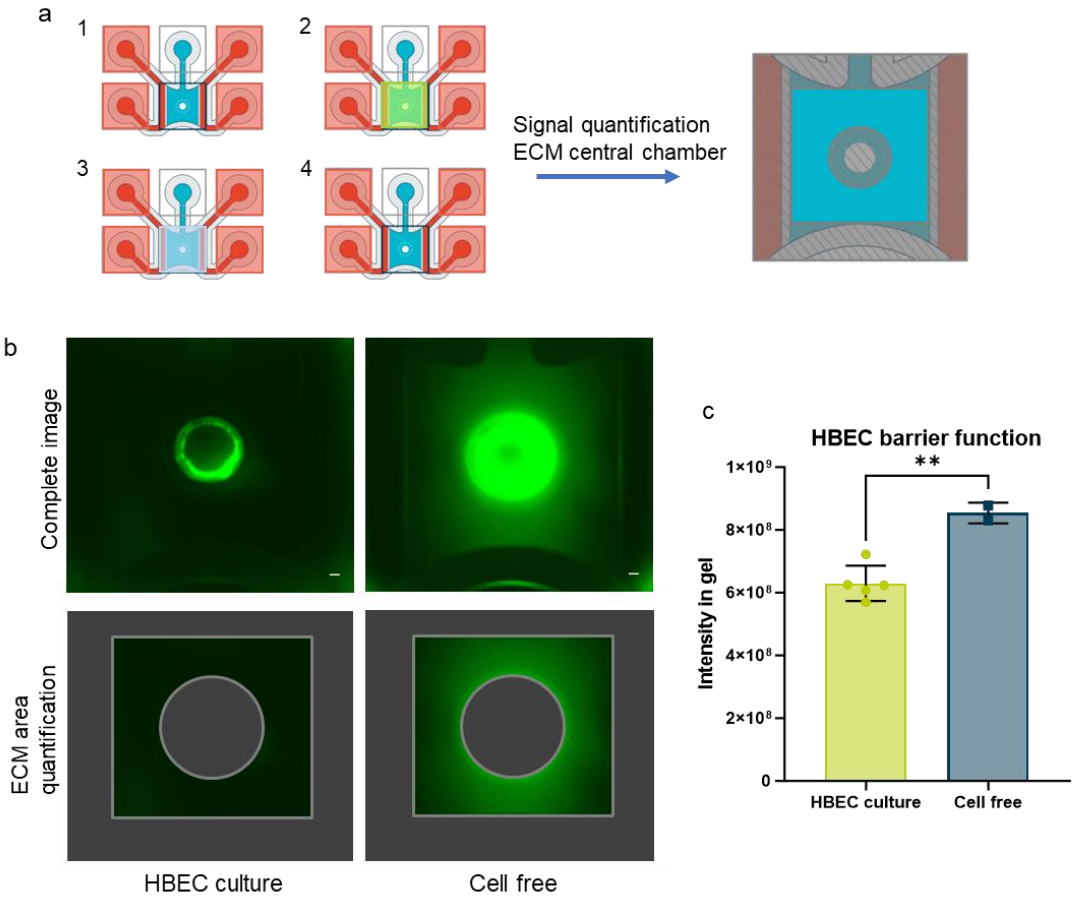
a
1
2
3
4
Signal quantification
ECM central chamber
b
Complete image
ECM area quantification
HBEC culture
Cell free
c
HBEC barrier function
**
Intensity in gel
1×10⁹
8×10⁸
6×10⁸
4×10⁸
2×10⁸
0
HBEC culture
Cell free
d
DNA ZO-1

Fig. 3.4. Assessment of barrier function in Bronchus-on-a-Chip.

(a) A schematic overview of the barrier integrity assay. Any liquid present in the central chamber is removed (1), fluorescent solution is added to the central chamber (2) and incubated for 15 min prior to a wash (3), and removal of liquid in the central chamber before imaging (4). The extracellular matrix (ECM) area is depicted for signal quantification, excluding the gray area from analysis. (b) Barrier integrity assay images of chips with and without cells on day 21 after applying 150 kDa FITC-Dextran. Scalebar = 100 µm. (c) Quantification of barrier integrity assay by measuring fluorescent intensity of the ECM area of the Bronchus-on-a-Chip, indicated in (a) and (b) as the area between the gray frames. Mean with error bars ± SD, chips with cells (n=5); cell-free chips (n=2). Statistical test – unpaired two-tailed *T*-test (** $p < 0.01$). (d) Fluorescence images Bronchus-on-a-chip, 10x maximum projection images of ZO-1 (green) and DNA (blue) in the left image and a magnification of the framed area in the right image. Scalebars = 100 µm (left image) and 50 µm (right image).

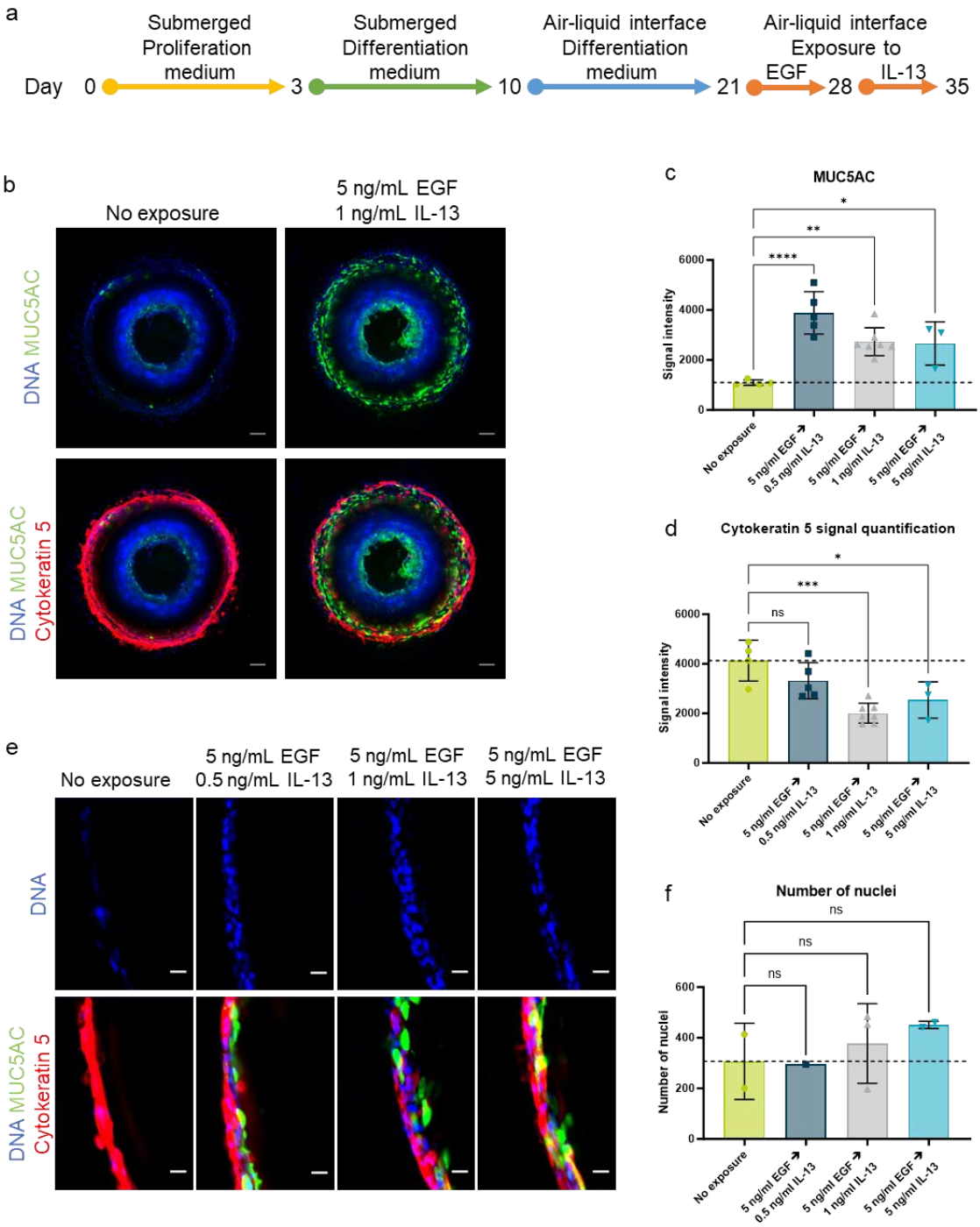
a
Submerged
Proliferation
medium
Submerged
Differentiation
medium
Air-liquid interface
Differentiation
medium
Air-liquid interface
Exposure to
EGF
IL-13
Day 0
3
10
21
28
35
b
No exposure
5 ng/mL EGF
1 ng/mL IL-13
DNA MUC5AC
DNA MUC5AC
Cytokeratin 5
c
MUC5AC
Signal intensity
No exposure
5 ng/ml EGF
0.5 ng/ml IL-13
5 ng/ml EGF
1 ng/ml IL-13
5 ng/ml EGF
5 ng/ml IL-13
d
Cytokeratin 5 signal quantification
Signal intensity
e
No exposure
5 ng/mL EGF
0.5 ng/mL IL-13
5 ng/mL EGF
1 ng/mL IL-13
5 ng/mL EGF
5 ng/mL IL-13
DNA
DNA MUC5AC
Cytokeratin 5
f
Number of nuclei
Number of nuclei

Fig. 3.5. Increased goblet cell formation after epidermal growth factor (EGF) and interleukin (IL)-13 exposure of Bronchus-on-a-Chip.

(a) Timeline of epithelial cell culture and exposure. Culture differentiation up to day 21, followed by 1-week exposure to EGF and 1-week exposure to IL-13. (b) Fluorescence images of Bronchus-on-a-Chip on day 35, after exposure to 5 ng/mL EGF followed by 1 ng/mL IL-13. 10× maximum projection images of MUC5AC (green), cytokeratin 5 (red), and DNA (blue). Scalebar = 100 µm. (c) Quantification of MUC5AC signal intensity after exposure to 5 ng/mL EGF and 0.5–5 ng/mL EGF (3–7 replicates). Mean with error bars ± SD. (d) Quantification of cytokeratin 5 signal intensity after exposure to 5 ng/mL EGF and 0.5–5 ng/mL EGF (3–7 replicates). Mean with error bars ± SD. (e) Magnified fluorescence images of Bronchus- on-a-Chip on day 35 after exposure to 5 ng/mL EGF and 0.5–5 ng/mL IL-13. Cross- section of area against gel, displaying MUC5AC (green), cytokeratin 5 (red), and DNA (blue). Scalebar = 20 µm. (f) Quantification of the number of nuclei in the complete cross-sections of which a magnified image is depicted in (e) (1–3 replicates). Mean with error bars ± SD. Statistical test – ordinary one-way ANOVA (ns = not significant, * $p < 0.05$, ** $p < 0.01$, *** $p < 0.001$, **** $p < 0.0001$).

Chapter 4

A revision of the multiple-path particle dosimetry model focusing on tobacco product aerosol dynamics

ABSTRACT

To assess the health impact of inhaled aerosols, it is necessary to understand aerosol dynamics and the associated dosimetry in the human respiratory tract. Although several studies have measured or simulated the dosimetry of aerosol constituents, the respiratory tract focus areas have been limited. In particular, the aerosols generated from tobacco products are complex composites and simulating their dynamics in the respiratory tract is challenging. To assess the dosimetry of the aerosol constituents of tobacco products, I developed a revised version of the Multiple-Path Particle Dosimetry (MPPD) model, which employs 1) new geometry based on CT-scanned human respiratory tract data, 2) convective mixing in the oral cavity and deep lung, and 3) constituent partitioning between the tissue and air, and clearance. Sensitivity analysis was conducted using aerosols composed of four major constituents of electronic cigarette (EC) aerosols to investigate the parameters that have a significant impact on the results. In addition, the revised model was run with four and ten constituents in ECs and conventional cigarettes (CCs), respectively. Sensitivity analysis revealed that the new modeling and the physicochemical properties of constituents had a considerable impact on the simulated aerosol concentration and dosimetry. The simulations could be carried out within 3 minutes even when 10 constituents of CC aerosols were analyzed simultaneously. The revised model based on MPPD is an efficient and easy-to-use tool for understanding the aerosol dynamics of CC and EC constituents and their effect on the human body.

Nomenclature

A	Airway cross-sectional area
A'	Airway total cross-sectional area
C_d	Concentration of the droplets in air
C_{inh}	Concentration leaving the oral cavity and entering the trachea
$\overline{C_{inh}}$	Average concentration leaving the oral cavity and entering the trachea
C_{mh}	Local concentration of the vapor in the puff throughout the oral cavity
$\overline{C_{mh}}$	Average vapor concentration at the end of the mouth hold
C_v	Vapor concentration of a constituent
$\overline{C_v}$	Average vapor concentration of a constituent
D_v	Diffusion coefficient of the vapor in air
D_d	Diffusion coefficient of droplets in air
F	Mass fraction of the constituent in the droplet
PC_{ta}	Tissue–air partition coefficient
V	Local volume of each oral cavity section
V_o	Volume of the oral cavity
V_p	Puff volume
m_d	Mass of a single droplet
m_{inh}	The mass of inhaled materials entering the lower respiratory tract following mouth hold
q	Airflow rate
q_d	Dilution airflow rate

r	Radial dimension
t	Elapsed time
t_{inh}	Total inhalation time
t_{mh}	Mouth hold time
t_{pw}	Puff withdrawal time
z	Axial distance
β	Coagulation kernel
$\lambda_d C_d$	Number of droplets lost to the walls per unit time per volume

1. Introduction

Understanding the dynamics of aerosols in the human airway is essential for investigating their influence on the body because the biological impact of inhaled substances at the cellular level depends on their local concentrations in the airway (Hashizume et al., 2023). In particular, aerosols of tobacco products such as conventional cigarettes (CCs), electronic cigarettes (ECs), and heated tobacco products are composed of a wide variety of constituents with different properties (Cunningham *et al.*, 2020; Hashizume et al., 2023), and it is difficult to understand their behavior in respiratory systems. For example, nicotine, which is a representative constituent in CCs and ECs, can easily evaporate from droplets (David *et al.*, 2020). Previous studies have reported methods for measuring the deposition and uptake amount of the constituents in tobacco product aerosols. Wall *et al.* (2022) used positron emission tomography imaging methods to visualize and analyze inhaled isotope-labeled nicotine, and Ishikawa *et al.* (2016) estimated the inhaled amounts of aerosols by analyzing the exhaled aerosols. These methods can be used for broad measures of the amount of aerosol deposition and uptake, such as total, organ-specific, or lung lobe-specific dosimetry; however, other approaches are necessary for analyzing local concentrations of aerosols. Computational modeling is a common approach for simulating the deposition and uptake amount in animal and human airways (Oakes *et al.*, 2017; Rostami, 2009; Tena *et al.*, 2017; Tena *et al.*, 2020). These days, simulated dosimetry is practically employed for toxicological assessment. For example, the Organisation for Economic Co-operation and Development (OECD) showed a case study in which human equivalent concentration was estimated by calculation based on computational fluid dynamics (CFD) modeling (Organisation for Economic Co-operation and Development, 2022). In the tobacco product research area, there are some CFD models that can be used to simulate the deposition amounts of aerosols and individual chemical constituents by solving equations for continuous aerosol flow in the airways (Asgari *et al.*, 2021; Feng *et al.*, 2016). Although CFD models enable the visualization of aerosol dynamics, a large amount of computational power would be required when considering the fate of multiple constituents throughout the entire airway. Therefore, the CFD approach is often used for site-specific modeling. Possible solutions for whole-airway modeling are semi-empirical models (International Commission on Radiological Protection 1994), as well as deterministic mathematical models. In particular, the Multiple-Path Particle Dosimetry (MPPD) model, which employs a multiple-path deterministic mathematical approach, is widely used as a particle dosimetry model

(Anjilvel & Asgharian, 1995; Asgharian et al., 2001).

Various modifications of the MPPD model have been proposed to simulate the deposition amount of tobacco product aerosols. Although MPPD v 3.04 (Applied Research Associates, USA) is suitable for modeling the deposition of inhalants and air pollutants, there are limitations when considering the characteristics of aerosols from tobacco products. For example, this model does not consider phase changes of aerosol constituents in the calculation. In tobacco product aerosols, constituents with medium vapor pressures (approximately 1 Pa–5 kPa at 37 °C), such as nicotine, change phase between the droplet and vapor (Duell *et al.*, 2020; Wu *et al.*, 2022). Thus, these dynamics should be considered when carrying out simulations for tobacco products. Models were established considering the phase change in the calculation (Asgharian, Price*, et al.*, 2018; Asgharian *et al.*, 2014; Asgharian, Rostami*, et al.*, 2018). However, there is still room for improvement in these models. The geometry in the current MPPD models is based on a silicone rubber cast model that was made during an autopsy in which the geometry may be different from that of a live person (Raabe, 1976). In addition, current models do not necessarily reflect tobacco product use behavior that causes mixing with diluted air in the body. When a person withdraws a puff of tobacco product, the puff is held in the mouth. After the mouth hold, dilution air enters the oral cavity and carries the puff into the deep lung, mixing the puff in the oral cavity (Marian *et al.*, 2009). Once the puff reaches the alveolar region, additional mixing by convection occurs when the inhaled puff and residing air merge. In addition, in the current model, constituents in the gas phase are estimated to be absorbed all at once upon adhering to the surface of lung tissue. In practice, they distribute between the tissue surface and the air and then they are cleared from the surface (Katritzky *et al.*, 2005; Meulenberg & Vijverberg, 2000).

To fill the gap between the real-life situation and the mathematical model, I developed a revised model in which the geometry is updated with a minimally invasive method, a computed tomography (CT) scan, and the modeling accounts for the physical processes of tobacco product consumption and the tissue–air partitioning and clearance rate of aerosol constituents. With the revised model, a sensitivity analysis was performed by comparing the current and revised models, and by measuring the relationships between model inputs and outputs to investigate the parameters that have a significant impact on the modeling results. The sensitivity analysis was conducted using aerosols composed of four constituents, water, nicotine, propylene glycol (PG), and glycerol, which are the major constituents of EC aerosols. I also confirmed whether the results of sensitivity

analysis were consistent with the well-known thermodynamic properties of aerosols. Finally, deposition simulation was performed with an increased number of chemical constituents that are typically found in CCs to investigate the applicability of the model for more complex aerosols.

2. Method

2.1. Revision of the MPPD model

The revised MPPD model for tobacco products was developed based on previous studies with the support of Applied Research Associates (Asgharian, Price, et al., 2018; Asgharian *et al.*, 2011; Asgharian et al., 2014; Asgharian, Rostami, et al., 2018). To reflect puff dynamics in the oral cavity, puff convective mixing with dilution air and reserved air in the alveoli, and the partitioning of constituents with a medium vapor pressure at the air–tissue interface in the lung, the following calculations for each constituent were incorporated into the revised model.

2.1.1. Geometry

The geometry of the oral cavity was created with the same method reported by Asgharian, Price, et al. (2018), based on a replica cast made by Cheng *et al.* (1997). The upper respiratory tract (URT) geometry included the oral cavity, oral pharynx, and larynx down to the beginning of the trachea. For computational purposes, the geometry was divided into 52 sections of 3-mm length. Each section was assumed to have a cylindrical geometry with a diameter equal to the hydraulic diameter of the entire section. Thus, similar to the lower respiratory tract, the oral cavity can be thought of as a typical 52-path generation model.

Here, a term, airway generation, is used to express the area from upper branch to deeper branch of the airway tract. The geometry data for the entrance to the lower respiratory tract up to airway generation 16 were obtained from CT and converted into an asymmetric model. The CT data were originally obtained in the previous study (Darquenne *et al.*, 2016). The study was approved by the Institutional Review Board at the University of Washington (USA) where the volunteer recruitment and CT imaging was performed. The University of Washington IRB approval number is 40712. Informed consent was obtained from each participant. The CT data was then processed by following procedure because information about the deep lung, including the branching angles, branch lengths, and branch diameters, cannot be obtained from a standard CT scan owing to resolution limitations. To reach down to airway generation 16, the arteries that travel alongside the airway branches were used as a surrogate for the airway paths.

In this process, the resolved airways and arterial branches were tracked separately, and then they were joined together to form a unified geometrical representation of the lung. Conversion of CT data with deep lung geometry into usable (i.e. standard triangulated language) format was performed and provided by Battelle Memorial Institute (Columbus, OH) and the Pacific Northwest National Laboratory (Richland, WA). The deep lung geometry after 17 generations was estimated as in a previous study (Yeh & Schum, 1980).

2.1.2. Convective mixing of the puff with the dilution air

Tobacco users hold the puff in the oral cavity following the puff withdrawal. After the mouth hold, dilution air is inhaled and mixed with puff carrying the mixture into the deep lung. In an idealistic scenario, the entire amount of dilution air completely and instantaneously mixes with the puff in the oral cavity before entering the lower respiratory tract. The idealistic mixture concentration is found from a simple mass balance:

$$\overline{C_{mh}}V_o = \overline{C_v}\left[V_o + \underbrace{q_d(t_{inh} - t_{pw} - t_{mh})}_{dilution\ volume}\right], \tag{1}$$

where $\overline{C_{mh}}$ is the average concentration of the vapor in the oral cavity at the end of the mouth hold, V_o is the volume of the oral cavity, $\overline{C_v}$ is the average vapor concentration of a constituent, q_d is the dilution airflow rate, and t_{inh}, t_{pw}, and t_{mh} are the times for the total inhalation, puff withdrawal, and mouth hold, respectively. Previous studies have adopted this idealistic scenario (Asgharian et al., 2014); however, mixing during the puff withdrawal of tobacco products is more complex.

The mouth is filled with the puff at the end of the mouth hold. The inhaled dilution air enters the oral cavity, mixes with the puff changing the puff concentration over time, and carries it into the lungs. A new mixing model of the oral cavity (Fig. 4.1) was adapted to simulate the tracheal inlet concentration during inhalation. In this model, the oral cavity with an initial uniform concentration is given by

$$\overline{C_{mh}} = \frac{1}{V_o}\int_0^{V_o} C_{mh}\,dV = \frac{\sum_{\delta V} C_{mh}\delta V}{V_o}, \tag{2}$$

where C_{mh} is the local concentration of the vapor in the puff throughout the oral cavity and V is the local volume of each oral cavity section. A mass balance is performed for the oral cavity for droplets and vapor constituents:

$$\frac{d(C_v V_p)}{dt} = -q_d c_v, \tag{3}$$

where C_v is the vapor concentration of a constituent, V_p is the puff volume, and t is the elapsed time. The concentration leaving the oral cavity and entering the trachea (C_{inh}) is found from the solution of the above equation and is given by

$$\frac{C_{inh}(t)}{\overline{C_{mh}}} = e^{-\frac{q_d}{V_o}(t-t_{pw}-t_{mh})}. \tag{4}$$

The constituent concentration leaving the oral cavity and entering the trachea is found from solving Eq. (3) and is time dependent. To simplify the computations, I find an average concentration at the entry to the lower respiratory tract (trachea) by averaging the concentration over total inhalation time (t_{inh}). The mass of inhaled materials entering the lower respiratory tract following the mouth hold (m_{inh}) is given by

$$m_{inh} = \overline{C_{inh}} q_d \left(t_{inh} - t_{pw} - t_{mh}\right) = \overline{C_{mh}} q_d \int_{t_{pw}+t_{mh}}^{t_{inh}} e^{-\frac{q_d}{V_o}(t-t_{pw}-t_{mh})} dt, \tag{5}$$

where $\overline{C_{inh}}$ is the average concentration of vapor leaving the oral cavity and entering the trachea. Thus, the average concentration entering the lower respiratory tract normalized by average concentration at the end of the mouth hold is represented as

$$\frac{\overline{C_{inh}}}{\overline{C_{\mathrm{mh}}}} = \int_{t_{pw}+t_{mh}}^{t_{inh}} e^{-\frac{q_d}{V_o}(t-t_{pw}-t_{mh})} dt = \frac{V_o}{q_d(t_{inh}-t_{pw}-t_{mh})}\left[1 - e^{-\frac{q_d}{V_o}(t_{inh}-t_{pw}-t_{mh})}\right]. \quad (6)$$

2.1.3. Convective mixing of the puff with the reserve air

The puff in the tracheobronchial (TB) region (airway generations 0–16) travels down into the deep lung by mixing with and pushing the existing air to the more distal airways. There is relatively little convective and diffusive mixing in the TB region because the airway expansion is small and the flow convection is high. Once the puff reaches the alveolar region, the axial convection is also small; however, lateral mixing via the expansion of the alveolar region occurs. Convective mixing of the puff with the reserve air in the deep lung occurs while the vapor is being transported through the airway and is being taken up by the airway tissue. Hence, mixing is coupled with uptake. Modeling details are provided below when introducing the transport model for vapors.

2.1.4. Modeling of coupled puff transport equations at the airway surface

The convective mixing of vapors in an airway composed of respiratory bronchioles and alveoli can be accounted for in the mass balance equation for vapors in a simplified model in which the airway contains a lumen (respiratory duct) and unsmooth space, as shown in Fig. 4.2. In Fig. 4.2, A is the duct cross-sectional area and A' is the total cross-sectional area, which includes the space in a single respiratory bronchiole.

After reaching the walls, gases are assumed to partition between the air and the lung tissue according to Henry's law (Spiess, 2009; Volckens & Leith, 2003). As the gas concentration increases in the tissue, its absorption tends to slow in proportion to its saturation vapor pressure (Raoult's law) (O'Shaughnessy *et al.*, 2020; Pichelstorfer *et al.*, 2021). The full set of transport equations during inhalation and exhalation are solved to determine the concentrations of vapor in the air and lung tissue during a smoking session. The mass balance equation for the inhaled vapor in the airway of radial dimension r is given by:

$$\frac{\partial \overline{C_v}}{\partial t} + \frac{qA}{A'^2}\frac{\partial \overline{C_v}}{\partial z} = D_v \frac{\partial^2 \overline{C_v}}{\partial z^2} - \frac{2}{r}K_o \overline{C_v} - \frac{2}{r}K_o \frac{k_i}{k_t} - \frac{\partial F C_d m_d}{\partial t}, \quad (7A)$$

where

$$\frac{1}{K_o} = \frac{1}{k_g} + \frac{1}{k_t}, \quad (7B)$$

$$\overline{C_v} = C_v + \frac{k_i}{k_t}, \quad (7C)$$

in which q is the airflow rate through the airway section, z is the axial dimension, D_v is the vapor diffusion coefficient in air, F is the mass fraction of a constituent in the droplet, C_d is the droplet concentration in air, m_d is the mass of a single droplet, and k_g, k_t, and k_i indicate the air and tissue phase mass transfer coefficients, which are determined by, for example, the tissue–air partition coefficient (PC_{ta}) and clearance rate (Asgharian et al., 2011; Asgharian *et al.*, 2012). Eq. (7A) holds during both inhalation and exhalation. This equation is also applicable in the TB airways by letting $A = A'$. The solution to Eq. (7A) is obtained numerically for the entire respiratory tract during inhalation, lung hold, and exhalation.

During lung hold, the following equation is used, which drops the convective term in Eq. (7):

$$\frac{\partial C_v}{\partial t} = D_v \frac{\partial^2 C_v}{\partial z^2} - \frac{2}{r}K_o C_v - \frac{2}{r}K_o \frac{k_i}{k_t} - \frac{\partial F C_d m_d}{\partial t}. \quad (8)$$

The dosimetry model for vapor constituents is coupled with the droplet transport model. The transport equation for the droplet concentration (C_d) in the air is given as:

$$\frac{\partial C_d}{\partial t} + \frac{q}{A}\frac{\partial C_d}{\partial z} = D_d \frac{\partial^2 C_d}{\partial z^2} - \lambda_d C_d - \beta C_d^2, \quad (9)$$

where D_d is the vapor diffusion coefficient in air, $\lambda_d C_d$ is the number of droplets lost to the walls per unit time per volume, and β is the coagulation kernel. The model is simplified to the following form for lung hold:

$$\frac{\partial C_d}{\partial t} = D_d \frac{\partial^2 C_d}{\partial z^2} - \lambda_d C_d - \beta C_d^2. \quad (10)$$

Eqs. (7) to (10) are used to calculate the concentration of an inhaled puff in the air and tissue throughout the respiratory tract during a full puff process, which consists of inhalation, lung hold, and exhalation. The deposition and uptake fractions in the lung airways are subsequently determined from the simulated concentrations. Additional details of the modeling approach are given in Asgharian, Price, et al. (2018).

2.2. Sensitivity analysis and calculation with EC and CC conditions

A sensitivity analysis was conducted by assuming the use of an EC whose puff mixture of vapors and droplets initially consists of water (1%), nicotine (3%), PG (48%), and vegetable glycerol (48%). The physicochemical properties of these constituents at 37 °C were simulated with the thermodynamics calculator, ProPhyPlus (ProSim, Toulouse, France) and the EPA On-line Tools for Site Assessment Calculation (United States Environmental Protection Agency 2021) (Table 4.1). Regarding PC_{ta}, I formally employed the blood–air partition coefficient estimated by the vapor pressure, octanol–water partition coefficient, and molecular weight (Abraham *et al.*, 2005; Buist *et al.*, 2012). All PC_{ta} of water, nicotine, PG, and glycerol were estimated as greater than 1000.

The puff volume and droplet concentration were 50 cm^3 and 1×10^9 droplets/cm^3, respectively. The initial droplet diameter was 0.5 μm. The same as in the previous models, droplet diameter distribution was not accounted for in this revised model. The total mass of all constituents per puff was 3.7 mg. The initial aerosol temperature of the EC was set at 60 °C (Table 4.3). The vapor pressures of water, nicotine, PG, and glycerol as a

function of temperature were estimated using the Antoine equation.

The constituents and their proportions in CC aerosol were obtained from the chemical analysis of a 3R4F reference cigarette (Table 4.2) (Takahashi et al., 2018). I chose 10 of the major constituents in the 3R4F cigarette aerosol with medium and low vapor pressures (<5 kPa) in addition to water. The physicochemical properties of these constituents were estimated using the same method as for the EC. The puff volume and droplet initial diameter were as in the EC condition. The droplet concentration and total mass inhaled were set as 2.7×10^{10} droplets/cm^3 and 1.85 mg/puff. The aerosol temperature was set at 37 °C (Table 4.3). Constituents whose PC_{ta} was estimated as lower than 1000 are styrene and pyridine whose PC_{ta} values were estimated as 34.0 and 228.9, respectively.

3. Results

3.1. Comparison of a new mixing model and idealistic mixture

When considering the puff concentration at the trachea inlet, simply averaging the dilution air with the entire puff is commonly used in current models (Asgharian et al., 2014). However, in a real-life situation, the dilution air pushes the puff into the trachea during which the puff concentration changes. To reflect this situation, a new mixing model was introduced in which the dilution air is mixed with the puff in the oral cavity (Eq. 6). Fig. 4.3 shows a comparison of the average inlet concentration normalized by the average concentration at the end of the mouth hold between the new mixing model and the simple averaging model. The solution volume was also normalized by the volume of the oral cavity. Compared with the simple averaging model, the new mixing model calculated an increased puff concentration. The difference between the two models was maximum with a 0.6–1.2 normalized dilution volume, corresponding to 30–60 mL of dilution air when the oral cavity volume is set as 50 mL. The two models converged with large volumes of dilution air.

3.2. Puff mixing in the deep lung

In addition to accounting for mixing in the oral cavity, the revised model considers mixing in the alveolar region. Fig. 4.4 shows the results of comparing the vapor uptake fraction in the alveolar region (i.e., airway generations 17 to 23) with and without mixing. The vapor uptake fraction with mixing was less than that without mixing. As the vapor went deeper, the difference in uptake fraction with and without mixing was reduced.

3.3. Tissue–air partitioning at the lung tissue surface

The tissue–air partition coefficient (PC_{ta}) was added as an input parameter in the revised model. PC_{ta} is a constituent-specific value, where $PC_{ta} = 1$ means that a constituent is equally distributed between the tissue and air. A PC_{ta} value less than or greater than 1 means that the constituent has a greater distribution in air or tissue, respectively. A sensitivity analysis of the PC_{ta} was performed with nicotine as a representative

constituent to evaluate the impact of this value when calculating the deposition and uptake when the PC_{ta} was estimated as more than 1000. As expected, the uptake and deposition fraction when nicotine was predominantly in air (PC_{ta} = 0.01) was lower in the TB and pulmonary regions than when an equal distribution was assumed (PC_{ta} = 1). In addition, by increasing the PC_{ta} to 100, the deposition and uptake fraction in the TB region increased, whereas in the alveolar region it was lower (Fig. 4.5).

3.4. Clearance from the lung tissue

To examine the impact of the clearance rate on the deposition and uptake fraction, I ran the model for nicotine, PG, and glycerol with two different clearance rates (0.0001/s and 1/s). Although the difference in deposition fraction between the 0.0001/s and 1/s calculations was less than 0.1%, the deposition and uptake fractions of all constituents were found to be higher with a clearance rate of 0.0001/s than with a rate of 1/s (Fig. 4.6). The change in dosimetry regardless of value of clearance rate was large in the order PG > nicotine > glycerol, which is consistent with the order of their vapor pressures.

3.5. Deposition and uptake of tobacco aerosol constituents

Fig. 4.7 shows the dosimetry results for each area and generation of the respiratory tract when inputting the new parameters, assuming that EC aerosols are composed of water, nicotine, PG, and glycerol. In the URT and TB regions, the deposition and uptake fractions were estimated to be in the order PG > nicotine > glycerol, which is consistent with the order of their vapor pressures (Table 4.1). However, the deposition and uptake fractions in the alveolar region did not show the same trends as in the URT and TB regions. In the alveolar region, especially for generations after 20, the deposition and uptake fraction of glycerol and nicotine were calculated to increase markedly.

I also calculated the deposition and uptake fraction of 10 representative constituents in CC aerosols (water, nicotine, PG, glycerol, triacetin, hydroquinone, catechol, phenol, pyridine, and styrene) in each airway region and airway generation (Fig. 4.8). Unlike the constituents of EC aerosols (composed of only water, nicotine, PG, and glycerol), the calculated deposition and uptake fractions of the CC constituents in the URT and TB

regions were not completely dependent on the vapor pressure (Table 4.2). Catechol has a vapor pressure in the middle range among the CC constituents, and this compound was simulated to behave similarly to hydroquinone, which is a nonvolatile compound.

Nicotine is a constituent in both EC and CC aerosols. For this compound, I found considerable differences in the deposition fraction modeled at each site of the respiratory tract. When simulating EC aerosol (composed of only water, nicotine, PG, and glycerol), only 6.9% of nicotine was simulated to deposit in the URT. In contrast, it was approximately 26% when simulating CC aerosol composed of 10 constituents. In addition, in EC aerosol, the deposition and uptake fraction of nicotine was simulated to increase with lung depth and was maximum in the deepest lung (generations 21–23). In contrast, in CC aerosol, airway generation 9 had the maximum deposition and uptake fraction of nicotine.

Importantly, these calculations were completed within 3 minutes using a typical laptop computer.

4. Discussion

When users consume tobacco products, the puff is withdrawn, held in the mouth, and then transported into the deep lungs along with air, which dilutes the puff. To represent the physical and thermodynamic processes during tobacco product consumption for one puff, the equations described in *"Section 2.1 Revision of the MPPD model"* were added to the previous MPPD model which simulate deposition of CC or EC aerosol accounting for changes in droplet sizes due to evaporation and humidity (Asgharian, Price, et al., 2018; Asgharian et al., 2014; Asgharian, Rostami, et al., 2018). To examine the effect of including these equations in the MPPD model, the model calculation was run with various input conditions. I also input constituents of ECs and CCs into the revised model to confirm the feasibility of performing these calculations for tobacco products.

When new mixing model in the oral cavity was compared to simple averaging model, the results suggest that the simple averaging method underestimates the puff concentration. I modeled puff mixing in the deep lung as well. The mixing made vapor uptake fraction less, reflecting that the airway cross-sectional area is wider than the duct cross-sectional area. The deeper aerosol goes, the less difference in uptake fraction between with and without mixing was. This is because the vapor concentration decreased in the deep lung. Vapor mixing was also employed for modeling the vapor released from droplets.

Once gas comes into contact with lung tissue, it partitions between the tissue and air. This partitioning is important for simulating the actual exposure dose because constituents distributed in the air transfer to different areas of the tissue or are exhaled. Fig. 4.5 shows that high PC_{ta} resulted in an increase of the deposition and uptake fraction in the TB and a decrease of it in the pulmonary region. This is because the amount of nicotine entering the pulmonary region was relatively low in the PC_{ta} = 100 condition, as a larger amount of nicotine would be trapped in the TB region. As such, varying the PC_{ta} affected not only the amount of total deposition but also deposition in specific regions of the respiratory tract. The use of PC_{ta} as a variable in deposition simulation is therefore important when calculating constituent-specific deposition trends. It should be noted that the actual airway surface property is complex and not uniform, i.e., the mixture of mucus and surfactants, whose proportion differs site by site in the airway (Rogers, 2002; Widdicombe, 2002; Winkler & Hohlfeld, 2013). I employed one value of each constituent's PC_{ta} for the whole airway to simplify the calculation in this study.

Deposited gaseous chemical constituents are absorbed and removed from the airway surface and eventually eliminated by metabolization. Because the constituent concentration at the airway surface affects its uptake (Raoult's law), clearance rate-related coefficients was introduced into the calculation (Eq. 7).

Considering dosimetry at the alveolar tissue surface, the order of deposition fractions of PG, nicotine, and glycerol was consistent with the order of their vapor pressures. This result indicates that vapor uptake is promoted when the concentration at the tissue surface is low. In addition, no big difference was observed even when the clearance rate was drastically changed. It was shown that the addition of the clearance rate calculation into the revised model had little effect on the simulation results. The major reason is that the model is to simulate one puff of aerosol. Potentially, models that account for accumulation from multiple puffs or daily use can have a large impact on values of clearance rate (Churg *et al.*, 2003), but it was not highly sensitive, at least when inputting representative EC constituents into this model.

Fig. 4.7 shows the results of dosimetry estimation. In modeling for EC, I believe that vapor uptake dominates in the URT and TB regions, whereas droplet deposition dominates in the alveolar region because the impaction and sedimentation of droplets tend to occur in complex airways, and the airways narrow as the airway depth increases (Darquenne, 2020; Tsuda *et al.*, 2013). I also input constituents from CC to the model. Because the estimated activity coefficient corrects the vapor pressure, constituents with a high activity coefficient (such as PG and triacetin) deposit in the URT more than those with a high vapor pressure in this model. The behavior of catechol was also owing to the activity coefficient; catechol had a low activity coefficient (<1) and its vapor pressure was suggested to be low, close to the level of a nonvolatile compound. Therefore, in addition to the vapor pressure, the value of the activity coefficient affected the airway dosimetry calculation results. Regarding nicotine, there were considerable differences resulted from differences in the aerosol properties of the EC and CC constituents, especially the difference in the activity coefficients. In this calculation, compared with EC aerosol, CC aerosol was set to contain a smaller number of droplets, and the constituents in CC aerosol could more easily evaporate. This results in smaller droplet diameters of CC aerosols; thus, nicotine evaporation is simulated to be higher for CC than for EC.

Notably, these calculations only required a low computational load. The model is suggested to enable the efficient evaluation of products with few constituents, such as

ECs, as well as products with many constituents, such as CCs and heated tobacco products (Cunningham et al., 2020; Uchiyama *et al.*, 2018).

The limitations of the model are that the calculation of deposition and uptake fraction are based only on theoretical aerosol dynamics. Because actual measurement of the deposition and uptake amount of chemicals in the respiratory tract is extremely difficult owing to the dynamic nature of chemical absorption and metabolism, combination with a physiologically based pharmacokinetics (PBPK) model would provide deeper insight into the model validity. For example, the pharmacokinetics of plasma nicotine profiles could be found in the literature (Yuki *et al.*, 2017), thus the combination of PBPK model and the model output would be more realistic. In addition, the MPPD simulation method is only for the airway generation to generation. This method enables low computational load and whole-airway modeling, while this model cannot calculate heterogeneous aerosol deposition within the oral cavity or one airway generation as reported by Kuga, et al. (2018; 2020; 2021) and Asgari et al. (2021). I need to choose an optimal modeling method fitting for the purpose. The MPPD model is chosen when a whole or deep airway aerosol simulation is needed. Feng et al. (2016) and Kannan *et al.* (2020) reported that lung geometries are found to be different in each individual and the difference critically affects the dynamics of aerosols in the airway. A model was developed with a geometry from one individual; therefore, the use of multiple geometries in the model would strengthen model reliability. I believe that the model revised in this study is useful for the calculation of human equivalent concentration, which plays a key role for *in vitro* to *in vivo* extrapolation in toxicological assessments without animal studies. However, aerosol chemistry of tobacco products is complex, thus estimating the deposition fraction of all the constituents in an aerosol is not realistic. Therefore, the human equivalent concentration of an aerosol should be calculated with the representative constituents such as nicotine. Together with the difficulty underlying complete validation of the model, adaptation of an uncertainty factor is warranted when the model is applied in the toxicological assessment.

5. Short summary

The MPPD model was revised in which a new geometry of the lung was adopted, and two aerosol dynamics were introduced: mixing in the oral cavity and deep lung, and constituent partitioning between the tissue surface and air. The revised MPPD enabled to calculate the deposition fraction of each chemical constituent of interest in each region and branching generation of the respiratory tract by inputting the physicochemical properties and aerosol properties. The model also accounts for tobacco product use behaviors. The model was run under various conditions of assumed EC and CC aerosol chemical constituents and user behavior, and the simulations were generally consistent with the global understanding of aerosol physics. Moreover, the calculations in this model could be performed rapidly, even when accounting for multiple chemical constituents. Although limitations are that the modeling was based only on theoretical calculations without validation by actual data and the geometry is constructed from only one donor, I believe that the model will be useful for investigating the actual exposure concentrations of chemical constituents in tobacco product aerosols, and it could be applied in toxicological studies with an uncertainty factor.

Figures and tables

Table 4.1. Physicochemical properties of the verification constituents at 37°C and vapor pressures at 60°C.

	Initial mass fraction	Vapor pressure (Pa)		Molecular weight (g/mol)	Density (g/cm^3)	Surface tension (dyn/cm)	Diffusion coefficient	Activity coefficient
		37°C	60°C					
Water	0.01	6.3×10^{3}	2.0×10^{4}	18.0	0.99	70.3	0.28	1.00
Nicotine	0.03	13.4	1.8×10^{2}	162.2	1.01	38.6	0.07	1.17
Propylene glycol	0.48	49.1	2.8×10^{2}	76.1	1.02	34.3	0.10	1.05
Glycerol	0.48	8.9×10^{-2}	0.9	92.1	1.25	62.2	0.10	1.10

Table 4.2. Constituents with medium and low vapor pressures in conventional cigarette 3R4F at 37 °C.

	Initial mass fraction	Vapor pressure (Pa)	Molecular weight (g/mol)	Density (g/cm^3)	Surface tension (dyn/cm)	Diffusion coefficient	Activity coefficient
Water	0.734	6.3×10^{3}	18.0	0.99	70.3	0.28	1.12
Nicotine	0.091	13.4	162.2	1.01	38.6	0.07	1.83
Propylene glycol	0.001	49.1	76.1	1.02	34.3	0.10	3.90
Glycerol	0.113	8.9×10^{-2}	92.1	1.25	62.2	0.10	6.41
Triacetin	0.050	1.1	218.2	1.14	34.9	0.06	8.69
Hydroquinone	0.004	0.2	110.1	1.30	55.6	0.08	0.06
Catechol	0.004	9.7	110.1	1.22	44.3	0.12	0.06
Phenol	0.001	1.4×10^{2}	94.1	1.06	39.5	0.09	0.56
Pyridine	0.001	5.2×10^{3}	79.1	0.97	35.1	0.98	1.42
Styrene	0.001	1.6×10^{3}	104.2	0.89	30.3	0.08	20.32

Table 4.3. Input aerosol properties of the EC and CC.

	Puff Volume (cm^3)	Initial diameter (μm)	Number concentration ($/cm^3$)	Total mass (mg/puff)	Initial aerosol temperature (°C)
EC	50	0.5	1×10^9	3.7	60
CC	50	0.5	2.7×10^{10}	1.85	37

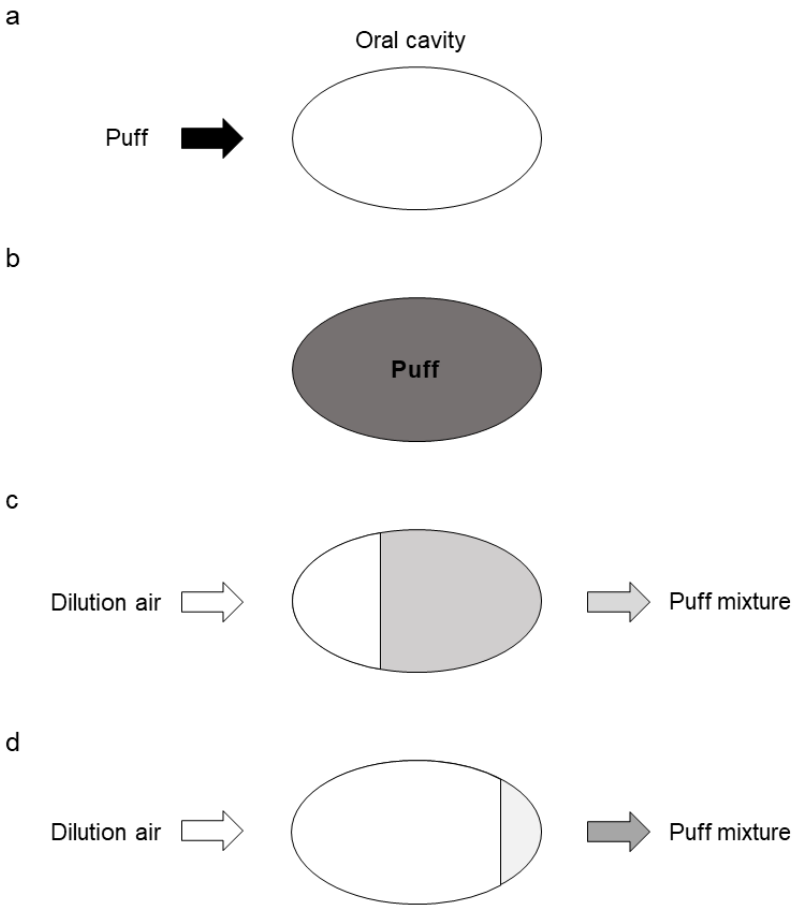

Fig. 4.1. A new mixing model of the oral cavity.

(a) Puff inhalation into the oral cavity, (b) mouth hold, (c), (d) dilution air is inhaled and mixed with the puff in the oral cavity, thus, the puff reaches the trachea at a different concentration.

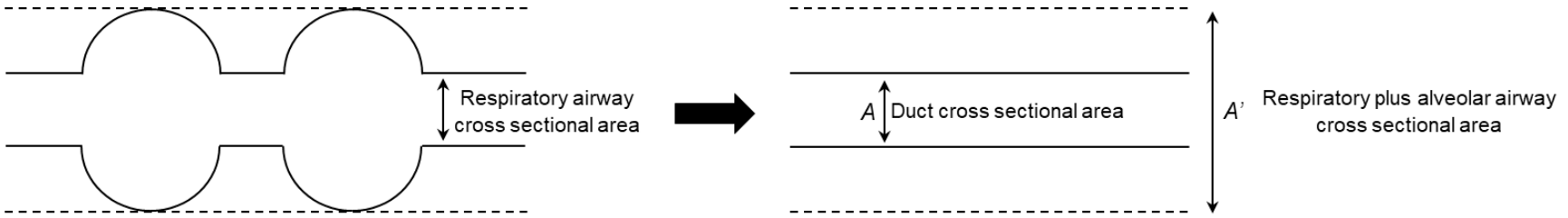

Fig. 4.2. Idealistic representation of the alveolar region surface.

The alveolar region is simplified, in which the airway contains a lumen (respiratory duct) and unsmooth space. A, the duct cross-sectional area; A' , the total cross-sectional area, which includes the space in a single respiratory bronchiole.

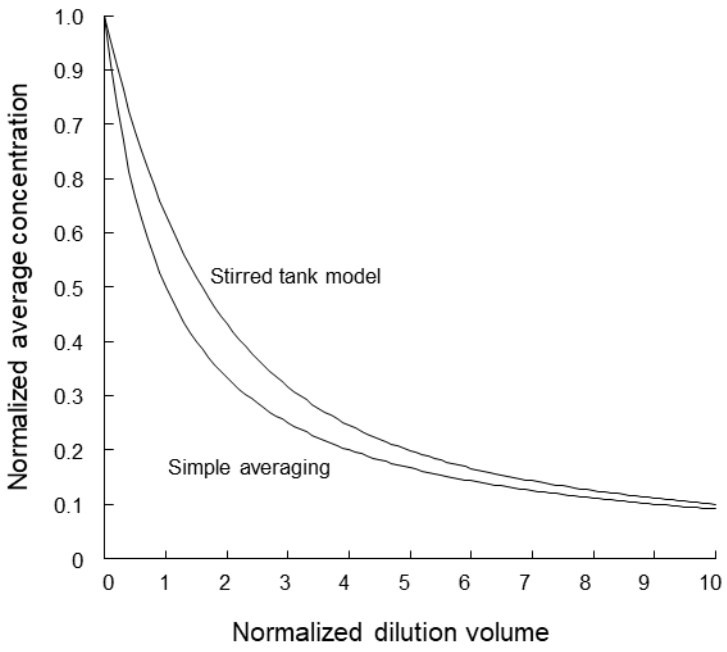

Fig. 4.3. Comparison of the average vapor concentration in the puff entering the lower respiratory tract simulated by the two mixing models.

Normalized dilution volume, dilution volume versus oral cavity volume; normalized average volume, vapor concentration at the trachea entrance versus vapor concentration at the end of the mouth hold.

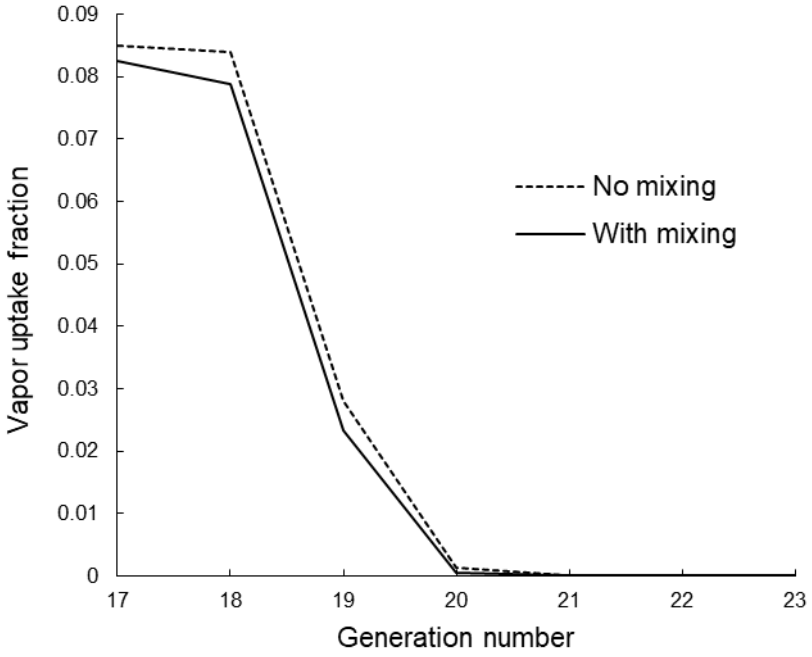

Fig. 4.4. Vapor uptake fraction in the alveolar region with and without convective mixing.

No mixing, result of calculation for vapor uptake fraction without consideration of mixing in the alveolar region; With mixing, result of calculation for vapor uptake fraction with equations expressing mixing in the alveolar region.

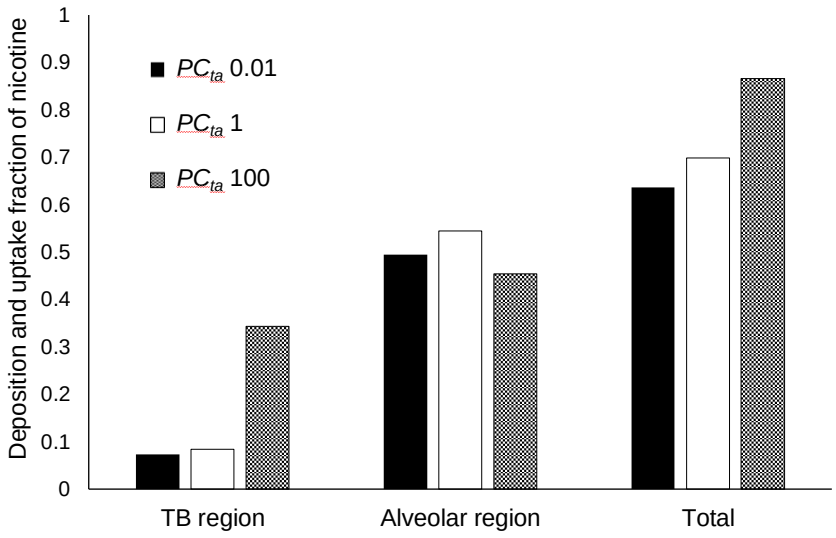

Fig. 4.5. Influence of the tissue–air partition coefficient on nicotine uptake and deposition.

Deposition and uptake fraction of nicotine is estimated for each airway region and total airway with various tissue–air partition coefficient. PC_{ta}, tissue–air partition coefficient; TB, tracheobronchial.

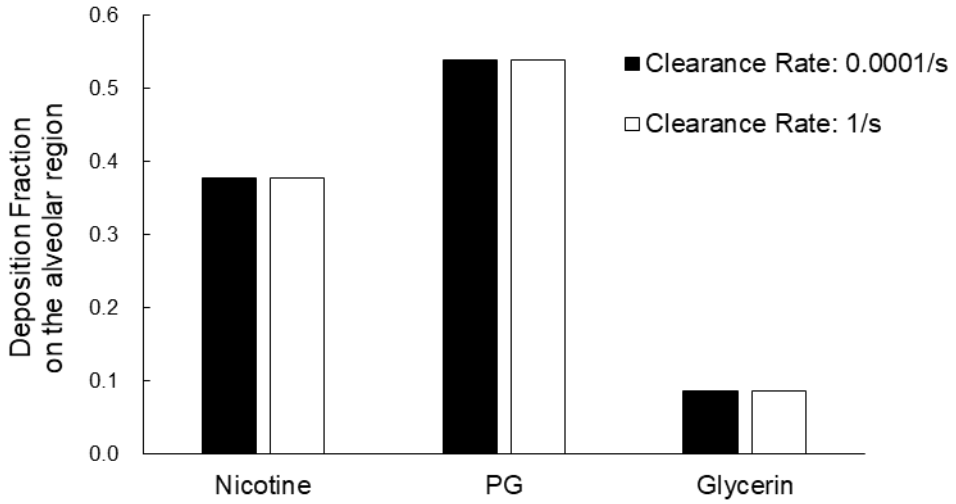

Fig. 4.6. Effect of clearance rate on the deposition fraction in the alveolar region for each constituent.

Deposition and uptake fractions of nicotine, PG, and glycerin are estimated for the total airway with different clearance rate. PG, propylene glycol.

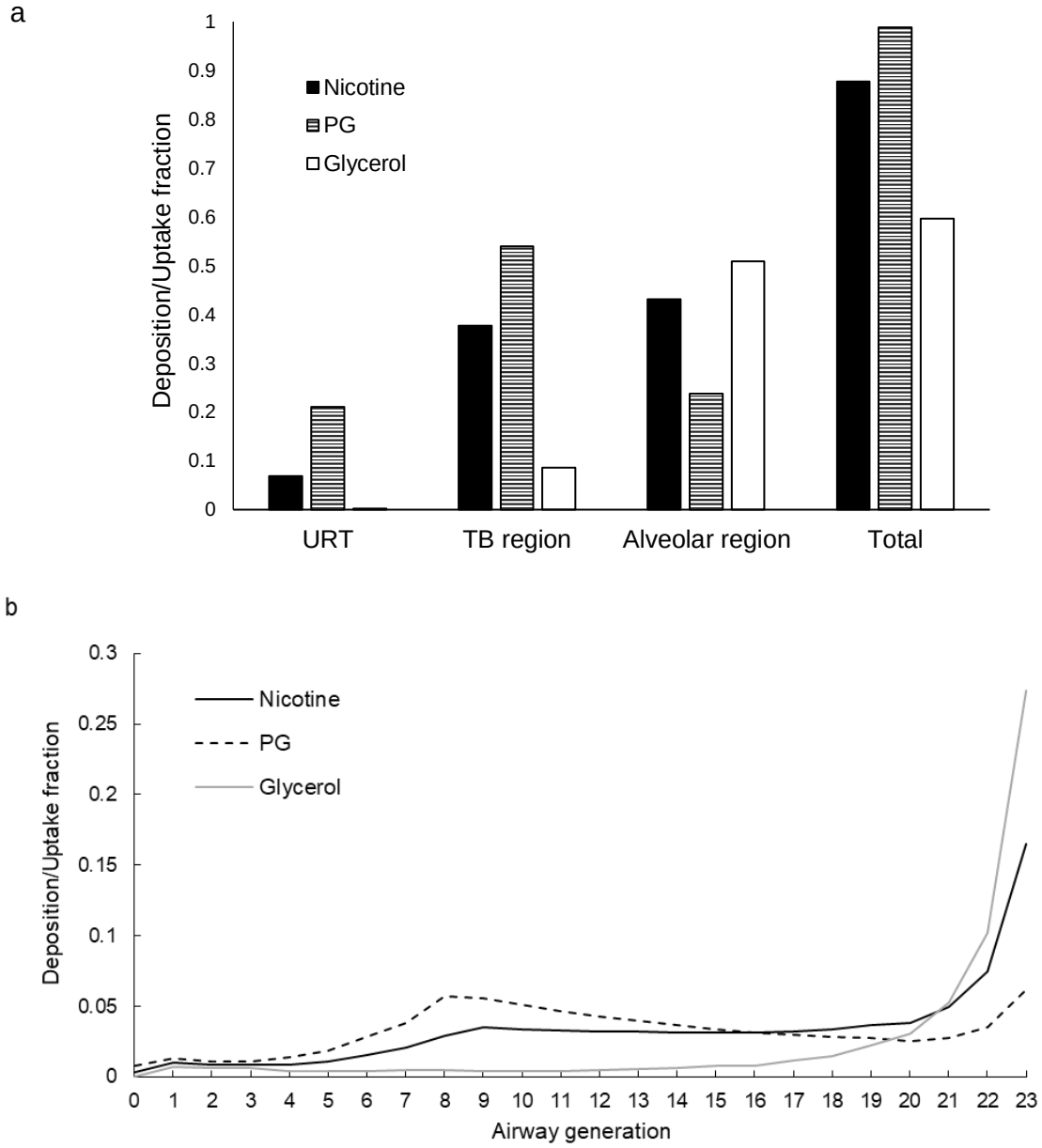

Fig. 4.7. EC deposition and uptake fraction in (a) each airway region and (b) each airway generation.

Deposition and uptake fractions of nicotine, PG, and glycerin of EC are estimated for each airway region and the total airway. EC, electronic cigarette; PG, propylene glycol; TB, tracheobronchial; URT, upper respiratory tract.

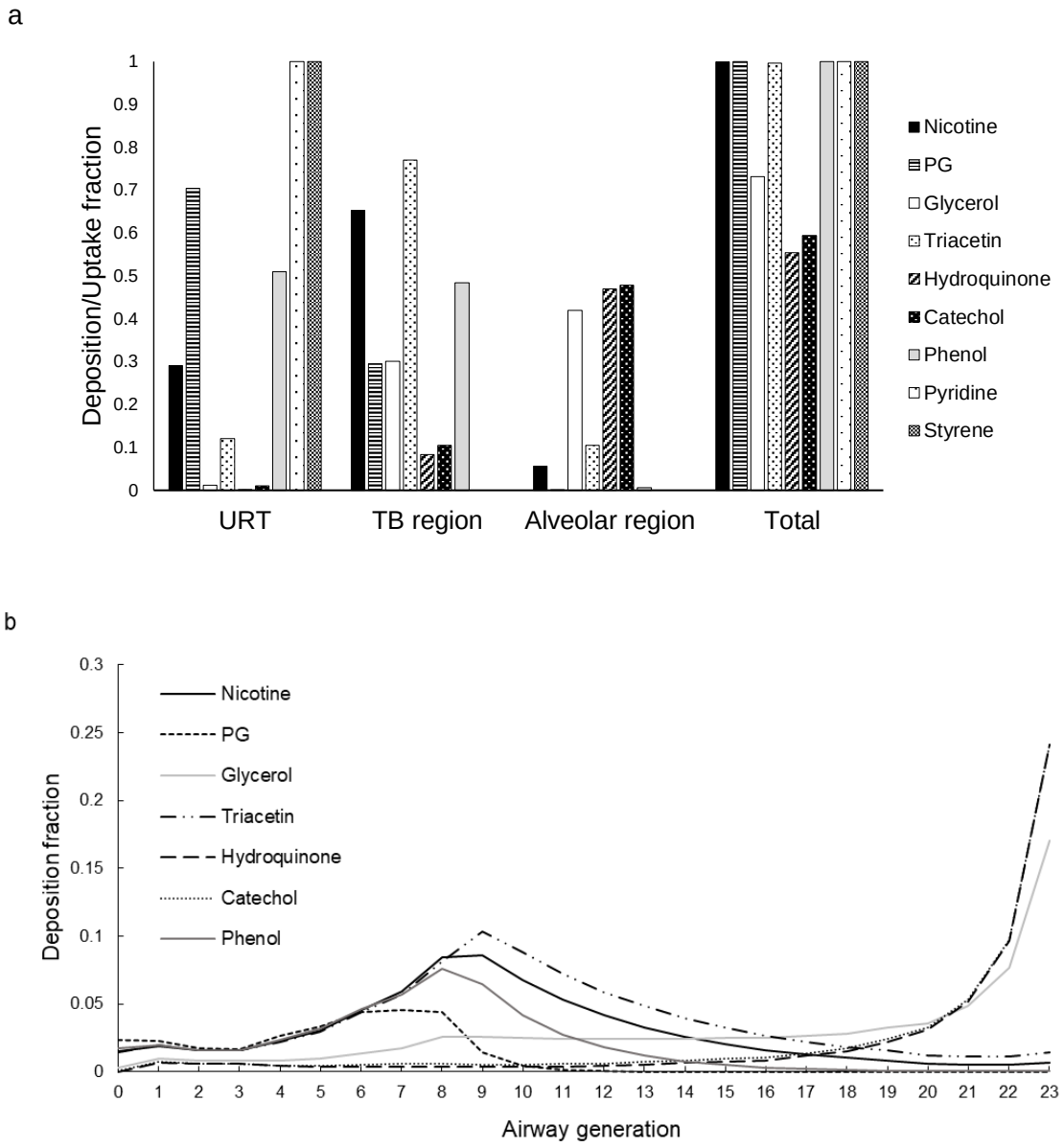

Fig. 4.8. CC deposition and uptake fraction in (a) each airway region and (b) each airway generation.

Deposition and uptake fractions of constituents of CC are estimated for each airway region and the total airway. Pyridine and styrene were excluded from the deposition fraction results in each airway generation because they are solely deposited in the URT region. CC, conventional cigarette; PG, propylene glycol; TB, tracheobronchial; URT, upper respiratory tract.

Conclusion

The airway owns an acute inflammatory response that originally exists to protect organs from outside irritants. However, when it becomes chronic, it can disrupt homeostasis and then lead to severe diseases in the airway, such as chronic obstructive pulmonary disease (COPD) and asthma. Although cigarette smoking is a known risk factor for COPD, a conclusive risk assessment method has not been established due to the complex mechanisms involved in the progression of the disease state. In this thesis, efforts from an *in vitro* to *in vivo* extrapolation (IVIVE) perspective were made to assess the risk of airway chronic inflammation related to cigarette smoking aiming to reduce animal testing.

The adverse outcome pathway (AOP) framework is employed to describe the pathway from a molecular initiating event to an adverse outcome, focusing on significant events. Although efforts to develop quantitative AOPs (qAOPs) for IVIVE have been made, existing qAOP models are limited and not adaptable to chronic diseases. In *Chapter 1*, a concept for qAOP modeling of chronic toxicity was proposed. This model employs Bayesian network modeling to logically link each node and consider the cumulative effects of repeated exposures. Using a hypothetically generated dataset, the qAOP modeling successfully estimated the risk of chronic adverse outcomes. In the modeling, lasso-based subset selection was suggested to exclude low-contributive nodes.

When cigarette aerosol reaches the bronchial tissue, it can induce inflammation in the presence of cytokines. Goblet cell hyperplasia (GCH) in the airway has been explained to be regulated by the level of cytokine stimulation released from immune cells. In this thesis, a new mechanism, the sensitivity of epithelial cells to interleukin (IL)-13, was focused on. The results suggest that cigarette smoke enhances the expression of the functional IL-13 receptor, IL-13Rα1, through aryl hydrocarbon receptor (AhR) stimulation. This suggestion was supported by an AhR inhibitor study. This novel point of view is expected to contribute to the IVIVE approach by integrating immune responses in an *in vitro* culture without the need for complicated co-culture.

Due to the thickening of the epithelial layer resulting from GCH, the bronchial tube becomes narrow, a condition known as stenosis. Stenosis is a typical symptom of airway

chronic inflammation, which disrupts airflow during breathing. To reproduce this phenomenon, a next-generation model is required. The microfluidic system in the conventional 384-well plate in Bronchus-on-a-Chip (BoC) enables the construction of tubular structures with airway epithelial cells while maintaining high throughput. Similar to the physiological epithelium and airway three-dimensional culture, cells in BoC differentiate into basal, ciliated, and goblet cells. Mucus production was increased by IL-13, indicating that BoC has the potential to reproduce chronic responses. Since toxicological assessments require data on dose-response relationships, this high-throughput BoC could contribute to IVIVE data acquisition as well as serve as a bronchial stenosis model.

Tobacco aerosol travels from the mouth to the deep lungs. The dynamics are unique because tobacco aerosol contains various constituents, and the puffing sequence is distinctive. The Multiple-Path Particle Dosimetry (MPPD) model was revised to include equations for detailed airway geometry, mixing in the oral cavity and deep lungs, and transportation across the lung surface. After the model's construction, a sensitivity analysis was performed, which aligned with the global understanding of aerosol physics. Although an uncertainty factor should be used due to the lack of real-world data validation, the aerosol dosimetry of cigarette aerosol could be estimated with this revised MPPD model.

These four models proposed in this thesis represent advanced *in silico* and *in vitro* modeling methods for assessing the effects of cigarette smoke, reflecting its mechanisms. Furthermore, the models have potential applications beyond cigarette smoke-associated airway diseases. For example, the qAOP model can be adapted to a variety of chronic diseases for which AOPs have been defined. Chemicals that induce airway inflammation could be assessed with *in vitro* models for GCH and airway stenosis. The revised MPPD model can simulate the dynamics of aerosols inhaled from the mouth, such as inhalants. The models developed in this thesis could be valuable IVIVE tools for research on airway diseases without the need for animal testing.

The qAOP model truly functions when data from molecular to phenotypic levels are inputted. In future studies, the following steps will be conducted: 1) cigarette smoke deposition will be simulated with the revised MPPD model, 2) data in BoC exposed to

cigarette smoke will be acquired reflecting the calculated concentration, 3) the levels of GCH and stenosis in BoC will be measured with the addition of IL-13 to mimic the presence of immune cells, 4) finally, AO risk might be estimated using the qAOP model by inputting the data (Graphical Abstract). As a limitation, the combined model will only use *in vitro* data and *in silico* estimations. Because models do not fully reflect all phenomena in the human body, validation is essential. After integrating these approaches, comparing the qAOP results to real-world data, such as epidemiological data, must be employed to determine the accuracy of the entire model.

In this thesis, I propose contributions to the IVIVE method for risk assessment of cigarette smoke-associated airway chronic inflammation by combining *in vitro* and *in silico* modeling. I believe the models can be employed to estimate chronic disease risk without animal testing, which contributes to reasonable decision-making for consumers, manufacturers, and regulators.

Acknowledgement

I would like to express my heartfelt gratitude to Professor Mayumi Ishizuka (Laboratory of Toxicology, Graduate School of Veterinary Medicine, Hokkaido University) for her greatest and kind support and supervision.

I extend my sincere thanks to Professor Ken-ichi Otsuguro (Laboratory of Pharmacology, Department of Biomedical Sciences, Graduate School of Veterinary Medicine, Hokkaido University), Associate Professor Shouta Nakayama (Laboratory of Toxicology, Graduate School of Veterinary Medicine, Hokkaido University), and Professor Satoru Konnai (Laboratory of Infectious Diseases, Department of Disease Control, Graduate School of Veterinary Medicine, Hokkaido University) for their insightful advice and critical review of this thesis.

I am deeply appreciative of continuous and patient support provided by Shigeaki Ito (Scientific Product Assessment Center, Japan Tobacco Inc.).

Finally, I would like to thank my wonderful colleagues at Japan Tobacco Inc. and JT International S.A. for their support and encouragement throughout my research journey.

References

Abraham, M. H., Ibrahim, A., & William E. Acree, J. (2005). Air to Blood Distribution of Volatile Organic Compounds: A Linear Free Energy Analysis. *Chemical Research in Toxicology, 18*(5), 904-911.

Aghasafari, P., George, U., & Pidaparti, R. (2019). A review of inflammatory mechanism in airway diseases. *Inflammation Research, 68*(1), 59-74.

Alepee, N., Bahinski, A., Daneshian, M., De Wever, B., Fritsche, E., Goldberg, A., Hansmann, J., Hartung, T., Haycock, J., Hogberg, H., Hoelting, L., Kelm, J. M., Kadereit, S., McVey, E., Landsiedel, R., Leist, M., Lubberstedt, M., Noor, F., Pellevoisin, C., Petersohn, D., Pfannenbecker, U., Reisinger, K., Ramirez, T., Rothen-Rutishauser, B., Schafer-Korting, M., Zeilinger, K., & Zurich, M. G. (2014). State-of-the-art of 3D cultures (organs-on-a-chip) in safety testing and pathophysiology. *Alternatives to animal experimentation, 31*(4), 441-477.

Ammous, Z., Hackett, N. R., Butler, M. W., Raman, T., Dolgalev, I., O'Connor, T. P., Harvey, B., & Crystal, R. G., (2008). Variability in Small Airway Epithelial Gene Expression Among Normal Smokers, NCBI Gene Expression Omnibus, GSE8545, https://www.ncbi.nlm.nih.gov/geo/query/acc.cgi?acc=GSE8545

Ancel, J., Belgacemi, R., Diabasana, Z., Perotin, J.-M., Bonnomet, A., Dewolf, M., Launois, C., Mulette, P., Deslée, G., Polette, M., & Dormoy, V. (2021). Impaired Ciliary Beat Frequency and Ciliogenesis Alteration during Airway Epithelial Cell Differentiation in COPD. *Diagnostics, 11*(9), 1579.

Angelis, N., Porpodis, K., Zarogoulidis, P., Spyratos, D., Kioumis, I., Papaiwannou, A., Pitsiou, G., Tsakiridis, K., Mpakas, A., Arikas, S., Tsiouda, T., Katsikogiannis, N., Kougioumtzi, I., Machairiotis, N., Argyriou, M., Kessisis, G., & Zarogoulidis, K. (2014). Airway inflammation in chronic obstructive pulmonary disease. *Journal of Thoracic Disease*, 167-172.

Anjilvel, S., & Asgharian, B. (1995). A Multiple-Path Model of Particle Deposition in the Rat Lung. *Fundamental and Applied Toxicology, 28*(1), 10.

Ankley, G. T., Bennett, R. S., Erickson, R. J., Hoff, D. J., Hornung, M. W., Johnson, R. D.,

Mount, D. R., Nichols, J. W., Russom, C. L., Schmieder, P. K., Serrrano, J. A., Tietge, J. E., & Villeneuve, D. L. (2009). Adverse outcome pathways: A conceptual framework to support ecotoxicology research and risk assessment. *Environmental Toxicology and Chemistry, 29*(3), 730-741.

Arigony, A. L., de Oliveira, I. M., Machado, M., Bordin, D. L., Bergter, L., Prá, D., & Henriques, J. A. (2013). The influence of micronutrients in cell culture: a reflection on viability and genomic stability. *BioMed Research International, 2013*, 597282.

Asgari, M., Lucci, F., & Kuczaj, A. K. (2021). Multispecies aerosol evolution and deposition in a human respiratory tract cast model. *Journal of Aerosol Science, 153*.

Asgharian, B., Hofmann, W., & Bergmann, R. (2001). Particle Deposition in a Multiple-Path Model of the Human Lung. *Aerosol Science and Technology, 34*(4), 332-339.

Asgharian, B., Price, O. T., Rostami, A. A., & Pithawalla, Y. B. (2018). Deposition of inhaled electronic cigarette aerosol in the human oral cavity. *Journal of Aerosol Science, 116*, 34-47.

Asgharian, B., Price, O. T., Schroeter, J. D., Kimbell, J. S., Jones, L., & Singal, M. (2011). Derivation of mass transfer coefficients for transient uptake and tissue disposition of soluble and reactive vapors in lung airways. *Annals of Biomedical Engineering, 39*(6), 1788-1804.

Asgharian, B., Price, O. T., Schroeter, J. D., Kimbell, J. S., & Singal, M. (2012). A lung dosimetry model of vapor uptake and tissue disposition. *Inhalation Toxicology, 24*(3), 182-193.

Asgharian, B., Price, O. T., Yurteri, C. U., Dickens, C., & McAughey, J. (2014). Component-specific, cigarette particle deposition modeling in the human respiratory tract. *Inhalation Toxicology, 26*(1), 36-47.

Asgharian, B., Rostami, A. A., Price, O. T., & Pithawalla, Y. B. (2018). Regional deposition of inhaled aerosol constituents from Electronic Nicotine Delivery Systems (ENDS) in the respiratory tract. *Journal of Aerosol Science, 126*, 7-20.

Atherton, H. C., Jones, G., & Danahay, H. (2003). IL-13-induced changes in the goblet cell density of human bronchial epithelial cell cultures: MAP kinase and phosphatidylinositol 3-kinase regulation. *American Journal of Physiology-Lung Cellular and Molecular Physiology, 285*(3), 730-739.

Atkinson, J. J., & Senior, R. M. (2003). Matrix Metalloproteinase-9 in Lung Remodeling. *American Journal of Respiratory Cell and Molecular Biology, 28*(1), 12-24.

Azizgolshani, H., Coppeta, J. R., Vedula, E. M., Marr, E. E., Cain, B. P., Luu, R. J., Lech, M. P., Kann, S. H., Mulhern, T. J., Tandon, V., Tan, K., Haroutunian, N. J., Keegan, P., Rogers, M., Gard, A. L., Baldwin, K. B., de Souza, J. C., Hoefler, B. C., Bale, S. S., Kratchman, L. B., Zorn, A., Patterson, A., Kim, E. S., Petrie, T. A., Wiellette, E. L., Williams, C., Isenberg, B. C., & Charest, J. L. (2021). High-throughput organ-on-chip platform with integrated programmable fluid flow and real-time sensing for complex tissue models in drug development workflows. *Lab on a Chip, 21*(8), 1454-1474.

Beane, J., & Spira, A., (2007). Reversible and Permanent effects of Tobacco Smoke Exposure on Airway Epithelial Gene Expression, NCBI Gene Expression Omnibus, GSE7895, https://www.ncbi.nlm.nih.gov/geo/query/acc.cgi?acc=GSE7895

Beedanagari, S. R., Bebenek, I., Bui, P., & Hankinson, O. (2009). Resveratrol Inhibits Dioxin-Induced Expression of Human CYP1A1 and CYP1B1 by Inhibiting Recruitment of the Aryl Hydrocarbon Receptor Complex and RNA Polymerase II to the Regulatory Regions of the Corresponding Genes. *Toxicological Sciences, 110*(1), 61-67.

Bell, S. M., Chang, X., Wambaugh, J. F., Allen, D. G., Bartels, M., Brouwer, K. L. R., Casey, W. M., Choksi, N., Ferguson, S. S., Fraczkiewicz, G., Jarabek, A. M., Ke, A., Lumen, A., Lynn, S. G., Paini, A., Price, P. S., Ring, C., Simon, T. W., Sipes, N. S., Sprankle, C. S., Strickland, J., Troutman, J., Wetmore, B. A., & Kleinstreuer, N. C. (2018). In vitro to in vivo extrapolation for high throughput prioritization and decision making. *Toxicology in Vitro, 47*, 213-227.

Benam, K. H., Villenave, R., Lucchesi, C., Varone, A., Hubeau, C., Lee, H.-H., Alves, S. E., Salmon, M., Ferrante, T. C., Weaver, J. C., Bahinski, A., Hamilton, G. A., & Ingber, D. E. (2016). Small airway-on-a-chip enables analysis of human lung inflammation and drug responses in vitro. *Nature Methods, 13*(2), 151-157.

Blanchette, A. D., Burnett, S. D., Grimm, F. A., Rusyn, I., & Chiu, W. A. (2020). A Bayesian Method for Population-wide Cardiotoxicity Hazard and Risk Characterization Using an In Vitro Human Model. *Toxicological Sciences, 178*(2), 391-403.

Blom, R. A. M., Erni, S. T., Krempaská, K., Schaerer, O., van Dijk, R. M., Amacker, M., Moser, C., Hall, S. R. R., von Garnier, C., & Blank, F. (2016). A Triple Co-Culture Model of the

Human Respiratory Tract to Study Immune-Modulatory Effects of Liposomes and Virosomes. *PLOS ONE, 11*(9), e0163539.

Bodas, M., Moore, A. R., Subramaniyan, B., Georgescu, C., Wren, J. D., Freeman, W. M., Brown, B. R., Metcalf, J. P., & Walters, M. S. (2020). Cigarette Smoke Activates NOTCH3 to Promote Goblet Cell Differentiation in Human Airway Epithelial Cells. *bioRxiv*, 195818.

Bonanini, F., Kurek, D., Previdi, S., Nicolas, A., Hendriks, D., de Ruiter, S., Meyer, M., Clapés Cabrer, M., Dinkelberg, R., García, S. B., Kramer, B., Olivier, T., Hu, H., López-Iglesias, C., Schavemaker, F., Walinga, E., Dutta, D., Queiroz, K., Domansky, K., Ronden, B., Joore, J., Lanz, H. L., Peters, P. J., Trietsch, S. J., Clevers, H., & Vulto, P. (2022). In vitro grafting of hepatic spheroids and organoids on a microfluidic vascular bed. *Angiogenesis, 25*(4), 455-470.

Booth, B. W., Adler, K. B., Bonner, J. C., Tournier, F., & Martin, L. D. (2001). Interleukin-13 induces proliferation of human airway epithelial cells in vitro via a mechanism mediated by transforming growth factor-alpha. *American Journal of Respiratory Cell and Molecular Biology, 25*(6), 739-743.

Bousquet, J., Jeffery, P. K., Busse, W. W., Johnson, M., & Vignola, A. M. (2000). Asthma. From bronchoconstriction to airways inflammation and remodeling. *American Journal of Respiratory and Critical Care Medicine, 161*(5), 1720-1745.

Bovard, D., Giralt, A., Trivedi, K., Neau, L., Kanellos, P., Iskandar, A., Kondylis, A., Luettich, K., Frentzel, S., Hoeng, J., & Peitsch, M. C. (2020). Comparison of the basic morphology and function of 3D lung epithelial cultures derived from several donors. *Current Research in Toxicology, 1*, 56-69.

Brozek, J. L., Canelo-Aybar, C., Akl, E. A., Bowen, J. M., Bucher, J., Chiu, W. A., Cronin, M., Djulbegovic, B., Falavigna, M., Guyatt, G. H., Gordon, A. A., Hilton Boon, M., Hutubessy, R. C. W., Joore, M. A., Katikireddi, V., LaKind, J., Langendam, M., Manja, V., Magnuson, K., Mathioudakis, A. G., Meerpohl, J., Mertz, D., Mezencev, R., Morgan, R., Morgano, G. P., Mustafa, R., O'Flaherty, M., Patlewicz, G., Riva, J. J., Posso, M., Rooney, A., Schlosser, P. M., Schwartz, L., Shemilt, I., Tarride, J.-E., Thayer, K. A., Tsaioun, K., Vale, L., Wambaugh, J., Wignall, J., Williams, A., Xie, F., Zhang, Y., & Schünemann, H. J. (2021). GRADE Guidelines 30: the GRADE approach to assessing the certainty of modeled evidence—An overview in the context of health decision-making. *Journal of Clinical Epidemiology, 129*, 138-150.

Buist, H. E., Wit-Bos, L., Bouwman, T., & Vaes, W. H. (2012). Predicting blood:air partition coefficients using basic physicochemical properties. *Regulatory Toxicology and Pharmacology, 62*(1), 23-28.

Bukowska, B., & Duchnowicz, P. (2022). Molecular Mechanisms of Action of Selected Substances Involved in the Reduction of Benzo[a]pyrene-Induced Oxidative Stress. *Molecules, 27*(4), 1379.

Burgoon, L. D., Angrish, M., Garcia-Reyero, N., Pollesch, N., Zupanic, A., & Perkins, E. (2020). Predicting the Probability that a Chemical Causes Steatosis Using Adverse Outcome Pathway Bayesian Networks (AOPBNs). *Risk Analysis, 40*(3), 512-523.

Calderon, A. A., Dimond, C., Choy, D. F., Pappu, R., Grimbaldeston, M. A., Mohan, D., & Chung, K. F. (2023). Targeting interleukin-33 and thymic stromal lymphopoietin pathways for novel pulmonary therapeutics in asthma and COPD. *European Respiratory Review, 32*(167), 220144.

Cao, X., Muskhelishvili, L., Latendresse, J., Richter, P., & Heflich, R. H. (2017). Evaluating the Toxicity of Cigarette Whole Smoke Solutions in an Air-Liquid-Interface Human In Vitro Airway Tissue Model. *Toxicological Sciences, 156*(1), 14-24.

Cao, X., Wang, Y., Xiong, R., Muskhelishvili, L., Davis, K., Richter, P. A., & Heflich, R. H. (2018). Cigarette whole smoke solutions disturb mucin homeostasis in a human in vitro airway tissue model. *Toxicology, 409*, 119-128.

Carnesecchi, E., Langezaal, I., Browne, P., Batista-Leite, S., Campia, I., Coecke, S., Dagallier, B., Deceuninck, P., Dorne, J. L. C. M., Tarazona, J. V., Le Goff, F., Leinala, E., Morath, S., Munn, S., Richardson, J., Paini, A., & Wittwehr, C. (2023). OECD harmonised template 201: Structuring and reporting mechanistic information to foster the integration of new approach methodologies for hazard and risk assessment of chemicals. *Regulatory Toxicology and Pharmacology, 142*, 105426.

Carolan, B., Harvey, B., De, B. P., Vanni, H., & Crystal, R. G., (2008). Decreased Expression of Intelectin 1 in The Human Airway Epithelium of Smokers Compared to Nonsmokers, NCBI Gene Expression Omnibus, GSE10006, https://www.ncbi.nlm.nih.gov/geo/query/acc.cgi?acc=GSE10006

Carolan, B., Heguy, A., Harvey, B., Leopold, P., Ferris, B., & Crystal, R., (2006a). Airway epithelium, large airways, phenotypically normal smokers vs non-smokers, MAS5 (HG-U133 2.0), NCBI Gene Expression Omnibus, GSE5059, https://www.ncbi.nlm.nih.gov/geo/query/acc.cgi?acc=GSE5059

Carolan, B., Heguy, A., Harvey, B., Leopold, P., Ferris, B., & Crystal, R., (2006b). Airway epithelium, large airways, phenotypically normal smokers vs non-smokers, MAS5 (HG-U133A), NCBI Gene Expression Omnibus, GSE5057, https://www.ncbi.nlm.nih.gov/geo/query/acc.cgi?acc=GSE5057

Carolan, B., Heguy, A., Harvey, B., Leopold, P., Ferris, B., & Crystal, R., (2006c). Airway epithelium, small airways, normal non-smokers, phenotypic normal smokers, smokers with COPD and early COPD, NCBI Gene Expression Omnibus, GSE5058, https://www.ncbi.nlm.nih.gov/geo/query/acc.cgi?acc=GSE5058

Carolan, B. J., Harvey, B., Hackett, N. R., O'Connor, T. P., Cassano, P. A., & Crystal, R. G., (2011). Disparate Oxidant-related Gene Expression of Human Small Airway Epithelium Compared to Autologous Alveolar Macrophages, NCBI Gene Expression Omnibus, GSE13931, https://www.ncbi.nlm.nih.gov/geo/query/acc.cgi?acc=GSE13931

Casalino-Matsuda, S. M., Monzón, M. E., & Forteza, R. M. (2006). Epidermal growth factor receptor activation by epidermal growth factor mediates oxidant-induced goblet cell metaplasia in human airway epithelium. *American Journal of Respiratory Cell and Molecular Biology, 34*(5), 581-591.

Castaldi, P. J., Dy, J., Ross, J., Chang, Y., Washko, G. R., Curran-Everett, D., Williams, A., Lynch, D. A., Make, B. J., Crapo, J. D., Bowler, R. P., Regan, E. A., Hokanson, J. E., Kinney, G. L., Han, M. K., Soler, X., Ramsdell, J. W., Barr, R. G., Foreman, M., van Beek, E., Casaburi, R., Criner, G. J., Lutz, S. M., Rennard, S. I., Santorico, S., Sciurba, F. C., DeMeo, D. L., Hersh, C. P., Silverman, E. K., & Cho, M. H. (2014). Cluster analysis in the COPDGene study identifies subtypes of smokers with distinct patterns of airway disease and emphysema. *Thorax, 69*(5), 415-422.

Celly, C. S., House, A., Sehring, S. J., Zhang, X. Y., Jones, H., Hey, J. A., Egan, R. W., & Chapman, R. W. (2006). Temporal profile of forced expiratory lung function in allergen-challenged Brown–Norway rats. *European Journal of Pharmacology, 540*(1), 147-154.

Chakraborty, A., Mastalerz, M., Ansari, M., Schiller, H. B., & Staab-Weijnitz, C. A. (2022). Emerging Roles of Airway Epithelial Cells in Idiopathic Pulmonary Fibrosis. *Cells, 11*(6), 1050.

Chandrala, L. D., Afshar-Mohajer, N., Nishida, K., Ronzhes, Y., Sidhaye, V. K., Koehler, K., & Katz, J. (2019). A Device for measuring the in-situ response of Human Bronchial Epithelial Cells to airborne environmental agents. *Scientific Reports, 9*(1), 7263.

Chen, D., Tian, T., Wang, H., Liu, H., Hu, Z., Wang, Y., Liu, Y., Ma, H., Fan, W., Miao, R., Sun, W., Wang, Y., Qian, J., Jin, L., Wei, Q., Shen, H., Huang, W., & Lu, D. (2009). Association of human aryl hydrocarbon receptor gene polymorphisms with risk of lung cancer among cigarette smokers in a Chinese population. *Pharmacogenetics and Genomics, 19*(1), 25-34.

Cheng, K. H., Cheng, Y. S., Yeh, H. C., & Swift, D. L. (1997). Measurements of airway dimensions and calculation of mass transfer characteristics of the human oral passage. *Journal of Biomechanical Engineering, 119*(4), 476-482.

Churg, A., Brauer, M., Avila-Casado, M. d. C., Fortoul, T. I., & Wright, J. L. (2003). Chronic exposure to high levels of particulate air pollution and small airway remodeling. *Environmental Health Perspectives, 111*(5), 714-718.

Conolly, R. B., Ankley, G. T., Cheng, W., Mayo, M. L., Miller, D. H., Perkins, E. J., Villeneuve, D. L., & Watanabe, K. H. (2017). Quantitative Adverse Outcome Pathways and Their Application to Predictive Toxicology. *Environmental Science & Technology Journal, 51*(8), 4661-4672.

Crystal, R. G., Randell, S. H., Engelhardt, J. F., Voynow, J., & Sunday, M. E. (2008). Airway epithelial cells: current concepts and challenges. *Proceedings of the American Thoracic Society, 5*(7), 772-777.

Cunningham, A., McAdam, K., Thissen, J., & Digard, H. (2020). The Evolving E-cigarette: Comparative Chemical Analyses of E-cigarette Vapor and Cigarette Smoke. *Front Toxicol, 2*, 586674.

Curran, D. R., & Cohn, L. (2010). Advances in mucous cell metaplasia: a plug for mucus as a therapeutic focus in chronic airway disease. *American Journal of Respiratory Cell and*

Molecular Biology, 42(3), 268-275.

Dabbagh, K., Takeyama, K., Lee, H.-M., Ueki, I. F., Lausier, J. A., & Nadel, J. A. (1999). IL-4 Induces Mucin Gene Expression and Goblet Cell Metaplasia In Vitro and In Vivo1. *The Journal of Immunology, 162*(10), 6233-6237.

Darquenne, C. (2020). Deposition Mechanisms. *Journal of Aerosol Medicine and Pulmonary Drug Delivery, 33*(4), 181-185.

Darquenne, C., Lamm, W. J., Fine, J. M., Corley, R. A., & Glenny, R. W. (2016). Total and regional deposition of inhaled aerosols in supine healthy subjects and subjects with mild-to-moderate COPD. *Journal of Aerosol Science, 99*, 27-39.

David, G., Parmentier, E. A., Taurino, I., & Signorell, R. (2020). Tracing the composition of single e-cigarette aerosol droplets in situ by laser-trapping and Raman scattering. *Scientific Reports, 10*(1), 7929.

Davis, C. W., & Dickey, B. F. (2008). Regulated Airway Goblet Cell Mucin Secretion. *Annual Review of Physiology, 70*, 487-512.

Davis, J. D., & Wypych, T. P. (2021). Cellular and functional heterogeneity of the airway epithelium. *Mucosal Immunology, 14*(5), 978-990.

De Blasi, R. A., Campagna, G., & Finazzi, S. (2021). A dynamic Bayesian network model for predicting organ failure associations without predefining outcomes. *PLOS ONE, 16*(4), e0250787.

de la Lastra, C. A., & Villegas, I. (2007). Resveratrol as an antioxidant and pro-oxidant agent: mechanisms and clinical implications. *Biochemical Society Transactions, 35*(5), 1156-1160.

Organisation for Economic Co-operation and Development (2022). *Case Study on the use of an Integrated Approach for Testing and Assessment (IATA) for New Approach Methodology (NAM) for Refining Inhalation Risk Assessment from Point of Contact Toxicity of the Pesticide, Chlorothalonil.* Retrieved January 24th, 2025 from https://one.oecd.org/document/env/cbc/mono(2022)31/en/pdf

Ding, Y., Weindl, P., Lenz, A.-G., Mayer, P., Krebs, T., & Schmid, O. (2020). Quartz crystal microbalances (QCM) are suitable for real-time dosimetry in nanotoxicological studies using

VITROCELL®Cloud cell exposure systems. *Particle and Fibre Toxicology, 17*(1), 44.

Duell, A. K., Pankow, J. F., & Peyton, D. H. (2020). Nicotine in tobacco product aerosols: 'It's déjà vu all over again'. *Tobacco Control, 29*(6), 656-662.

Eenjes, E., Mertens, T. C. J., Buscop-van Kempen, M. J., van Wijck, Y., Taube, C., Rottier, R. J., & Hiemstra, P. S. (2018). A novel method for expansion and differentiation of mouse tracheal epithelial cells in culture. *Scientific Reports, 8*(1), 7349.

Elias, Z., Wang, G., Alice, L., Hristo, A., Huan, Y., Cleo, T., Ghislaine, G., Paul, J., Magdalini, S., Joost, B., Beltman., & Frederic, Y., Bois. (2019). Application of three approaches for quantitative AOP development to renal toxicity. *Computational Toxicology, 11*, 1-13.

Esterly, J. R., & Heard, B. E. (1965). Multiple bronchiolar stenoses in a patient with generalized airways obstruction. *Thorax, 20*(4), 309-316.

Fahy, J. V., & Dickey, B. F. (2010). Airway mucus function and dysfunction. *The New England Journal of Medicine 363*(23), 2233-2247.

Feng, Y., Kleinstreuer, C., Castro, N., & Rostami, A. (2016). Computational transport, phase change and deposition analysis of inhaled multicomponent droplet–vapor mixtures in an idealized human upper lung model. *Journal of Aerosol Science, 96*, 96-123.

Fichtner-Feigl, S., Strober, W., Kawakami, K., Puri, R. K., & Kitani, A. (2006). IL-13 signaling through the IL-13 α 2 receptor is involved in induction of TGF-β 1 production and fibrosis. *Nature Medicine, 12*(1), 99-106.

Fu, C., Li, Y., Xi, H., Niu, Z., Chen, N., Wang, R., Yan, Y., Gan, X., Wang, M., Zhang, W., Zhang, Y., & Lv, P. (2022). Benzo(a)pyrene and cardiovascular diseases: An overview of pre-clinical studies focused on the underlying molecular mechanism. *Frontiers in Nutrition,* 9, 978475.

Gabryelska, A., Kuna, P., Antczak, A., Białasiewicz, P., & Panek, M. (2019). IL-33 Mediated Inflammation in Chronic Respiratory Diseases—Understanding the Role of the Member of IL-1 Superfamily. *Frontiers in Immunology,* 10, 692.

Galkina, E., & Ley, K. (2009). Immune and inflammatory mechanisms of atherosclerosis. *Annual Review of Immunology, 27*, 165-197.

Gao, W., Kanagarajah, K. R., Graham, E., Soon, K., Veres, T., Moraes, T. J., Bear, C. E., Veldhuizen, R. A., Wong, A. P., & Gunther, A. (2024). Collagen Tubular Airway-on-Chip for Extended Epithelial Culture and Investigation of Ventilation Dynamics. *Small*, e2309270.

Gohy, S., Carlier, F. M., Fregimilicka, C., Detry, B., Lecocq, M., Ladjemi, M. Z., Verleden, S., Hoton, D., Weynand, B., Bouzin, C., & Pilette, C. (2019). Altered generation of ciliated cells in chronic obstructive pulmonary disease. *Scientific Reports, 9*(1), 17963.

Gour, N., & Wills-Karp, M. (2015). IL-4 and IL-13 signaling in allergic airway disease. *Cytokine, 75*(1), 68-78.

Gower, A. C., Steiling, K., Brothers, J. F., 2nd, Lenburg, M. E., & Spira, A. (2011). Transcriptomic studies of the airway field of injury associated with smoking-related lung disease. *Proc Am Thorac Soc, 8*(2), 173-179.

Gu, A., Ji, G., Jiang, T., Lu, A., You, Y., Liu, N., Luo, C., Yan, W., & Zhao, P. (2012). Contributions of Aryl Hydrocarbon Receptor Genetic Variants to the Risk of Glioma and PAH-DNA Adducts. *Toxicological Sciences, 128*(2), 357-364.

Gunduz, I., Nordlund, M., King, J., Gustin, B., Cudazzo, G., Nesovic, M., Butin, Y., Stura, E., Alriquet, M., Chauhan, M., Rossoll, A., Szostak, J., & Belushkin, M. (2025). A comparative assessment of HPHC yields and in vitro toxicity for 1R6F reference cigarette smoke versus aerosol generated by Tobacco Heating System 3.0. *Aerosol Science and Technology, 59*(2), 146-162.

Gupta, G., Vallabani, S., Bordes, R., Bhattacharya, K., & Fadeel, B. (2021). Development of Microfluidic, Serum-Free Bronchial Epithelial Cells-on-a-Chip to Facilitate a More Realistic In vitro Testing of Nanoplastics. *Frontiers in Toxicology, 3*.

Hübner, R., Schwartz, J. D., De, B. P., Ferris, B., Hackett, N. R., & Crystal, R. G., (2009). NCBI Gene Expression Omnibus, GSE11952, https://www.ncbi.nlm.nih.gov/geo/query/acc.cgi?acc=GSE11952

Hamid, Q., & Tulic, M. (2009). Immunobiology of Asthma. *Annual Review of Physiology, 71*, 489-507.

Harkema, J. R., Carey, S. A., & Wagner, J. G. (2006). The Nose Revisited: A Brief Review of the Comparative Structure, Function, and Toxicologic Pathology of the Nasal Epithelium.

Toxicologic Pathology, 34(3), 252-269.

Harvey, B. G., Heguy, A., & Crystal, R. G., (2005). Gene expression profile of small airway epithelium of normal non-smokers and normal smokers, NCBI Gene Expression Omnibus, GSE3320, https://www.ncbi.nlm.nih.gov/geo/query/acc.cgi?acc=GSE3320

Hashizume, T., Ishikawa, S., Matsumura, K., Ito, S., & Fukushima, T. (2023). Chemical and in vitro toxicological comparison of emissions from a heated tobacco product and the 1R6F reference cigarette. *Toxicology Reports, 10*, 281-292.

Hastie, T., Tibshirani, R., & Friedman, J. (2009). *The elements of statistical learning: data mining, inference, and prediction*. Springer Science & Business Media.

Haswell, L. E., Smart, D., Jaunky, T., Baxter, A., Santopietro, S., Meredith, S., Camacho, O. M., Breheny, D., Thorne, D., & Gaca, M. D. (2021). The development of an in vitro 3D model of goblet cell hyperplasia using MUC5AC expression and repeated whole aerosol exposures. *Toxicol Lett, 347*, 45-57.

Heguy, A., Harvey, B., Leopold, P., Carolan, B., Ferris, B., & Crystal, R., (2006). Expression data of small airway epithelium from phenotypically normal smokers and non-smokers, NCBI Gene Expression Omnibus, GSE4498, https://www.ncbi.nlm.nih.gov/geo/query/acc.cgi?acc=GSE4498

Heijink, I. H., Kuchibhotla, V. N. S., Roffel, M. P., Maes, T., Knight, D. A., Sayers, I., & Nawijn, M. C. (2020). Epithelial cell dysfunction, a major driver of asthma development. *Allergy, 75*(8), 1902-1917.

Hiemstra, P. S., Grootaers, G., van der Does, A. M., Krul, C. A. M., & Kooter, I. M. (2018). Human lung epithelial cell cultures for analysis of inhaled toxicants: Lessons learned and future directions. *Toxicology in Vitro, 47*, 137-146.

Hill, D. B., Button, B., Rubinstein, M., & Boucher, R. C. (2022). Physiology and pathophysiology of human airway mucus. *Physiological Reviews, 102*(4), 1757-1836.

Hogg, J. C., Chu, F., Utokaparch, S., Woods, R., Elliott, W. M., Buzatu, L., Cherniack, R. M., Rogers, R. M., Sciurba, F. C., Coxson, H. O., & Paré, P. D. (2004). The Nature of Small-Airway Obstruction in Chronic Obstructive Pulmonary Disease. *New England Journal of Medicine, 350*(26), 2645-2653.

Holz, Jörres, R. A., & Magnussen, H. (2000). Monitoring central and peripheral airway inflammation in asthma. *Respiratory Medicine, 94 Suppl D*, S7-12.

Hong, H., Liao, S., Chen, F., Yang, Q., & Wang, D.-Y. (2020). Role of IL-25, IL-33, and TSLP in triggering united airway diseases toward type 2 inflammation. *Allergy, 75*(11), 2794-2804.

Houghton, A. M. (2015). Matrix metalloproteinases in destructive lung disease. *Matrix Biology, 44-46*, 167-174.

Huh, D., Matthews, B. D., Mammoto, A., Montoya-Zavala, M., Hsin, H. Y., & Ingber, D. E. (2010). Reconstituting Organ-Level Lung Functions on a Chip. *Science, 328*(5986), 1662-1668.

International Commission on Radiological Protection (1994). *Human Respiratory Tract Model for Radiological Protection. ICRP Publication 66* [Book]. Pergamon Press.

International Organization for Standardization (1999). *Tobacco and tobacco products — Atmosphere for conditioning and testing*.

International Organization for Standardization (2018). *Cigarettes -Routine Analytical Cigarette Smoking Machine - Definitions and Standard Conditions with an Intense Smoking Regime*.

Ishikawa, S., Nagata, Y., & Suzuki, T. (2016). Analysis of Cigarette Smoke Deposition Within an In Vitro Exposure System for Simulating Exposure in the Human Respiratory Tract. *Beiträge zur Tabakforschung International/Contributions to Tobacco Research, 27*(1), 20-29.

Ito, S., Ishimori, K., & Ishikawa, S. (2018). Effects of repeated cigarette smoke extract exposure over one month on human bronchial epithelial organotypic culture. *Toxicology Reports, 5*, 864-870.

Ito, S., Matsumura, K., Ishimori, K., & Ishikawa, S. (2020). In vitro long-term repeated exposure and exposure switching of a novel tobacco vapor product in a human organotypic culture of bronchial epithelial cells. *Journal of Applied Toxicology, 40*(9), 1248-1258.

Jaccard, G., Djoko, D. T., Korneliou, A., Stabbert, R., Belushkin, M., & Esposito, M. (2019). Mainstream smoke constituents and in vitro toxicity comparative analysis of 3R4F and 1R6F

reference cigarettes. *Toxicology Reports, 6*, 222-231.

Jang, K.-J., & Suh, K.-Y. (2010). A multi-layer microfluidic device for efficient culture and analysis of renal tubular cells. *Lab on a Chip, 10*(1), 36-42.

Jeffery, P. K. (2001). Remodeling in asthma and chronic obstructive lung disease. *American Journal of Respiratory and Critical Care Medicine, 164*(10 Pt 2), S28-38.

Jeffery, P. K. (2004). Remodeling and Inflammation of Bronchi in Asthma and Chronic Obstructive Pulmonary Disease. *Proceedings of the American Thoracic Society, 1*(3), 176-183.

Jennings, P., Koppelstaetter, C., Pfaller, W., Morin, J. P., Hartung, T., & Ryan, M. P. (2004). Assessment of a new cell culture perfusion apparatus for in vitro chronic toxicity testing. Part 2: toxicological evaluation. *Alternatives to animal experimentation, 21*(2), 61-66.

Jeong, J., Song, T., Chatterjee, N., Choi, I., Cha, Y. K., & Choi, J. (2018). Developing adverse outcome pathways on silver nanoparticle-induced reproductive toxicity via oxidative stress in the nematode Caenorhabditis elegans using a Bayesian network model. *Nanotoxicology, 12*(10), 1182-1197.

Jetten, M. J., Ruiz-Aracama, A., Coonen, M. L., Claessen, S. M., van Herwijnen, M. H., Lommen, A., van Delft, J. H., Peijnenburg, A. A., & Kleinjans, J. C. (2016). Interindividual variation in gene expression responses and metabolite formation in acetaminophen-exposed primary human hepatocytes. *Archives of Toxicology, 90*(5), 1103-1115.

Kannan, R., Chen, Z., Przekwas, A., Segars, P., Martin, F., Kuczaj, A. K., & Hoeng, J. (2020). Anthropometry-based generation of personalized and population-specific human airway models. *International Journal for Numerical Methods in Biomedical Engineering, 36*(5), e3324.

Kato, K., Chang, E. H., Chen, Y., Lu, W., Kim, M. M., Niihori, M., Hecker, L., & Kim, K. C. (2020). MUC1 contributes to goblet cell metaplasia and MUC5AC expression in response to cigarette smoke in vivo. *American Journal of Physiology-Lung Cellular and Molecular Physiology, 319*(1), L82-L90.

Katritzky, A. R., Kuanar, M., Fara, D. C., Karelson, M., Acree, W. E., Solov'ev, V. P., & Varnek, A. (2005). QSAR modeling of blood:air and tissue:air partition coefficients using theoretical

descriptors. *Bioorganic & Medicinal Chemistry, 13*(23), 6450-6463.

Khelloufi, M.-K., Loiseau, E., Jaeger, M., Molinari, N., Chanez, P., Gras, D., & Viallat, A. (2018). Spatiotemporal organization of cilia drives multiscale mucus swirls in model human bronchial epithelium. *Scientific Reports, 8*(1), 2447.

Kim, J. S., McKinnis, V. S., Nawrocki, A., & White, S. R. (1998). Stimulation of Migration and Wound Repair of Guinea-Pig Airway Epithelial Cells in Response to Epidermal Growth Factor. *American Journal of Respiratory Cell and Molecular Biology, 18*(1), 66-74.

Kimura, H., Sakai, Y., & Fujii, T. (2018). Organ/body-on-a-chip based on microfluidic technology for drug discovery. *Drug Metabolism and Pharmacokinetics, 33*(1), 43-48.

Kimura, Y., Shinoda, M., Shinkai, M., & Kaneko, T. (2023). Solithromycin inhibits IL-13-induced goblet cell hyperplasia and MUC5AC, CLCA1, and ANO1 in human bronchial epithelial cells. *PeerJ, 11*, e14695.

Kirsten, G., Brigitte, L., Andrew, W., Sharon, M., Taina, P., & Maurice, W. (2017). The Adverse Outcome Pathway approach in nanotoxicology. *Computational Toxicology, 1*, 3-11.

Kistemaker, L. E. M., Hiemstra, P. S., Bos, I. S. T., Bouwman, S., Berge, M. v. d., Hylkema, M. N., Meurs, H., Kerstjens, H. A. M., & Gosens, R. (2015). Tiotropium attenuates IL-13-induced goblet cell metaplasia of human airway epithelial cells. *Thorax, 70*(7), 668-676.

Knowles, M. R., & Boucher, R. C. (2002). Mucus clearance as a primary innate defense mechanism for mammalian airways. *The Journal of Clinical Investigation, 109*(5), 571-577.

Koller, D., & Friedman, N. (2009). *Probabilistic Graphical Models: Principles and Techniques*. MIT Press.

Komori, M., Inoue, H., Matsumoto, K., Koto, H., Fukuyama, S., Aizawa, H., & Hara, N. (2001). PAF mediates cigarette smoke-induced goblet cell metaplasia in guinea pig airways. *American Journal of Physiology-Lung Cellular and Molecular Physiology, 280*(3), L436-L441.

Koppelstaetter, C., Jennings, P., Ryan, M. P., Morin, J. P., Hartung, T., & Pfaller, W. (2004). Assessment of a new cell culture perfusion apparatus for in vitro chronic toxicity testing. Part 1: technical description. *Alternatives to animal experimentation, 21*(2), 51-60.

Koyama, Y., & Brenner, D. A. (2017). Liver inflammation and fibrosis. *Journal of Clinical Investigation, 127*(1), 55-64.

Krewski, D., Acosta, D., Andersen, M., Anderson, H., Bailar, J. C., Boekelheide, K., Brent, R., Charnley, G., Cheung, V. G., Green, S., Kelsey, K. T., Kerkvliet, N. I., Li, A. A., McCray, L., Meyer, O., Patterson, R. D., Pennie, W., Scala, R. A., Solomon, G. M., Stephens, M., Yager, J., Zeise, L., Staff of Committee on Toxicity, T., & Assessment of Environmental, A. (2010). Toxicity Testing in the 21st Century: A Vision and a Strategy. *Journal of Toxicology and Environmental Health, Part B, 13*(2-4), 51-138.

Kuga, K., Ito, K., Chen, W., Wang, P., Fowles, J., & Kumagai, K. (2021). Secondary indoor air pollution and passive smoking associated with cannabis smoking using electric cigarette device–demonstrative in silico study. *PLOS Computational Biology, 17*(5), e1009004.

Kuga, K., Ito, K., Chen, W., Wang, P., & Kumagai, K. (2020). A numerical investigation of the potential effects of e-cigarette smoking on local tissue dosimetry and the deterioration of indoor air quality. *Indoor Air, 30*(5), 1018-1038.

Kuga, K., Ito, K., Yoo, S.-J., Chen, W., Wang, P., Liao, J., Fowles, J., Shusterman, D., & Kumagai, K. (2018). First- and second-hand smoke dispersion analysis from e-cigarettes using a computer-simulated person with a respiratory tract model. *Indoor and Built Environment, 27*(7), 898-916.

Lagowala, D. A., Kwon, S., Sidhaye, V. K., & Kim, D. H. (2021). Human microphysiological models of airway and alveolar epithelia. *American Journal of Physiology-Lung Cellular and Molecular Physiology, 321*(6), L1072-l1088.

Larsen, G. L., & Holt, P. G. (2000). The Concept of Airway Inflammation. *American Journal of Respiratory and Critical Care Medicine, 162* (supplement_1), S2-S6.

Li, R., Zhou, R., & Zhang, J. (2018). Function of PM2.5 in the pathogenesis of lung cancer and chronic airway inflammatory diseases (Review). *Oncology Letters, 15*(5), 7506-7514.

Liang, R., Wu, C., Liu, S., & Zhao, W. (2022). Targeting interleukin-13 receptor α2 (IL-13Rα2) for glioblastoma therapy with surface functionalized nanocarriers. *Drug Delivery, 29*(1), 1620-1630.

Linden, S. K., Sutton, P., Karlsson, N. G., Korolik, V., & McGuckin, M. A. (2008). Mucins in

the mucosal barrier to infection. *Mucosal Immunology, 1*(3), 183-197.

Livraghi, A., & Randell, S. H. (2007). Cystic Fibrosis and Other Respiratory Diseases of Impaired Mucus Clearance. *Toxicologic Pathology, 35*(1), 116-129.

Marescotti, D., Bovard, D., Morelli, M., Sandoz, A., Luettich, K., Frentzel, S., Peitsch, M., & Hoeng, J. (2020). In Vitro High-Content Imaging-Based Phenotypic Analysis of Bronchial 3D Organotypic Air–Liquid Interface Cultures. *SLAS Technology, 25*(3), 247-252.

Marian, C., O'Connor, R. J., Djordjevic, M. V., Rees, V. W., Hatsukami, D. K., & Shields, P. G. (2009). Reconciling human smoking behavior and machine smoking patterns: implications for understanding smoking behavior and the impact on laboratory studies. *Cancer Epidemiology Biomarkers and Prevention, 18*(12), 3305-3320.

Marone, G., Granata, F., Pucino, V., Pecoraro, A., Heffler, E., Loffredo, S., Scadding, G. W., & Varricchi, G. (2019). The Intriguing Role of Interleukin 13 in the Pathophysiology of Asthma. *Frontiers in Pharmacology, 10*, 1387.

Mete, A., & Akbudak, İ. H. (2018). *Functional Anatomy and Physiology of Airway*. Riza Hakan E. (Ed.), *Tracheal Intubation* (Ch. 1). IntechOpen.

Mattes, J., Yang, M., Siqueira, A., Clark, K., MacKenzie, J., McKenzie, A. N. J., Webb, D. C., Matthaei, K. I., & Foster, P. S. (2001). IL-13 Induces Airways Hyperreactivity Independently of the IL-4Rα Chain in the Allergic Lung1. *The Journal of Immunology, 167*(3), 1683-1692.

Meulenberg, C. J. W., & Vijverberg, H. P. M. (2000). Empirical Relations Predicting Human and Rat Tissue:Air Partition Coefficients of Volatile Organic Compounds. *Toxicology and Applied Pharmacology, 165*(3), 206-216.

Moe, S. J., Wolf, R., Xie, L., Landis, W. G., Kotamaki, N., & Tollefsen, K. E. (2021). Quantification of an Adverse Outcome Pathway Network by Bayesian Regression and Bayesian Network Modeling. *Integrated Environmental Assessment and Management, 17*(1), 147-164.

Mokarizadeh, A., Faryabi, M. R., Rezvanfar, M. A., & Abdollahi, M. (2015). A comprehensive review of pesticides and the immune dysregulation: mechanisms, evidence and consequences. *Toxicology Mechanisms and Methods, 25*(4), 258-278.

Mori, S., Ishimori, K., Matsumura, K., Ishikawa, S., & Ito, S. (2022). Donor-to-donor variability of a human three-dimensional bronchial epithelial model: A case study of cigarette smoke exposure. *Toxicology In Vitro, 82*, 105391.

Munitz, A., Brandt, E. B., Mingler, M., Finkelman, F. D., & Rothenberg, M. E. (2008). Distinct roles for IL-13 and IL-4 via IL-13 receptor α1 and the type II IL-4 receptor in asthma pathogenesis. *Proceedings of the National Academy of Sciences, 105*(20), 7240-7245.

Murata, T., Husain, S. R., Mohri, H., & Puri, R. K. (1998). Two different IL-13 receptor chains are expressed in normal human skin fibroblasts, and IL-4 and IL-13 mediate signal transduction through a common pathway. *International Immunology, 10*(8), 1103-1110.

Muratani, S., Ichikawa, S., Erami, K., & Ito, S. (2023). Oxidative stress-mediated epidermal growth factor receptor activation by cigarette smoke or heated tobacco aerosol in human primary bronchial epithelial cells from multiple donors. *Journal of Applied Toxicology, 43*(9), 1347-1357.

Mwilola, P. N., Mukumbuta, I., Shitumbanuma, V., Chishala, B. H., Uchida, Y., Nakata, H., Nakayama, S., & Ishizuka, M. (2020). Lead, Zinc and Cadmium Accumulation, and Associated Health Risks, in Maize Grown near the Kabwe Mine in Zambia in Response to Organic and Inorganic Soil Amendments. *International Journal of Environmental Research and Public Health, 17*(23), 9038.

Nagarajan, R., Scutari, M., & Lèbre, S. Bayesian networks in r with applications in systems biology 2013. *New York, NYSpringer-Verlag*.

Nikula, K. J., & Green, F H. (2000). Animal models of chronic bronchitis and their relevance to studies of particle-induced disease. *Inhalation Toxicology, 12*(sup4), 123-153.

O'Shaughnessy, P. T., LeBlanc, L., Pratt, A., Altmaier, R., Rajaraman, P. K., Walenga, R., & Lin, C. L. (2020). Assessment and Validation of a Hygroscopic Growth Model with Different Water Activity Estimation Methods. *Aerosol Science and Technology, 54*(10), 1169-1182.

O'Boyle, N., Sutherland, E., Berry, C. C., & Davies, R. L. (2018). Optimisation of growth conditions for ovine airway epithelial cell differentiation at an air-liquid interface. *PLOS ONE, 13*(3), e0193998.

Oakes, J. M., Shadden, S. C., Grandmont, C., & Vignon-Clementel, I. E. (2017). Aerosol

transport throughout inspiration and expiration in the pulmonary airways. *International Journal for Numerical Methods in Biomedical Engineering, 33*(9), e2847.

Ochiai, S., Jagot, F., Kyle, R. L., Hyde, E., White, R. F., Prout, M., Schmidt, A. J., Yamane, H., Lamiable, O., Le Gros, G., & Ronchese, F. (2018). Thymic stromal lymphopoietin drives the development of IL-13+ Th2 cells. *Proceedings of the National Academy of Sciences, 115*(5), 1033-1038.

Oldham, M. J., Castro, N., Zhang, J., Lucci, F., Kosachevsky, P., Rostami, A. A., Gilman, I. G., Pithawalla, Y. B., Kuczaj, A. K., Hoeng, J., & Lee, K. M. (2020). Comparison of experimentally measured and computational fluid dynamic predicted deposition and deposition uniformity of monodisperse solid particles in the Vitrocell® AMES 48 air-liquid-interface in-vitro exposure system. *Toxicology in Vitro, 67*, 104870.

Paini, A., Campia, I., Cronin, M. T. D., Asturiol, D., Ceriani, L., Exner, T. E., Gao, W., Gomes, C., Kruisselbrink, J., Martens, M., Meek, M. E. B., Pamies, D., Pletz, J., Scholz, S., Schüttler, A., Spînu, N., Villeneuve, D. L., Wittwehr, C., Worth, A., & Luijten, M. (2022). Towards a qAOP framework for predictive toxicology - Linking data to decisions. *Computational Toxicology, 21*, 100195.

Palmer-Crocker, R. L., Hughes, C. C., & Pober, J. S. (1996). IL-4 and IL-13 activate the JAK2 tyrosine kinase and Stat6 in cultured human vascular endothelial cells through a common pathway that does not involve the gamma c chain. *Journal of Clinical Investigation, 98*(3), 604-609.

Park, S., & Young, E. W. K. (2021). E-FLOAT: Extractable Floating Liquid Gel-Based Organ-on-a-Chip for Airway Tissue Modeling under Airflow. *Advanced Materials Technologies, 6*(12), 2100828.

Patwa, A., & Shah, A. (2015). Anatomy and physiology of respiratory system relevant to anaesthesia. *Indian Journal of Anaesthesia, 59*(9), 533-541.

Pauluhn, J., & Mohr, U. (2000). Review Article: Inhalation Studies in Laboratory Animals—Current Concepts and Alternatives. *Toxicologic Pathology, 28*(5), 734-753.

Perkins, E. J., Ashauer, R., Burgoon, L., Conolly, R., Landesmann, B., Mackay, C., Murphy, C. A., Pollesch, N., Wheeler, J. R., Zupanic, A., & Scholz, S. (2019). Building and Applying

Quantitative Adverse Outcome Pathway Models for Chemical Hazard and Risk Assessment. *Environmental Toxicology and Chemistry, 38*(9), 1850-1865.

Perrais, M., Pigny, P., Copin, M.-C., Aubert, J.-P., & Van Seuningen, I. (2002). Induction of MUC2 and MUC5AC Mucins by Factors of the Epidermal Growth Factor (EGF) Family Is Mediated by EGF Receptor/Ras/Raf/Extracellular Signal-regulated Kinase Cascade and Sp1. *Journal of Biological Chemistry, 277*(35), 32258-32267.

Pichelstorfer, L., Winkler-Heil, R., Boy, M., & Hofmann, W. (2021). Aerosol dynamics simulations of the anatomical variability of e-cigarette particle and vapor deposition in a stochastic lung. *Journal of Aerosol Science, 158*, 105706.

Prytherch, Z., Job, C., Marshall, H., Oreffo, V., Foster, M., & BéruBé, K. (2011). Tissue-Specific stem cell differentiation in an in vitro airway model. *Macromolecular Bioscience, 11*(11), 1467-1477.

Qiu, F., Liang, C.-L., Liu, H., Zeng, Y.-Q., Hou, S., Huang, S., Lai, X., & Dai, Z. (2016). Impacts of cigarette smoking on immune responsiveness: Up and down or upside down? *Oncotarget, 8*(1).

Qu, W., Tokar, E. J., Kim, A. J., Bell, M. W., & Waalkes, M. P. (2012). Chronic cadmium exposure in vitro causes acquisition of multiple tumor cell characteristics in human pancreatic epithelial cells. *Environ Health Perspect, 120*(9), 1265-1271.

Raabe, O. G. (1976). Tracheobronchial geometry: human, dog, rat, hamster--a compilation of selected data from the project respiratory tract deposition models. U.S. Energy Research and Development Administration.

Raby, K. L., Michaeloudes, C., Tonkin, J., Chung, K. F., & Bhavsar, P. K. (2023). Mechanisms of airway epithelial injury and abnormal repair in asthma and COPD. *Frontiers in Immunology, 14*, 1201658.

Rayner, R. E., Makena, P., Prasad, G. L., & Cormet-Boyaka, E. (2019). Optimization of Normal Human Bronchial Epithelial (NHBE) Cell 3D Cultures for in vitro Lung Model Studies. *Scientific Reports, 9*(1), 500.

Rock, J. R., Randell, S. H., & Hogan, B. L. M. (2010). Airway basal stem cells: a perspective on their roles in epithelial homeostasis and remodeling. *Disease Models & Mechanisms, 3*(9-

10), 545-556.

Rogers, D. F. (2002). Airway goblet cell hyperplasia in asthma: hypersecretory and anti-inflammatory? *Clinical & Experimental Allergy, 32*(8), 1124-1127.

Rogers, D. F. (2007). Physiology of Airway Mucus Secretion and Pathophysiology of Hypersecretion. *Respiratory Care, 52*(9), 1134-1149.

Ronaghan, N. J., Soo, M., Pena, U., Tellis, M., Duan, W., Tabatabaei-Zavareh, N., Kramer, P., Hou, J., & Moraes, T. J. (2022). M1-like, but not M0- or M2-like, macrophages, reduce RSV infection of primary bronchial epithelial cells in a media-dependent fashion. *PLOS ONE, 17*(10), e0276013.

Rose, M. C., & Voynow, J. A. (2006). Respiratory Tract Mucin Genes and Mucin Glycoproteins in Health and Disease. *Physiological Reviews, 86*(1), 245-278.

Rostami, A. A. (2009). Computational Modeling of Aerosol Deposition in Respiratory Tract: A Review. *Inhalation Toxicology, 21*(4), 262-290.

Saetta, M., Turato, G., Baraldo, S., Zanin, A., Braccioni, F., Mapp, C. E., Maestrelli, P., Cavallesco, G., Papi, A., & Fabbri, L. M. (2000). Goblet Cell Hyperplasia and Epithelial Inflammation in Peripheral Airways of Smokers with Both Symptoms of Chronic Bronchitis and Chronic Airflow Limitation. *American Journal of Respiratory and Critical Care Medicine, 161*(3), 1016-1021.

Sakai, Y., Mori, S., Yanagimachi, M., Takahashi, T., Shibuya, K., Kumagai, A., Ishikawa, S., Ito, S., & Fukushima, T. (2020). Inter-Laboratory Reproducibility and Interchangeability of 3R4F and 1R6F Reference Cigarettes in Mainstream Smoke Chemical Analysis and Toxicity Assays. *Contributions to Tobacco & Nicotine Research, 29*(3), 119-135.

Samardzija Nenadov, D., Tesic, B., Fa, S., Pogrmic-Majkic, K., Kokai, D., Stanic, B., & Andric, N. (2022). Long-term in vitro exposure of human granulosa cells to the mixture of endocrine disrupting chemicals found in human follicular fluid disrupts steroidogenesis. *Toxicol In Vitro, 79*, 105302.

Schamberger, A. C., Staab-Weijnitz, C. A., Mise-Racek, N., & Eickelberg, O. (2015). Cigarette smoke alters primary human bronchial epithelial cell differentiation at the air-liquid interface. *Scientific Reports, 5*(1), 8163.

Scutari, M. (2010). Learning Bayesian Networks with the bnlearn R Package. *Journal of Statistical Software, 35*(3).

Scutari, M., & Denis, J. B. (2014). *Bayesian Networks: With Examples in R*. CRC Press.

Sécher, T., Bodier-Montagutelli, E., Guillon, A., & Heuzé-Vourc'h, N. (2020). Correlation and clinical relevance of animal models for inhaled pharmaceuticals and biopharmaceuticals. *Advanced Drug Delivery Reviews, 167*, 148-169.

Sengupta, A., Dorn, A., Jamshidi, M., Schwob, M., Hassan, W., De Maddalena, L. L., Hugi, A., Stucki, A. O., Dorn, P., Marti, T. M., Wisser, O., Stucki, J. D., Krebs, T., Hobi, N., & Guenat, O. T. (2023). A multiplex inhalation platform to model in situ like aerosol delivery in a breathing lung-on-chip. *Frontiers in Pharmacology, 14*, 1114739.

Shao, M. X. G., Nakanaga, T., & Nadel, J. A. (2004). Cigarette smoke induces MUC5AC mucin overproduction via tumor necrosis factor-α-converting enzyme in human airway epithelial (NCI-H292) cells. *American Journal of Physiology-Lung Cellular and Molecular Physiology, 287*(2), L420-L427.

Shaykhiev, R., & Crystal, R. G. (2014). Early Events in the Pathogenesis of Chronic Obstructive Pulmonary Disease. Smoking-induced Reprogramming of Airway Epithelial Basal Progenitor Cells. *Annals of the American Thoracic Society, 11*(Supplement 5), S252-S258.

Shaykhiev, R., Zuo, W.-L., Chao, I., Fukui, T., Witover, B., Brekman, A., & Crystal, R. G. (2013). EGF shifts human airway basal cell fate toward a smoking-associated airway epithelial phenotype. *Proceedings of the National Academy of Sciences, 110*(29), 12102-12107.

Shinichi, N., & Holger, S. (2013). A general and simple method for obtaining R2 from generalized linear mixed-effects models. *Methods in Ecology and Evolution, 4*(2), 133-142.

Sidhaye, V. K., Schweitzer, K. S., Caterina, M. J., Shimoda, L., & King, L. S. (2008). Shear stress regulates aquaporin-5 and airway epithelial barrier function. *Proceedings of the National Academy of Sciences, 105*(9), 3345-3350.

Sisson, J. H., Stoner, J. A., Ammons, B. A., & Wyatt, T. A. (2003). All-digital image capture and whole-field analysis of ciliary beat frequency. *J Microsc, 211*(Pt 2), 103-111.

Sone, N., Konishi, S., Igura, K., Tamai, K., Ikeo, S., Korogi, Y., Kanagaki, S., Namba, T., Yamamoto, Y., Xu, Y., Takeuchi, K., Adachi, Y., Chen-Yoshikawa, T. F., Date, H., Hagiwara, M., Tsukita, S., Hirai, T., Torisawa, Y.-s., & Gotoh, S. (2021). Multicellular modeling of ciliopathy by combining iPS cells and microfluidic airway-on-a-chip technology. *Science Translational Medicine, 13*(601), eabb1298.

Soriano, J. B., & Rodríguez-Roisin, R. (2011). Chronic Obstructive Pulmonary Disease Overview. *Proceedings of the American Thoracic Society, 8*(4), 363-367.

Spiess, B. D. (2009). Perfluorocarbon emulsions as a promising technology: a review of tissue and vascular gas dynamics. *Journal of Applied Physiology, 106*(4), 1444-1452.

Spinu, N., Cronin, M. T. D., Enoch, S. J., Madden, J. C., & Worth, A. P. (2020). Quantitative adverse outcome pathway (qAOP) models for toxicity prediction. *Archives of Toxicology, 94*(5), 1497-1510.

Spinu, N., Cronin, M. T. D., Lao, J., Bal-Price, A., Campia, I., Enoch, S. J., Madden, J. C., Mora Lagares, L., Novic, M., Pamies, D., Scholz, S., Villeneuve, D. L., & Worth, A. P. (2022). Probabilistic modelling of developmental neurotoxicity based on a simplified adverse outcome pathway network. *Computational Toxicology, 21*, 100206.

Spira, A., Beane, J., Shah, V., Liu, G., Schembri, F., Yang, X., Palma, J., & Brody, J., (2004). Effects of cigarette smoke on the human airway epithelial cell transcriptome, NCBI Gene Expression Omnibus, GSE994, https://www.ncbi.nlm.nih.gov/geo/query/acc.cgi?acc=GSE994

Steiling, K. A., Bergerat, A., Kadar, A. Y., Flanigon, J., Brody, J. S., Steffen, M., & Spira, A., (2009). Proteomic and Genomic Profiling of Bronchial Epithelial Cells in Never and Current Smokers, NCBI Gene Expression Omnibus, GSE4635, https://www.ncbi.nlm.nih.gov/geo/query/acc.cgi?acc=GSE4635

Strzelak, A., Ratajczak, A., Adamiec, A., & Feleszko, W. (2018). Tobacco Smoke Induces and Alters Immune Responses in the Lung Triggering Inflammation, Allergy, Asthma and Other Lung Diseases: A Mechanistic Review. *International Journal of Environmental Research and Public Healths, 15*(5).

Sun, Y., Shi, Z., Lin, Y., Zhang, M., Liu, J., Zhu, L., Chen, Q., Bi, J., Li, S., Ni, Z., & Wang, X.

(2021). Benzo(a)pyrene induces MUC5AC expression through the AhR/mitochondrial ROS/ERK pathway in airway epithelial cells. *Ecotoxicology and Environmental Safety, 210*, 111857.

Sutherland, E. R., & Martin, R. J. (2003). Airway inflammation in chronic obstructive pulmonary disease: Comparisons with asthma. *Journal of Allergy and Clinical Immunology, 112*(5), 819-827.

Takahashi, Y., Kanemaru, Y., Fukushima, T., Eguchi, K., Yoshida, S., Miller-Holt, J., & Jones, I. (2018). Chemical analysis and in vitro toxicological evaluation of aerosol from a novel tobacco vapor product: A comparison with cigarette smoke. *Regulatory Toxicology and Pharmacology, 92*, 94-103.

Tanabe, T., Fujimoto, K., Yasuo, M., Tsushima, K., Yoshida, K., Ise, H., & Yamaya, M. (2008). Modulation of mucus production by interleukin-13 receptor alpha2 in the human airway epithelium. *Clinical & Experimental Allergy, 38*(1), 122-134.

Tena, A. F., Fernández, J., Álvarez, E., Casan, P., & Walters, D. K. (2017). Design of a numerical model of lung by means of a special boundary condition in the truncated branches. *International Journal for Numerical Methods in Biomedical Engineering, 33*(6).

Tena, A. F., Perotti, R. B., Marigorta, E. B., & Blanco, A. P. (2020). In silico prototype of a human lung with a single airway to predict particle deposition. *International Journal for Numerical Methods in Biomedical Engineering, 36*(6), e3339.

Thavagnanam, S., Parker, J. C., McBrien, M. E., Skibinski, G., Heaney, L. G., & Shields, M. D. (2011). Effects of IL-13 on Mucociliary Differentiation of Pediatric Asthmatic Bronchial Epithelial Cells. *Pediatric Research, 69*(2), 95-100.

Thompson, L. A., Darwish, W. S., Ikenaka, Y., Nakayama, S. M., Mizukawa, H., & Ishizuka, M. (2017). Organochlorine pesticide contamination of foods in Africa: incidence and public health significance. *The Journal of Veterinary Medical Science, 79*(4), 751-764.

Thorne, D., & Adamson, J. (2013). A review of in vitro cigarette smoke exposure systems. *Experimental and Toxicologic Pathology, 65*(7), 1183-1193.

Tollefsen, K. E., Scholz, S., Cronin, M. T., Edwards, S. W., de Knecht, J., Crofton, K., Garcia-Reyero, N., Hartung, T., Worth, A., & Patlewicz, G. (2014). Applying Adverse Outcome

Pathways (AOPs) to support Integrated Approaches to Testing and Assessment (IATA). *Regulatory Toxicology and Pharmacology, 70*(3), 629-640.

Tratnjek, L., Sibinovska, N., Kristan, K., & Kreft, M. E. (2021). In Vitro Ciliotoxicity and Cytotoxicity Testing of Repeated Chronic Exposure to Topical Nasal Formulations for Safety Studies. *Pharmaceutics, 13*(11).

Truong, V.-L., Jun, M., & Jeong, W.-S. (2018). Role of resveratrol in regulation of cellular defense systems against oxidative stress. *BioFactors, 44*(1), 36-49.

Tsuda, A., Henry, F. S., & Butler, J. P. (2013). Particle transport and deposition: basic physics of particle kinetics. *Comprehensive Physiology, 3*(4), 1437-1471.

Turetz, M. L., O'Connor, T. P., Tilley, A. E., Strulovici-Barel, Y., Salit, J., Dang, D., Teater, M., Masey, J., Clark, A. G., & Crystal, R. G., (2009). NCBI Gene Expression Omnibus, GSE13933, https://www.ncbi.nlm.nih.gov/geo/query/acc.cgi?acc=GSE13933

United States Environmental Protection Agency. (2021). *EPA On-line Tools for Site Assessment Calculation*. Retrieved January 26th, 2025 from https://www3.epa.gov/ceampubl/learn2model/part-two/onsite/estdiffusion.html

U.S. food and drug administration. (2024). *Rules and Regulations Related to Tobacco Products*. Retrieved January 13th, 2025 from https://www.fda.gov/tobacco-products/rules-regulations-and-guidance-related-tobacco-products/rules-and-regulations-related-tobacco-products

Uchiyama, S., Noguchi, M., Takagi, N., Hayashida, H., Inaba, Y., Ogura, H., & Kunugita, N. (2018). Simple Determination of Gaseous and Particulate Compounds Generated from Heated Tobacco Products. *Chemical Research in Toxicology, 31*(7), 585-593.

University of California Santa Cruz. *USCS Genome Browser*. Retrieved Feb. 6th, 2025 from http://genome.ucsc.edu/index.html

van der Zalm, A. J., Barroso, J., Browne, P., Casey, W., Gordon, J., Henry, T. R., Kleinstreuer, N. C., Lowit, A. B., Perron, M., & Clippinger, A. J. (2022). A framework for establishing scientific confidence in new approach methodologies. *Archives of Toxicology, 96*(11), 2865-2879.

Vanni, H., Kazeros, A., Harvey, B., Ferris, B., De, B. P., Carolan, B. J., Hübner, R., & Crystal, R. G., (2009). Cigarette Smoking Induces Overexpression of a Fat Depleting Gene AZGP1 in the Human Airway Epithelium, NCBI Gene Expression Omnibus, GSE10135, https://www.ncbi.nlm.nih.gov/geo/query/acc.cgi?acc=GSE10135

Varricchi, G., Ferri, S., Pepys, J., Poto, R., Spadaro, G., Nappi, E., Paoletti, G., Virchow, J. C., Heffler, E., & Canonica, W. G. (2022). Biologics and airway remodeling in severe asthma. *Allergy, 77*(12), 3538-3552.

Vázquez-Gómez, G., Rocha-Zavaleta, L., Rodríguez-Sosa, M., Petrosyan, P., & Rubio-Lightbourn, J. (2018). Benzo[a]pyrene activates an AhR/Src/ERK axis that contributes to CYP1A1 induction and stable DNA adducts formation in lung cells. *Toxicology Letters, 289*, 54-62.

Vinken, M. (2013). The adverse outcome pathway concept: a pragmatic tool in toxicology. *Toxicology, 312*, 158-165.

Volckens, J., & Leith, D. (2003). Partitioning Theory for Respiratory Deposition of Semivolatile Aerosols. *The Annals of Occupational Hygiene, 47*(2), 157-164.

Vulto, P., Podszun, S., Meyer, P., Hermann, C., Manz, A., & Urban, G. A. (2011). Phaseguides: a paradigm shift in microfluidic priming and emptying. *Lab on a Chip, 11*(9), 1596-1602.

Wall, A., Roslin, S., Borg, B., McDermott, S., Walele, T., Nahde, T., O'Connell, G., Thompson, J., Lubberink, M., & Antoni, G. (2022). E-Cigarette Aerosol Deposition and Disposition of [11C]Nicotine Using Positron Emission Tomography: A Comparison of Nicotine Uptake in Lungs and Brain Using Two Different Nicotine Formulations. *Pharmaceuticals, 15*(3), 367.

Welte, T., & Groneberg, D. A. (2006). Asthma and COPD. *Experimental and Toxicologic Pathology, 57*, 35-40.

Widdicombe, J. H. (2002). Regulation of the depth and composition of airway surface liquid. *Journal of Anatomy, 201*(4), 313-318.

Wills-Karp, M., Luyimbazi, J., Xu, X., Schofield, B., Neben, T. Y., Karp, C. L., & Donaldson, D. D. (1998). Interleukin-13: Central Mediator of Allergic Asthma. *Science, 282*(5397),

2258-2261.

Winkler, C., & Hohlfeld, J. M. (2013). Surfactant and allergic airway inflammation. *Swiss Medical Weekly, 143*, w13818.

World Health Organization. (2024a). *Asthma*. Retrieved January 23rd, 2025 from https://www.who.int/news-room/fact-sheets/detail/asthma

World Health Organization. (2024b). *The top 10 causes of death*. Retrieved January 23rd, 2025 from https://www.who.int/news-room/fact-sheets/detail/the-top-10-causes-of-death

Wright, J. L., Cosio, M., & Churg, A. (2008). Animal models of chronic obstructive pulmonary disease. *American Journal of Physiology-Lung Cellular and Molecular Physiology, 295*(1), L1-L15.

Wu, J., Gao, Y., Li, D., & Gao, N. (2022). Emission and Gas/Particle Partitioning Characteristics of Nicotine in Aerosols for Electronic Cigarettes. *Chemical Research in Toxicology, 35*(5), 890-897.

Wu, Q., Liu, J., Wang, X., Feng, L., Wu, J., Zhu, X., Wen, W., & Gong, X. (2020). Organ-on-a-chip: recent breakthroughs and future prospects. *BioMedical Engineering OnLine, 19*(1), 9.

Wu, Z., Jiang, J., Lischka, F. W., & Zhao, K. (2024). Is the mouse nose a miniature version of a rat nose? A computational comparative study. *Computer Methods and Programs in Biomedicine, 254*, 108282.

Yeh, H.-C., & Schum, G. M. (1980). Models of human lung airways and their application to inhaled particle deposition. *Bulletin of Mathematical Biology, 42*(3), 20.

Yoshida, T., & Tuder, R. M. (2007). Pathobiology of Cigarette Smoke-Induced Chronic Obstructive Pulmonary Disease. *Physiological Reviews, 87*(3), 1047-1082.

Yuki, D., Sakaguchi, C., Kikuchi, A., & Futamura, Y. (2017). Pharmacokinetics of nicotine following the controlled use of a prototype novel tobacco vapor product. *Regulatory Toxicology and Pharmacology, 87*, 30-35.

Zhen, G., Park, S. W., Nguyenvu, L. T., Rodriguez, M. W., Barbeau, R., Paquet, A. C., & Erle,

D. J. (2007). IL-13 and epidermal growth factor receptor have critical but distinct roles in epithelial cell mucin production. *American Journal of Respiratory Cell and Molecular Biology, 36*(2), 244-253.

Zou, H., & Hastie, T. (2005). Regularization and variable selection via the elastic net. *Journal of the royal statistical society: series B (statistical methodology), 67*(2), 301-320.

Zurawski, S. M., Chomarat, P., Djossou, O., Bidaud, C., McKenzie, A. N. J., Miossec, P., Banchereau, J., & Zurawski, G. (1995). The Primary Binding Subunit of the Human Interleukin-4 Receptor Is Also a Component of the Interleukin-13 Receptor &#x2217. *Journal of Biological Chemistry, 270*(23), 13869-13878.

Zwicker, D., Ostilla-Mónico, R., Lieberman, D. E., & Brenner, M. P. (2018). Physical and geometric constraints shape the labyrinth-like nasal cavity. *Proceedings of the National Academy of Sciences, 115*(12), 2936-2941.

Japanese abstract

呼吸器が外部からの刺激に曝されると様々な防御機構が働く。急性期の反応は防御機構として機能するが、炎症が慢性的に続くと組織やその機能を障害し、慢性閉塞性肺疾患（COPD）や喘息などの重篤な疾患を引き起こす可能性がある。喫煙は COPD のリスク要因の一つとされているが、慢性的なヒト疾病のリスクを評価できる実験系は確立されていない。吸入物質の慢性毒性はこれまで動物試験によってそのリスクが評価されてきた。しかし、動物試験はヒト外挿性の課題に加え、倫理的な観点からも削減が求められている。近年、動物試験の代替として、*in vitro* データを計算モデルを用いて統合することで生体の反応を予測する *in vitro* to *in vivo* extrapolation（IVIVE）というアプローチが採用されている。喫煙を対象に IVIVE を適用した慢性呼吸器疾患のリスク評価を行うため、*in vitro* および *in silico* モデルを開発・改作した。

AOP（Adverse outcome pathway）は有害事象（Adverse outcome; AO）を引き起こす様々な反応のうち、重要な機構を選び出し、その連関を明らかにしたものである。さらに、IVIVE の取り組みの一環として、AOP を基に計算モデルを作成し、定量的リスク評価を行う定量的 AOP（qAOP）が開発され始めている。しかし、慢性疾患に適用できる qAOP モデルは確立されていない。本研究では Bayesian network（BN）解析を使用して慢性疾患に対する qAOP の構想を検証した。急性期および慢性期の反応から構成される AOP を仮定し、各事象における仮想データを生成した。このデータを BN に組み込み、用量反応相関および各反応同士の相関を解析した。また、AO 推定への寄与が低い反応は排除して AOP を更新し、慢性疾患のリスクを予測するモデルを構築した。

呼吸器での慢性炎症には呼吸器組織の細胞だけでなく免疫細胞の応答も関与する。慢性炎症性呼吸器疾患の症状には呼吸機能の低下があり、これは気管支上皮の肥厚による気道狭窄が一因である。炎症による上皮の肥厚はこれまで免疫細胞が放出するインターロイキン（IL）-13 をはじめとしたサイトカインにより引き起こされ、その反応強度はサイトカイン量に依存すると考えられてきた。しかし、たばこ煙抽出物を曝露した気管支上皮細胞で、IL-13 の機能的受容体である IL-13 receptor（R）α1 の発現が上昇していることが分かった。さらに、たばこ煙中成分であるベンゾ(a)ピレンが IL-13Rα1 の発現を上昇させ、この反応が芳香族炭化水素受容体（AhR）を介して起こることが示唆された。この経路の発見は気管支上皮細胞の肥厚に関する新たな知見となり、IL-13 を添加する

ことで免疫細胞と共培養せずに、免疫細胞の影響を含むモデルを提唱したと言える。

慢性炎症性呼吸器疾患では気管支の狭窄により呼吸機能の低下が引き起こされるが、従来の水平細胞培養ではこの状態を模倣することができない。Organ-on-a-Chip は特別な筐体上で細胞を培養することで、このような再現困難な生体内環境を体外で再現する培養方法である。そこで、気管支上皮の肥厚による気道狭窄を再現するため、Bronchus-on-a-Chip（BoC）を開発した。BoC 上では気道上皮細胞が管腔状に生育し、サイトカインの曝露により気道狭窄に寄与する杯細胞の過形成も確認された。また、BoC は高スループット性を持ち、IVIVE に必要とされるデータ取得にも対応できる。

慢性炎症の IVIVE リスク評価のためには、各組織での曝露量を測定する必要があるが、たばこ煙の呼吸器局所の沈着量を測定する手法は存在しない。そこで、空気中の粒子の呼吸器内での挙動を予測する Multiple-Path Particle Dosimetry（MPPD）モデルに喫煙特有のエアロゾル動態を加味した計算式を組み込む改変を行った。改変した MPPD モデルで予測した結果は一般的な空気力学に基づいて説明され、たばこエアロゾル沈着量も計算可能であった。この改変 MPPD モデルにより、*in vitro* 試験の曝露容量をヒトに外挿する際に重要となるたばこ煙の推定曝露量が計算可能となった。

開発したモデルはいずれも喫煙に関連する慢性炎症のメカニズムを踏まえた評価に使用されるものである。さらに、これらのモデルは喫煙を標的にしたリスク評価のみでなく、呼吸器炎症の研究、様々な慢性疾患のリスク評価にも応用可能である。また、qAOP モデルは仮想データに基づいており、*in vitro* で取得したデータを入力することができれば実際の AO が予測可能となる。慢性疾患の AO 予測では、分子レベルの急性期応答と組織レベルの慢性期応答のデータを入力することでその予測精度が向上する。今回開発した呼吸器沈着モデル、模擬共培養モデル、BoC はそれぞれに IVIVE に向けたデータ取得に活用でき、さらに、たばこ煙の呼吸器内動態から免疫細胞の影響、気道狭窄を取り入れた慢性炎症性疾患のリスク評価 qAOP の樹立も期待される。

Supplementary Materials

Supplementary Material 1.1. Algorithm of each calculation and R packages.

We used freely downloadable software package called bnlearn to perform all our analysis. We used it mostly for parameter learning, and re-sampling using logic sampling algorithms. Bnlearn allows user to also specify pre-defined parameter values using a function called custom.fit. We used that function when needed. Below, we share the pseudo-codes used for our work. All the codes were written in R version 4.04. We refer readers to section 2.1 of the main text for notation convention

---

Algorithm BN update: Train GBN using posterior from previous exposure and re-sample

---

$\mathcal{D} \leftarrow \emptyset$
$for\ n = 1,..,.,N$
  $for\ d \in D$
    $for\ e = 1,.,.,E$
      Load $\boldsymbol{\mu}^{(n,e,d)}, \mathbb{O}_{|V|\times|V|}^{(n,e,d)}$ from the saved library
      Draw κ samples $\mathbb{X}_{\kappa\times|V|}{}^{(n,e,d)} \sim \mathcal{MN}\left(\boldsymbol{\mu}^{(n,e,d)}, \mathbb{O}_{|V|\times|V|}^{(n,e,d)}\right)$, and mean center the data
      $for\ v \in V_{\neq rn} \subset V$ (where $V_{\neq rn}$ denotes set of all nodes except the root nodes)
        Calculate $\widehat{\boldsymbol{\beta}}_{\boldsymbol{OLS}}$ & $\hat{\sigma}^2$ (see section 2.6 main text)
        If $e = 1$

$$\boldsymbol{\beta}^{(e)}{}_{pos} = \widehat{\boldsymbol{\beta}}_{\boldsymbol{OLS}}$$

$$\mathbb{V}^{(e)}{}_{pos} = \left(\mathbb{X}_{\kappa\times\Pi_v}{}^{T}\mathbb{X}_{\kappa\times\Pi_v}\right)^{-\mathbf{1}}\hat{\sigma}^2$$

        else

$$\boldsymbol{\beta}^{(e)}{}_{pr}, \mathbb{V}^{(e)}{}_{pr} = \widehat{\boldsymbol{\beta}}^{(e-1)}{}_{pos}, \mathbb{V}^{(e-1)}{}_{pos}$$ (see section 2.6 main text)

Store posteriors in a list
$for\ n = 1,..,.,N$
  $for\ d \in D$
    $for\ e = 1,.,.,E$
      Topologically order node based on **Fig. 1 main text**
      Draw $\mathcal{R}$ replicates for the root nodes $\in V_{rn} \subset V$; $\mathbb{X}_{\mathcal{R}\times|V_{rn}|}{}^{(n,e,d)} \sim \mathcal{MN}\left(\boldsymbol{\mu}_{|\boldsymbol{V_{rn}}|}{}^{(n,e,d)}, \mathbb{O}_{|\boldsymbol{V_{rn}}|\times|\boldsymbol{V_{rn}}|}^{(n,e,d)}\right)$ and mean center it.

Using GBN shown in **Fig. 1 main text** and topological ordering, predict $\boldsymbol{x}^{(v)}{}_{pred} \sim P\left(\boldsymbol{x}^{(v)}{}_{pred} | \mathbb{X}^{(n,e,d)}_{\mathcal{R}\times|\Pi_v|}, \sigma^2\mathbb{I}\right)$ for all downstream nodes (see section 2.6)

$\mathcal{D} \leftarrow$ append $(\mathcal{D}, \boldsymbol{x}^{(v)}{}_{pred} + \mu^{(n,e,d,v)}\mathbb{1})$

Output $\mathcal{D}$ in desired format $\mathbb{X}_{out}$

Algorithm: Bayesian Network analysis

$for\ e = 1, 2, ., E$

$GBN^e = bn.fit\left(Fig.1, \mathbb{X}^{(e)}\right)$ (uses linear regression to learn parameters)

$for\ v\ in\ KEs \subset V$

Cutoff_arr = $seq\left(from = mean\left(\boldsymbol{x}^{(e,v)}\right), to = max\left(\boldsymbol{x}^{(e,v)}\right), by = bw\right)$

$for\ d \in D$

Calculate $\xi_d^{(v,e)} = P(v > \log_{10} 2\,|d \in [d \pm \varepsilon])$, using logic sampling ($\varepsilon$ is the tolerance)

$for\ c\ in$ Cutoff_arr

Calculate $Surf_{c,d}^{(v,e)} = P(v > c|d \in [d \pm \varepsilon])$ using logic sampling.

Calculate $VUS^{(v,e)} = \iint Surf_{c,d}^{(v)}$

Return $VUS^{(v,e)}$, $\boldsymbol{\xi}^{(v,e)}$

Algorithm: Dynamic Bayesian Model for probability of AO based on activation of KEs upstream KEs

---

Inputs:

- Inference Node=AO
- Start point = e_s
- Number of time slices τ

If $e_s < 1$ or $e_s + \tau > E$ print("Mistake") & quit

$Exp.seq \leftarrow seq(from = e_s + \tau, to = e_s + 1, by = -1)$

$C.nd \leftarrow$ AO

$r.nd \leftarrow$ root.nodes (DAG in Fig. 1 main text)

$r.nd.visit.time \leftarrow \emptyset$ (a list or dictionary with nodes as keys)

$for\ e\ in\ Exp.seq$

$tmp \leftarrow \emptyset$

$if(C.nd \cap r.nd \neq \emptyset)$

$for\ v\ in\ C.nd \cap r.nd$

$r.nd.visit.time[v] \leftarrow append(r.nd.visit.time[v], e)$

$for\ v\ in\ (C.nd - C.nd \cap r.nd)$

tmp $\leftarrow$ append(tmp, Π_v)

If $|\Pi_v| > 1$

fit ridge model $cv.glmnet\left(y = \boldsymbol{x}^{(e,v)}, x = \mathbb{X}^{(e-1,\Pi_v)}, \alpha = 0, n.flds = LOOCV\right)$

else

fit linear regression $\boldsymbol{x}^{(e,v)} = \beta_0\mathbb{1} + \beta_1\boldsymbol{x}^{(e-1,v)} + \boldsymbol{\varepsilon} \sim N(0, \sigma^2\mathbb{I})$ with LOOCV using caret package

$C.nd \leftarrow$ unique(tmp)

If $(C.nd = r.nd)$ break

$e^* = e - 1$

$for\ v\ in\ C.nd$

$\boldsymbol{x}^{(e^*,v)} \sim \beta_0 + \varepsilon \sim N(0, \sigma^2)$, where $\beta_0 = mean\left(\boldsymbol{x}^{(e^*,v)}\right)$ & $\sigma = sd\left(\boldsymbol{x}^{(e^*,v)}\right)$

If $(r.nd.visit.time \neq \emptyset)$

$for\ v\ in\ r.nd.visit.time$

$for\ e^*\ in\ r.nd.visit.time[v]$

$\boldsymbol{x}^{(e^*,v)} \sim \beta_0 + \varepsilon \sim N(0, \sigma^2)$, where $\beta_0 = mean\left(\boldsymbol{x}^{(e^*,v)}\right)$ & $\sigma = sd\left(\boldsymbol{x}^{(e^*,v)}\right)$

Customize BN using the fitted parameters and custom.fit function in bnlearn

Return customized BN

Algorithm: Pruning based on WoE of DBNs (changes from the previous algorithm are highlighted)

Inputs:

- Inference Node=AO
- Start point = e_s
- Number of time slices τ

If $e_s < 1$ or $e_s + \tau > E$ print("Mistake") & quit

$Exp.seq \leftarrow seq(from = e_s + \tau, to = e_s + 1, by = -1)$

$C.nd \leftarrow$ inference.node

$r.nd \leftarrow$ root.nodes (DAG in Fig. 1 main text)

$r.nd.visit.time \leftarrow \emptyset$

$for\ e\ in\ Exp.seq$

  $tmp \leftarrow \emptyset$

  $if(C.nd \cap r.nd \neq \emptyset)$

    $for\ v\ in\ C.nd \cap r.nd$

      $r.nd.visit.time[v] \leftarrow append(r.nd.visit.time[v], e)$

  $for\ v\ in\ (C.nd - C.nd \cap r.nd)$

    tmp $\leftarrow$ append(tmp, Π_v)

    If $|\Pi_v| > 1$

      fit lasso model $cv.glmnet\left(y = \boldsymbol{x}^{(e,v)}, x = \mathbb{X}^{(e-1,\Pi_v)}, \alpha = 1, n.flds = LOOCV\right)$

      only include predictors $\Pi_v' \subset \Pi_v$ whose lasso coefficients are non-zero

    else

      fit linear regression $\boldsymbol{x}^{(e,v)} = \beta_0\mathbb{1} + \beta_1\boldsymbol{x}^{(e-1,v)} + \boldsymbol{\varepsilon} \sim N(0, \sigma^2\mathbb{I})$ with LOOCV using caret package

      if p.value$(\beta_1) > 0.05$

        set $\beta_1 = 0$

  $C.nd \leftarrow$ unique(tmp)

  If $(C.nd = r.nd)$ break

$e^* = e - 1$

$for\ v\ in\ C.nd$

  $\boldsymbol{x}^{(e^*,v)} \sim \beta_0 + \varepsilon \sim N(0, \sigma^2)$, where $\beta_0 = mean\left(\boldsymbol{x}^{(e^*,v)}\right)$ & $\sigma = sd\left(\boldsymbol{x}^{(e^*,v)}\right)$

If $(r.nd.visit.time \neq \emptyset)$

  $for\ v\ in\ r.nd.visit.time$

    $for\ e^*\ in\ r.nd.visit.time[v]$

      $\boldsymbol{x}^{(e^*,v)} \sim \beta_0 + \varepsilon \sim N(0, \sigma^2)$, where $\beta_0 = mean\left(\boldsymbol{x}^{(e^*,v)}\right)$ & $\sigma = sd\left(\boldsymbol{x}^{(e^*,v)}\right)$

Customize BN using the fitted parameters and custom.fit function in bnlearn

Return customized BN

Supplementary Material 1.2. Donor means and standard deviations.

By dose

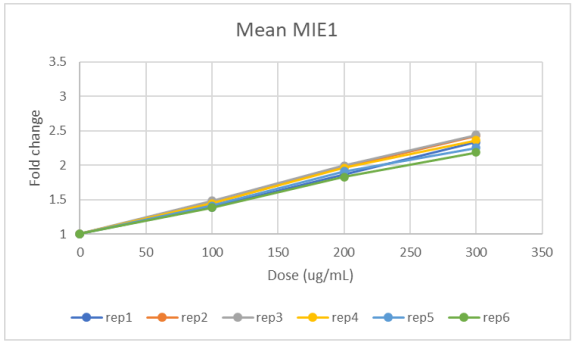

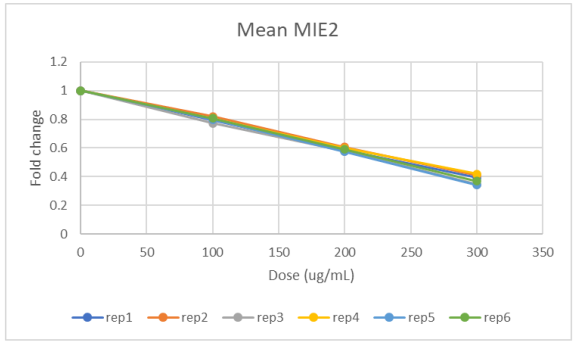

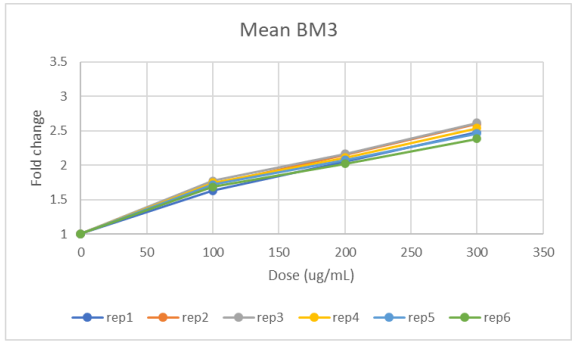

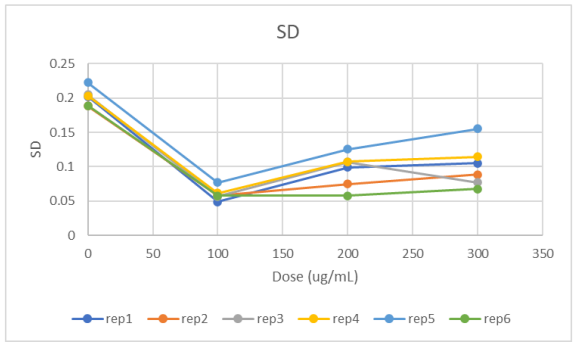

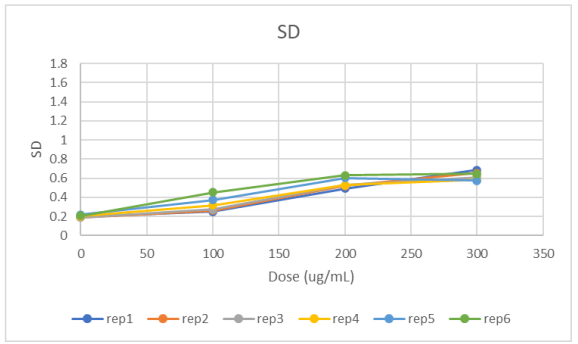

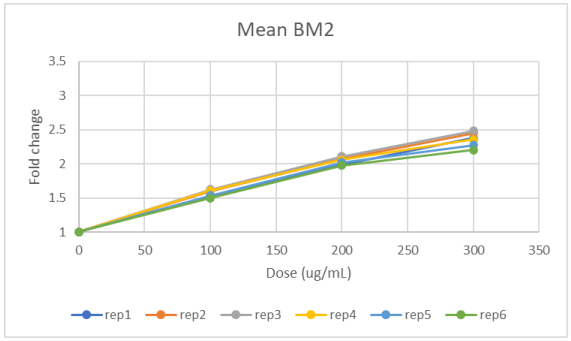
Mean BM2
Fold change
Dose (ug/mL)
rep1 rep2 rep3 rep4 rep5 rep6

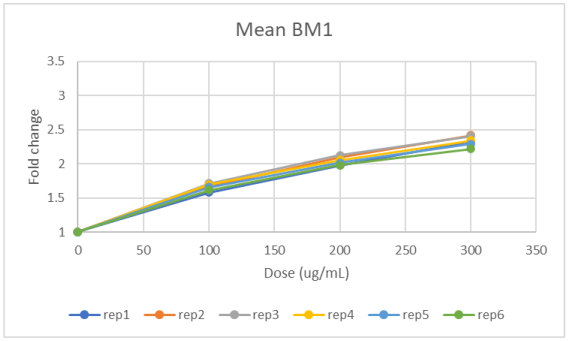
Mean BM1
Fold change
Dose (ug/mL)
rep1 rep2 rep3 rep4 rep5 rep6

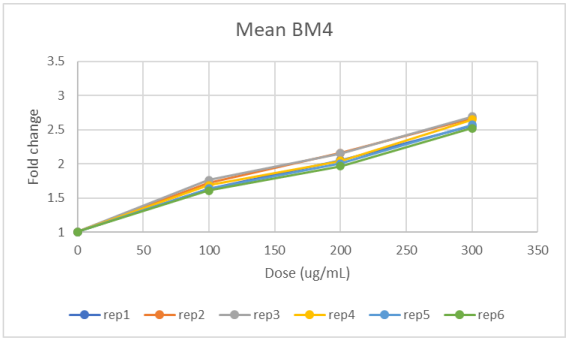
Mean BM4
Fold change
Dose (ug/mL)
rep1 rep2 rep3 rep4 rep5 rep6

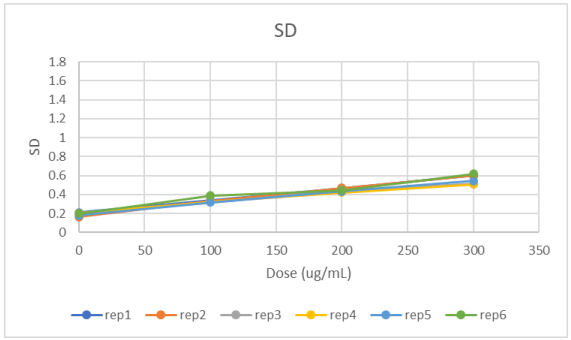
SD
SD
Dose (ug/mL)
rep1 rep2 rep3 rep4 rep5 rep6

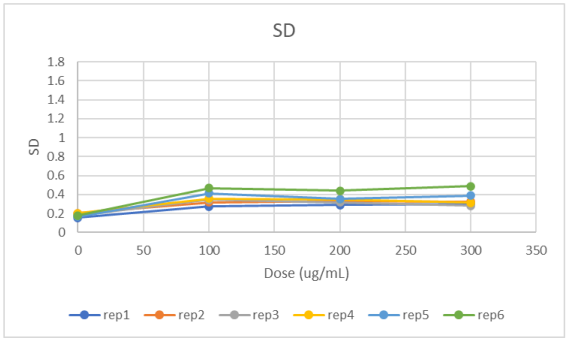
SD
SD
Dose (ug/mL)
rep1 rep2 rep3 rep4 rep5 rep6

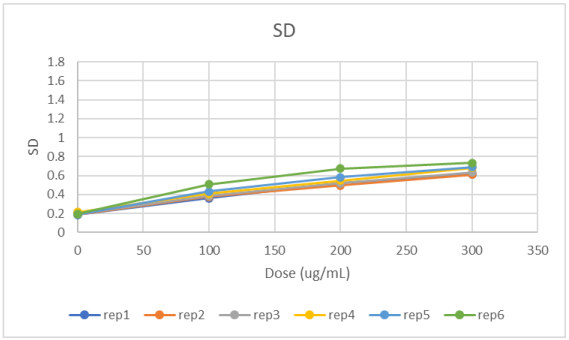
SD
SD
Dose (ug/mL)
rep1 rep2 rep3 rep4 rep5 rep6

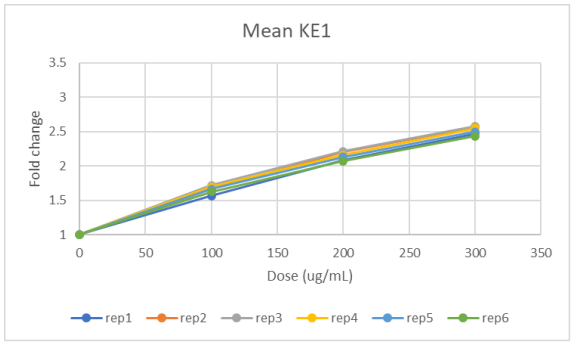
Mean KE1
Fold change
Dose (ug/mL)
rep1 rep2 rep3 rep4 rep5 rep6

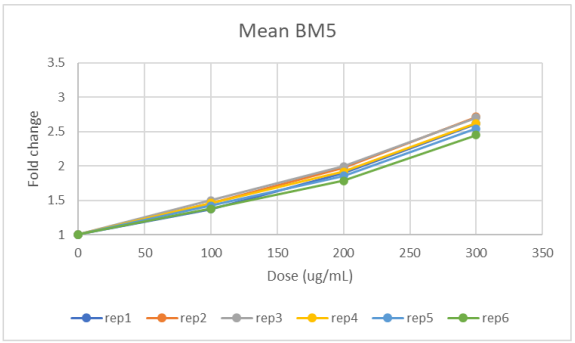
Mean BM5
Fold change
Dose (ug/mL)
rep1 rep2 rep3 rep4 rep5 rep6

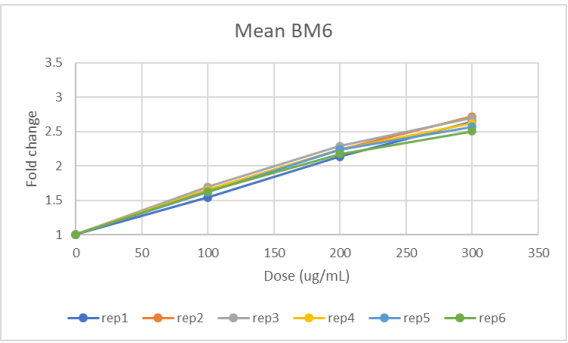
Mean BM6
Fold change
Dose (ug/mL)
rep1 rep2 rep3 rep4 rep5 rep6

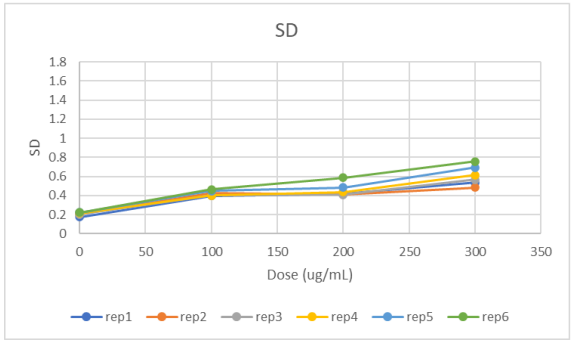
SD
SD
Dose (ug/mL)
rep1 rep2 rep3 rep4 rep5 rep6

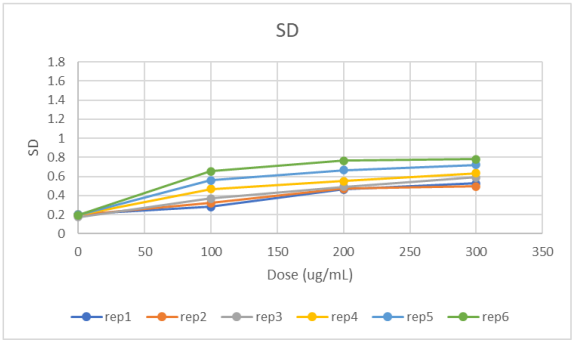
SD
SD
Dose (ug/mL)
rep1 rep2 rep3 rep4 rep5 rep6

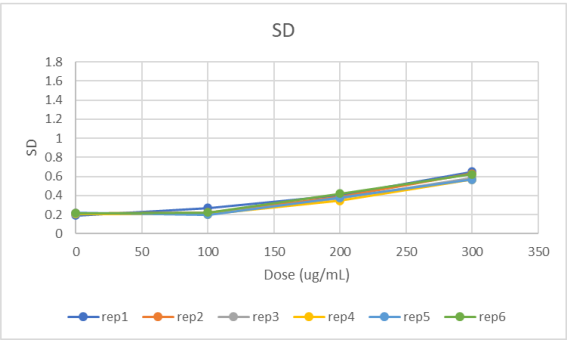
SD
SD
Dose (ug/mL)
rep1 rep2 rep3 rep4 rep5 rep6

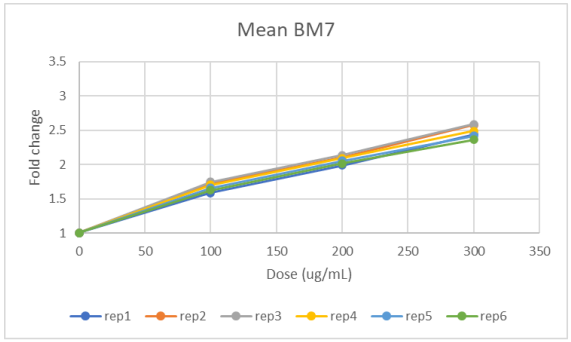
Mean BM7
Fold change
Dose (ug/mL)
rep1 rep2 rep3 rep4 rep5 rep6

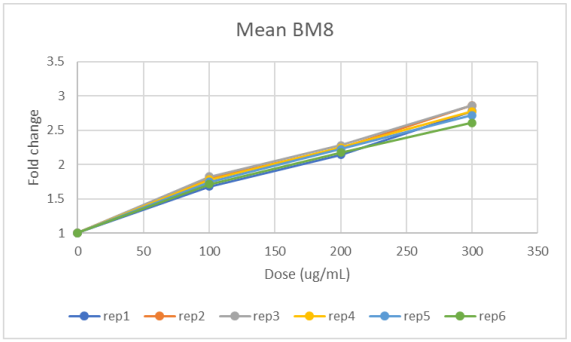
Mean BM8
Fold change
Dose (ug/mL)
rep1 rep2 rep3 rep4 rep5 rep6

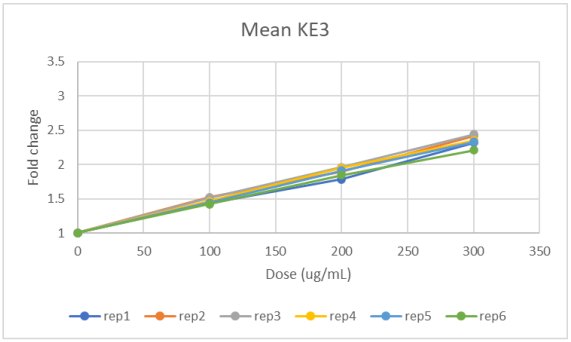
Mean KE3
Fold change
Dose (ug/mL)
rep1 rep2 rep3 rep4 rep5 rep6


SD
SD
Dose (ug/mL)
rep1 rep2 rep3 rep4 rep5 rep6

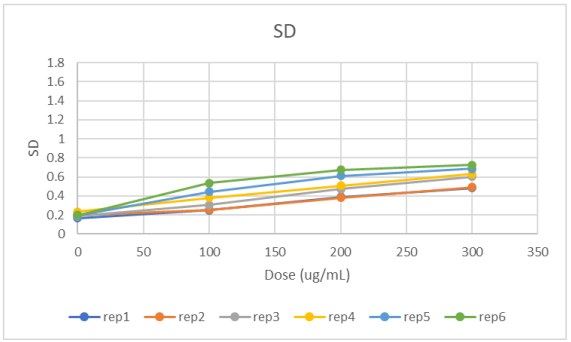
SD
SD
Dose (ug/mL)
rep1 rep2 rep3 rep4 rep5 rep6

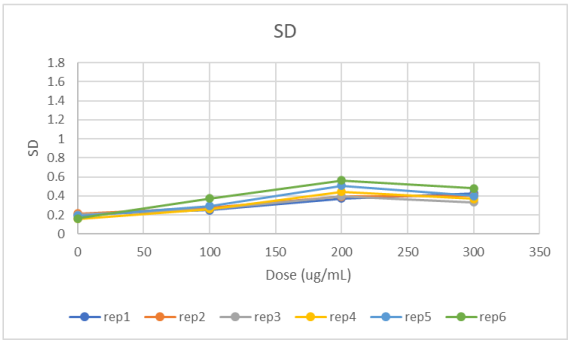
SD
SD
Dose (ug/mL)
rep1 rep2 rep3 rep4 rep5 rep6

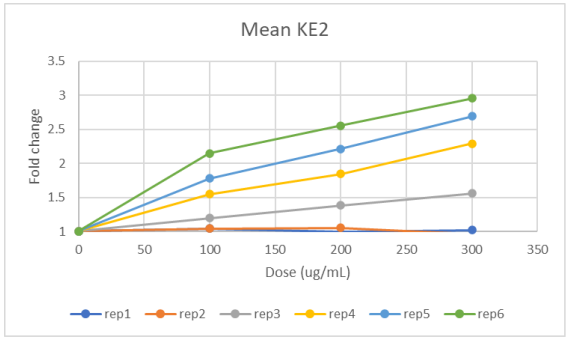
Mean KE2
Fold change
Dose (ug/mL)
rep1 rep2 rep3 rep4 rep5 rep6

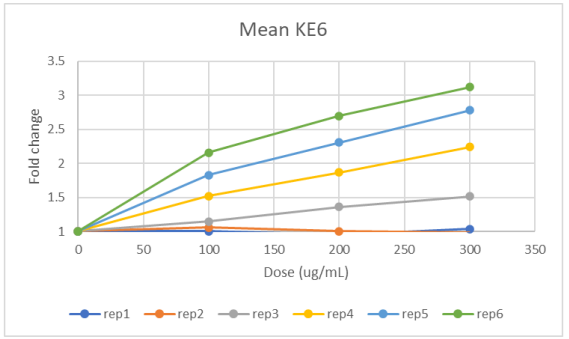
Mean KE6
Fold change
Dose (ug/mL)
rep1 rep2 rep3 rep4 rep5 rep6

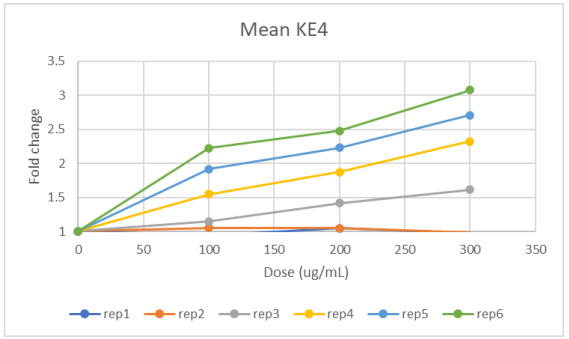
Mean KE4
Fold change
Dose (ug/mL)
rep1 rep2 rep3 rep4 rep5 rep6

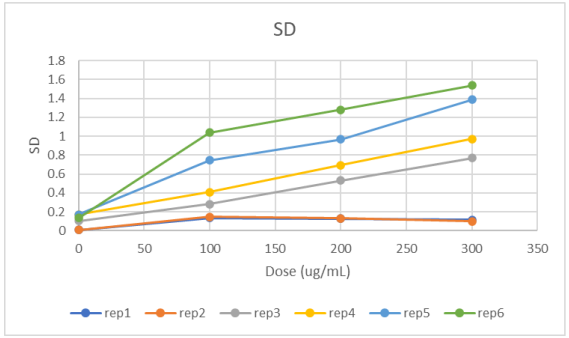
SD
SD
Dose (ug/mL)
rep1 rep2 rep3 rep4 rep5 rep6

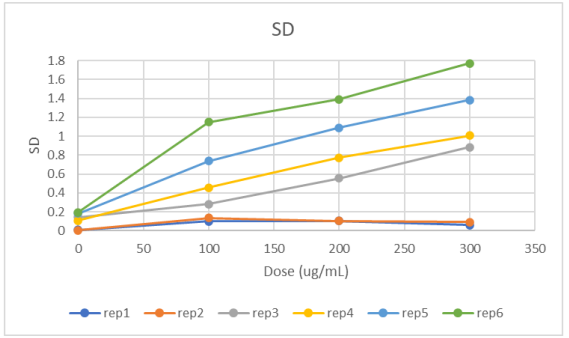
SD
SD
Dose (ug/mL)
rep1 rep2 rep3 rep4 rep5 rep6

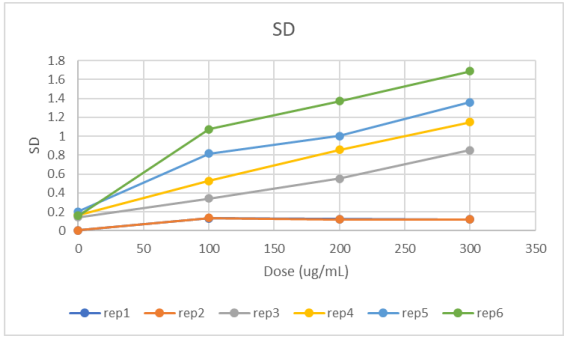
SD
SD
Dose (ug/mL)
rep1 rep2 rep3 rep4 rep5 rep6

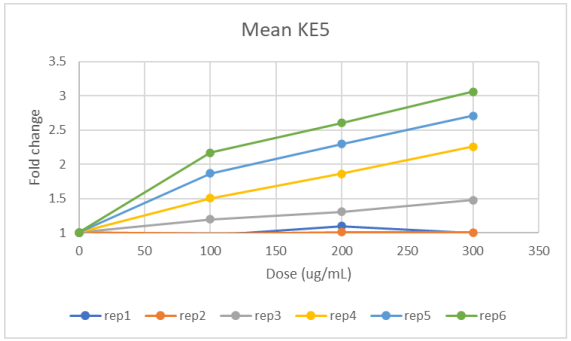
Mean KE5
Fold change
Dose (ug/mL)
rep1
rep2
rep3
rep4
rep5
rep6

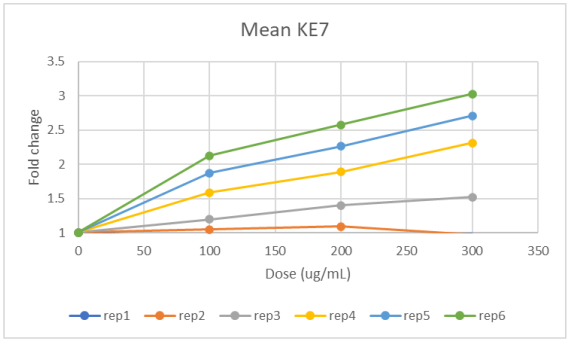
Mean KE7
Fold change
Dose (ug/mL)
rep1
rep2
rep3
rep4
rep5
rep6

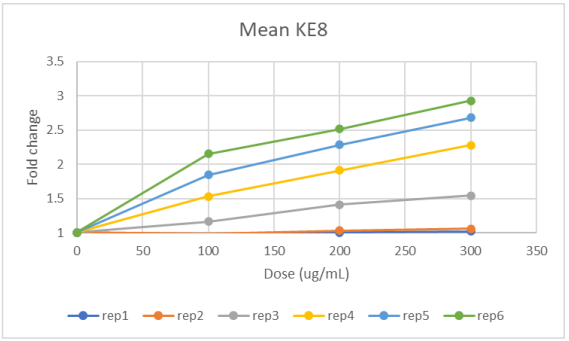
Mean KE8
Fold change
Dose (ug/mL)
rep1
rep2
rep3
rep4
rep5
rep6

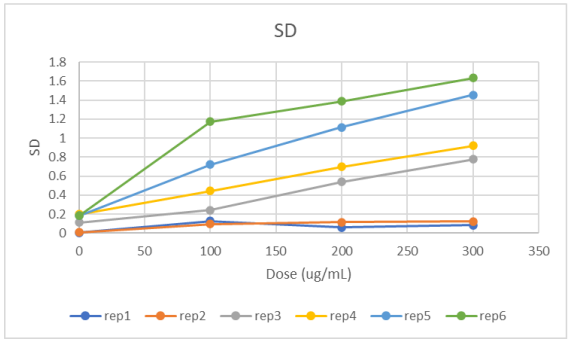
SD
Dose (ug/mL)
rep1
rep2
rep3
rep4
rep5
rep6

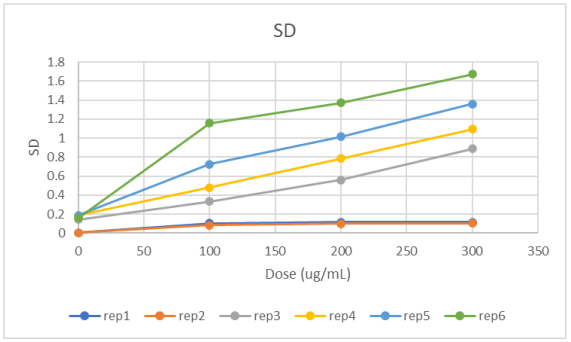
SD
Dose (ug/mL)
rep1
rep2
rep3
rep4
rep5
rep6

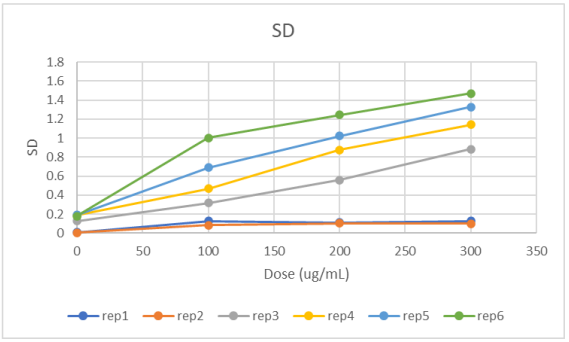
SD
Dose (ug/mL)
rep1
rep2
rep3
rep4
rep5
rep6

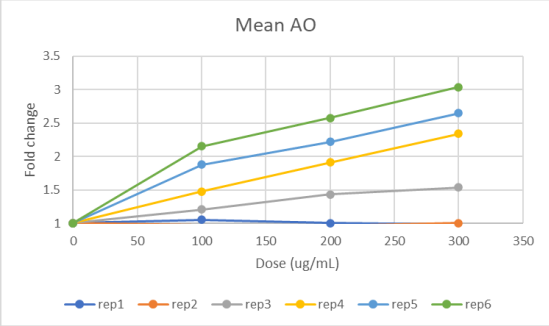
Mean AO
Fold change
3.5
3
2.5
2
1.5
1
0
50
100
150
200
250
300
350
Dose (ug/mL)
rep1
rep2
rep3
rep4
rep5
rep6

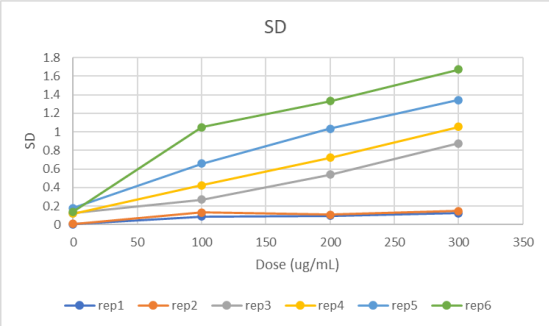
SD
SD
1.8
1.6
1.4
1.2
1
0.8
0.6
0.4
0.2
0
0
50
100
150
200
250
300
350
Dose (ug/mL)
rep1
rep2
rep3
rep4
rep5
rep6

By exposure rep.

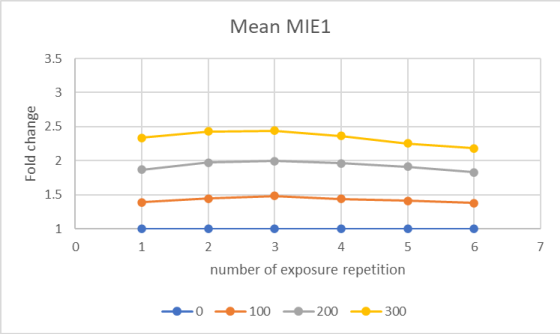

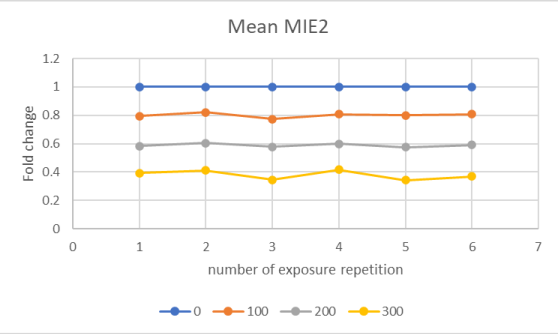

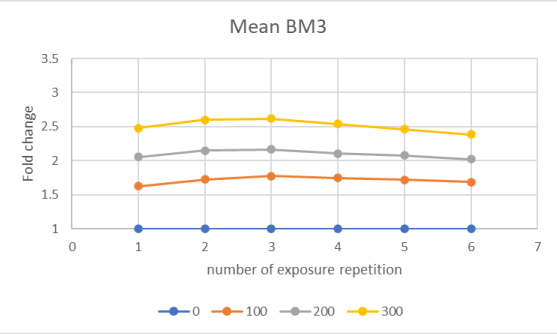

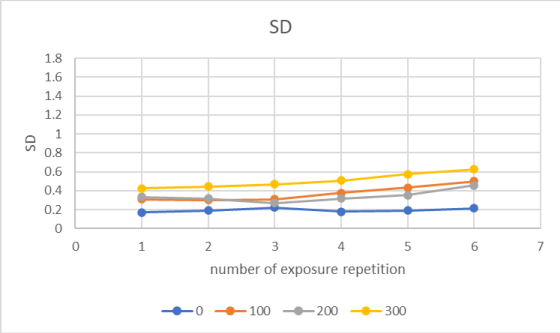

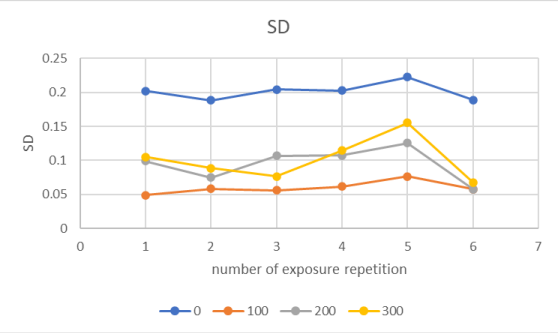

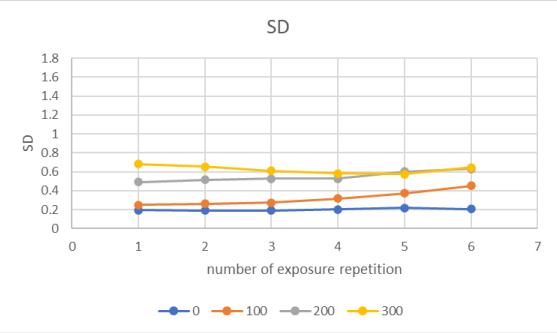

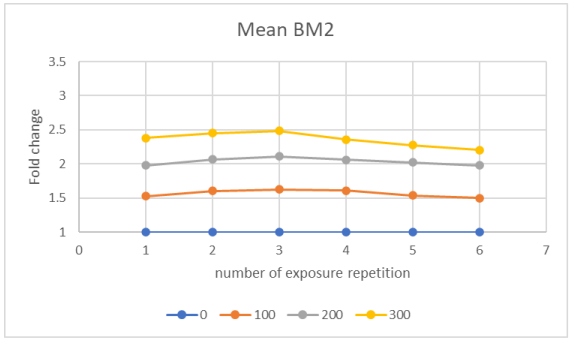
Mean BM2
Fold change
number of exposure repetition
0
100
200
300

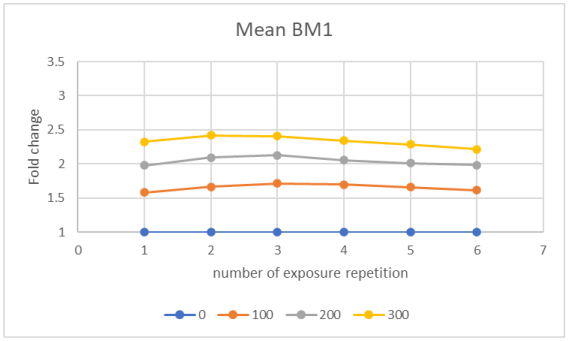
Mean BM1
Fold change
number of exposure repetition
0
100
200
300

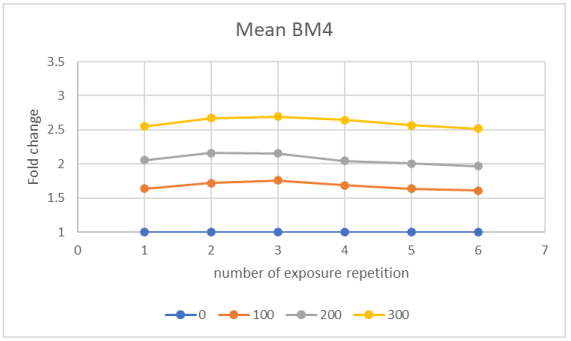
Mean BM4
Fold change
number of exposure repetition
0
100
200
300

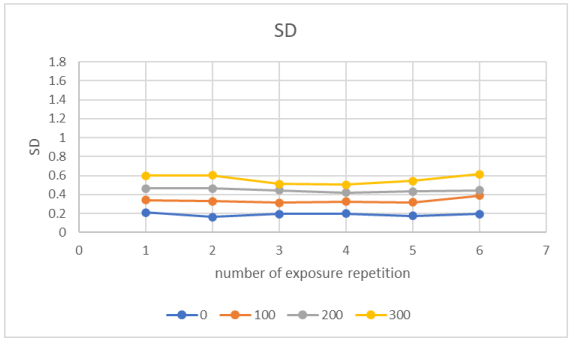
SD
number of exposure repetition
0
100
200
300

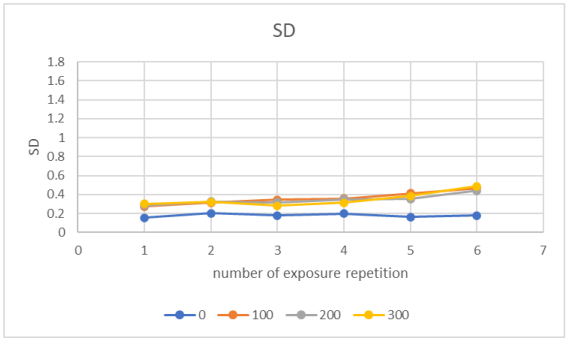
SD
number of exposure repetition
0
100
200
300

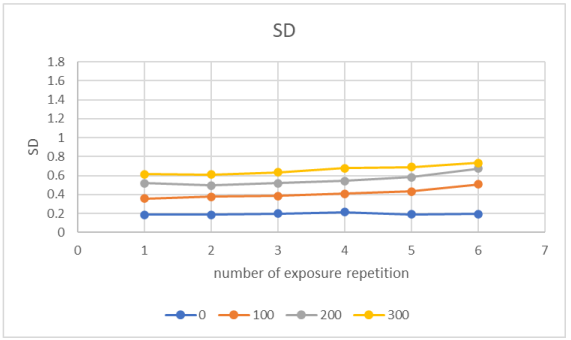
SD
number of exposure repetition
0
100
200
300

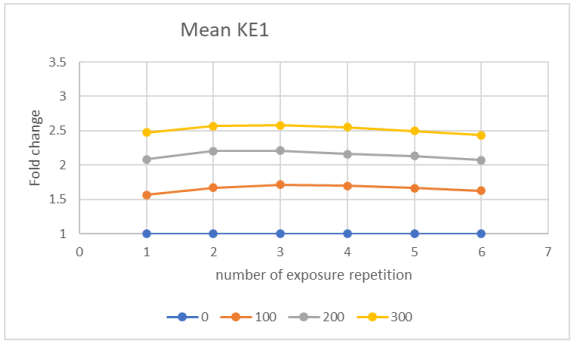
Mean KE1
Fold change
number of exposure repetition
0
100
200
300

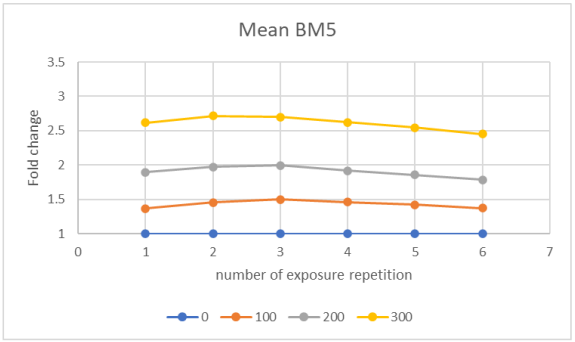
Mean BM5
Fold change
number of exposure repetition
0
100
200
300

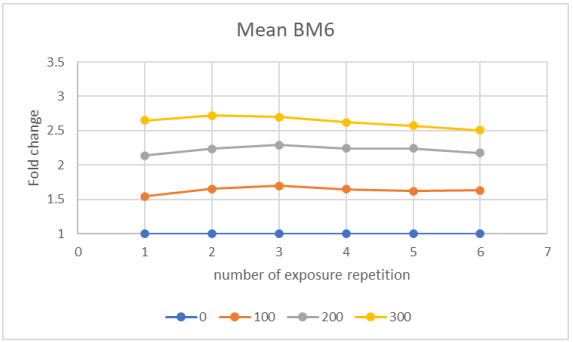
Mean BM6
Fold change
number of exposure repetition
0
100
200
300

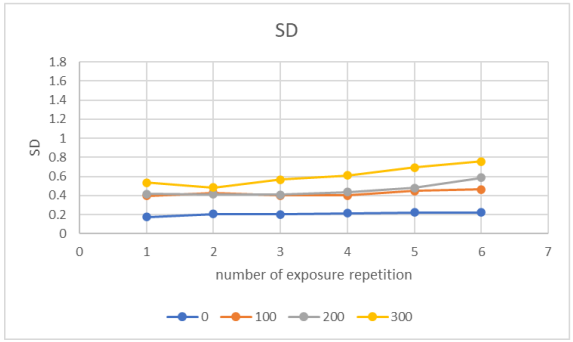
SD
SD
number of exposure repetition
0
100
200
300

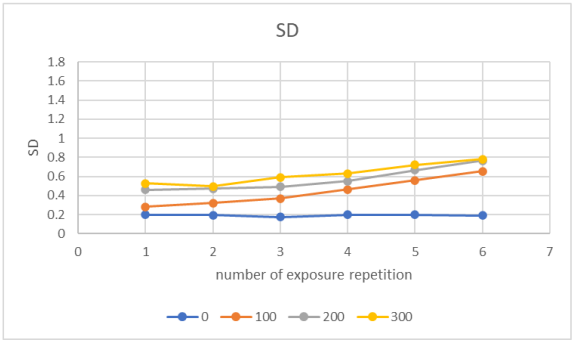
SD
SD
number of exposure repetition
0
100
200
300

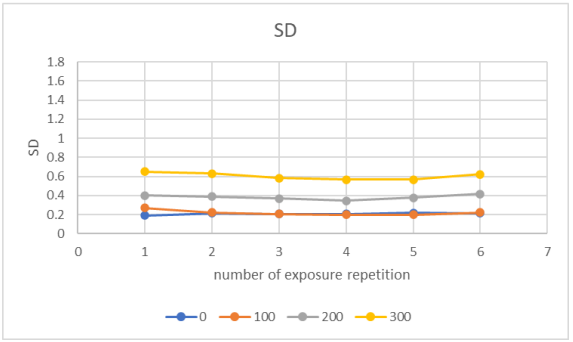
SD
SD
number of exposure repetition
0
100
200
300

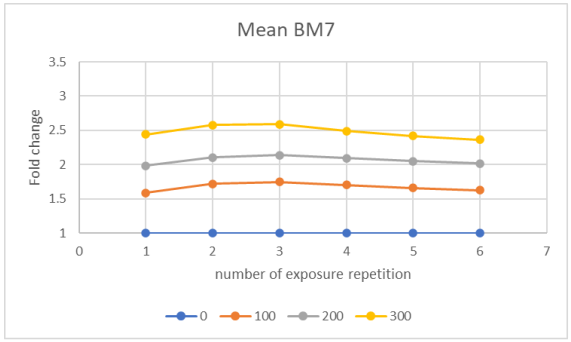
Mean BM7
Fold change
number of exposure repetition
0
100
200
300

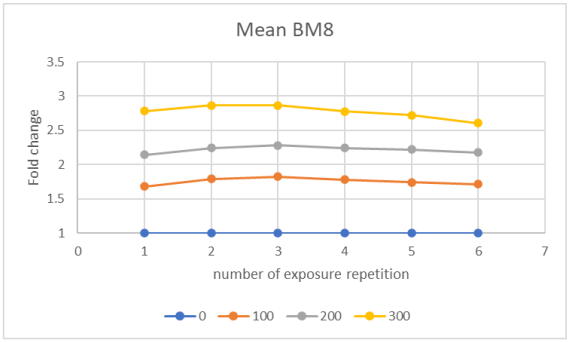
Mean BM8
Fold change
number of exposure repetition
0
100
200
300

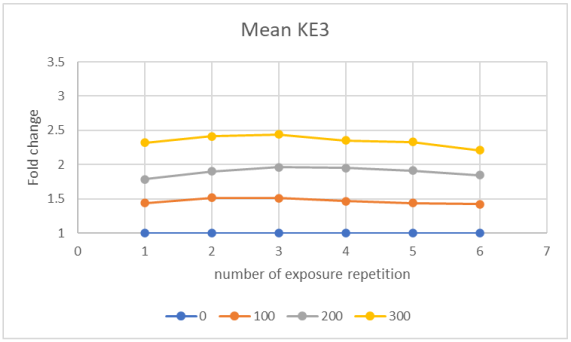
Mean KE3
Fold change
number of exposure repetition
0
100
200
300

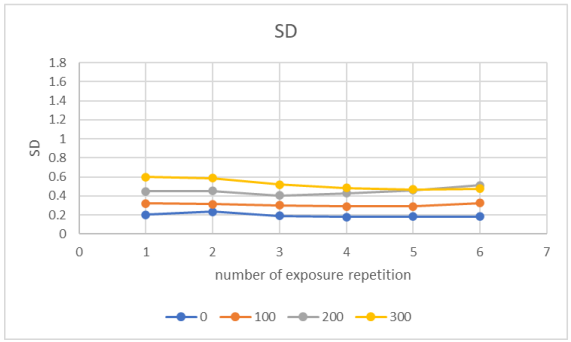
SD
SD
number of exposure repetition
0
100
200
300

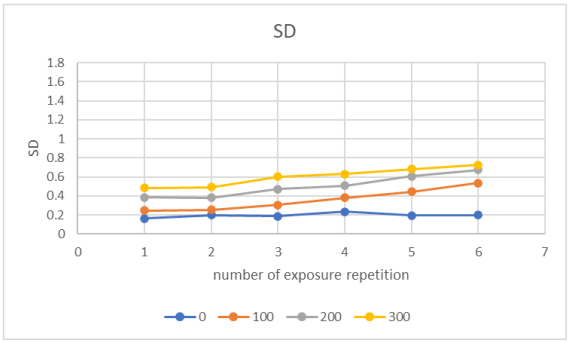
SD
SD
number of exposure repetition
0
100
200
300

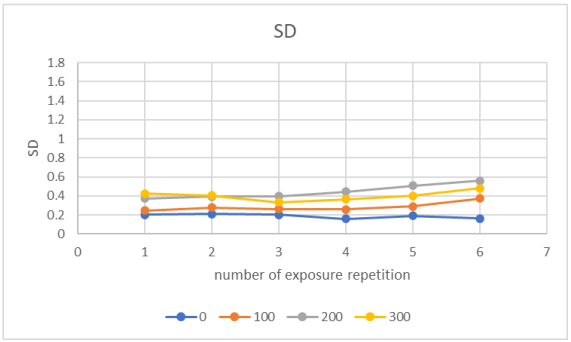
SD
SD
number of exposure repetition
0
100
200
300

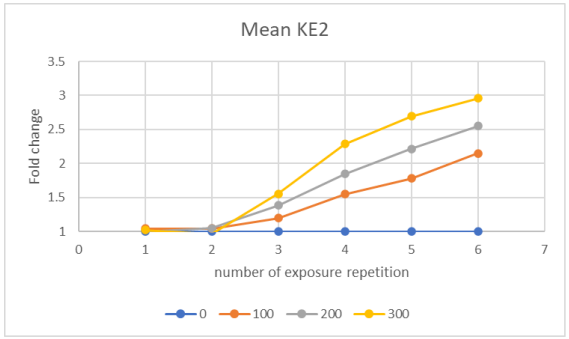
Mean KE2
Fold change
number of exposure repetition
0
100
200
300

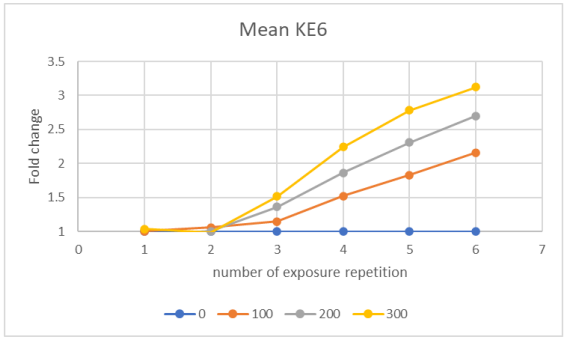
Mean KE6
Fold change
number of exposure repetition
0
100
200
300

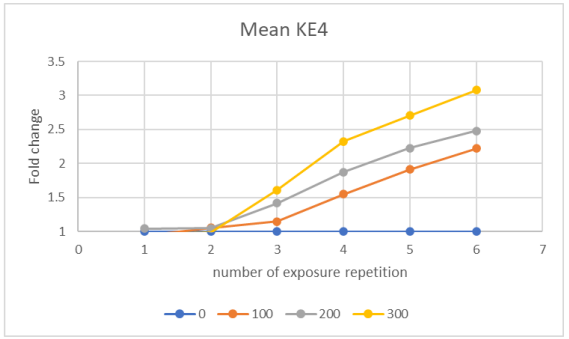
Mean KE4
Fold change
number of exposure repetition
0
100
200
300

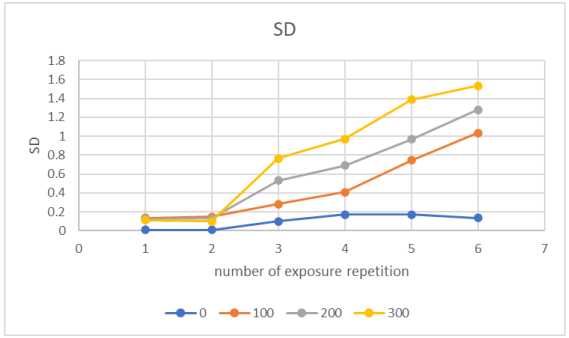
SD
number of exposure repetition
0
100
200
300


SD
number of exposure repetition
0
100
200
300


SD
number of exposure repetition
0
100
200
300

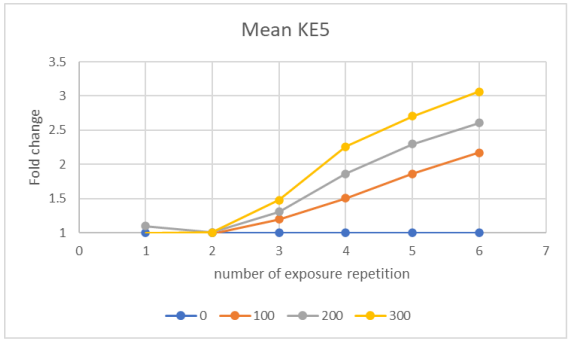
Mean KE5
Fold change
number of exposure repetition
0
100
200
300

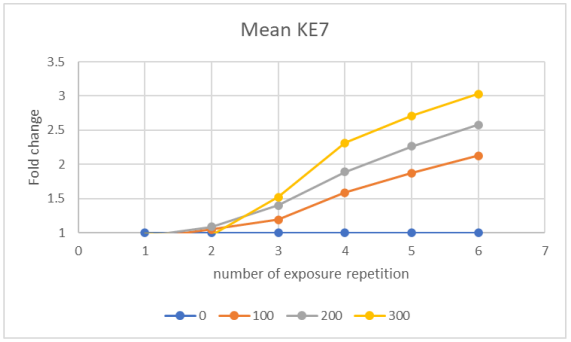
Mean KE7
Fold change
number of exposure repetition
0
100
200
300

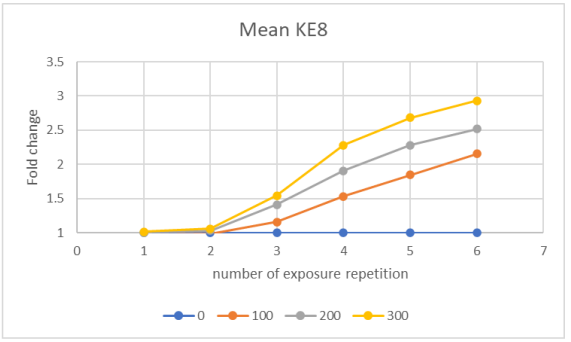
Mean KE8
Fold change
number of exposure repetition
0
100
200
300

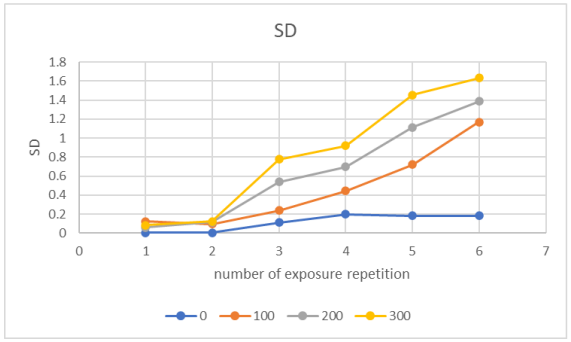
SD
SD
number of exposure repetition
0
100
200
300


SD
SD
number of exposure repetition
0
100
200
300

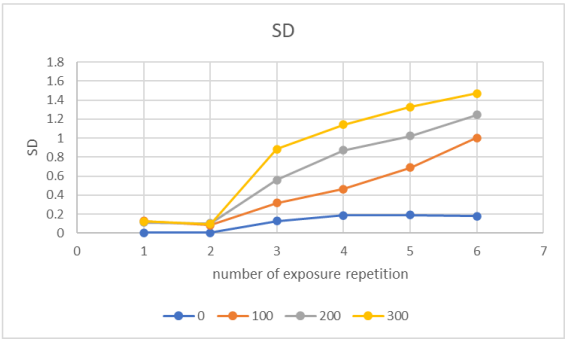
SD
SD
number of exposure repetition
0
100
200
300

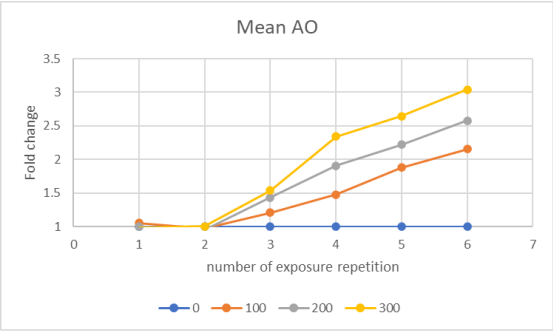
Mean AO
Fold change
3.5
3
2.5
2
1.5
1
0
1
2
3
4
5
6
7
number of exposure repetition
0
100
200
300

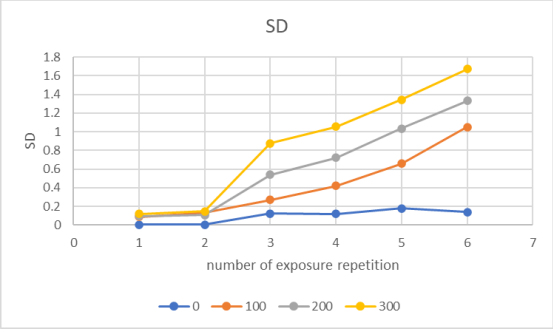
SD
SD
1.8
1.6
1.4
1.2
1
0.8
0.6
0.4
0.2
0
0
1
2
3
4
5
6
7
number of exposure repetition
0
100
200
300

Supplementary Tables 1.1. Fitted parameter values for Bayesian Network modeling

Exposure Repetition 1

Node	Fit.param
AO	-0.008
Dose	1.695
KE1	0.05+0.68*KER1-0.041*KER2+0.061*KER3+0.126*KER4
KE2	-0.016
KE3	0.009+0.69*KER8
KE4	-0.019
KE5	-0.017
KE6	-0.003
KE7	-0.022
KE8	-0.003
KER1	0.045+0.426*MIE1-0.414*MIE2
KER2	0.008+0.878*MIE1-0.04*MIE2
KER3	0.05+0.012*MIE1-0.713*MIE2
KER4	0.057-0.044*MIE1-0.784*MIE2
KER5	-0.003
KER6	0.066+0.724*KER5
KER7	0.039+0.758*KER6
KER8	0.104+0.699*KER7
MIE1	-0.015+0.118*Dose
MIE2	0.039-0.144*Dose

Supplementary Tables 1.1. Fitted parameter values for Bayesian Network modeling

Exposure Repetition 2

Node	Fit.param
AO	-0.016
Dose	1.695
KE1	-0.016
KE2	0.006-0.033*KER8
KE3	0.018+0.684*KER8
KE4	0.004+0.015*KE2
KE5	-0.005
KE6	-0.011
KE7	0.011-0.029*KE3
KE8	0.004+0.295*KE4+0.37*KE5-0.099*KE6+0.379*KE7
KER1	0.085+0.796*MIE1+0.063*MIE2
KER2	0.049+0.832*MIE1+0.042*MIE2
KER3	0.092+0.271*MIE1-0.454*MIE2
KER4	0.106+0.488*MIE1-0.186*MIE2
KER5	0.008+0.859*KE1
KER6	0.096+0.662*KER5
KER7	0.065+0.78*KER6
KER8	0.04+0.843*KER7
MIE1	-0.044+0.149*Dose
MIE2	0.029-0.133*Dose

Supplementary Tables 1.1. Fitted parameter values for Bayesian Network modeling

Exposure Repetition 3

Node	Fit.param
AO	0.015+0.924*KE8
Dose	1.695
KE1	0.035+0.43*KER1+0.028*KER2+0.337*KER3+0.077*KER4
KE2	0.064+0.057*KER8
KE3	0.057+0.617*KER8
KE4	-0.011
KE5	-0.004
KE6	-0.011
KE7	-0.013
KE8	0+0.428*KE4+0.24*KE5-0.126*KE6+0.46*KE7
KER1	0.054+0.775*MIE1-0.068*MIE2
KER2	0.079+0.513*MIE1-0.229*MIE2
KER3	0.035+0.611*MIE1-0.347*MIE2
KER4	0.063+0.558*MIE1-0.289*MIE2
KER5	0.038+0.787*KE1
KER6	0.071+0.806*KER5
KER7	0.056+0.748*KER6
KER8	0.051+0.873*KER7
MIE1	-0.014+0.124*Dose
MIE2	0.036-0.151*Dose

Supplementary Tables 1.1. Fitted parameter values for Bayesian Network modeling

Exposure Repetition 4

Node	Fit.param
AO	0.019+0.939*KE8
Dose	1.695
KE1	0.034+0.67*KER1+0.029*KER2+0.153*KER3+0.075*KER4
KE2	0.06+0.461*KER8
KE3	0.021+0.695*KER8
KE4	-0.017
KE5	-0.002
KE6	-0.003
KE7	0.058+0.591*KE3
KE8	-0.01
KER1	0.053+0.72*MIE1-0.142*MIE2
KER2	0.045+0.699*MIE1-0.163*MIE2
KER3	0.068+0.555*MIE1-0.298*MIE2
KER4	0.071+0.506*MIE1-0.33*MIE2
KER5	-0.03
KER6	0.112+0.661*KER5
KER7	0.034+0.791*KER6
KER8	0.083+0.717*KER7
MIE1	-0.037+0.137*Dose
MIE2	0.039-0.136*Dose

Supplementary Tables 1.1. Fitted parameter values for Bayesian Network modeling

Exposure Repetition 5

Node	Fit.param
AO	-0.022
Dose	1.695
KE1	0.042+0.735*KER1-0.006*KER2+0.112*KER3+0.041*KER4
KE2	0.141+0.328*KER8
KE3	0.026+0.654*KER8
KE4	0.001+1.014*KE2
KE5	0+1.013*KE2
KE6	0.018+0.968*KE2
KE7	0.129+0.534*KE3
KE8	0.009+0.168*KE4+0.104*KE5+0.533*KE6+0.161*KE7
KER1	0.059+0.727*MIE1-0.06*MIE2
KER2	0.076+0.449*MIE1-0.192*MIE2
KER3	0.104+0.364*MIE1-0.223*MIE2
KER4	0.082+0.369*MIE1-0.298*MIE2
KER5	-0.024
KER6	0.131+0.587*KER5
KER7	0.053+0.726*KER6
KER8	0.011+0.982*KER7
MIE1	-0.059+0.146*Dose
MIE2	0.037-0.168*Dose

Supplementary Tables 1.1. Fitted parameter values for Bayesian Network modeling

Exposure Repetition 6

Node	Fit.param
AO	-0.044
Dose	1.695
KE1	0.011+0.847*KER1+0.107*KER2+0.129*KER3-0.057*KER4
KE2	0.186+0.298*KER8
KE3	0.02+0.66*KER8
KE4	-0.02
KE5	-0.002
KE6	-0.011
KE7	0.176+0.426*KE3
KE8	0.033+0.192*KE4+0.216*KE5+0.247*KE6+0.244*KE7
KER1	0.058+0.631*MIE1-0.206*MIE2
KER2	0.05+0.549*MIE1-0.245*MIE2
KER3	0.045+0.53*MIE1-0.347*MIE2
KER4	0.062+0.331*MIE1-0.451*MIE2
KER5	-0.02
KER6	0.153+0.495*KER5
KER7	0.037+0.754*KER6
KER8	0.038+0.883*KER7
MIE1	-0.007+0.099*Dose
MIE2	0.054-0.148*Dose

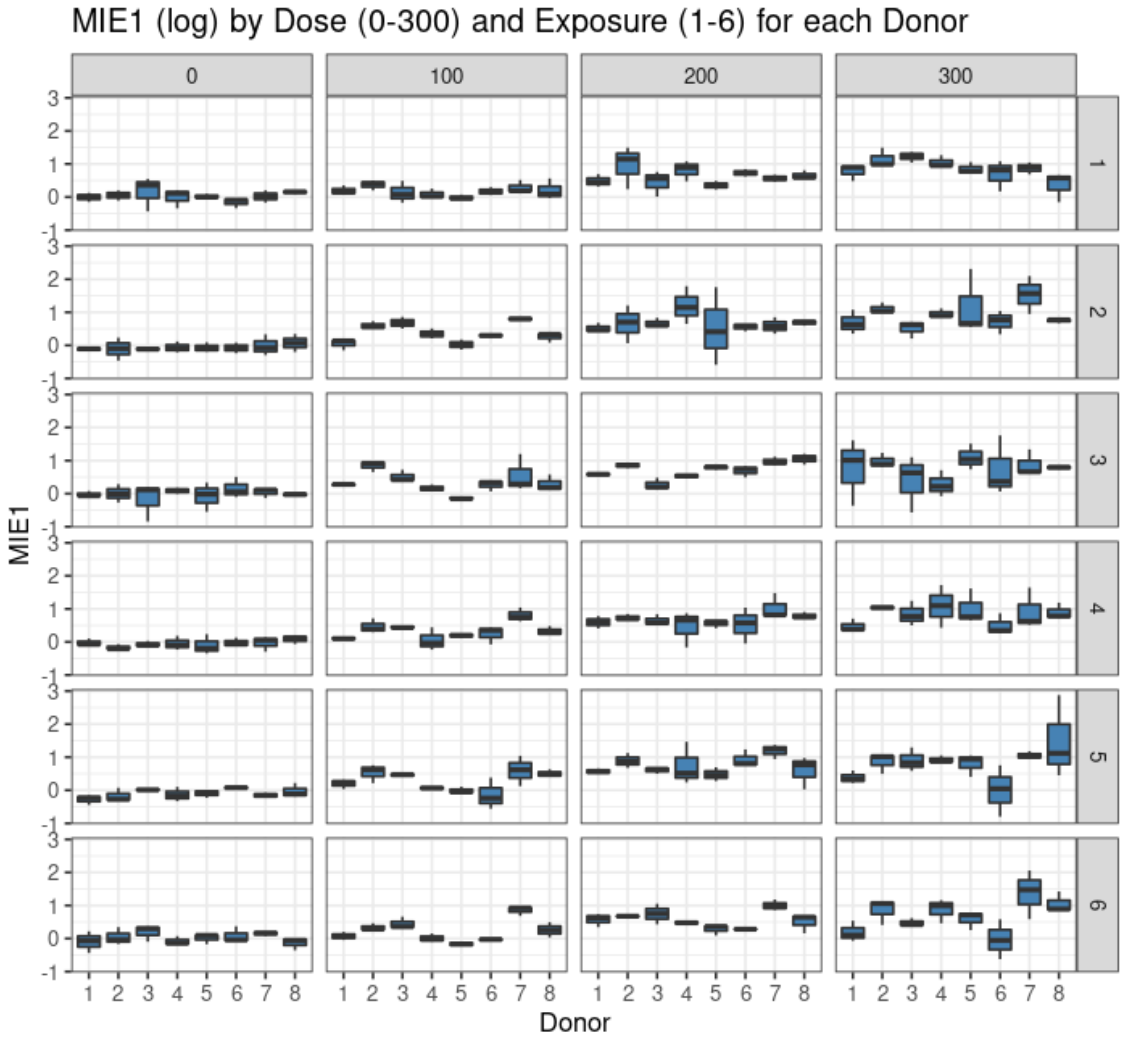
MIE1 (log) by Dose (0-300) and Exposure (1-6) for each Donor
0
100
200
300
1
2
3
4
5
6
MIE1
Donor

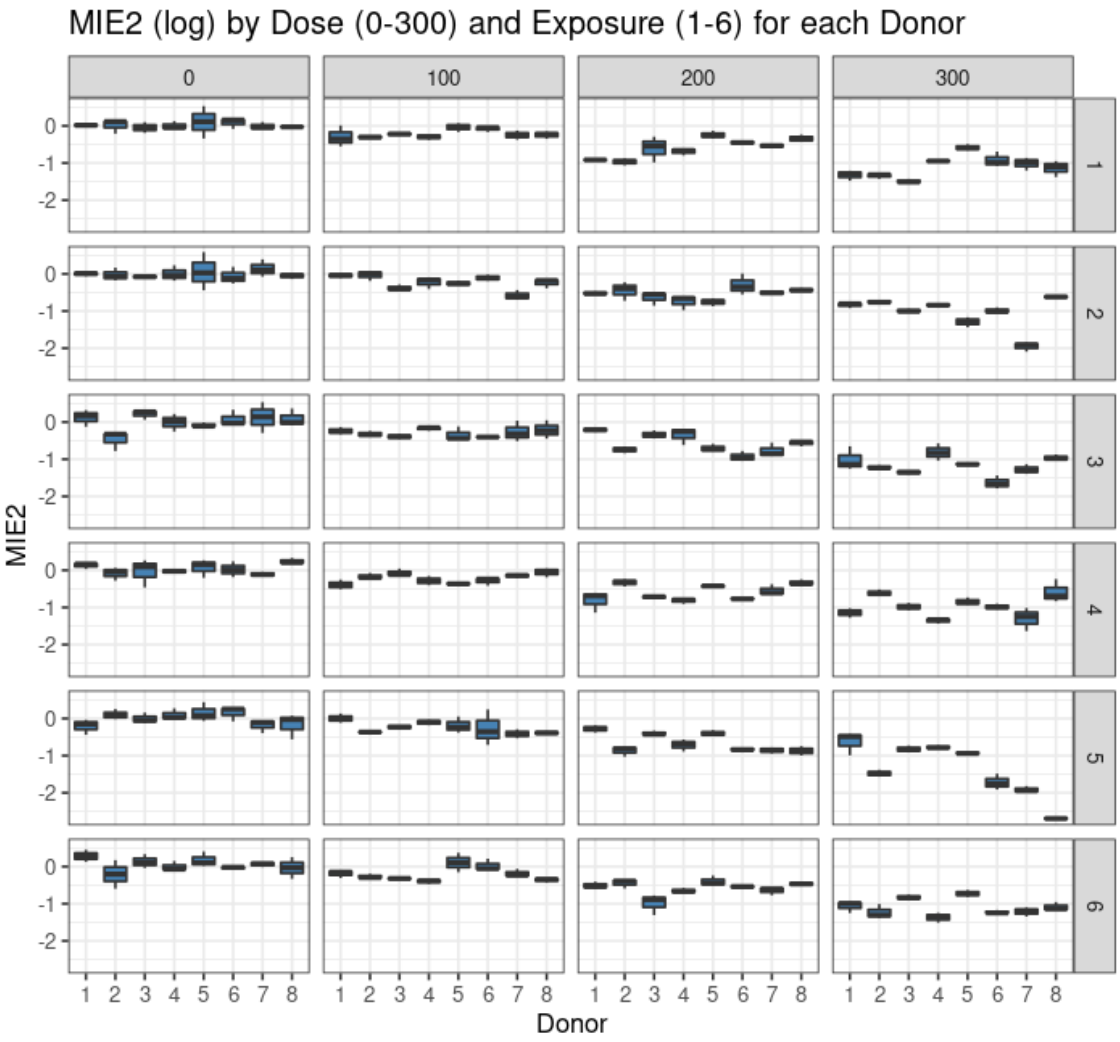
MIE2 (log) by Dose (0-300) and Exposure (1-6) for each Donor
0
100
200
300
1
2
3
4
5
6
MIE2
0
-1
-2
1 2 3 4 5 6 7 8
Donor

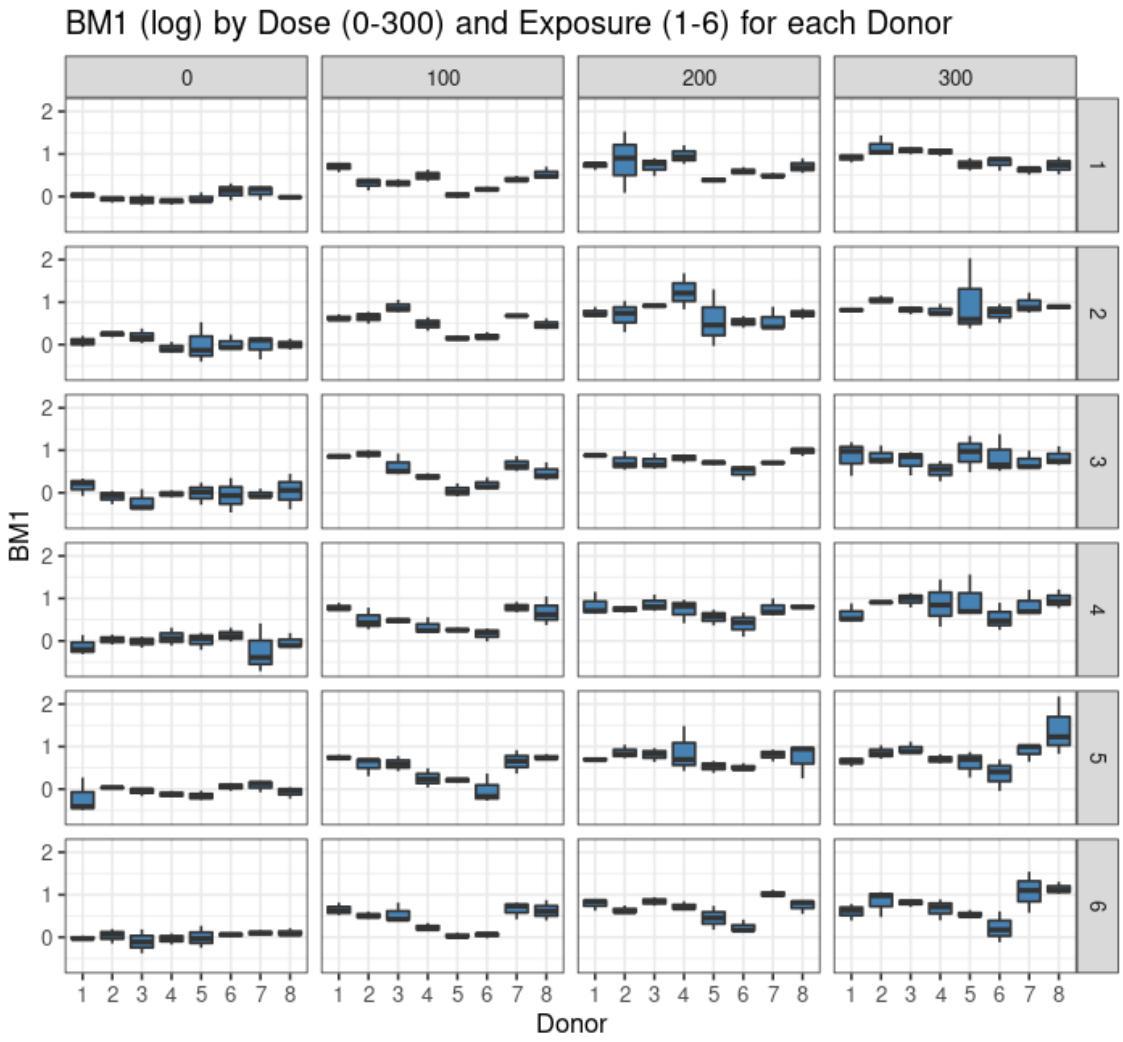
BM1 (log) by Dose (0-300) and Exposure (1-6) for each Donor
0
100
200
300
1
2
3
4
5
6
BM1
Donor

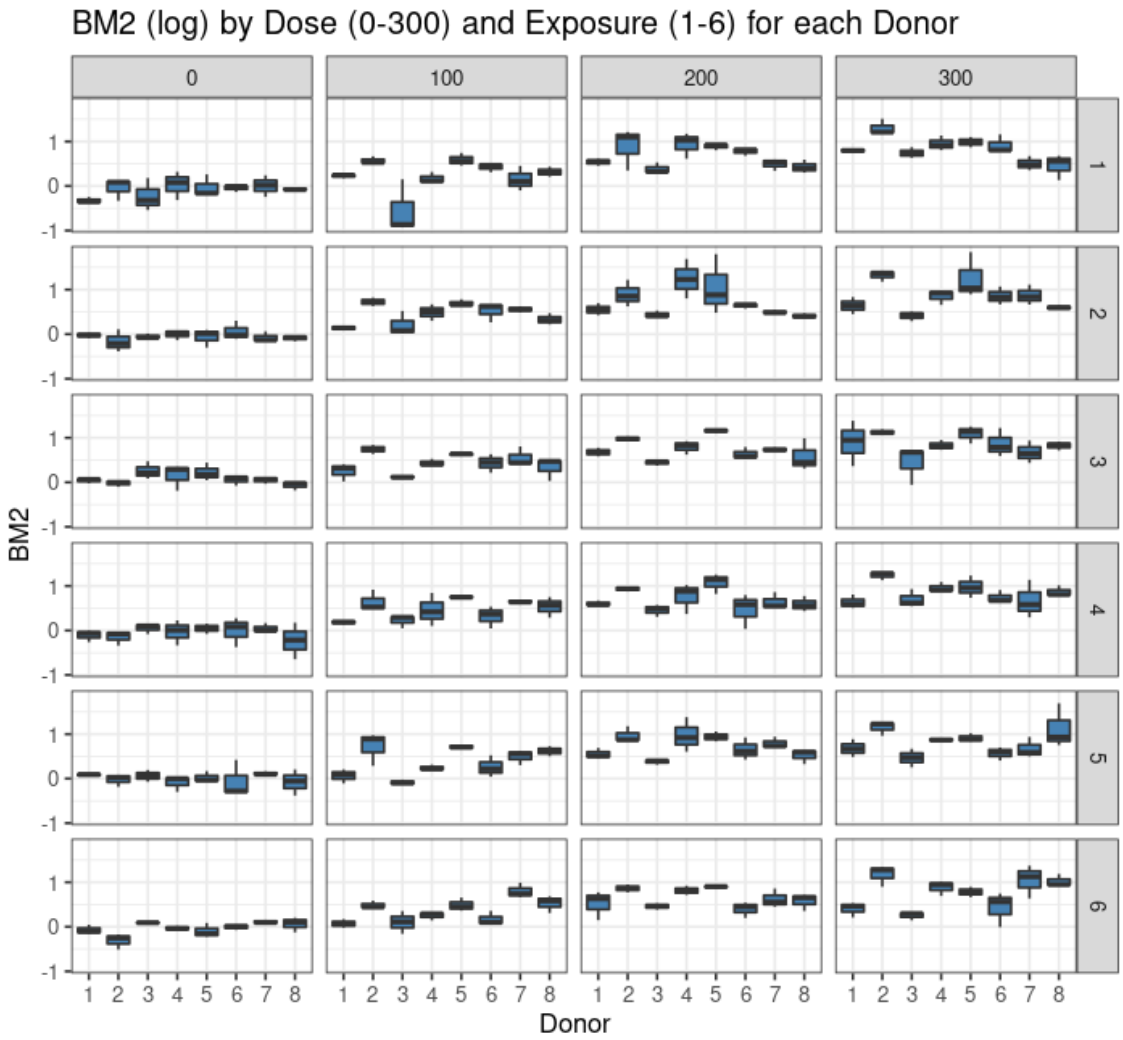
BM2 (log) by Dose (0-300) and Exposure (1-6) for each Donor
0
100
200
300
1
2
3
4
5
6
BM2
Donor

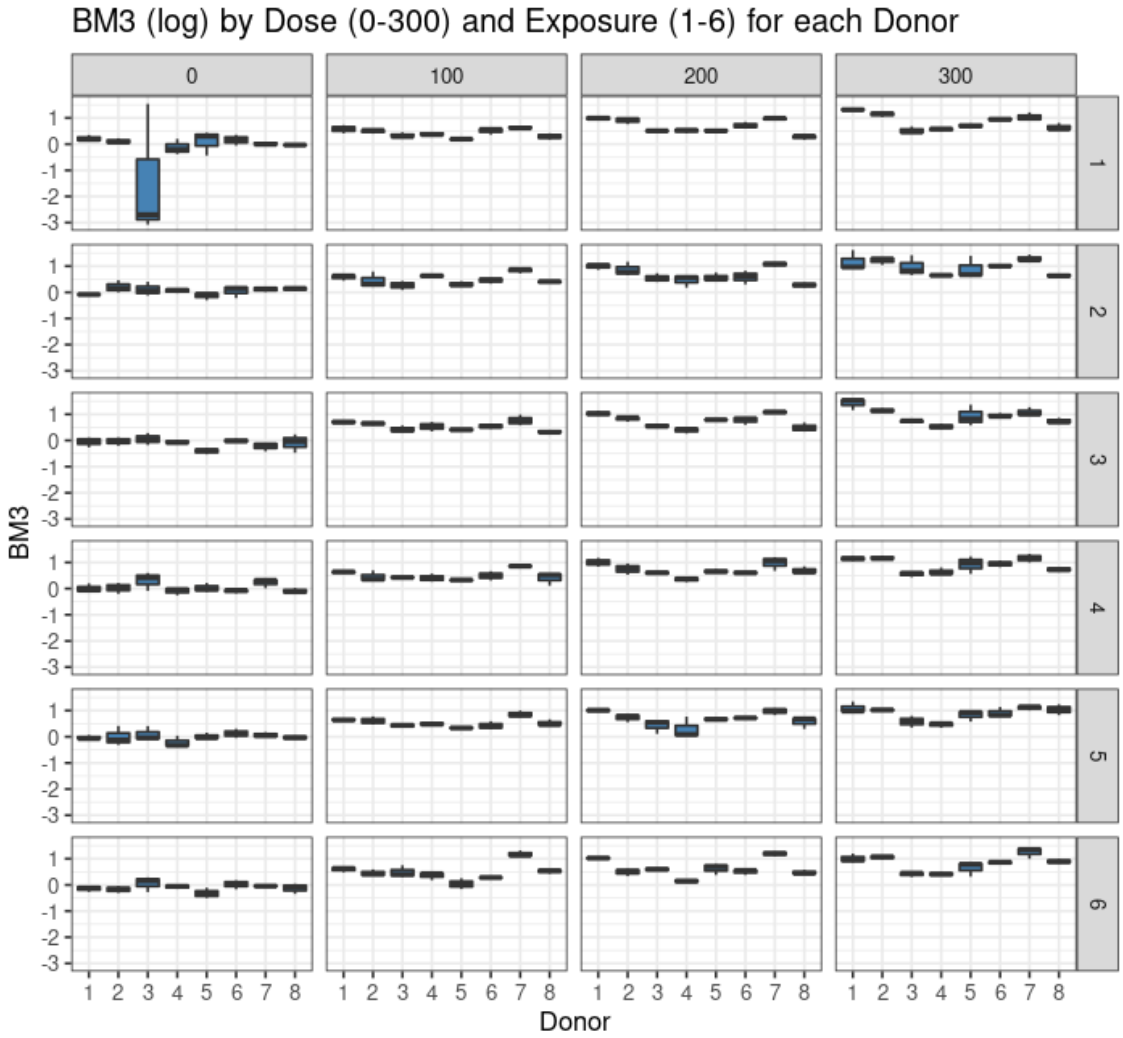
BM3 (log) by Dose (0-300) and Exposure (1-6) for each Donor
0
100
200
300
1
2
3
4
5
6
BM3
Donor

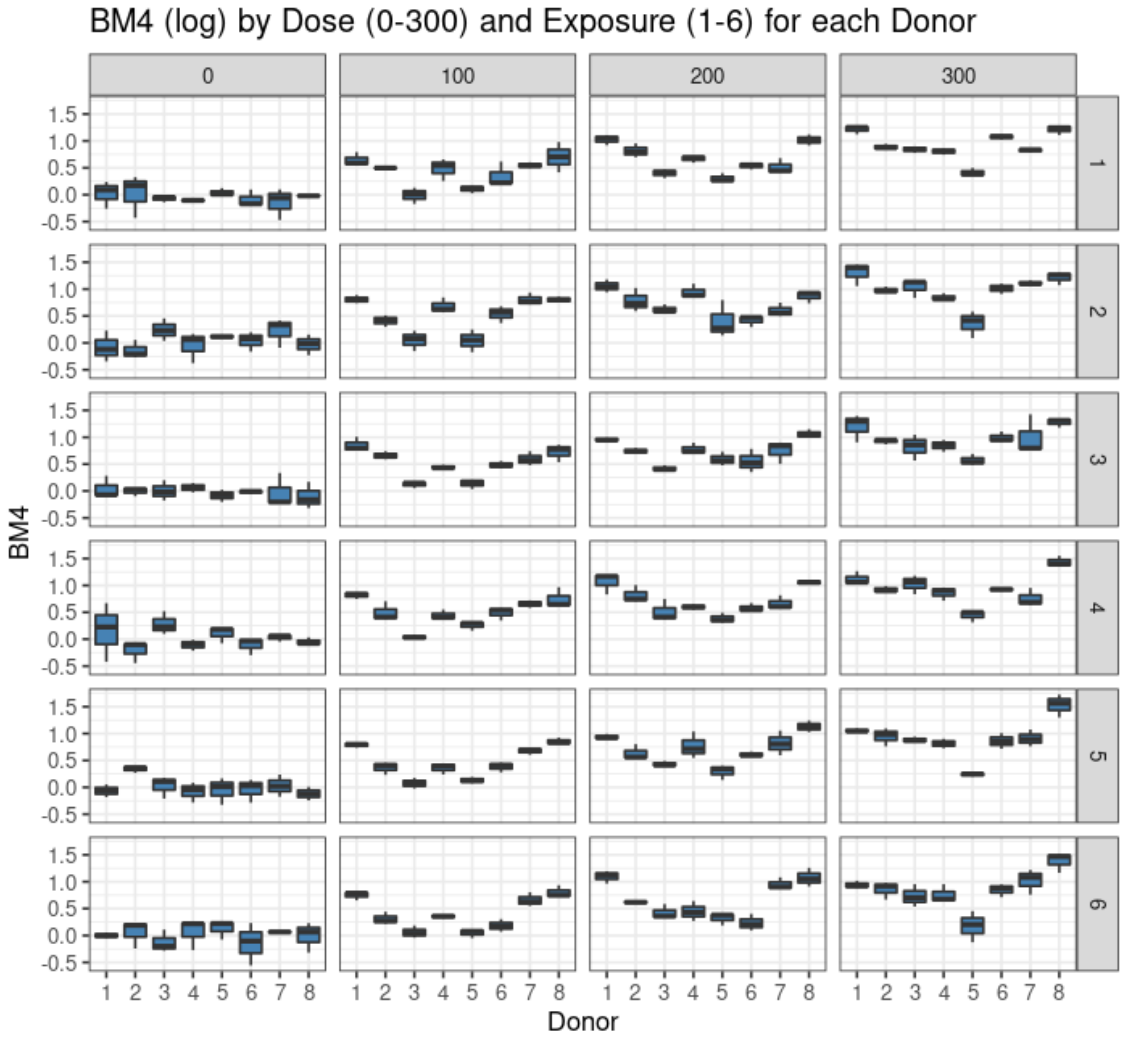
BM4 (log) by Dose (0-300) and Exposure (1-6) for each Donor
0
100
200
300
1
2
3
4
5
6
BM4
1.5
1.0
0.5
0.0
-0.5
1 2 3 4 5 6 7 8
Donor

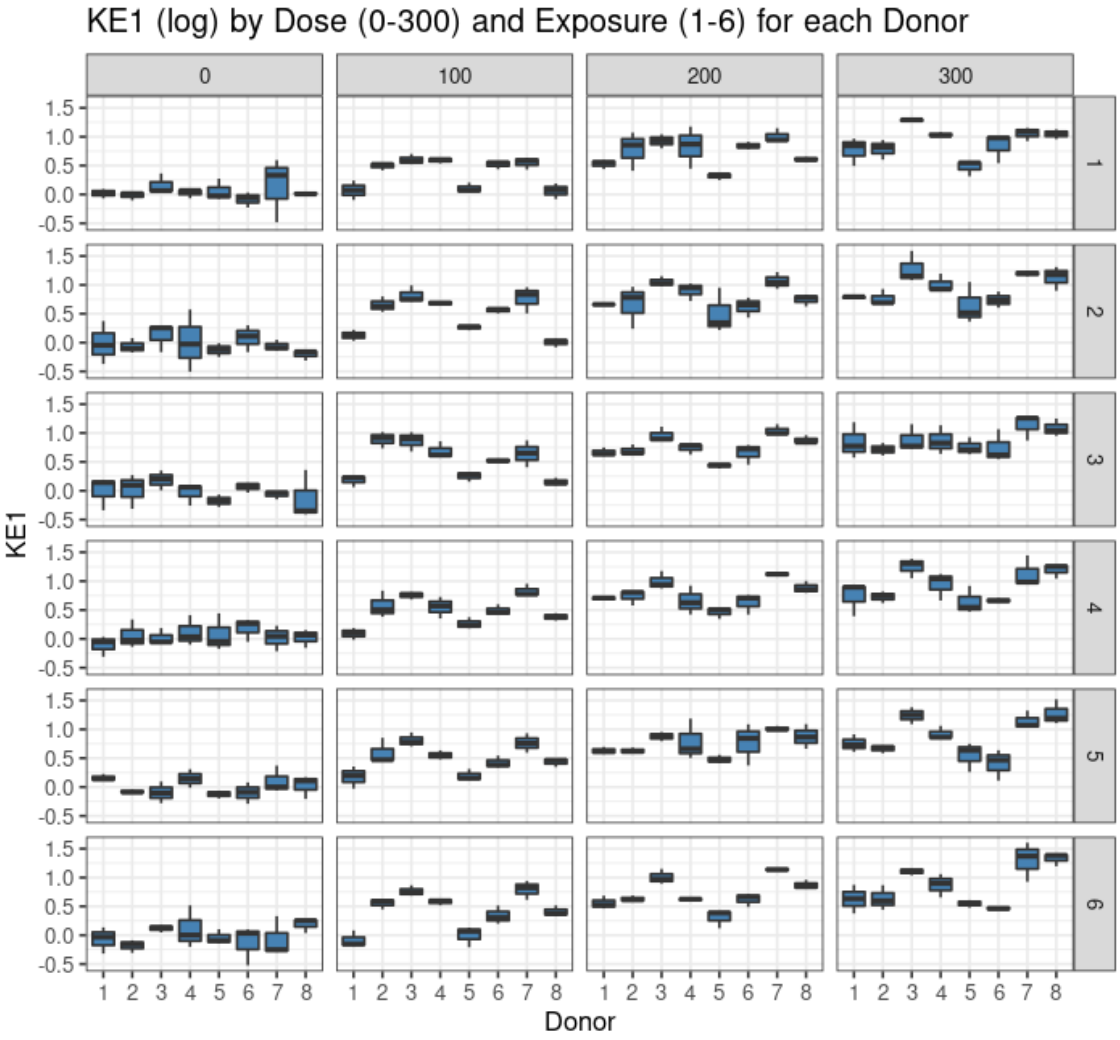
KE1 (log) by Dose (0-300) and Exposure (1-6) for each Donor
0
100
200
300
1
2
3
4
5
6
KE1
1.5
1.0
0.5
0.0
-0.5
1 2 3 4 5 6 7 8
Donor

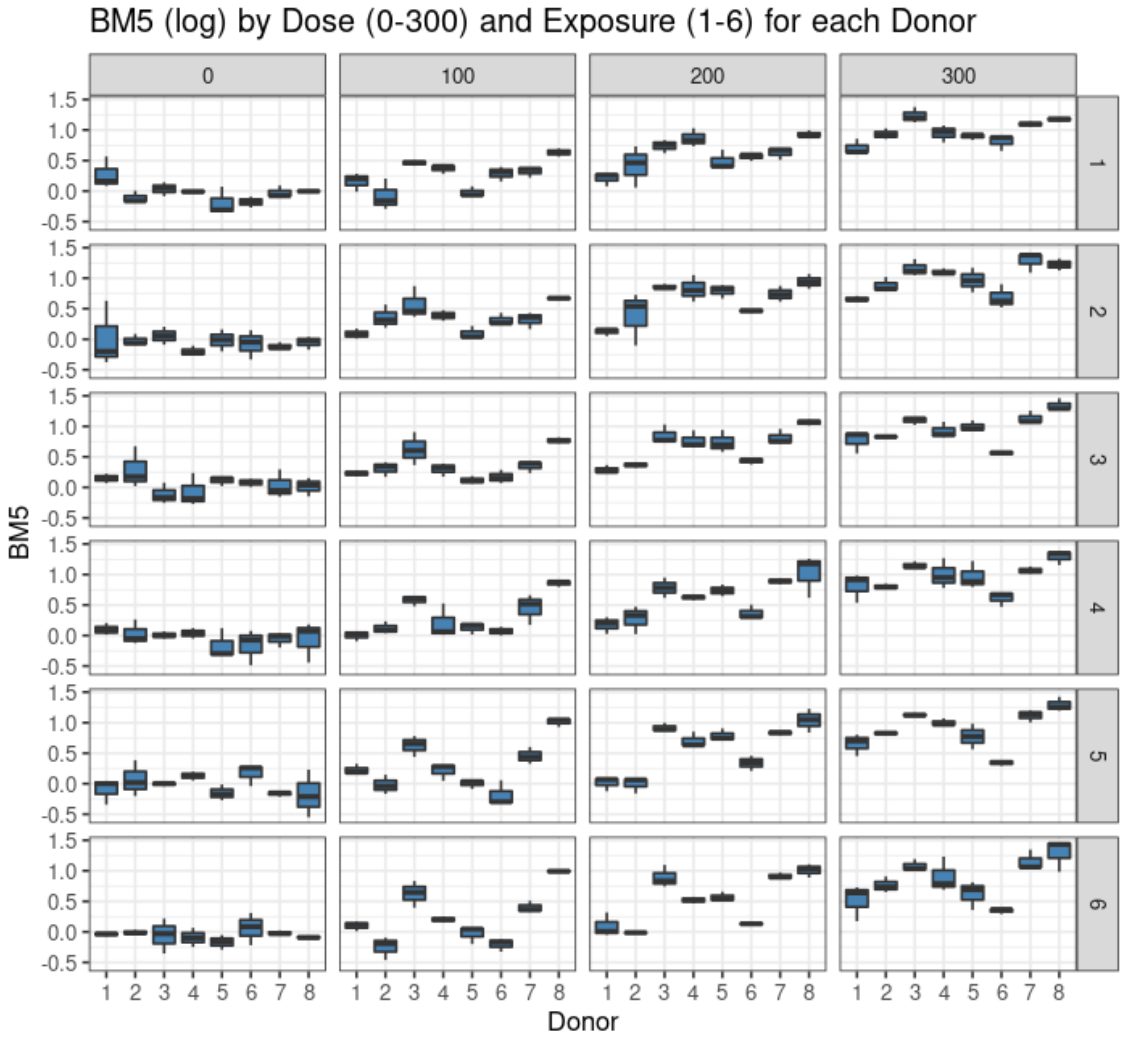
BM5 (log) by Dose (0-300) and Exposure (1-6) for each Donor
0
100
200
300
1
2
3
4
5
6
BM5
1.5
1.0
0.5
0.0
-0.5
1 2 3 4 5 6 7 8
Donor

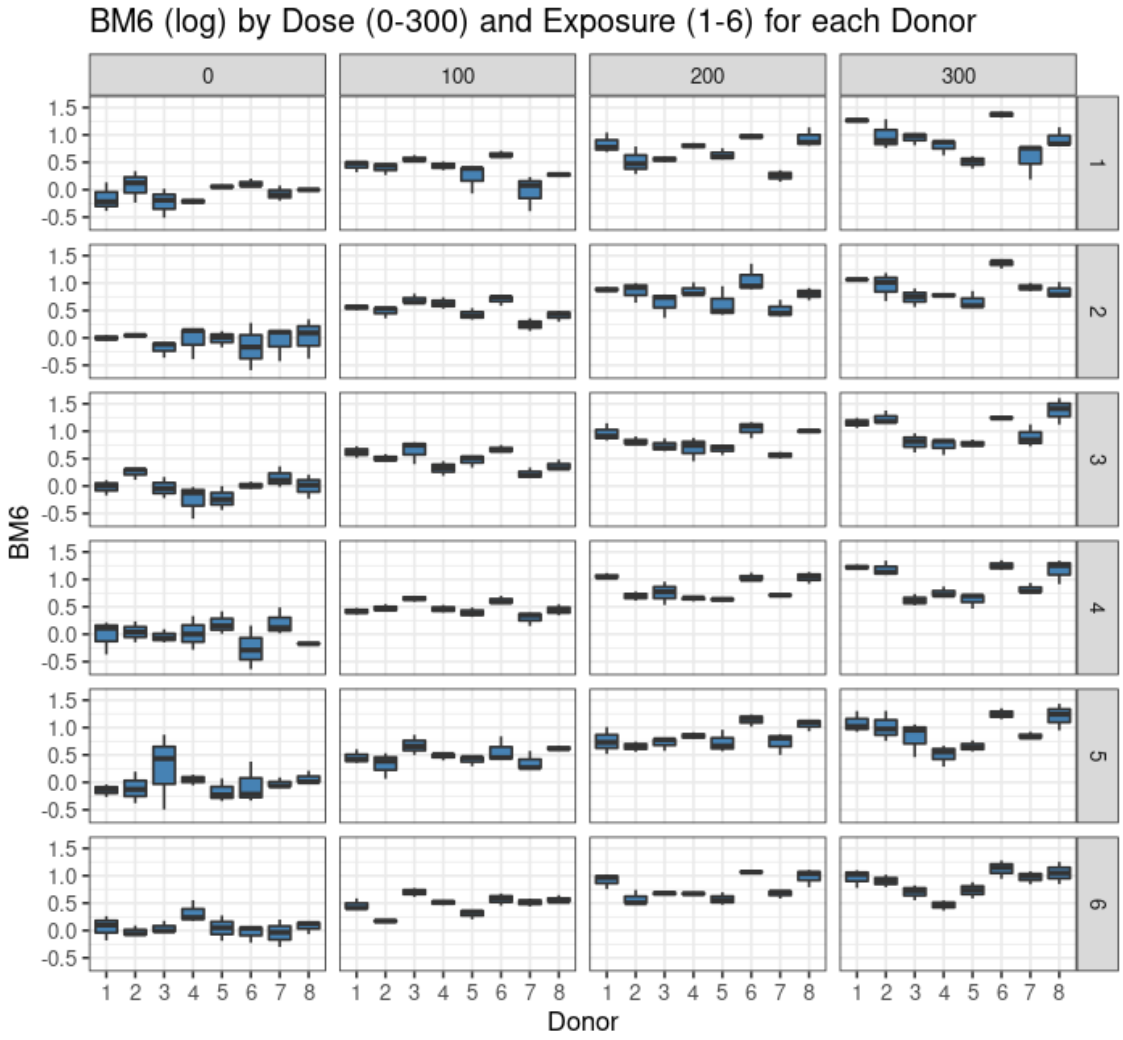
BM6 (log) by Dose (0-300) and Exposure (1-6) for each Donor
0
100
200
300
1
2
3
4
5
6
BM6
1.5
1.0
0.5
0.0
-0.5
1 2 3 4 5 6 7 8
Donor

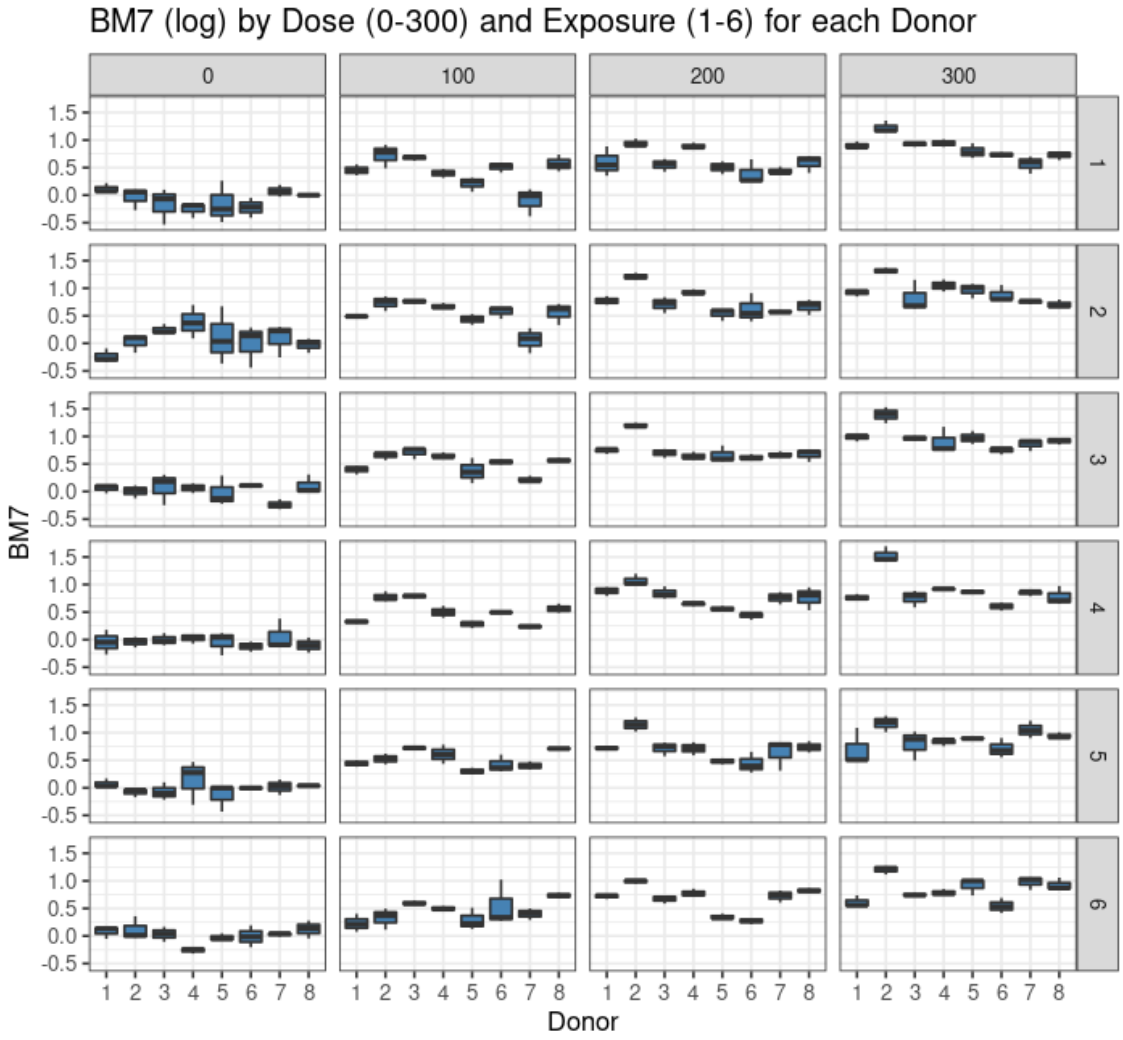
BM7 (log) by Dose (0-300) and Exposure (1-6) for each Donor
0
100
200
300
1
2
3
4
5
6
BM7
1.5
1.0
0.5
0.0
-0.5
1 2 3 4 5 6 7 8
Donor

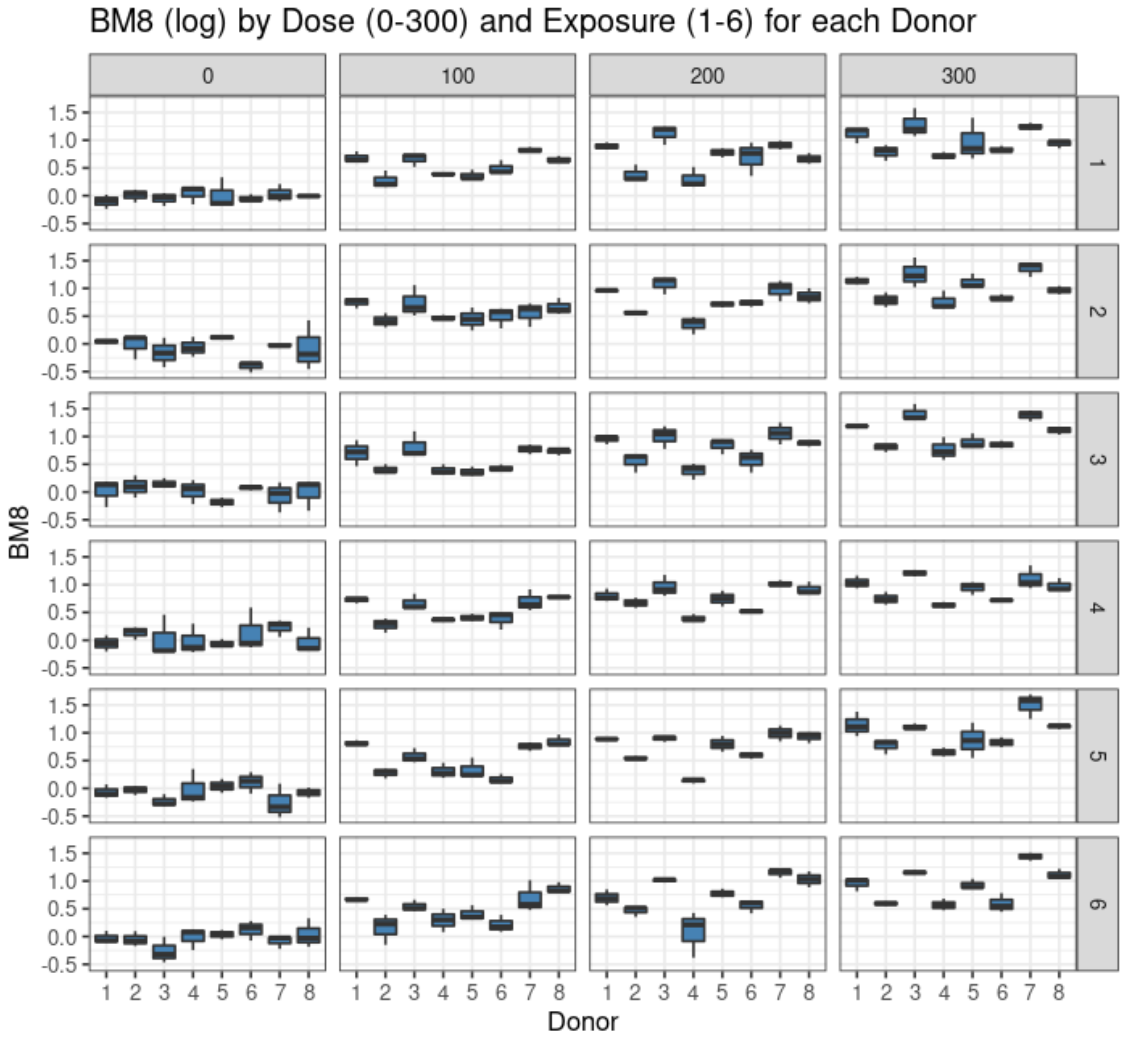
BM8 (log) by Dose (0-300) and Exposure (1-6) for each Donor
0
100
200
300
1
2
3
4
5
6
BM8
1.5
1.0
0.5
0.0
-0.5
1 2 3 4 5 6 7 8
Donor

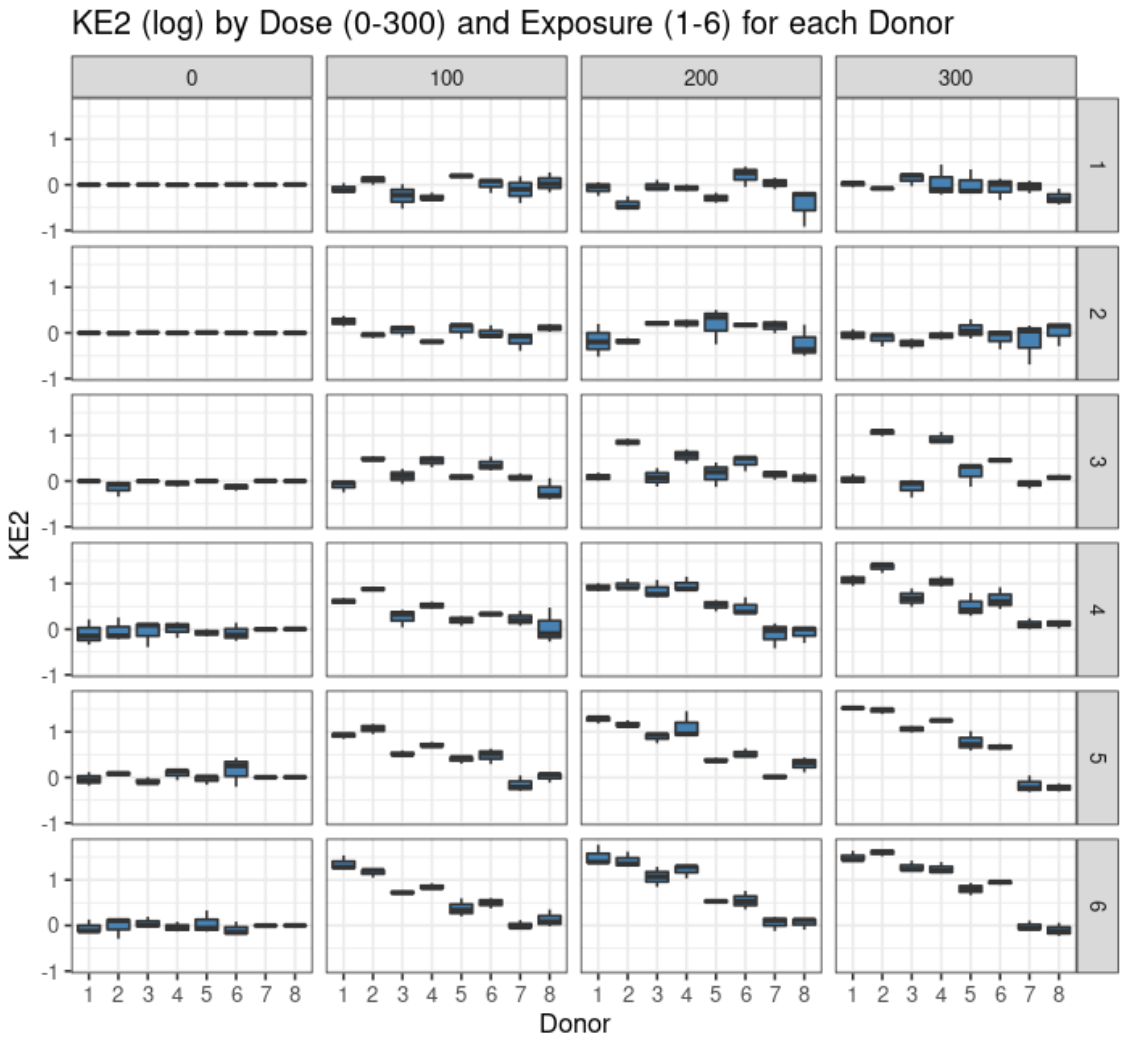
KE2 (log) by Dose (0-300) and Exposure (1-6) for each Donor
0
100
200
300
1
2
3
4
5
6
KE2
Donor

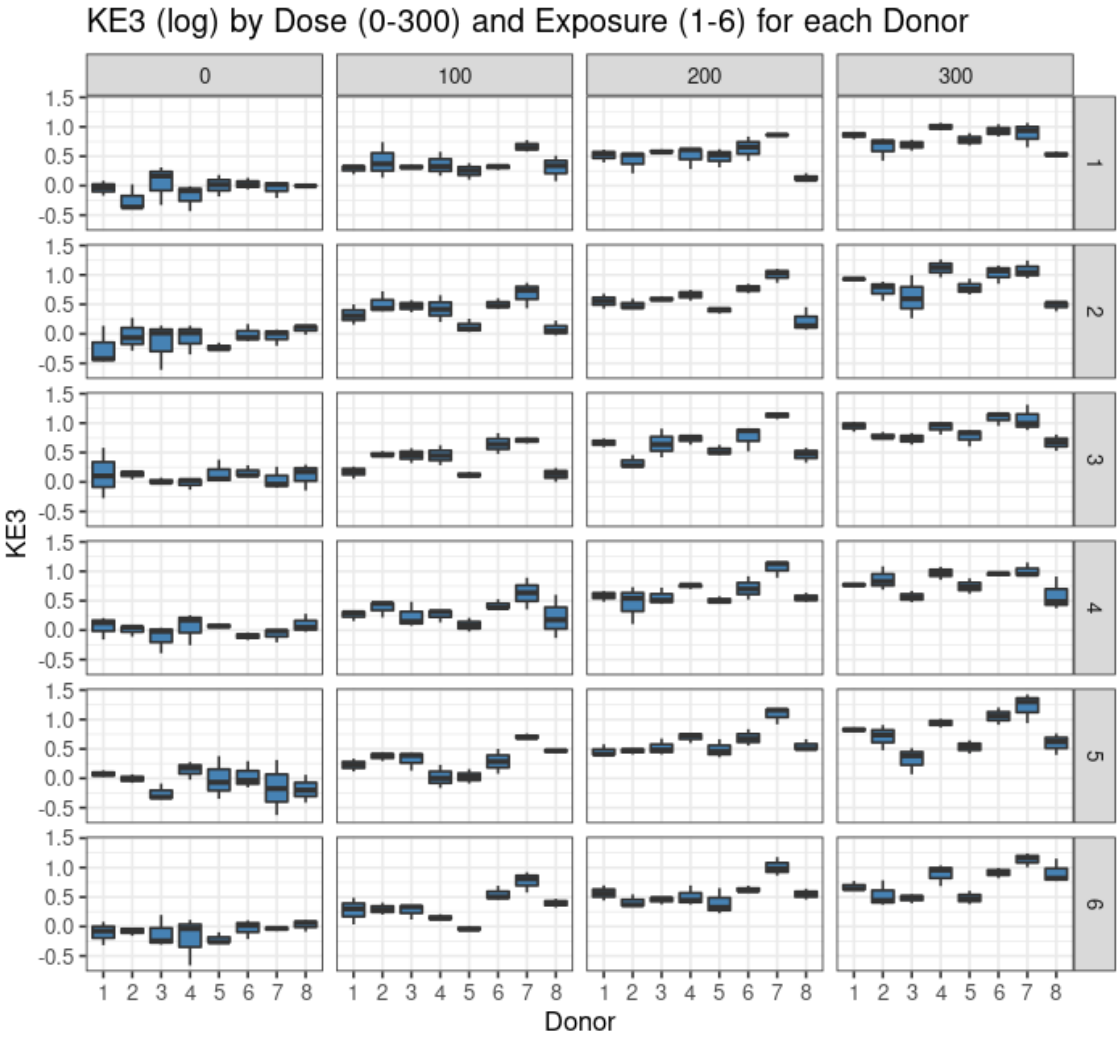
KE3 (log) by Dose (0-300) and Exposure (1-6) for each Donor
0
100
200
300
1
2
3
4
5
6
KE3
1.5
1.0
0.5
0.0
-0.5
1 2 3 4 5 6 7 8
Donor

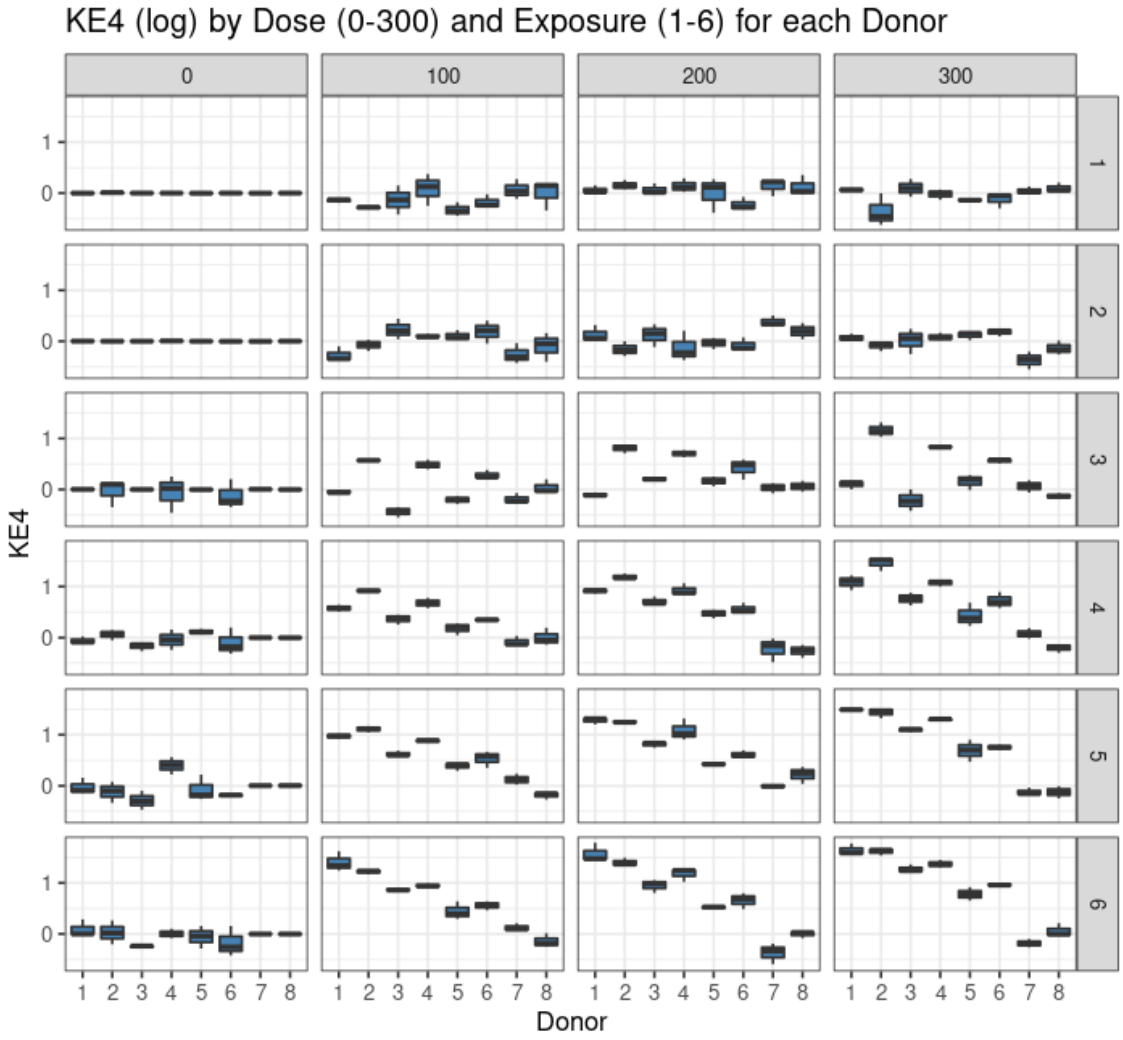
KE4 (log) by Dose (0-300) and Exposure (1-6) for each Donor
0
100
200
300
1
2
3
4
5
6
KE4
1
0
1 2 3 4 5 6 7 8
Donor

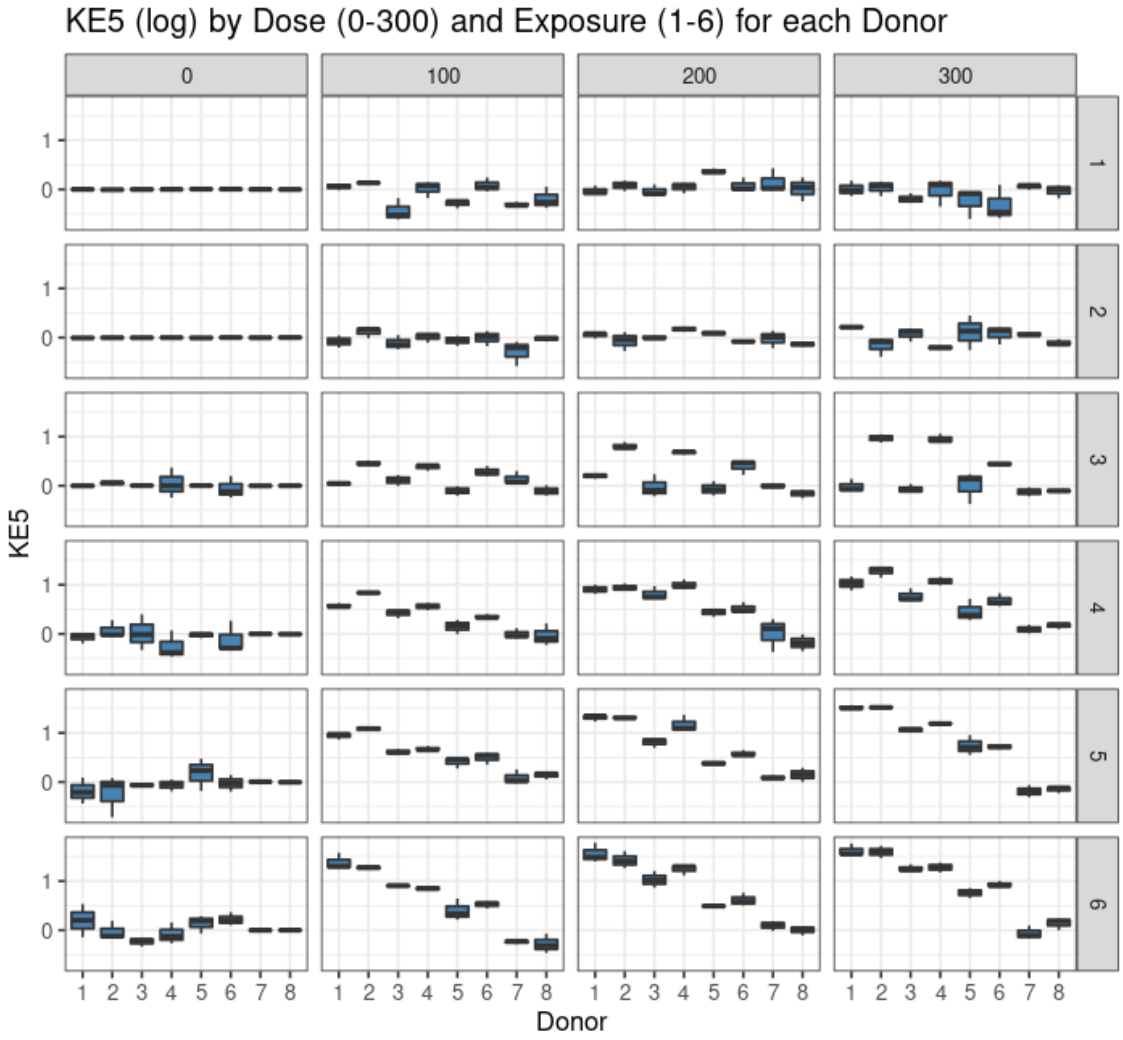
KE5 (log) by Dose (0-300) and Exposure (1-6) for each Donor
0
100
200
300
1
2
3
4
5
6
KE5
1
0
Donor
1 2 3 4 5 6 7 8

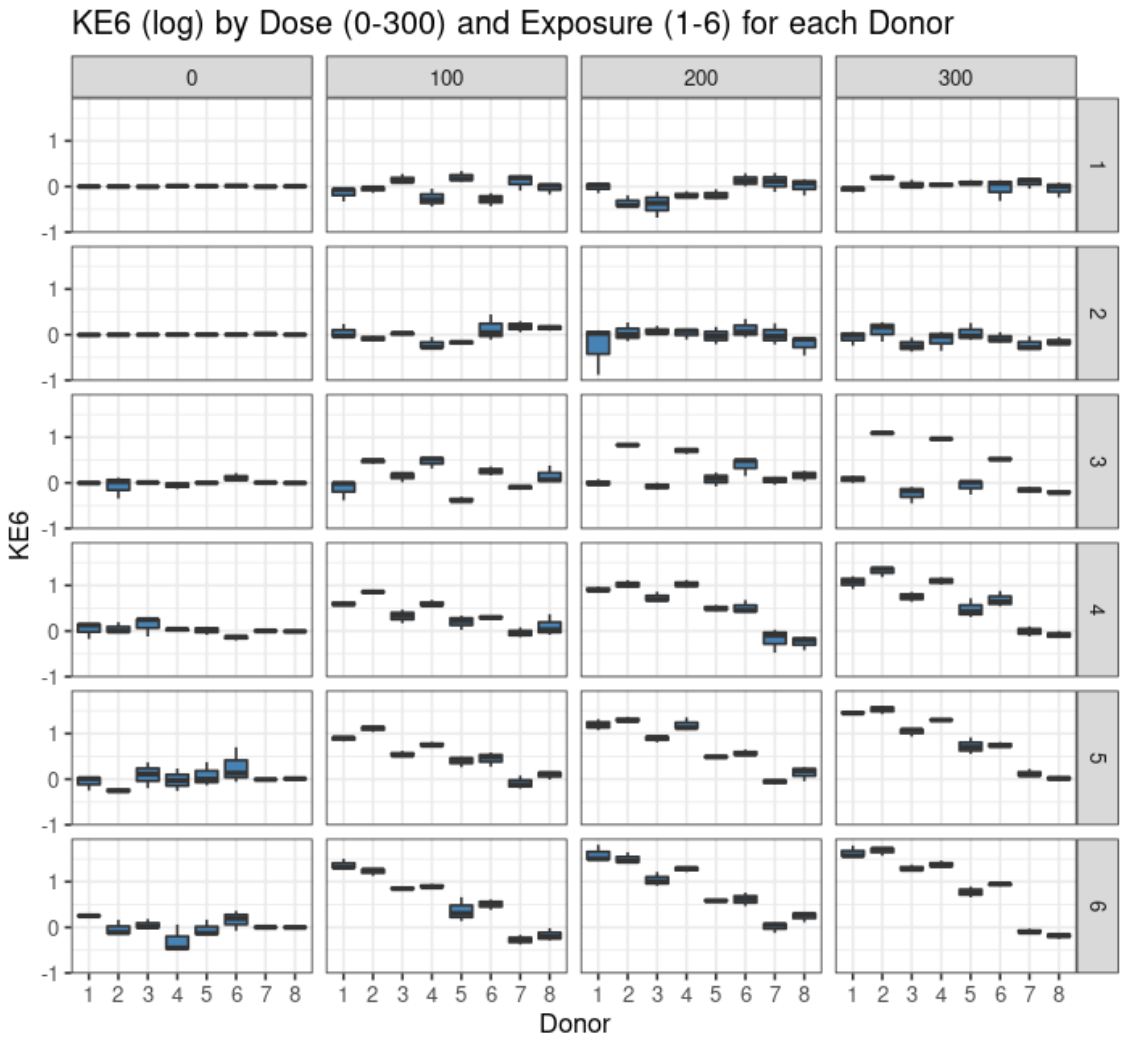
KE6 (log) by Dose (0-300) and Exposure (1-6) for each Donor
0
100
200
300
1
2
3
4
5
6
KE6
Donor

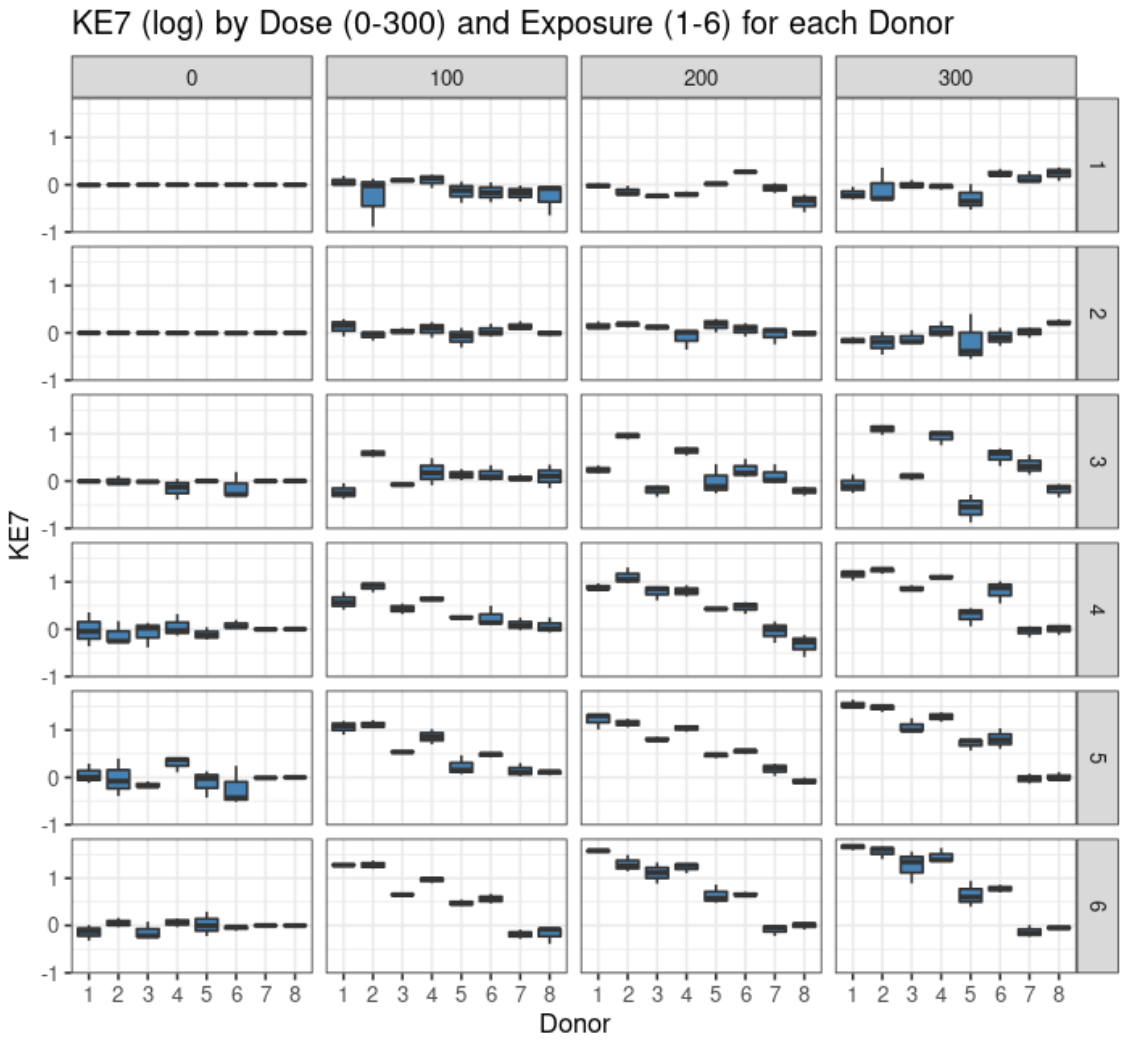
KE7 (log) by Dose (0-300) and Exposure (1-6) for each Donor
0
100
200
300
1
2
3
4
5
6
KE7
Donor

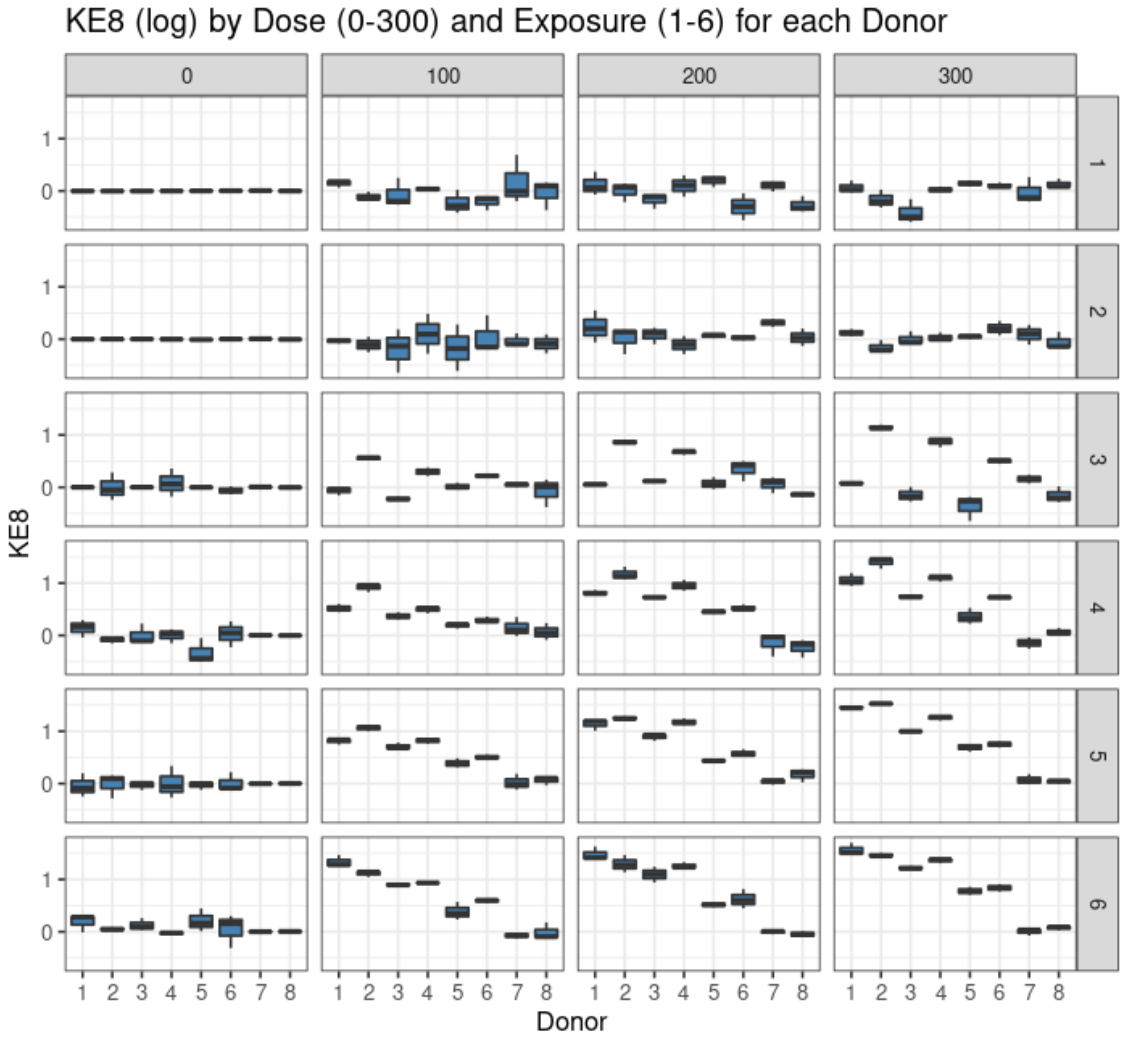
KE8 (log) by Dose (0-300) and Exposure (1-6) for each Donor
0
100
200
300
1
2
3
4
5
6
KE8
1
0
Donor
1 2 3 4 5 6 7 8

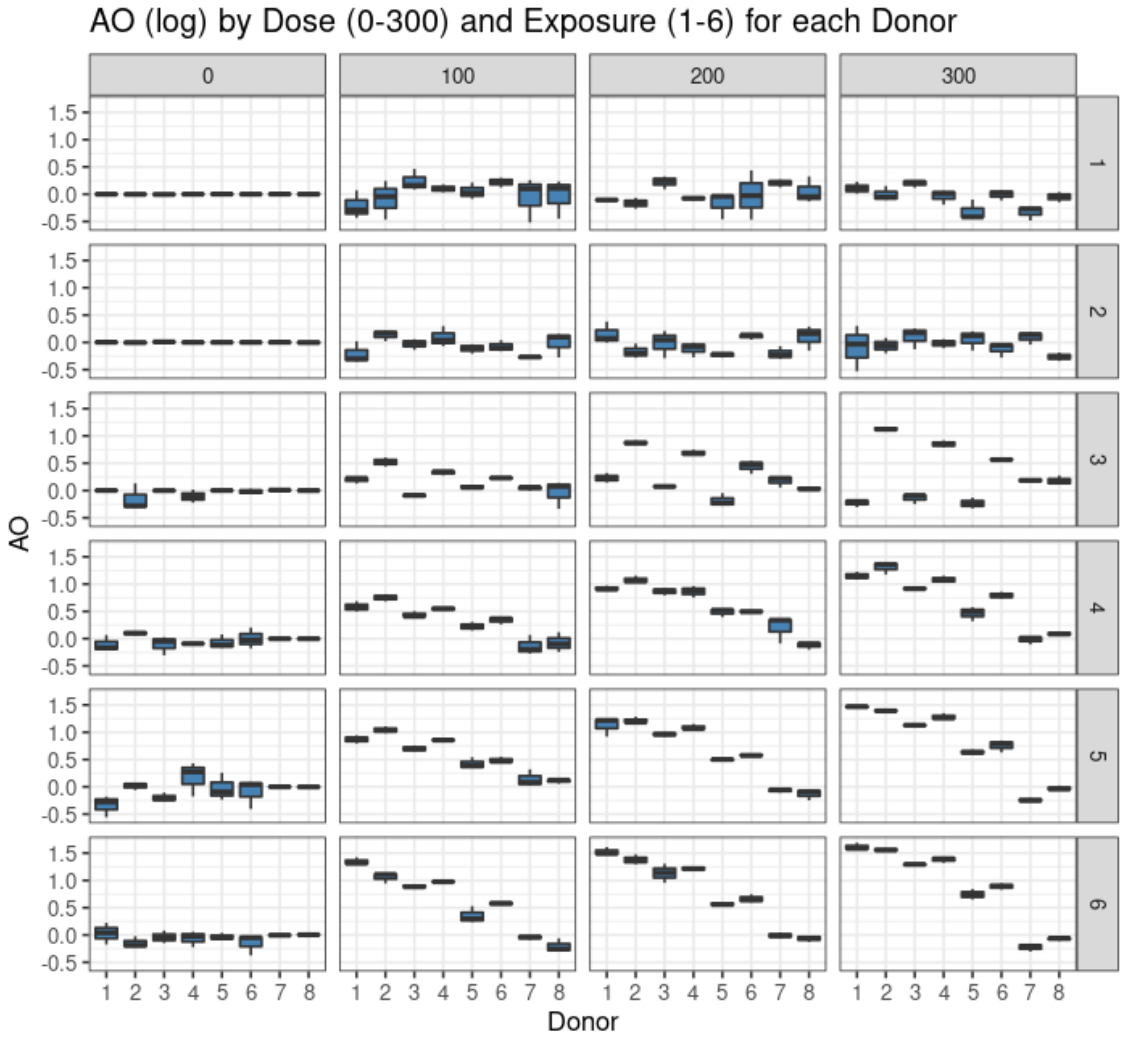

Supplementary Fig. 1.1. Dose response of resampled data at each exposure repetition

Data were resampled with Bayesian Network formalism. The resampled data of each biological events are presented as boxplots. The box and line within the box represent the interquartile range and the median respectively. The whiskers represent the minimum and maximum.

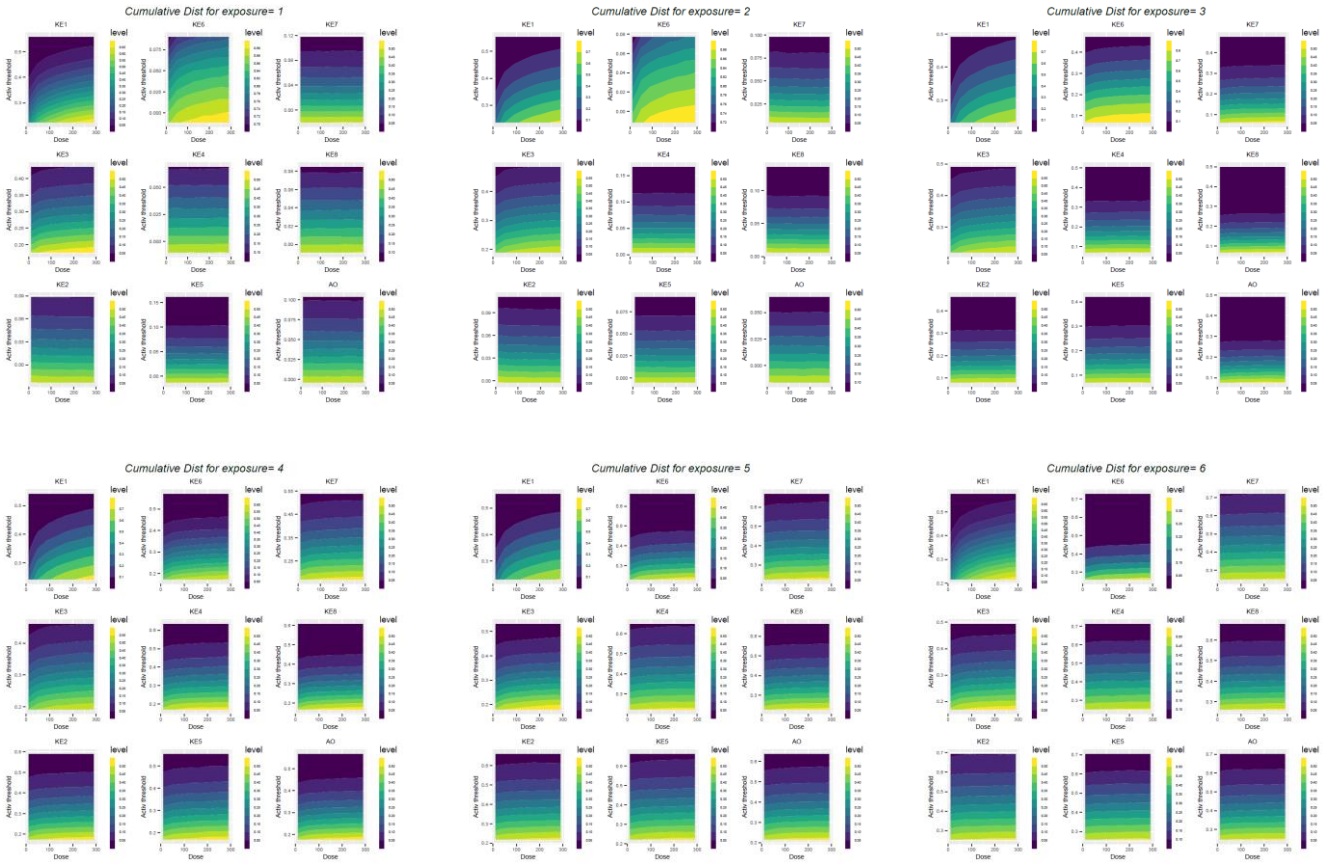

Supplementary Fig. 1.2. Cumulative distribution plot at each exposure repetition.

The probabilities were calculated by fitting the GBN to the virtual data by varying activation threshold Δ and the dose d. The data are represented as cumulative distribution plot.

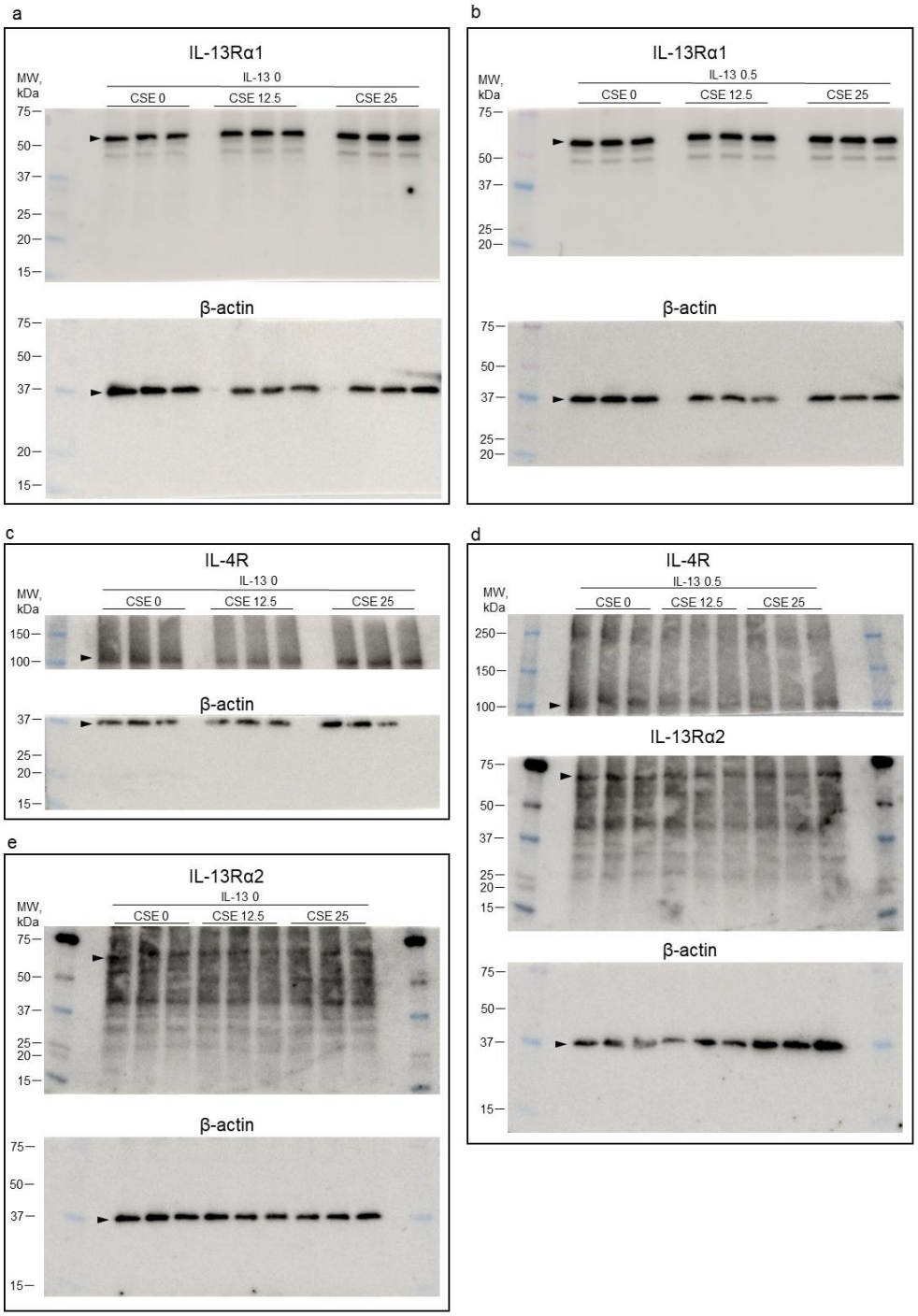

Supplementary Fig. 2.1. Western blot image for day 14 samples exposed to each concentration of IL-13 and/or CSE. Target protein is pointed by arrowhead. CSE: cigarette smoke extract, IL: interleukin, R: receptor.

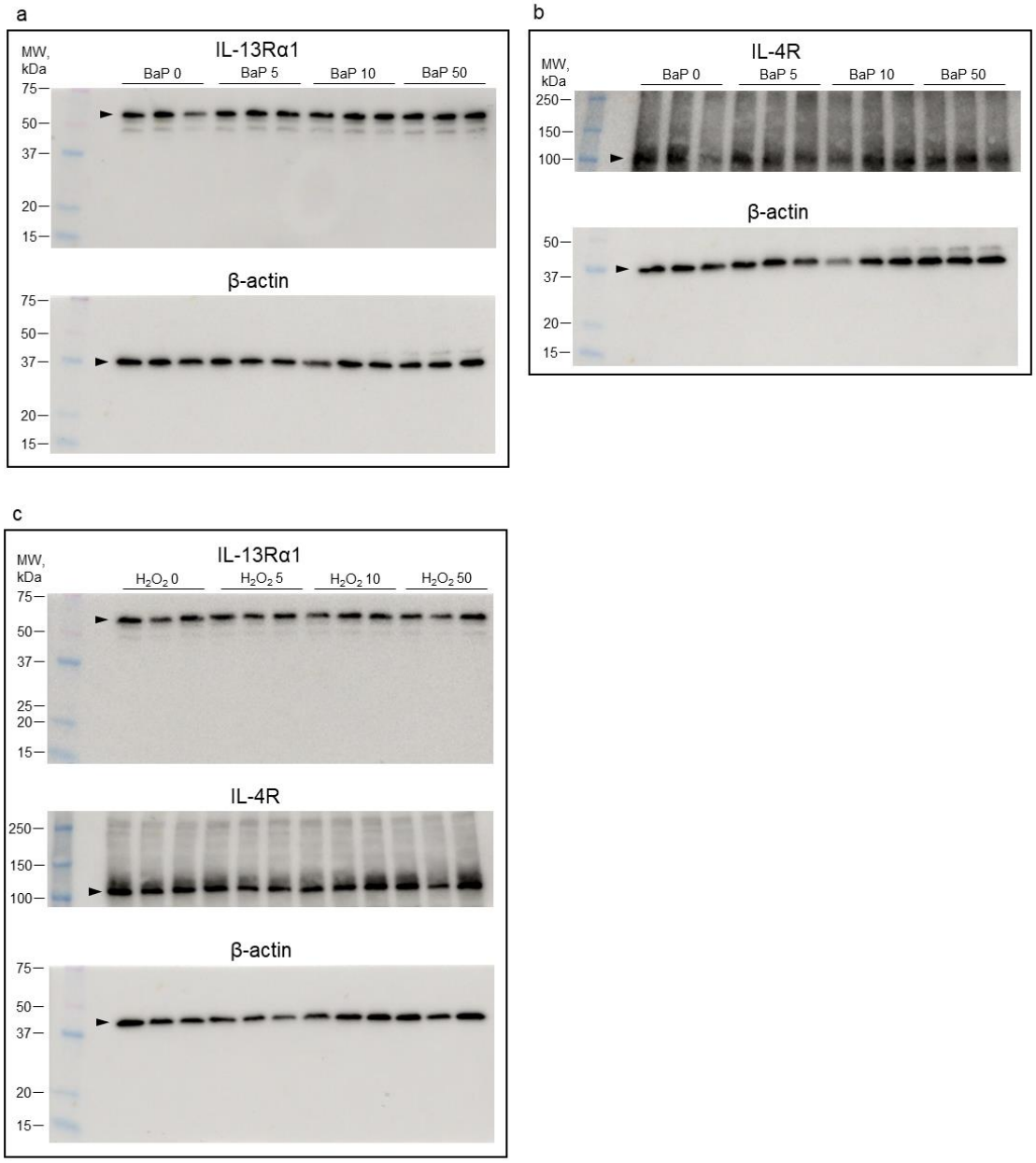

Supplementary Fig. 2.2. Western blot image for day 14 samples exposed to each concentration of benzo(a)pyrene (BaP) and H_2O_2. Target protein is pointed by arrowhead. IL: interleukin, R: receptor.

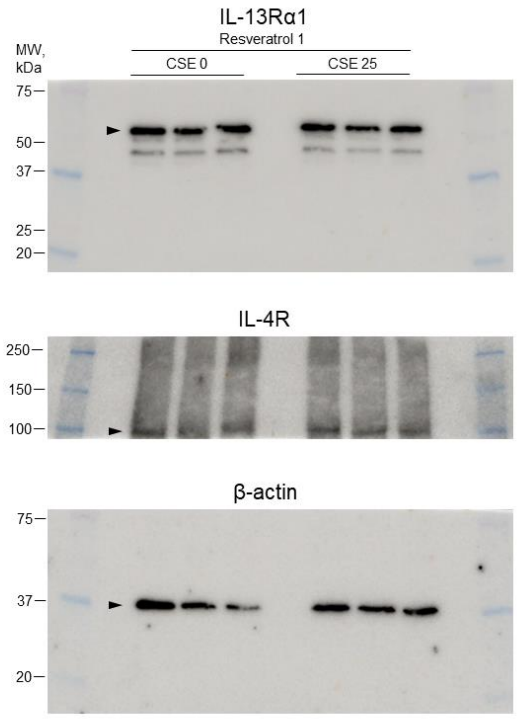

Supplementary Fig. 2.3. Western blot image for day 14 samples exposed to each concentration of resveratrol and CSE. CSE: cigarette smoke extract, IL: interleukin, R: receptor.

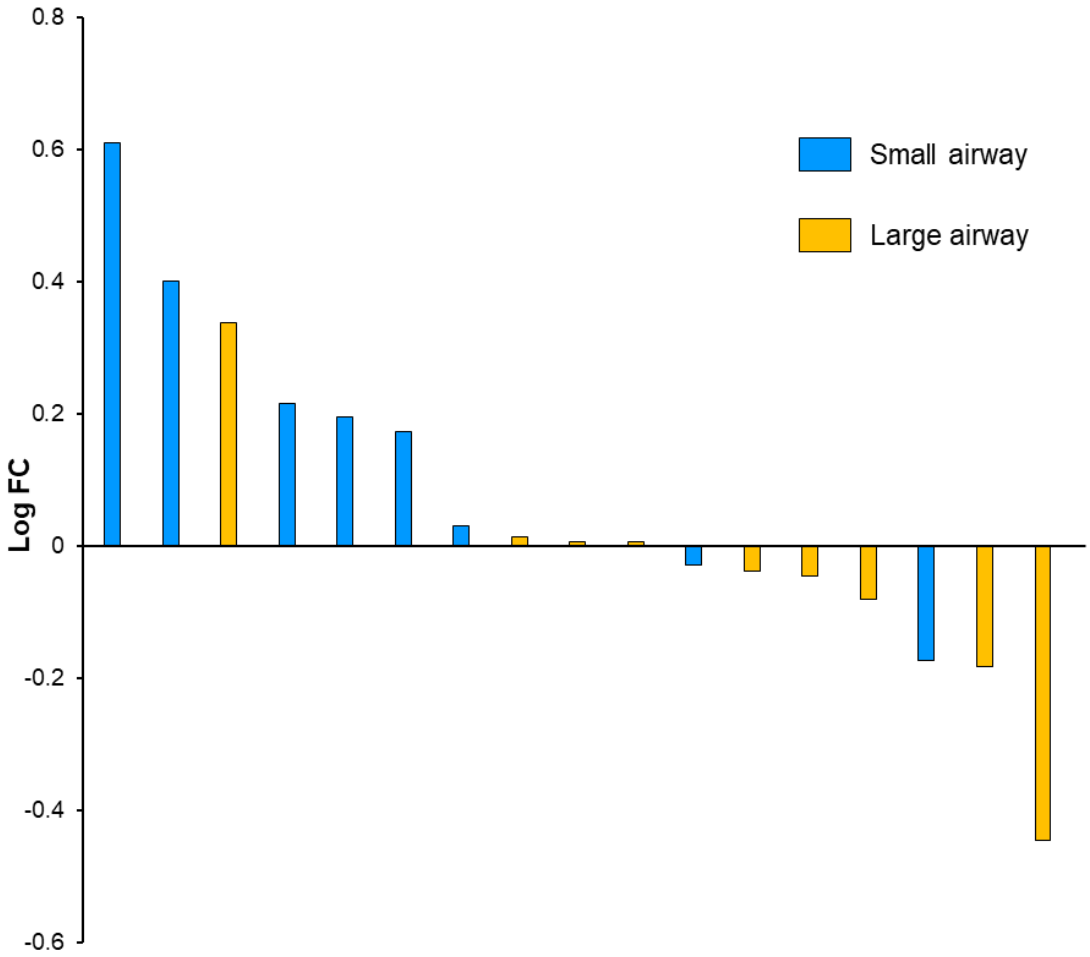

Supplementary Fig. 2.4. IL13RA1 gene expression comparison between cigarette smokers and non-smokers. Log fold change (Log FC) compares the gene expression levels in cigarette smokers versus non-smokers.

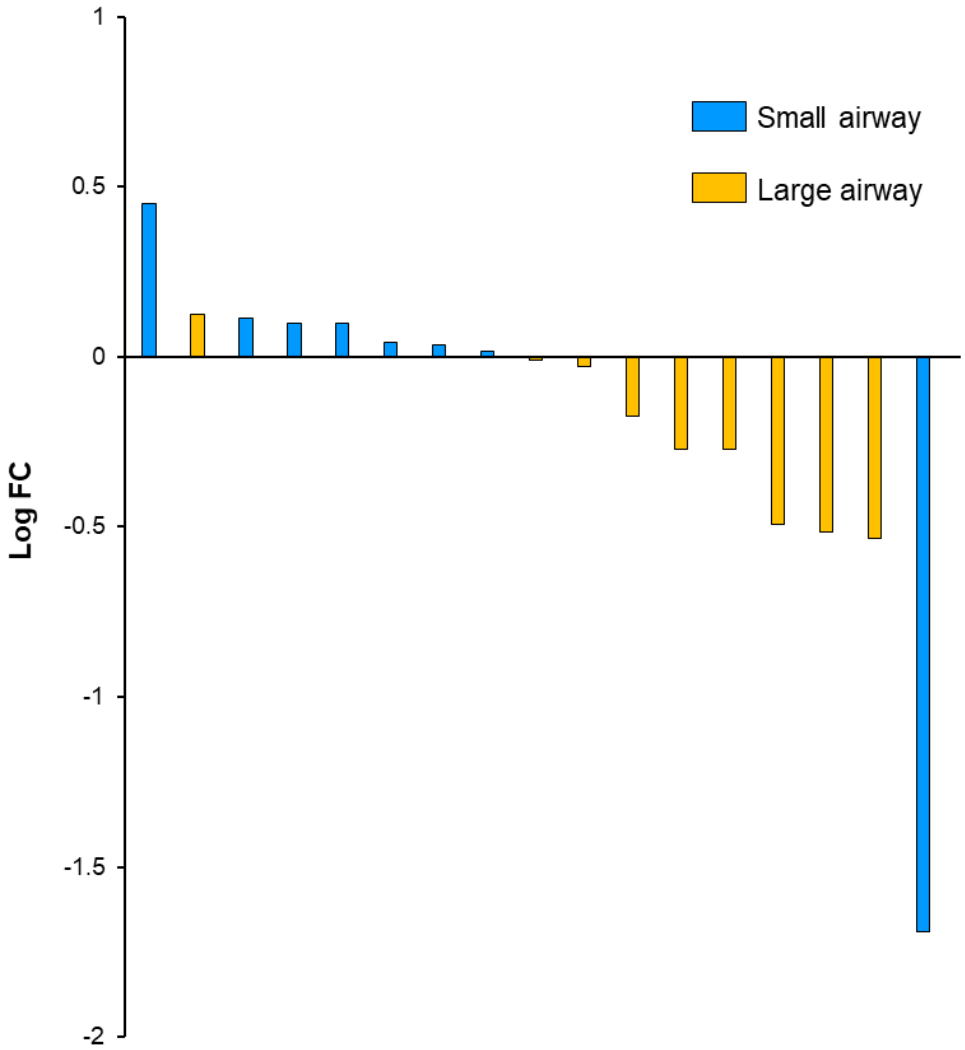

Supplementary Fig. 2.5. IL13RA2 gene expression comparison between cigarette smokers and non-smokers. Log fold change (Log FC) compares the gene expression levels in cigarette smokers versus non-smokers.

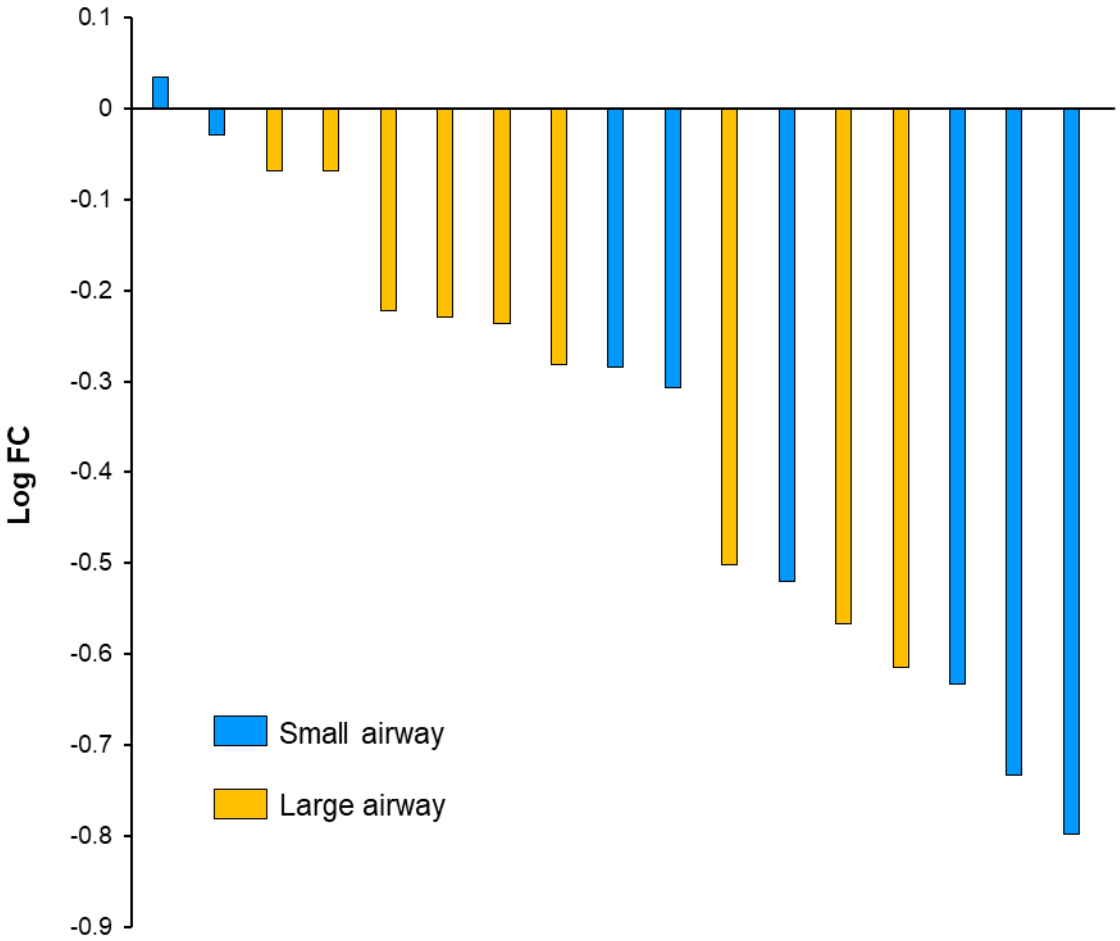

Supplementary Fig. 2.6. IL4R gene expression comparison between cigarette smokers and non-smokers. Log fold change (Log FC) compares the gene expression levels in cigarette smokers versus non-smokers.